UCLouvain

École polytechnique de Louvain

Atomic collision processes limiting the efficiency of negative ion beam production relevant to fusion plasma heating

Author: **Arnaud Schils**
Supervisor: **Xavier Urbain**
Readers: **Benoit Hackens, Clément Lauzin**
Academic year 2018–2019
Master [120] in Physical Engineering

Abstract

The International Thermonuclear Experimental Reactor (ITER) experiment aims to demonstrate the feasibility of fusion energy. To reach ultra-high temperatures required to overcome the Coulomb repulsion between nuclei and initiate their fusion, plasma confined in a tokamak is heated up by momentum transfer from a highly energetic neutral beam. This neutral beam is created by neutralization of electrostatically accelerated negative ions D^-.

This pushes the need for efficient negative ions sources. Inside these sources, a plasma is created in a Deuterium gas. This plasma is composed of many different compounds: neutrals (D, D_2), anions (D^-), cations(D^+, D_2^+, D_3^+) all possibly in an excited state.

This master thesis focuses on the mutual neutralization of D_2^+ with D^- that happens in the plasma of negative ions source. The experimental spectrum of the kinetic energy released by this mutual neutralization reaction is compared to computational and theoretical results. The goal is to find out the dominant output channel between $D_2^* + D$ and $D_2 + D^*$. Results tend to point out the dominance of the first one with the favored electronically excited states D_2^* being the singlets $3s^1\Sigma_g^+(H\bar{H})$, $3d^1\Sigma_g^+(GK)$ and $3p^1\Sigma_u^+(B')$.

The output channel $D + D + D$ has also been studied from measurements performed with a three-body detection system. Analysis of the experimental kinetic energy release spectrum reveals the passage by some triplet states of D_2^* which dissociates by radiative coupling to the dissociative state $D_2(b^3\Sigma_u^+)$.

Acknowledgments

La fin de ce mémoire marque la fin d'un marathon de 3.02π années d'étude passées dans mon Alma Mater, l'Université Catholique de Louvain [1]. Je commence par remercier cette institution, et tout l'écosystème qui s'y rattache, qui offre un cadre si propice à l'apprentissage et au bien être de ses étudiants.

Je remercie évidemment mon promoteur, le Professeur Xavier Urbain. Tout d'abord pour m'avoir permis de réaliser un mémoire de recherche sur des thématiques inexplorées jusqu'à ce jour intéressantes et utiles. Je le remercie également pour sa grande patience puisqu'il a fallu de nombreuses explications afin de me familiariser avec le monde fort complexe de la physique atomique et moléculaire expérimentale.

Cette discipline constitue en effet un cocktail assez détonnant de complexité pour un nouveau venu, mêlant multiplicité de modèles théoriques, subtilités expérimentales, traitement de données, développement (débugage) informatique,... Je le remercie également pour ses nombreuses relectures détaillées, ses retours rapides sur mon travail, les nombreux courriels échangés et sa disponibilité.

Je remercie les différents membres du NAPS m'ayant aidé dans la réalisation de mon travail. Tout d'abord le Docteur Thibaut Launoy pour son aide dans le débugage du modèle Landau-Zener multi-canal et la figure de la source d'anions. Ensuite Arnaud Dochain pour les explications, les codes et les figures. Je remercie aussi le Docteur Jérôme Loreau pour son aide par rapport aux valeurs de certaines variables dans le modèle Landau-Zener.

Je remercie également le Professeur Bernard Piraux pour l'article sur la normalisation des fonctions d'onde du continuum. Je tiens à remercier aussi mes deux lecteurs les Professeurs Benoit Hackens et Clément Lauzin qui ont accepté de donner de leur temps pour lire ce manuscrit et assister à ma défense de mémoire.

Enfin je remercie le NAPS pour les nombreux cafés.

[1] Certaines statistiques amusantes: 104 unités créditées pour un total de 543 crédits, 24 blocus ou encore $\approx$ 2 ans de blocus.

Contents

Introduction

The growing need for clean and secure energy sources has pushed mankind to develop alternatives to both fossil and nuclear fission energy. Such ideal energy sources are already at work for several billion years in the whole universe. This source of energy is the nuclear fusion, occurring in the stars, which allows them not to collapse on themselves under the effect of gravitational attraction. Moreover, nuclear fusion in stars makes possible stellar nucleosynthesis, i.e. the production of heavier atoms essential for life, from lighter atoms such as Hydrogen, Helium and Lithium produced during the Big Bang.

The International Thermonuclear Experimental Reactor (ITER) organization, which brings together more that 35 countries from all around the world, aims to bring back fusion energy to Earth. The goal of ITER is to construct the first nuclear fusion facility able to produce ten times the amount of power consumed: a 50 MW input must produce a 500 MW output.

However, ITER is only a milestone towards the construction of long run operating fusion power plants. The first objective is indeed to test technologies in real plasma conditions and demonstrate the feasibility of energy efficient nuclear fusion reactor. Use of ITER will consist in many small experiments for a 400 hours total use time.

The post-ITER project planned for 2040, named the "DEMOnstration Power Plant" (DEMO), aims to achieve a 25 times energy gain ratio by producing 2000 MW from a 80 MW consumption. The advent of DEMO should be followed by the first industrial prototypes of nuclear fusion power plants.

Principle of nuclear fusion

Nuclear fusion is the production of a heavier nucleus from the fusion of two lighter nuclei. This fusion results from the strong nuclear force which is a short range attractive force between nuclei (see Figure 1). Let R be the inter-nuclei distance, this strong nuclear force is repulsive for $R \lesssim 0.7$ fm, vanishes for $R \gtrsim 3$ fm and is attractive for $0.7 \lesssim R \lesssim 3$ fm. The mechanism underlying the strong nuclear force is the more fundamental strong interaction. However, the electric force between two nuclei is repulsive and works against their fusion. In comparison with the strong nuclear force, the electric force has a much

longer range, decreases much less with R and is repulsive for any R.

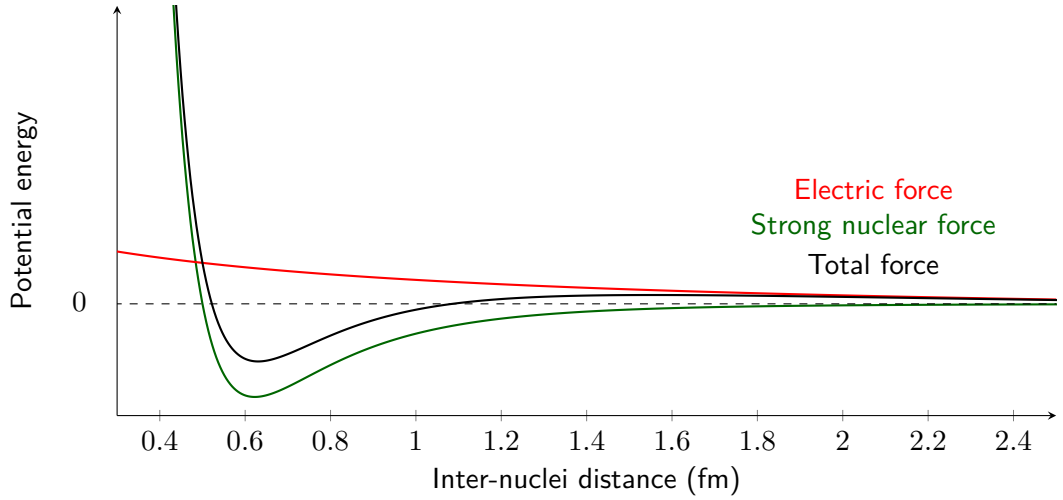

Figure 1: Evolution of the potential energy of a two light nuclei system with the inter-nuclei distance.

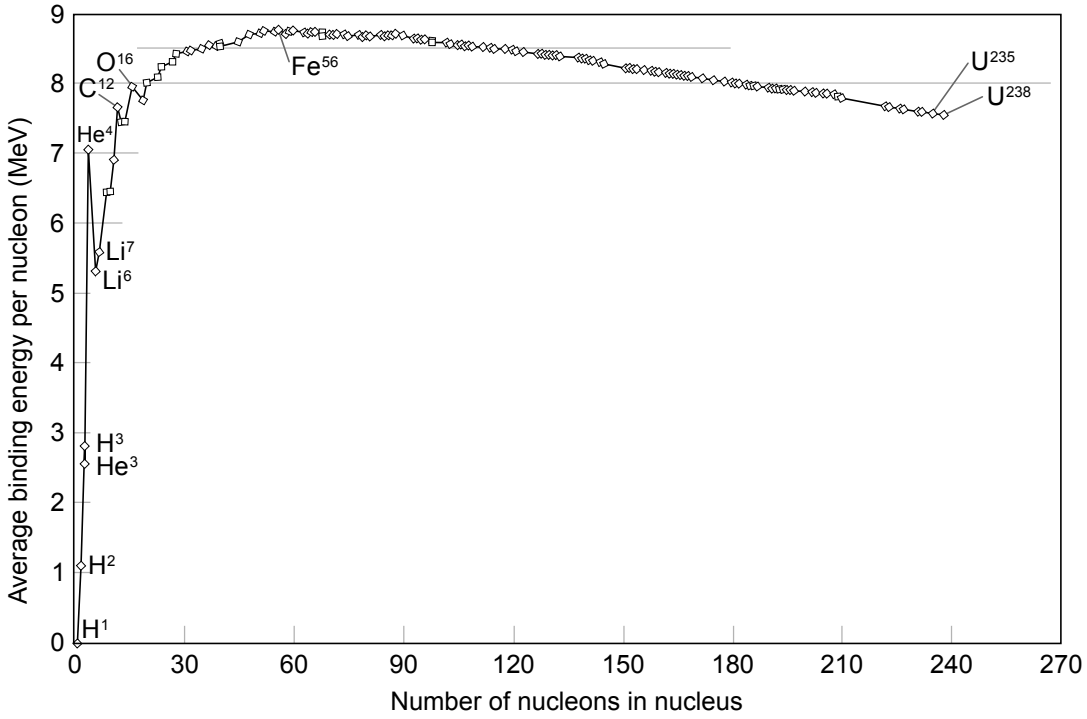

Figure 2: Evolution of the binding energy per nucleon with respect to the number of nucleons in the nucleus. Figure source [1].

The range of the strong nuclear force exceeds the nuclear volume for nuclei composed of few nucleons. In this case, the addition of more nucleons increases the binding energy and is therefore energetically favorable (see Figure 2). As nucleons are added and the nucleus volume increases, the range of the strong nuclear force becomes comparable to the nuclear radius.

From this point, additional protons are more repelled by electric force than they are attracted by strong nuclear force. Adding neutrons is more favorable because it does not involve Coulomb repulsion. The binding energy is maximum for Iron nucleus composed of 26 protons and 30 neutrons. Therefore, nuclei become more stable when their number of nucleons gets closer to that of Iron.

Nuclear fusion is therefore easier to achieve with light nuclei and when neutrons help to reduce Coulomb repulsion between protons in the nucleus. It is why fusion at ITER will be achieved merging two isotopes of Hydrogen, the Deuterium (1 proton, 1 neutron) and the Tritium (1 proton, 2 neutrons):

$$^{2}_{1}\mathrm{D} + ^{3}_{1}\mathrm{T} \rightarrow ^{4}_{2}\mathrm{He}(3.5\ \mathrm{MeV}) + ^{1}_{0}\mathrm{n}(14.1\ \mathrm{MeV}). \tag{1}$$

Lawson et al. [2] report that the minimum temperature required for this fusion reaction is 30 millions °K which is therefore far less than the 150 millions °K required for fusion of two Deuterium atoms:

$$^{2}_{1}\mathrm{D} + ^{2}_{1}\mathrm{D} \rightarrow ^{3}_{1}\mathrm{T}(1\ \mathrm{MeV}) + ^{1}_{1}\mathrm{p}(3\ \mathrm{MeV}). \tag{2}$$

Advantages of nuclear fusion with respect to other energy sources

This section explains why nuclear fusion is the Holy Grail of energy production.

Firstly, fusion reactions release a huge amount of energy. Because the nucleus produced by a fusion reaction has a greater binding energy than the two reagents, an excess of energy ΔE is released. This excess of energy is computed from the difference between the mass of the reagents and the mass of the products. For reaction (1) it yields:

$$\begin{aligned}\Delta m &= m_{\mathrm{D}} + m_{\mathrm{T}} - m_{\mathrm{He}} - m_n \\ &= (2.014102 + 3.016050 - 4.002603 - 1.008665)m_p = 0.0188884 m_p,\end{aligned} \tag{3}$$

where m_{D} is the Deuteron mass [2], m_{T} the Triton mass, m_{He} the Helium four nucleus mass, m_n the neutron mass and m_p the proton mass. The energy produced by one fusion reaction is then:

[2]The term Deuteron/Triton refer to the nucleus of the Deuterium/Tritium atom.

$$\Delta E = \Delta mc^2 = 0.0188884\ 1.66056\ 10^{-27}\ \text{kg}\ 3^2\ 10^{16}\text{m}^2/\text{s}^2 = 2.7\ 10^{-12}\text{J}. \quad (4)$$

A single mole of Deuteron reacting with a single mole of Triton then produces:

$$\Delta E = 2.7\ 10^{-12}\ N_A\ \text{J}\ \approx 1.6\ \text{TJ}. \quad (5)$$

The energy per nucleon produced by nuclear fusion is one order of magnitude higher than the one produced by nuclear fission of Uranium 235.

Secondly, nuclear fusion is a clean energy source. It only produces short-lived radioactive wastes. Radioactive wastes are only a problem when their lifetime is intermediate. Indeed, short lifetime (a few years) compounds can easily be stored underground until they lose their radioactivity. As for long lifetime (millions of years) compounds they are weakly radioactive and not much harmful. The main product of fusion is Helium four which is a non-toxic gas very useful in cryogenic applications. Moreover, fusion does not emit greenhouse gases.

Thirdly, fusion fuel, i.e. Deuterium and Tritium, is easily found. Deuterium is abundantly available in seawater and retrieved by distillation from there. Tritium is synthesized by the interaction of the tokamak walls with neutrons produced by the fusion reaction itself. These walls are covered with materials such as Li_2TiO_3 and Li_4SiO_4. Lithium in these materials interact with neutrons as follows:

$$^6_3\text{Li} + \text{n} \rightarrow {}^4_2\text{He} + {}^3_1\text{T}. \quad (6)$$

This Tritium production process is named Tritium breeding. There are vast reserves of Lithium required for Tritium breeding on land and in the sea.

Fourthly, energy produced by nuclear fusion is eventually expected not to be more expensive than the one produced by fission.

Finally, fusion energy is safe. Indeed, conditions for fusion would not be satisfied as soon as the reactor would adopt a faulty behavior. In this case, the plasma would cool down quickly and the fusion would stop.

Condition for a self-sustaining plasma

To induce nuclear fusion, the potential barrier due to Coulomb repulsion must be overcome. Two parameters can be tuned to ease the crossing of this potential barrier:

1. The temperature T, which means increasing the average kinetic energy between the nuclei. Nuclear fusion reactions occur at very high temperatures (a few millions kelvin). At these temperatures, the gas if fully ionized, i.e. is composed of nuclei

and free electrons. This state of matter is named a plasma and is the most common phase of matter in the universe.

2. The density of nuclei n_n.

A major difficulty is to minimize energy loss in order to maintain high temperature and to stay in the plasma state in the long run. Fusion reactions must produce at least enough power P_f to maintain the plasma temperature, i.e. to compensate for power loss P_l:

$$P_f \geq P_l. \tag{7}$$

Power is lost due to emission of light (radiation) and due to the particles leaving the plasma carrying away their energy (conduction) [2].

Considering the plasma as a perfect gas in addition to assuming identical temperatures and densities of electrons and nuclei (i.e. $T_e = T_n = T, n_e = n_n = n$), the energy density of the plasma writes:

$$E = \frac{3}{2} k_b (n_n T_n + n_e T_e) = 3 n k_b T, \tag{8}$$

where k_b is the Boltzmann constant. Let n_D and n_T be the densities of Deuteron and Triton, respectively. From Collision theory, the frequency of fusion reactions per unit volume f_f writes:

$$f_f = n_D n_T < \sigma v >, \tag{9}$$

where v is the speed of a nuclei and σ the nuclear fusion cross section [3]. The average $< \sigma v >$ has to be computed over the Maxwell velocity distribution and its increase with temperature is found to be approximately quadratic, i.e. $< \sigma v > \propto T^2$. Assuming each fusion reaction produces an energy E_f and $n_D = n_T = n/2$, the total power produced by the fusion reactions in the tokamak is:

$$P_f = E_f f_f = n_D n_T < \sigma v > E_f = \frac{n^2}{4} < \sigma v > E_f. \tag{10}$$

The condition for the plasma to be self-sustained (Equation (7)) then becomes:

$$\frac{n^2}{4} < \sigma v > E_f \geq P_l. \tag{11}$$

[3] The cross section of the interaction between two particles is the area transverse to their relative motion within which they must meet in order to interact.

The energy containment time τ_E is defined as the plasma energy density over the power loss by unit volume: $\tau_E = E/P_l$. It quantifies the rate at which a system loses energy to the environment. Introducing this quantity in the previous equation yields:

$$\frac{n^2}{4} < \sigma v > E_f \geq \frac{3nk_bT}{\tau_E} \Leftrightarrow n\tau_E \geq \frac{12k_bT}{E_f < \sigma v >}. \tag{12}$$

The inequality presented in Equation (12) is called the Lawson criterion. Figure 3 shows that this criterion for the plasma to be self-sustained is most easily satisfied for the fusion between Deuteron and Triton.

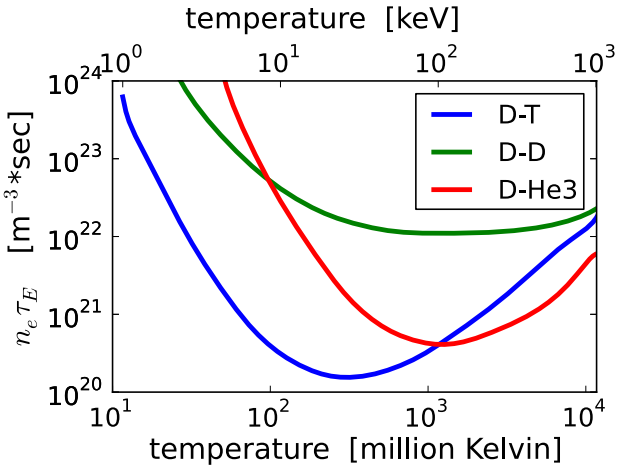

Figure 3: These curves show the minimum product of the energy containment time τ_E with the electron density $n_e = n$ required for the plasma to compensate itself the power loss due to radiation and conduction. The fusion reaction between Deuteron and Triton minimizes this product which explains its use in ITER. Figure source [2].

The quadratic dependence of $< \sigma v >$ with T in the considered temperature range implies that the Lawson criterion is more easily satisfied at high temperature:

$$n\tau_e T \geq \frac{12k_b}{E_f < \sigma v > /T^2}. \tag{13}$$

Magnetic confinement of plasma

High densities n are achieved by ITER thanks to magnetic confinement which is possible because all particles in the plasma are electrically charged (excepting neutrons). Transfer of energy by conduction is only possible to other particles in the plasma. Therefore, energy loss using magnetic confinement is lower than when using mechanical confinement.

Mechanical confinement is anyway currently impossible since most materials existing at this day would melt in contact with plasma.

To easily describe the behavior of charged plasma particles under the influence of a uniform magnetic field $\vec{B}$ two assumptions are made. Firstly, the inter-particles interaction are neglected with the exception of collisions inducing fusion. Secondly, the electromagnetic field created by motion of the plasma charged particles is neglected. These approximations constitute the so called single-particle approach. A Lorentz force

$$\vec{F} = q\vec{v} \times \vec{B} \tag{14}$$

is obviously applied on the charged particles, q being the particle electric charge and $\vec{v}$ its velocity. Under the effect of this force, particles undergo an helical motion with a radius of gyration r_c:

$$r_c = -\frac{mv_\perp}{qB}, \tag{15}$$

where m is the particle mass and $v_\perp$ the velocity component perpendicular to the magnetic field $\vec{B}$. Since particles with different masses, charges and velocities compose the plasma one value of B is associated to a range of radii of gyration. Defining r_m as the maximum radius of gyration and assuming that the volume V occupied by the plasma is proportional to r_m^2:

$$n = \frac{N}{V} \propto \frac{1}{r_m^2} \propto B^2, \tag{16}$$

where N is the total number of charged particles in the plasma. Equation (16) shows that increasing the magnetic field decreases the radius of gyration and therefore increases the confinement.

There are two different doughnut-shaped geometrical setups designed to magnetically confine plasma: stellarators and tokamaks [3]. ITER uses the later. The difference between stellarators and tokamaks is the existence of a plasma current contributing to the effective magnetic field in tokamaks.

There are three magnetic fields in the tokamak: the toroidal, poloidal and vertical fields [3]. The toroidal field is generated by coils traversed by the torus and its lines are oriented along the torus (field B_φ in Figure 4). Its main purpose is to contain the plasma. However, the magnetic field generated by a current I flowing in a circular loop of radius a is not homogeneous. Indeed the field in the direction z of the symmetry axis of the loop depends on the radial distance r from the center of the loop [4]:

$$B_z = -\frac{\mu_0 I a^2}{4(a^2+r^2)^{5/2}} \left[2a^2 - r^2 + \frac{15a^2r^2(4a^2-3r^2)}{8(a^2+r^2)^2} + ... \right], \tag{17}$$

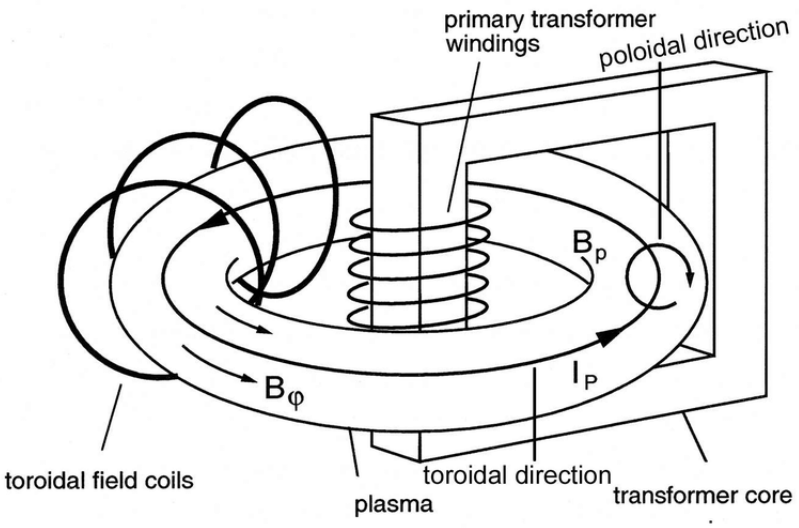

Figure 4: Magnetic fields, coils, plasma current and transformer in the ITER tokamak. The toroidal field B_φ created by the toroidal field coils confines the plasma. The poloidal field B_p induced by the plasma current I_p stabilizes the plasma. The plasma current I_p is increased by inductive coupling between the primary transformer windings and the plasma torus. Figure source [5].

where μ_0 is the vacuum permeability. Consequently, the toroidal field is the strongest at the center of the torus and weakens with the distance from the center. Under the effect of this gradient of magnetic field, particles drift towards the walls of the tokamak, i.e. outside the plasma torus. The presence of the poloidal field solves this issue.

The poloidal field is generated by the plasma current itself and its lines form circles in the plane perpendicular to the plasma current direction (field B_p in Figure 4). The combination of the toroidal and poloidal fields yields helical field lines in the torus [4] (see Figure 5). The helical field contains the plasma inside a torus far enough from the toroidal coils. Thanks to this helical field, the drift effect is averaged to zero.

The plasma current and therefore the intensity of the poloidal field are controlled by electromagnetic induction. Varying the current flowing in a solenoid concentric with the torus (primary transformer windings in Figure 4) induces a varying magnetic flux in the solenoid and in the plasma loop. An electromotive force then appears in the plasma torus to oppose this change of flux which increases the plasma current. This process heats the plasma by Joule effect due to its non-zero electrical resistance.

Finally, the vertical field prevents plasma diffusion. When plasma particles move at really high speeds, collisions may result in high velocity in the direction perpendicular to the plasma current. Consequently, particles may move to other field lines. After

[4] In stellarators, this helical field is obtained with helical coils wrapping up the torus rather than by combination of a field induced by the plasma current with a toroidal field.

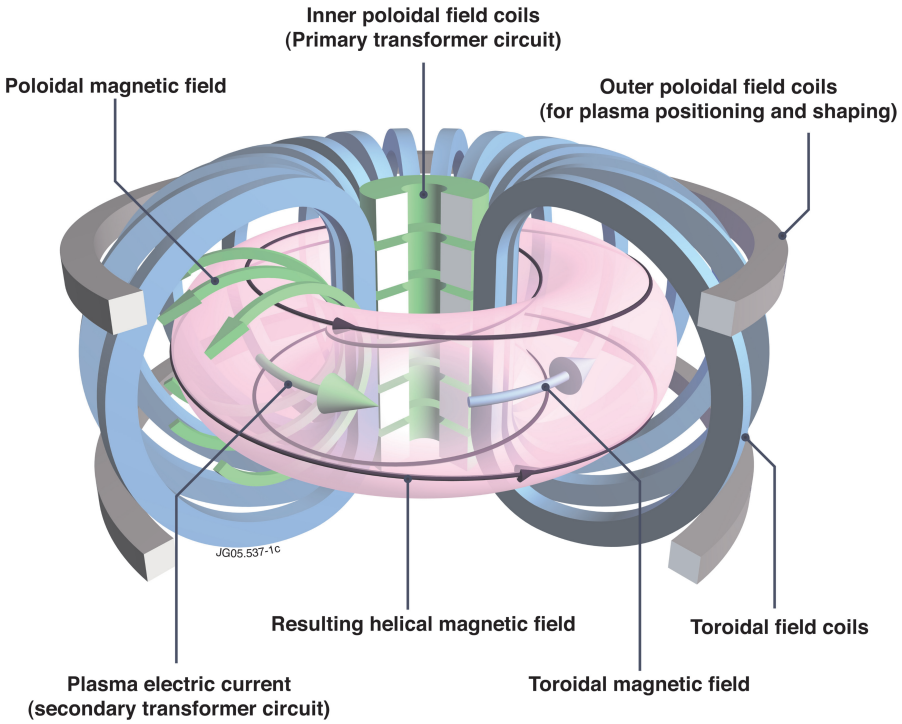

Figure 5: Outer poloidal field coils in the ITER tokamak prevents plasma diffusion keeping it away from the walls. Figure source [6].

some time, the whole plasma may drift to the walls of the tokamak. The vertical field, generated by the outer poloidal field coils (see Figure 5) keeps the plasma away from the walls.

Plasma heating

As for reaching very high plasma temperatures, ITER proceeds as follows. Temperature is firstly increased by ohmic heating: a changing magnetic is applied in the tokamak. Plasma charged particles are accelerated under the effect of the Lorentz force therefore increasing their speed, energy and temperature. The increase of temperature propagates by collision of particles in the plasma. These collisions cause electrical resistance and heating by Joule effect. From a certain temperature, the resistance tends to zero and the ohmic heating is not able to increase temperature anymore.

Two methods are investigated at the Joint European Torus (JET) in Oxford to further increase the temperature. The first one is heating by microwaves. Energy of plasma particles is increased by absorption of high frequency electromagnetic waves whose wavelengths land in their absorption spectrum. The second one is heating by neutral beam injection. Neutral beams are injected tangentially in the tokamak to heat the plasma by

momentum transfer. These neutral beams are produced by neutralizing electrostatically accelerated Deuterium negative ions. This work focuses on atomic collisions processes occurring in these negative ions sources.

Terminology of atomic collisions processes

This sections introduces the terminology of some physical processes occurring when two atoms or molecules collide. In a mutual neutralization reaction, an anion is neutralized by losing one or several electrons to a cation yielding only neutral products in the output channel:

$$A^+ + B^- \rightarrow A + B. \tag{18}$$

When an exchange of electrons between two reagents produces ions in the output channel:

$$A^+ + B \rightarrow A + B^+, \tag{19}$$

the reaction is simply named a charge exchange reaction.

The reaction is said to be dissociative if a molecular reagent dissociates due to the charge exchange:

$$\begin{cases} (AB)^+ + C^- \rightarrow A + B + C, \\ (AB)^+ + C \rightarrow A + B + C^+. \end{cases} \tag{20}$$

A molecule is said to dissociate when the separation of its constituents is performed by transition to a dissociative state. A dissociative state is unstable and characterized by an unbound or repulsive potential energy: there is no minimum in the potential energy which smoothly decreases with increasing inter-atomic distance while the atoms repel each other. A dissociative state has continuum vibrational energy levels. The kinetic energy released by the dissociation and carried out by the fragments is the energy of one dissociative state. Therefore, the spectrum of the kinetic energy release is a continuum. For example, transition to the dissociative state $D_2(b^3\Sigma_u^+)$ of D_2 can occur by electron capture of the molecular ion D_2^+ or by radiative transition from excited electronic states D_2^*.

A molecule predissociates when the separation of its constituents is due to rovibrational coupling with a dissociative state of same energy. The electrons rearrange internally to an unbound state. In this case, the kinetic energy released by the reaction and carried out by the fragments is the potential energy of the molecule. Therefore, because molecular energy levels are discrete, the spectrum of the kinetic energy release is composed of discrete peaks. For example, many excited states D_2^* are predissociative. The lifetime of predissociative states is most often very short (≈ 1 ps).

Overview of the contributions

In this work, results from an experiment measuring the kinetic energy in the center of mass frame of fragments produced by reactions involving ions have been analyzed.

The first contribution is the development of a software developed in the *python* programming language to compute the cross section of reactions occurring when a cation beam and an anion beam overlap in a confluent beam configuration. This software takes as input measurements and parameters of the experiment. It computes the evolution of the cross section with the relative energy of the reagents and with the observation potential. A graphical user interface (GUI) allows the user to easily input parameters and to specify the results output file as well as input signal and background files. The GUI displays relevant plots allowing the user to zoom in and out and to save the plot in many different formats. User inputs undergo a sanity check and limit cases are properly handled to avoid faulty behavior of the software. The software has been used for months in the laboratory always yielding valid results.

The second contribution is the development of scripts allowing to quickly compute the vibrational levels of an electronic bound or unbound molecular state. It is achieved by solving the Schrodïnger equation for 1D potentials of the molecular states of interest. The developed script selects the boundaries and the step of the numerical domain automatically for bound molecular states. Obtained eigenvectors and eigenvalues have been successfully computed for more than 20 different potentials including double-well potentials. Results have proved to match those found in the literature [7].

The third contribution is the study of the high-energy interaction between the molecular cation D_2^+ and the residual gas of the experiment vacuum chamber. Computational results of the kinetic energy released by the dissociative charge exchange reaction:

$$D_2^+ + H_2 \rightarrow D + D + H_2^+ \tag{21}$$

perfectly match the experimental kinetic energy release (KER) spectrum. This reaction therefore explains experimental results.

The fourth contribution is the study of the mutual neutralization of the molecular cation D_2^+ with the anion D^-, a physical process occurring in negative ions sources. Experimental kinetic energy released by reactions yielding two products in the output channel has first been measured with a two-body detection system. This experimental spectrum has been compared to computational spectra yielded by the two reactions:

$$D_2^+(v) + D^- \rightarrow \begin{cases} D_2^*(\Lambda, v') + D, \\ D_2(v') + D^*, \end{cases} \tag{22}$$

where v, v' are any of the possible vibrational levels and Λ is any of the many possible excited electronic levels. Results obtained with the Franck-Condon matrix and from the

multi-channel Landau-Zener model exclude the excited atomic Deuterium output channel. Moreover, results show that the following electronically excited states D_2^*, the singlets $3s^1\Sigma_g^+(H\bar{H})$, $3d^1\Sigma_g^+(GK)$ and $3p^1\Sigma_u^+(B')$, are visible in the experimental spectrum. However, the high number of events for KER between 1.3 and 2.3 eV is not explained by the results. This highlights the preliminary nature of the available theoretical models which do not properly and extensively deal with rovibrationally excitation.

Finally, experimental kinetic energy released by the dissociative mutual neutralization between D_2^+ and D^- yielding three products in the output channel has been analyzed with a three body detection system. Because one of the three detectors is not position-sentitive, the first step was to find a way to compute the KER without knowing the detection position of the third fragment while removing as much background as possible. The second contribution is the computation, by software-assisted simulation, of the acceptance of the three-body detection system. Then, analysis of the obtained KER spectra reveals that detected three-body events are produced by radiative transitions from gerade $N = 2, 3$ triplet states of D_2^* to the dissociative state $D_2(b^3\Sigma_u^+)$.

Organization of the Master's Thesis

This master thesis is organized in seven chapters. The remainder of this manuscript is structured as follows:

- Chapter 1 explains the operation of negative ions sources, their importance for plasma heating and how this master thesis helps to better understand how they work.
- Chapter 2 presents the two and three-body experimental setups used to measure the kinetic energy release by studied atomic and molecular reactions.
- Chapter 3 shows how the cross section of confluent beams is computed. The software developed to compute this quantity is presented.
- Chapter 4 explains how the vibrational levels of D_2^+, D_2, $D_2(b^3\Sigma_u^+)$ and D_2^* have been computed by solving the 1D time-independent Schrodïnger equation with a matrix-based method.
- Chapter 5 compares experimental and computational KER for the dissociation of D_2^+ due to charge exchange with the residual gas of the vacuum chamber. The reasons of the interest in this reaction are explained.
- Chapter 6 presents the computation of the kinetic energy released by mutual neutralization of the molecular cation D_2^+ with the anion D^- to the many possible output channels. The output channels $D_2^* + D$ and $D_2 + D^*$ are investigated to find out the one explaining better the experimental KER spectrum.

- Chapter 7 is about the three-body experiment. The processing of the experimental data is detailed: experimental KER computation from measurements, acceptance correction and background removal. Obtained KER spectra are presented and interpreted.
- Appendix A gives the vibrational states of D_2^+ and of a number of electronic states of D_2^*.

Chapter 1

Negative ions sources for production of high energy neutral beams heating up plasma in nuclear fusion tokamaks

High current density beams of D^- and H^- have many applications in various domains such as production of radioisotopes for the pharmaceutical industry, surface treatments, high-energy accelerators and nuclear fusion [8]. This Chapter focuses on this last application, i.e. the important role of negative ions sources in the International Thermonuclear Experimental Reactor (ITER) experiment which aims for development of efficient nuclear fusion. The goal of this Chapter is also to explain how this work contributes to better understanding and design of negative ions sources.

Negative Deuterium beams D^- are indeed used to produce high energy large flux neutral beams of Deuterium D [9]. A plasma current is first produced and heated up in the tokamak by electromagnetic induction. Once the whole plasma is ionized, its ohmic resistance drops sharply and the heating stops. The neutral beam injectors (NBI) then inject the neutral beam in the plasma confined in the tokamaks to heat further up the plasma by transfer of momentum from the neutral beam to the particles composing the plasma [10]. These neutral beams are produced by accelerating with electromagnetic fields the anions D^- before neutralizing them [11].

Neutral Deuterium beams can also be produced by neutralizing D^+ cations beams. However, at the required beams energy [1], neutralization of cations is very inefficient (the probability of electron capture by D^+ cation is too low), which explains the preference for anions beams.

Performance of the ITER Heating NBI depends on many aspects such as the uniformity

[1] More precisely when the kinetic energy of the cation is greater than 60 keV/amu [10].

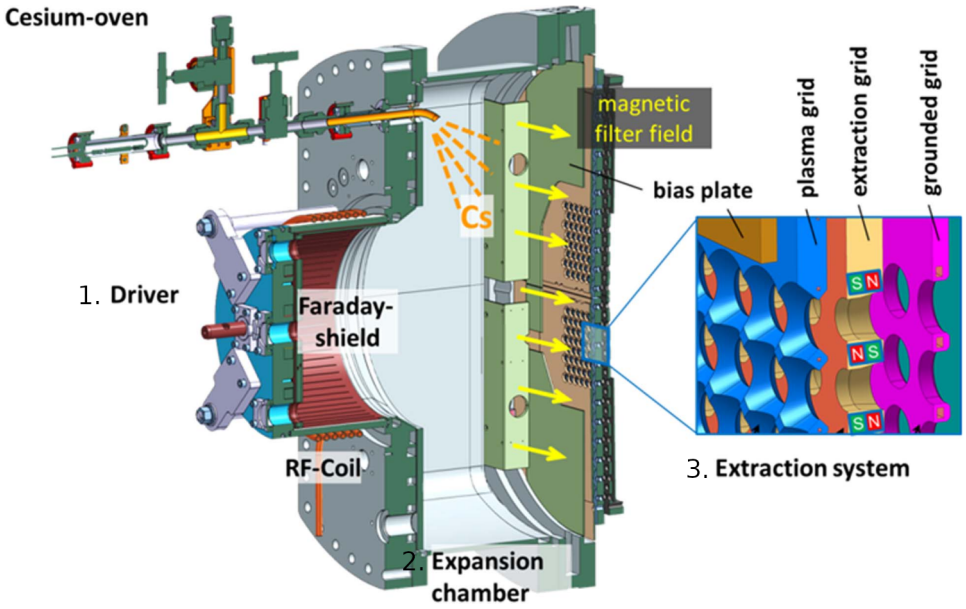

Figure 1.1: Cross section through SPIDER. Figure source [13].

and density of the produced anionic beam, the development of materials able to sustain high heat loads and the capacity to maintain the high voltage required to obtain a 40 A beam with 1 MeV particle energy [11].

The operation of the NBI is composed of four main steps. The first step is the production of the anions. The second step is the extraction of the anions from the source. The third step is the acceleration of the anions. Finally, the last step is the neutralization of the anionic beam. These two first and two last steps are explained in the first and second sections of this Chapter, respectively. The last section shows why the mutual neutralization reaction $D_2^+ + D^-$ is important for negative ions production.

1.1 Anions production and extraction

The ions source used by NBI, named "The source for productions of ions of deuterium extracted from RF plasma (SPIDER)", is composed of three parts [12] (see Figure 1.1).

The first part is the cylindrical driver responsible for the generation and sustainability of the plasma using radio-frequency (RF) coils [13] (see Figure 1.2). This driver is a quartz or Al_2O_3 cylinder surrounded by a six turns RF coil. A Faraday shield protects the inside of the driver from plasma erosion. Vertical slits in this shield nevertheless allow the passage of the magnetic RF field.

A small filament and a pressure increase are required to start the plasma, i.e. to create some first free electrons and cations. A 180kW alternative current power supply working

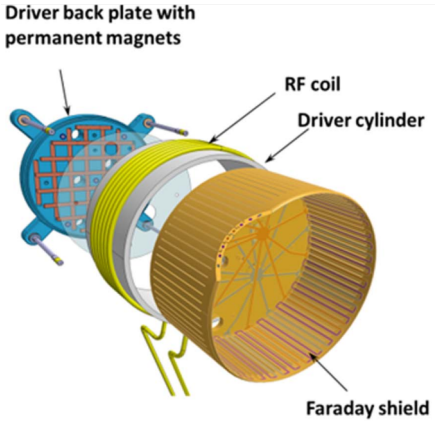

Figure 1.2: Exploded view of the driver. Figure source [13].

at 1 MHz is connected to the external coil. When AC current flows in the coil, this generates by induction an oscillating magnetic field below and above the coil. This in turns generates a primarily azimuthal RF electric field [14] which starts an electrons avalanche creating the plasma.

RF sources have been chosen instead of arc driven sources because they are maintenance free and without evaporation of Tungsten [13]. Another advantage of RF sources is that there are more possible wall materials. It offers more flexibility to optimize surface production of anions with respect to filament sources. Indeed, in filament sources inner walls are coated with Tungsten from the filaments during operation [13]. Furthermore, RF sources are modular. Large source such as SPIDER can be created by adding many drivers to one common expansion chamber. This expansion chamber is the second part of SPIDER and is a rectangular expansion region where the plasma expands. Note that, even when there are many drivers, only a single small filament in one of them is enough to start the plasma.

The last part is the extraction region. There are three grids in the extraction region: the plasma grid in contact with the source and on which Caesium has been deposited for anions production, the extraction grid which uses a magnetic field to remove electrons while keeping the anions and the grounded grid (see Figure 1.1).

1.1.1 Anions production

SPIDER produces D^- negative ions in two ways. The first one is by dissociative attachement of electrons to ro-vibrationally excited Deuterium molecules in the plasma volume [11, 15]:

$$\mathrm{e} + \mathrm{D}_2(\mathrm{X}^1\Sigma_\mathrm{g}^+, \mathrm{v}) \rightarrow \mathrm{D}_2^-(\mathrm{X}^2\Sigma_\mathrm{u}^+) \rightarrow \mathrm{D}^- + \mathrm{D}(1\mathrm{s}), \tag{1.1}$$

$$\rightarrow \mathrm{D}_2^-(\mathrm{B}^2\Sigma_\mathrm{g}^+) \rightarrow \mathrm{D}^- + \mathrm{D}(1\mathrm{s}), \tag{1.2}$$

$$\rightarrow \mathrm{D}_2^-(\mathrm{N}_\mathrm{i}^2\Lambda_\mathrm{g}) \rightarrow \begin{cases} \mathrm{D}^- + \mathrm{D}(1\mathrm{s}), \text{ if } \mathrm{N_i} \geq 2, \\ \mathrm{D}^- + \mathrm{D}(\mathrm{n} \geq 2) \text{ otherwise}, \end{cases} \tag{1.3}$$

$$\mathrm{e} + \mathrm{D}_2^*(\mathrm{N}^{1,3}\Lambda_\mathrm{g}, \mathrm{v}) \rightarrow \mathrm{D}_2^-(\mathrm{N}_\mathrm{i}^2\Lambda_\mathrm{g}) \rightarrow \mathrm{D}^- + \mathrm{D}(\mathrm{n}). \tag{1.4}$$

The production of the D^- ions via this method is then performed in two steps [9]: first the production of rovibrationally excited Deuterium molecules $\mathrm{D}_2(\mathrm{v})$ and then successive electron attachment to these excited molecules. Because the production involves dissociative attachment of electrons to Hydrogen/Deuterium molecules and loss of $\mathrm{H}^-/\mathrm{D}^-$ by diffusion, the negative ions production is a non linear process [9]. The number of produced negative Hydrogen or Deuterium ions increases in proportion to the third power of electron density in density range below 10^{10} cm^{-3} [9].

Bacal et al. [10] report that the cross section of dissociative attachment of electrons to $\mathrm{H}_2(\mathrm{v})$ molecules,

$$\mathrm{H}_2(v) + e \rightarrow \mathrm{H}_2^- \rightarrow \mathrm{H}^- + \mathrm{H}, \tag{1.5}$$

increases strongly with the vibrational level v: the cross section is four orders of magnitude higher for $v = 4$ than for $v = 0$. This increase is stronger for Deuterium molecules than for Hydrogen molecules. This effect is explained by the increase of the amplitude of the vibrational motion with the increase of the vibrational level v. When the amplitude is higher, the electron can be captured at larger distance from the center of mass of the molecule, which dissociates before autodetachment takes place.

Finally, an increase of the cross section for higher H_2 rotational levels due to centrifugal stretching in excited rotational states is also reported [10]. Some models claim that this increase is much smaller than the one due to vibrational levels, while others claim that rotational heating increases more the cross section than vibrational heating.

The decay of the H_2^- molecule can also lead to the increase of the vibrational excitation:

$$\mathrm{H}_2(\mathrm{v}) + \mathrm{e} \rightarrow \mathrm{H}_2^- \rightarrow \mathrm{H}_2(\mathrm{v}' > \mathrm{v}) + \mathrm{e}. \tag{1.6}$$

Because the cross section of reaction (1.5) increases with the vibrational level, this reaction (1.6) helps increase the efficiency of negative ions production in the plasma volume.

The increase of the cross section of reaction (1.5) with rovibrational excitation has pushed the need for rovibrationally excited $\mathrm{H}_2/\mathrm{D}_2$ sources. Rovibrationally excited $\mathrm{H}_2/\mathrm{D}_2$ molecules are generated by two different processes: firstly collisions between these molecules and electrons in the plasma volume and secondly recombinative desorption of atomic Hydrogen from wall surfaces.

The first process is named *E-V singlet excitation* and is associated to the reaction:

$$H_2(X^1\Sigma_g^+, v = 0) + e \rightarrow H_2^*(2p^1\Sigma_u^+(B) \text{ or } 2p^1\Pi_u(C)) + e \rightarrow H_2(X^1\Sigma_g^+, v') + h\nu + e. \quad (1.7)$$

Due to the collision between ground state Hydrogen molecules and energetic electrons, the molecule is excited to both singlet and triplet electronic levels [10]. The most populated singlet states are $2p^1\Sigma_u^+(B)$ and $2p^1\Pi_u(C)$. Most of the populated singlet states decay radiatively to the ground state $H_2(X^1\Sigma_g^+, v')$. The population of these generated ground state Hydrogen molecules is more excited vibrationally than the initial population. Most of the negative ions produced in the plasma volume result from dissociative attachment of electrons to H_2 molecules in the upper ten vibrationals levels. As for the triplet states, they dissociate producing atomic fragments.

The second anions production way, which is the most effective, is the surface production. This is the capture of one or two electrons by backscattering of Deuterium or Hydrogen neutral atoms or cations on low work function [2] surfaces facing the plasma [11]. In SPIDER, this type of ions production is performed by the plasma grid in the extraction region.

The deposited Caesium on the plasma grid lowers the material work function and therefore increases the electron capture efficiency by neutral atoms or cations [16]. Caesium is required because the electronic affinity of Hydrogen is 0.754 eV far from the surface, therefore much smaller than the surface work functions of metals immersed in dense plasma which exceed 4 eV [10]. Thanks to the adsorption of Caesium by the metal surface, the work function drops to 2.2 eV [17]. The Hydrogen electronic affinity, which increases when the distance from the surface decreases, therefore becomes higher than the work function of the surface close to the plasma grid [10]. In this case, a Hydrogen atom is able to capture an electron from the metal and then to escape from the surface as an anion H^-.

Caesium helps produce H^- in other ways. Presence of Caesium increases the number of secondary electrons emitted by the walls therefore changing the energy distribution of the electrons population. Furthermore, adsorption on the walls is increased which decreases the concentration of atomic Hydrogen. The decrease of this concentration reduces the loss of H^- by associative and non-associative detachment by atomic Hydrogen in the plasma volume.

Addition of Caesium highly increases the number of anions produced by the surface in addition to narrowing the energy spread of the H^- beam [10]. Addition of Caesium into an ions source is reported by Bacal et al. [10] to increase the H^- current by a factor ranging from two to eight while reducing the operating pressure of the source and the number of co-extracted electrons.

[2] The work function is the thermal energy required to remove an electron from the surface of the material, when the material is surrounded by perfect vacuum.

Unfortunately, the deposition of Caesium has some drawbacks [16]. Firstly, Caesium must be continuously injected on the plasma grid which implies huge Caesium consumption (from 5 to 10 μgs^{-1}). Secondly, Caesium may leak from the extraction region to the beam electrostatic accelerator. This may cause voltage breakdowns or create parasitic beams. Thirdly, formation of Caesium layers on walls of the ions source decreases the efficiency of the source by altering Hydrogen recycling [10]. Finally, the use of Caesium makes the operational stability in the long run difficult and bottlenecks the improvement of ions source. These drawbacks motivate researchers to look for alternative materials to Caesium-coated metals [16] such as Carbon-based materials [10].

Neutral Hydrogen/Deuterium atoms are not the only compound producing the anions H^-/D^- by backscattering on the plasma gate. Indeed, according to simulations performed by Taccogna et al. [12], 54% of the anions production by backscattering on the plasma gate comes from conversion of the ions H^+ and H_2^+. The remaining 46 % comes from neutral atomic conversion.

The presence of H_2^+ molecular ions is explained by direct ionization of H_2 [12]. The presence of H^+ is explained by two channels, firstly the dissociative ionization of H_2 and secondly the direct ionization of H. The population of cations is distributed as follows: 56% H_2^+ and 44% H^+. Measurements of the velocity distribution of produced H^- has allowed to identify a third contribution from H_3^+ in addition to the contributions of H^+ and H_2^+ forseen by simulation [10].

1.1.2 Extraction of the produced anions from the source

The anions produced by the source must be extracted while minimizing the number of co-extracted electrons. Indeed, because the presence of electrons is mandatory to produce the anions, and because they have same electric charges, the extraction of some electrons from the source is difficult to avoid completely. Moreover, collisions with electrons having energies higher than 2 eV can neutralize the produced anions [11]. The current due to electrons presence in the extraction region is of the order of tens of Amperes [11]. To reach full performance operation, the electron-anion current ratio must be brought back to less than one.

The extraction grid is therefore equipped with permanent magnets. These magnets produce a magnetic filter parallel to the extraction grid. This strong and localized magnetic field decreases the amount and temperature of electrons in the extraction region. Moreover, a magnetic filter is created in front of the plasma grid by a current of several kA flowing through the plasma grid [13].

As a result, these fields trap the electrons for some time while they collide and therefore lose energy, which decreases the temperature of the electrons population [12]. The magnetic filtering operates directly in the ions source because it is easier to stop electrons before their energies increase due to acceleration of the beam.

1.2 Acceleration and neutralization of the anionic beam

The extracted anions are accelerated up to 1 MeV by a 5-stage electrostatic accelerator, each stage increasing the electric potential by 200 kV [11]. Then the 1 MeV anionic beam is neutralized passing through a gas cell neutralizer. The remaining charged particles are removed with the electrostatic residual ion dump (RID). The power of the obtained neutral beams is close to 17 MW. This neutral beam must have huge energy and particles flux, low divergence and high uniformity.

During its transport, the anionic beam interacts with the background gas of the chamber, producing electrons and ions (both fast and slow). This interaction has both beneficial and detrimental effects. The presence of this background partially neutralizes the beam, helping to turn the anionic beam to the desired neutral beam. Moreover, the cations created by collisions with the background gas help prevent the divergence of the anionic beam due to Coulomb repulsion. However, the background gas is heated by the passage of the beam and this heat propagates to the surfaces exposed to the beam.

In addition to the role played by the background gas, the divergence of the whole beam and individual beamlets is controlled by finely tuned electric and magnetic fields [11]. These fields also help to protect grids from heat loads and to get rid of electrons remaining after the extraction phase. The engineering of the beam optics is assisted by numerical simulations. Two complementary approaches are possible: a local 2D approach focusing on the optics of a single beamlet, and a global 3D approach considering the whole beam and a detailed geometry of the grids.

The local approach solves the Poisson's equation in cylindrical coordinates to find out the electric field in the accelerator [11]. Its advantage is to be really fast which allows numerical optimization of the geometry of the grid apertures through a large number of runs. On the other side, the global approach allows to compute edge effects, inter-beamlets repulsion, effects of the detailed shape of the whole grid and of the protrusions of the grids due to bolted structures (called kerbs). Modifying the electric fields depending on results of the global approach is mandatory to ensure the overall aiming of the whole beam.

1.3 Importance of the mutual neutralization reaction between D_2^+ and D^- for efficient negative ions production

This section explains why an in depth understanding of the mutual neutralization reaction between D_2^+ and D^- would help to design better negative ions source.

Population densities of atoms, molecules and ions in plasma are computed with collisional radiative models (CR) [18]. CR models apply when the electron densities are intermediate, i.e. between the very high ($10^{24}\mathrm{m}^{-3}$) and very low ($10^{17}\mathrm{m}^{-3}$) thresholds. Yacora is one of these models specialized to low temperature and low pressure hydro-

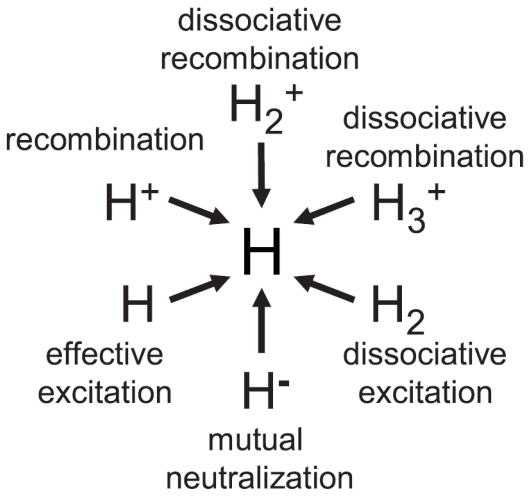

Figure 1.3: Excitation channels considered in the Yacora model.

gen plasmas. This model considers six possible excitation channels: excitation of H, recombination of H^+, dissociative excitation of H_2, dissociative recombination of H_2^+, dissociative recombination of H_3^+ and mutual neutralizations of H^- with H^+, H_2^+ and H_3^+ (see Figure 1.3). Excitation is modeled to be compared to spectroscopic observations of the plasma.

Electron densities are intermediate in sources for negative Hydrogen ions, which justifies the use of the Yacora model [18]. In this range of electron densities, processes involving H_2, H_2^+ and H^- may influence the population of excited states. Furthermore, some of the plasma particles may have sufficient energy to take part in excitation processes. Therefore, for the model to be accurate, corresponding cross sections and the energy distribution functions of the involved particles have to be precisely known. Cross sections of thousand reactions have to be known to build the model, the complexity sharply increasing when rovibrational excited states of molecules are considered.

The number of reaction included in the Yacora model is 2359 [18]. Most of them are electron collision processes and radiation. The mutual neutralizations of H^- with H^+, H_2^+ and H_3^+ are the only considered heavy particle collisions. Wünderlich et al. [18] report that these reactions have a significant impact on the population density of some atomic Hydrogen excited states. A cumulative cross section is used for these three possible mutual neutralizations. Moreover, due to lack of experimental and theoretical information, modeling of plasma is performed assuming the mutual neutralization of H_2^+ with H^- follows with equal probability the two output channels $H_2^* + H$ and $H_2 + H^*$.

Accurate knowledge of the cross sections associated to the possible H^-/D^- interactions with the Hydrogen/Deuterium cations (D^+, D_2^+, D_3^+) would therefore improve the accuracy of plasma simulations and allow better negative ions source design. Moreover, there remain many other unanswered questions about the operation of negative ions sources,

which would be answered by better knowledge of the mutual neutralization between D_2^+ and D^-. For example, are the excited Deuterium atoms D_n^* with n= $4, 5, 6$ observed in negative ions sources produced by the reaction $D_2^+ + D^- \rightarrow D_2 + D_n^*$ (they may also be produced by the reaction $D_3^+ + e \rightarrow D_2 + D_n^*$ or $D_2^+(v) + e \rightarrow D + D_n^*$)? Does the mutual neutralization between D_2^+ and D^- strongly decrease the efficiency of negative ions production?

Chapter 2

Experimental setup: confluent beams

This Chapter presents the experimental setup used to retrieve the KER spectra analyzed throughout this work. The objective is to give the reader all information required to understand the rest of this manuscript. Readers looking for more details about the experimental setup may refer to the theses of Launoy et al. [19], Fabre et al. [20] and Nzeyimana et al. [21].

This Chapter is organized as follows. The first and second sections present a global overview of the two and three-body experiments, respectively. The third section explains how the ions D^- and D_2^+ are produced from D_2 gas using duoplasmatron and electron cyclotron resonance sources, respectively. Finally, the last section briefly reviews the operating principle of the used position-sensitive detectors.

2.1 The two-body detection experimental setup

In this work, the interaction between ions is studied based on the kinetic energy released (KER) by the reaction in the center of mass frame. As will be explained in Section 5.2, this KER is computed from measurements of the velocities $\vec{V_i}$ of the products of reaction. This Chapter explains how ultra low collision energies are possible thanks to a confluent merged beams configuration and how measurements required to compute the KER are performed.

In a confluent merged beams configuration, a positively and a negatively charged ionic beam propagate along the same direction and overlap in a region of space referred as the interaction region. Ions are produced in their respective source before being accelerated and guided towards this region with electric fields.

Because the beams overlap in this region, and thanks to the Coulomb attraction between the ions, the ions interact. If the interaction is exothermic, the potential energy of the

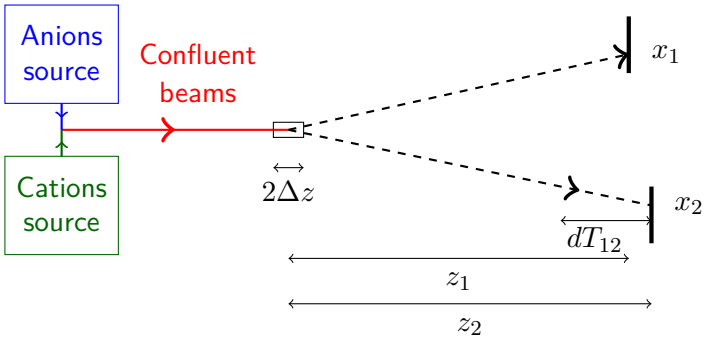

Figure 2.1: Anions and cations are produced in their respective sources then accelerated, collimated and put in a confluent beams configuration (in red). The confluent beams travel in the direction $\hat{z}$ at an average velocity V_{cm}. Collisions having occurred in the interaction region which has a length of $2\Delta z$ will produce possibly measurable products. After the collision, the produced particles travel to the detection planes. The first particle hits a detector at the position (x_1, y_1, z_1) and time t_1. The second particle hits a detector at position (x_2, y_2, z_2) and time $t_2 = t_1 + dT_{12}$.

products is smaller than the potential energy of the reagents and the excess of energy may be released in form of kinetic energy carried out by the products.

For example, Chapter 6 studies the mutual neutralization reaction:

$$\mathrm{D}_2^+(\mathrm{v_i}) + \mathrm{D}^- \rightarrow \mathrm{D}_2^*(\mathrm{v_j}) + \mathrm{D}, \tag{2.1}$$

where the produced pair $(\mathrm{D}_2^*, \mathrm{D})$ has an additional kinetic energy KER with respect to the reagents. The reagents are part of a beam collimated in a well defined direction $\hat{z}$. On the contrary, the additional kinetic energy transferred to the products gives them, in most cases, non zero velocities along the two other directions $\hat{x}$ and $\hat{y}$. Therefore, the neutral fragments will move away from the beams and some of them will hit detectors (see Figure 2.1). The ions that went through the interaction region without interacting are deviated away from the detectors with electric fields.

The confluent beams method allows to benefit from the advantages of high velocities in the laboratory frame (ease of propagation and detection) while nevertheless producing ultra low collision energy events [19]. Indeed, because the velocities of the anions and cations are very close, their relative velocity and collision energy are very small.

Figure 2.1 is not at scale. If the origin $(x = 0, y = 0, z = 0)$ of the reference frame is located in the middle of the interaction region, the positions of the centers of the two detectors composed of three multichannel plates (MCP) and one resistive anode are separated by 10cm. Their distances from the interaction region are 3.16m and 2.92m, respectively. Their radii are 1.92 and 1.9 cm (see [19] for a more detailed schema of the experimental setup).

The two detectors are able to record the positions $\{(x_1, y_1), (x_2, y_2)\}$ of the two particles hitting them. Digital electronic circuits then record the time of flight difference between the two particles $dT_{12} = t_2 - t_1$ (see Figure 2.1). One detector is located 10cm further from the interaction region for easier set up of the connections to the detectors.

The last data retrieved from the experiment are the distances z_1 and z_2 between the position of the interaction and the detection planes. Because the ions may interact anywhere while the beams are confluent (i.e. in the red region in Figure 2.1) , a difficulty is to know precisely the location of the interaction between the ions. This is why an electrical potential V_{obs}, the observation potential, is applied in the region where the two beams overlap completely. The observation potential modifies the relative energy E_{rel} between the two beams in this region. Indeed, because the particles in both beams carry an electric charge q_i, their kinetic energy E_i depends on the electric potential:

$$E_i = q_i(V_{acc,i} - V_{obs}), \tag{2.2}$$

where $V_{acc,i}$ is the acceleration potential applied to the ion source. The relative energy is defined as follows:

$$E_{rel} = \mu \left(\frac{E_1}{m_1} + \frac{E_2}{m_2} - 2\sqrt{\frac{E_1 E_2}{m_1 m_2}} \right), \tag{2.3}$$

where $E_1 = \frac{m_1 v_1^2}{2}$, m_1, $E_2 = \frac{m_2 v_2^2}{2}$, m_2 are the energies in the laboratory frame and masses of the particles composing the beams 1 and 2, respectively. The quantity μ is the reduced mass:

$$\mu = \frac{m_1 m_2}{m_1 + m_2}. \tag{2.4}$$

This difference in relative energy implies that the products of the reaction formed in the region where the observation potential is applied have different kinetic energies with regard to the products formed in other regions. Therefore, the products for which the interaction length is known can be extracted. Because the length of the interaction region is $2\Delta z$, the uncertainty on z_1 is Δz ($z_2 = z_1 + 10$cm). This is the main source of uncertainty in the computation of the kinetic energy release.

The observation potential has two important purposes in addition to allow to precisely know z_1 and z_2 [19]. Firstly, it allows to restrict the ultra high vacuum (10^{-10} mbar) region to the interaction region while the remaining volume can be kept in high vacuum (10^{-7} mbar). Secondly, it is easier to measure the evolution of the cross section with the collision energy simply by changing the value of the observation potential.

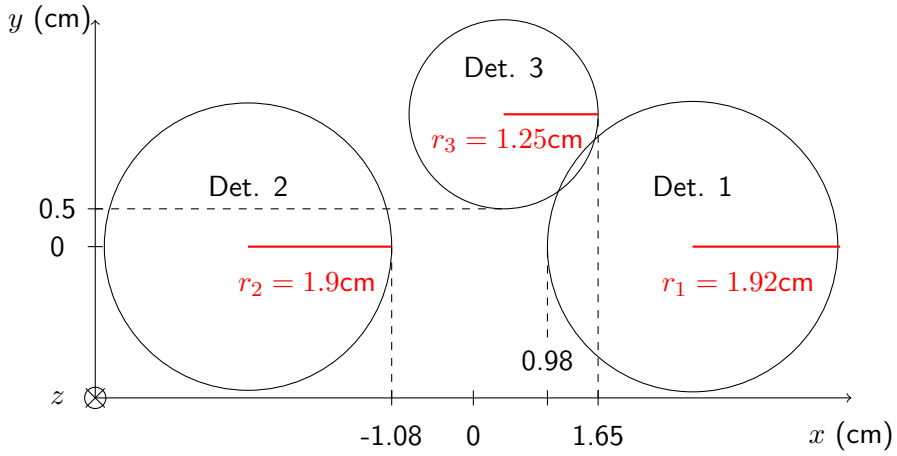

Figure 2.2: In this Figure, the three black circles are the three detectors observed from the interaction region.

2.2 The three-body detection experimental setup

This section explains the changes made to the two-body detection system in order to be able to detect three-body events.

A third detector has been added (see Figure 2.2). Its center is located at $(x = 0.4, y = 1.75, z = 292)$cm and its radius is 1.25 cm. This detector slightly overshadows the first detector. Unlike the two others, this detector is not position-sensitive: the location of the impact produced by the detected particle is not provided by the detector. Fortunately, as it will be shown in Chapter 7, this position can be retrieved thanks to equations arising from momentum conservation of the physical process of interest.

The only additional data provided by the three-body detection system with respect to the two-body detection system are the time of flight difference between the particles hitting the third and first detector $dT_{13} = t_3 - t_1$ and, obviously, the position of the third detection plane (that is, z_3).

2.3 Ions production

This section briefly explains how the ions D^- and D_2^+ studied in this work are produced.

The anion D^- is produced by a duoplasmatron source [19]. This source is composed of a cathode filament made of thoriated Tungsten in a vacuum chamber (see Figure 2.3). This material improves the production of electrons at temperatures below 2700 °C. Deuterium gas (D_2) is introduced in small quantities into the chamber. The filament then heats up by Joule effect and emits electrons thanks to the thermionic effect: the thermal energy becomes sufficient for the electrons to escape from the surface of the material. These

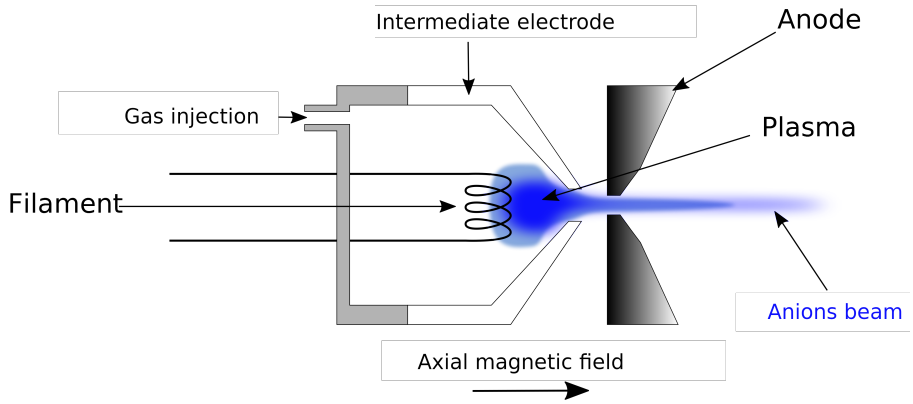

Figure 2.3: Duoplasmatron negative ions source. Figure source: translation from [19].

electrons are then accelerated towards the anode and confined by an axial magnetic field [19]. The gas is ionized with the free electrons from the cathode while excited molecules attach electron at the plasma periphery, forming D- by dissociative electron attachment.

Molecular ions D_2^+ are produced in an ECR (electron cyclotron resonance) source. In this type of source, the gas is ionized by collision with free electrons. A static and uniform magnetic field is applied in a volume containing low pressure gas. Due to the presence of this field, the electrons undergo an helical motion being the superposition of the initial electron motion parallel to the field and a cyclotron motion with frequency:

$$f_c = \frac{eB}{2\pi m_e}, \tag{2.5}$$

where e is the electron charge, B the amplitude of the magnetic field and m_e the electron mass. Microwaves whose frequency $f = f_c \approx 5$GHz are generated in the volume. The alternating electric field of these waves is synchronous with the gyration period $T = 2\pi m_e/(eB)$ of the electrons. It follows that the electric field accelerates the electrons in the plane perpendicular to the magnetic field. As the kinetic energy of free electrons increases, it eventually becomes greater than the ionization potential of the gas atoms or molecules. Their collisions with the gas extract electrons from the gas, therefore producing cations. ECR sources are able to produce high intensities cationic beams ($\approx$ 100 mA). Note that the pressure inside the source must stay sufficiently low to achieve a sufficiently long mean free path necessary for electron acceleration and avoid recombination of cations with free electrons.

The choice of the production method of the molecular ions D_2^+ determines their vibrational population [15]. If the cations are produced by electron-impact ionization, like in this work with the ECR source, then the vibrational population depends on the energy of the free electrons. Urbain et al. [22] have measured precisely the vibrational population of the produced molecular ions by dissociative charge exchange of D_2^+ on a potassium

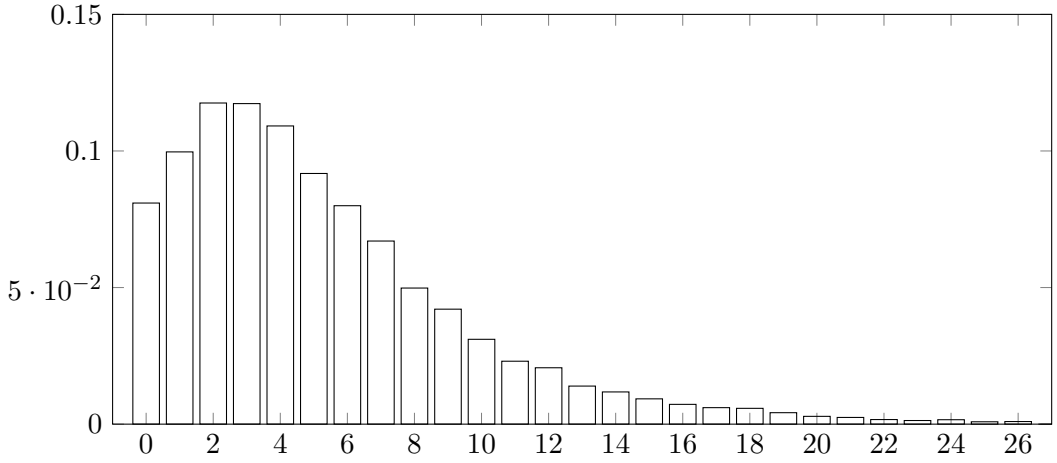

Figure 2.4: Vibrational population of the produced molecular ion D_2^+.

target. Their results are presented in Figure 2.4. The third and fourth vibrational levels ($v = 2$ and 3) are the most populated.

2.4 Position-sensitive detectors

This section explains the operating principle of the two position-sensitive detectors. These detectors are composed of two parts: three stacked microchannel plates which act as electron multipliers and a resistive anode which allows to retrieve the position of the impact.

Microchannel plates are made of semiconductor lead glass [19]. These plates are usually 1 mm thick and contain many holes of typically 10-30 microns in diameter, forming a honeycomb-like structure (see Figure 2.5). The holes are slightly inclined with respect to the normal to the face of the plate. An electric field is applied between the two metal coated faces of the plate (typically 800 V/mm).

If a particle enters a hole, it will eventually hit the side of the inclined hole. This collision extracts secondary electrons from the hit side. Due to the presence of the electric field, these secondary electrons are accelerated, and they will extract more secondary electrons form the side, and so on. This process produces a so called "cascade of electrons". Once the electrons reach the end of the first plate, the amplification process goes on in the two next plates. The overall stack of plates amplifies the signal by a factor 10^6 to 10^8 [20].

The output electrons, whose total charge is Q_{tot}, then hit a resistive anode located behind the third microchannel plate. This charge Q_{tot} flows through the fourth corners (A,B,C,D) of the anode. The ratio of charges $(Q_A, Q_B, Q_C, Q_D)/Q_{tot}$ measured at each corner depends on the position of the impact. For example, if the impact is located at the center of the anode, the ratio is 1/4 at each corner. A signal proportional to the

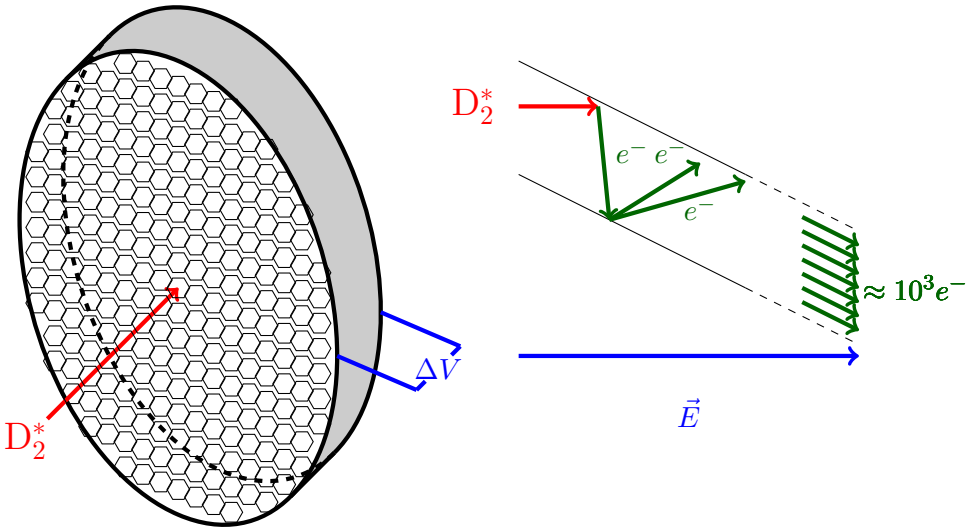

Figure 2.5: On the left, the whole microchannel plate. On the right cascade of electrons inside one channel of the microchannel plate.

coordinates x and y of the impact on the detector is obtained as follows [20]:

$$\begin{cases} x = \frac{Q_B+Q_C}{Q_A+Q_B+Q_C+Q_D}, \\ y = \frac{Q_A+Q_B}{Q_A+Q_B+Q_C+Q_D}. \end{cases} \tag{2.6}$$

The spatial resolution of the detection system is approximately 100 μm. For two successive events to be properly detected, the time difference between the two hits must be at least 10 μs [20]. This imposes the use of a pair of such detectors for coincident detection of reaction products.

Chapter 3

Cross section of confluent beams

In the confluent beams configuration of interest, two beams are superimposed and their charged particles interact by charge exchange. The current Chapter presents the cross section for the interaction of two confluent ionic beams and the program allowing to easily compute this quantity.

The study of a particular physical process occurring when two beams overlap in a volume V is considered. Each occurrence of this process is considered as an event. The beam i has the following characteristics [21]:

- q_i is the electric charge of one particle,
- $\vec{v}_i$ is the velocity of the particles in the beam,
- n_i is the particle density,
- I_i is the current of the beam,
- $\vec{j}_i = n_i \vec{v}_i$ is the flux of particles.

The beam sectional area is supposed to be perfectly circular. The interaction volume V is then the intersection between two cylinders (see Figure 3.1). Moreover, the two beams are assumed to be parallel such that $\vec{v}_1$ and $\vec{v}_2$ are colinear. A laboratory frame is defined such that $\hat{z}$ is colinear with $\vec{v}_1$ and $\vec{v}_2$.

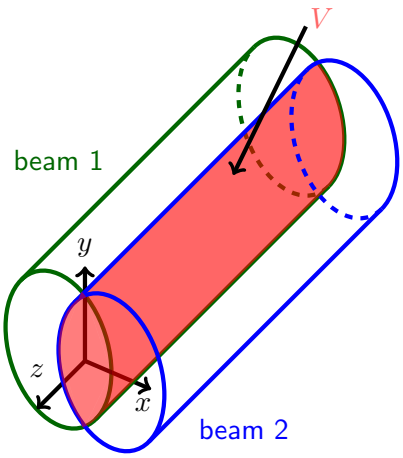

Figure 3.1: The two confluent beams overlap and interact in the interaction volume V. When V increases, the number of events N and the form factor F both increase.

Let S be the area of the section through V perpendicular to $\vec{v}_1$ and $\vec{v}_2$. The cross section σ is then defined as the number of events N over the number of trials per unit area ν [23]:

$$\sigma \equiv \frac{N}{\nu} = \frac{dN/dt}{d\nu/dt}. \tag{3.1}$$

The number of trials per unit of time on one particle of beam 1 located at (x, y, z) in the laboratory frame is the product of the density of particles of beam 2 at this position $n_2(x, y, z)$ with the relative velocity between the particles of the two beams $v_r = |v_1 - v_2|$:

$$\frac{d\nu}{dt} = n_2(x, y, z)\ |\vec{v}_1 - \vec{v}_2| \equiv n_2(x, y, z)\ v_r, \tag{3.2}$$

Since there are $n_1 dV$ particles in a volume $dV \subset V$, the total number of trials per unit of time in the volume dV is then:

$$\frac{d\nu}{dt} = n_2(x, y, z) n_1(x, y, z) dV v_r. \tag{3.3}$$

Inserting this result in Equation (3.1) and redefining N as the number of events per unit of time yields:

$$dN = v_r\ \sigma n_2(x, y, z)\ n_1(x, y, z)\ dV, \tag{3.4}$$

$$N = v_r\ \sigma \int_V n_2(x,y,z)\ n_1(x,y,z)\ dV = v_r\ \sigma \int_V \frac{|\vec{j}_1(x,y,z)|}{|\vec{v}_1|}\frac{|\vec{j}_2(x,y,z)|}{|\vec{v}_2|}\ dV, \tag{3.5}$$

$$= \frac{v_r\ \sigma}{v_1 v_2}\int_V j_1(x,y,z)\ j_2(x,y,z)\ dV. \tag{3.6}$$

The overlapping degree of the two beams is described by a quantity called the form factor F [21]:

$$F = \frac{\int_L \int_{-\infty}^{\infty}\int_{-\infty}^{\infty} j_1(x,y,z)\ j_2(x,y,z)dxdydz}{\int_{-\infty}^{\infty}\int_{-\infty}^{\infty} j_1(x,y,z)dxdy \int_{-\infty}^{\infty}\int_{-\infty}^{\infty} j_2(x,y,z)dxdy}, \tag{3.7}$$

where L is the length of the overlapping region along the beams direction $\hat{z}$. The form factor only depends on the geometry of the beams and their relative positions. Moreover, it is considered as time-independent during the measurement time. Therefore, F is a constant [21].

The form factor is introduced in Equation (3.6) as follows:

$$N = \frac{v_r\ \sigma}{v_1 v_2}\int_{-\infty}^{-\infty}\int_{-\infty}^{-\infty} j_1(x,y,z)dxdy \int_{-\infty}^{-\infty}\int_{-\infty}^{-\infty} j_2(x,y,z)dxdy$$
$$\frac{\int_L \int_{-\infty}^{-\infty}\int_{-\infty}^{-\infty} j_1(x,y,z)\ j_2(x,y,z)dxdydz}{\int_{-\infty}^{-\infty}\int_{-\infty}^{-\infty} j_1(x,y,z)dxdy \int_{-\infty}^{-\infty}\int_{-\infty}^{-\infty} j_2(x,y,z)dxdy} \tag{3.8}$$

$$= \frac{v_r\ \sigma F}{v_1 v_2}\int_{-\infty}^{-\infty}\int_{-\infty}^{-\infty} j_1(x,y,z)dxdy \int_{-\infty}^{-\infty}\int_{-\infty}^{-\infty} j_2(x,y,z)dxdy. \tag{3.9}$$

The current of a beam is related to the flux of particles as follows:

$$I_i = q_i \int\int j_i(x,y,z)dx\ dy. \tag{3.10}$$

The conservation of the current implies that I_i is independent of z. The following expression for the number of events per unit of time N is then obtained:

$$N = \frac{v_r\ \sigma F I_1 I_2}{v_1 v_2 q_1 q_2}. \tag{3.11}$$

The cross section σ is then :

$$\boxed{\sigma = \frac{N q_1 q_2 v_1 v_2}{v_r I_1 I_2 F a \eta}}. \tag{3.12}$$

The additional factors a and η are the acceptance and the efficiency, respectively. The acceptance is the solid angle covered by the detector divided by the maximum solid

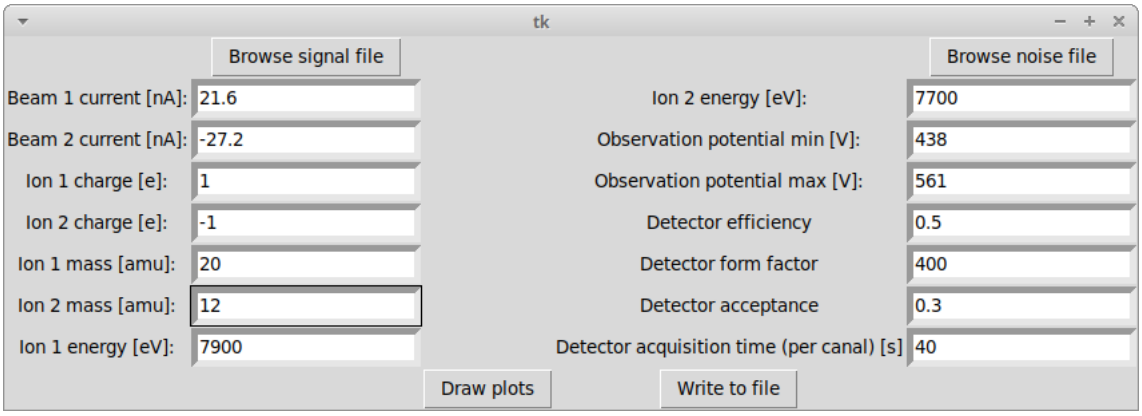

Figure 3.2: Main window of the program allowing to compute the cross section of confluent beams (Equation (3.12)).

angle 4π. Note that both solid angles refer to the center-of-mass frame, and reduce to a cone in the laboratory frame due to the high beam velocities. The detector does not cover the entire cross sectional area of the cone of events to be detected. The acceptance correction is then required to take into account missed events due to the limited geometry of the detector. From the other part, η models the fraction of events detected in the solid angle covered by the detector. The efficiency correction deals with events hitting the detection system but not detected due to physical limitation of the detector [1] (i.e. quantum efficiency and transparency of microchannel plates).

The main window of the program allowing to compute the cross section is presented in Figure 3.2. The program takes as input the various parameters of the beams as well as the signal and background files given by the experiment. The format of these files is one integer per line, the integer at line i being the number of events measured for the channel i, i.e. for an observation potential V_i.

The program outputs a file with, for each channel:

- the observation potential V_i,
- the relative energy E_{rel} between the two beams,
- the number of events n,
- the cross section σ,
- and the error on the computed cross section $\Delta\sigma$. Let s be the signal and b the background, the absolute error on the measured number of events per second is computed from properties of the Poisson distribution:

[1] Typical values for η are between 50% and 70%.

$$\Delta e = \frac{\sqrt{s + 2b}}{\Delta t}, \tag{3.13}$$

where Δt is the detector acquisition time per channel. The absolute error on the cross section is then computed as follows:

$$\Delta \sigma = \frac{\sigma \Delta e}{N}. \tag{3.14}$$

In addition to this text file, the program outputs plots showing the evolution of the cross section with regard to both the relative energy (see Figure 3.3) and the observation potential (see Figure 3.4). The program supports features such as zooming on specific areas of the figure or saving the figure in many different formats [2].

The program is designed to handle properly invalid inputs and risks of division by zero. For example, a safety check ensures that I_1, I_2, F, a and η are not equal to zero. More over, when a relative speed $v_r = 0$ is encountered, the case is properly handled and vertical red lines are drawn at appropriate positions in the generated plots.

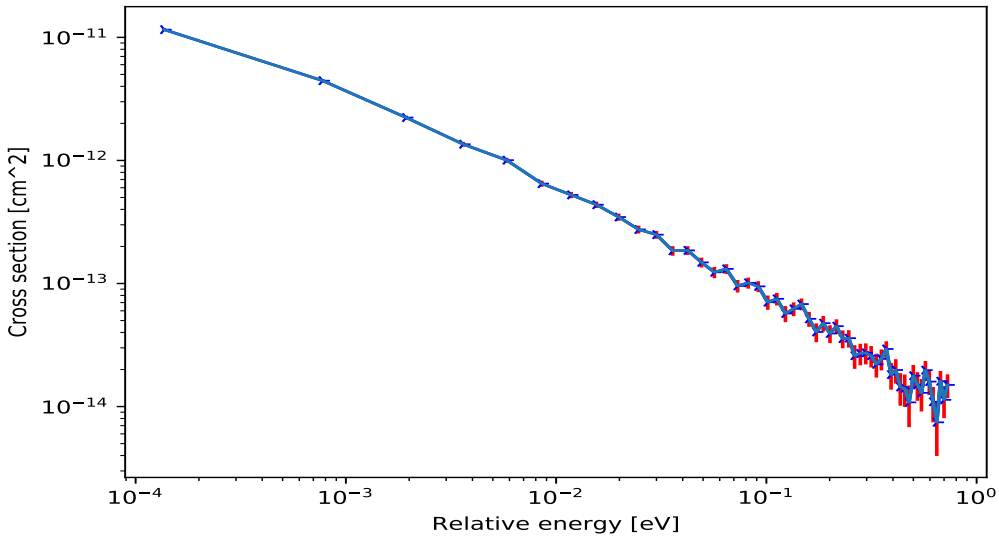

Figure 3.3: Plot of the cross section with regard to the relative energy. Parameters used to draw this plot are presented in Figure 3.2. Used signal and background files originate from the interaction between Neon and Carbon ions.

[2] 'ps': 'Postscript', 'eps': 'Encapsulated Postscript', 'pdf': 'Portable Document Format', 'pgf': 'PGF code for LaTeX', 'png': 'Portable Network Graphics', 'raw': 'Raw RGBA bitmap', 'rgba': 'Raw RGBA bitmap', 'svg': 'Scalable Vector Graphics', 'svgz': 'Scalable Vector Graphics', 'jpg': 'Joint Photographic Experts Group', 'jpeg': 'Joint Photographic Experts Group', 'tif': 'Tagged Image File Format', 'tiff': 'Tagged Image File Format'.

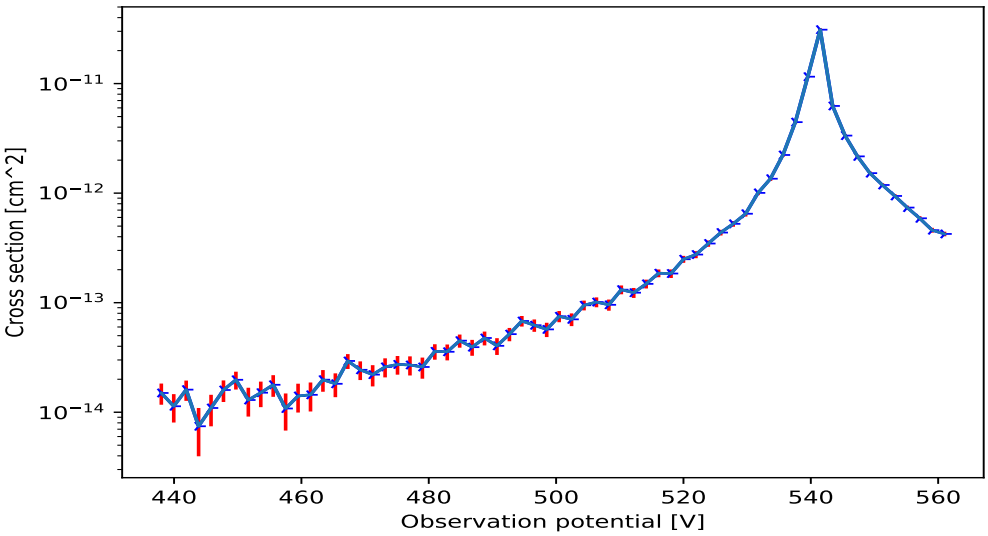

Figure 3.4: Plot of the cross section with regard to the observation potential. Parameters used to draw this plot are presented in Figure 3.2. Used signal and background files originate from the interaction between Neon and Carbon ions.

Chapter 4

Numerical methods to compute vibrational states of the D_2^+ molecular ion and D_2 molecule

This Chapter presents the numerical methods used to compute the vibrational states of the D_2^+ molecular ion in its ground state $D_2^+(X\ ^2\Sigma_g^+)$, as well as many states of the D_2 molecule such as the ground state $D_2(X\ ^1\Sigma_g^+)$, the dissociative state $D_2(b^3\Sigma_u^+)$ and many electronically excited states D_2^*. The implemented *python* script is generic and is able to solve the 1D Schrödinger equation for bound and unbound potentials.

The first section explains how the Schrödinger equation can be expressed as a simple eigenvalue problem using the Numerov numerical scheme. The second section presents the strategy followed by the algorithm to select both the boundaries of the numerical domain and the density of points in the grid. The third section describes how the wavefunctions obtained by solving the eigenvalue problem are normalized. The obtained vibrational states for the ground and first excited potential energy curves of the D_2^+ molecular ion and the ground electronic state of the D_2 molecule as well as several potential energy curves of the electronically excited molecule D_2^* are presented in Appendix A.

4.1 Matrix Numerov's representation of the Hamiltonian

In order to obtain the vibrational levels of the studied electronic states, the time independent 1D Schrödinger's equation must be solved:

$$\Psi''(x) = f(x)\Psi(x). \tag{4.1}$$

The Numerov's numerical method is well suited to solve this form of differential equa-

tion [24]. The numerical scheme is obtained as follows. Using the Taylor's series expansion:

$$\Psi(x_i + d) = \Psi(x_i) + \Psi'(x_i)d + \Psi''(x_i)\frac{d^2}{2} + \Psi'''\frac{d^3}{6} + \Psi''''\frac{d^4}{24} + \Psi'''''\frac{d^5}{120} + \mathcal{O}(d^6), \quad (4.2)$$

$$\Psi(x_i - d) = \Psi(x_i) - \Psi'(x_i)d + \Psi''(x_i)\frac{d^2}{2} - \Psi'''\frac{d^3}{6} + \Psi''''\frac{d^4}{24} - \Psi'''''\frac{d^5}{120} + \mathcal{O}(d^6), \quad (4.3)$$

where d is the step of the numerical domain.

Writing $\Psi(x_i)$ as Ψ_i, $\Psi(x_i + d)$ as Ψ_{i+1}, $\Psi(x_i - d)$ as Ψ_{i-1} and summing Equations (4.2) and (4.3) yields:

$$\Psi_{i+1} + \Psi_{i-1} = 2\Psi_i + \Psi_i''d^2 + \Psi_i''''\frac{d^4}{12} + \mathcal{O}(d^6). \quad (4.4)$$

From Equation (4.1) and second order Taylor's expansion,

$$\Psi_i'''' = \left(\frac{d^2}{dx^2}(f(x)\Psi(x))\right)_{x=x_i} \approx \frac{f_{i+1}\Psi_{i+1} - 2f_i\Psi_i + f_{i-1}\Psi_{i-1}}{d^2}. \quad (4.5)$$

From Equations (4.4) and (4.5), one gets an expression for the second derivative of Ψ:

$$\Psi_i'' = \frac{\Psi_{i+1} - 2\Psi_i + \Psi_{i-1}}{d^2} - \frac{f_{i+1}\Psi_{i+1} - 2f_i\Psi_i + f_{i-1}\Psi_{i-1}}{12}. \quad (4.6)$$

Finally, from Equation (4.1):

$$\frac{\Psi_{i+1} - 2\Psi_i + \Psi_{i-1}}{d^2} - \frac{f_{i+1}\Psi_{i+1} - 2f_i\Psi_i + f_{i-1}\Psi_{i-1}}{12} = f_i\Psi_i, \quad (4.7)$$

$$\frac{\Psi_{i+1} - 2\Psi_i + \Psi_{i-1}}{d^2} - \frac{f_{i+1}\Psi_{i+1} + 10f_i\Psi_i + f_{i-1}\Psi_{i-1}}{12} = 0. \quad (4.8)$$

Considering the Schrödinger equation, $f(x) = -2m(E - V(x))/\hbar^2$:

$$-\frac{\hbar^2}{2m}\frac{\Psi_{i-1} - 2\Psi_i + \Psi_{i+1}}{d^2} + \frac{V_{i-1}\Psi_{i-1} + 10V_i\Psi_i + V_{i+1}\Psi_{i+1}}{12} = E\frac{\Psi_{i-1} + 10\Psi_i + \Psi_{i+1}}{12}. \quad (4.9)$$

Now the column vector $\Psi = (..., \Psi_{i-1}, \Psi_i, \Psi_{i+1}, ...)$ and the matrices $A = (I_{-1} - 2I_0 + I_1)/d^2$, $B = (I_{-1} + 10I_0 + I_1)/12$ and $V = \mathrm{diag}(..., V_{i-1}, V_i, V_{i+1}, ...)$ are introduced [24],

where I_p is a matrix of ones along the p_{th} diagonal and zeros elsewhere. Equation (4.9) can be expressed as follows [24]:

$$\frac{-\hbar^2}{2m} A\Psi + BV\Psi = EB\psi. \tag{4.10}$$

This matrix expression of the Schrödinger equation implies the boundary conditions $\Psi_0 = 0$ and $\Psi_{N+1} = 0$, the matrix dimensions being $N \times N$. Indeed, the first and last equations of this linear system are respectively:

$$-\frac{\hbar^2}{2m}\left(\frac{-2\Psi_1 + \Psi_2}{d^2}\right) + \frac{10V_1\Psi_1 + V_2\Psi_2}{12} = E\left(\frac{10\Psi_1 + \Psi_2}{12}\right), \tag{4.11}$$

$$-\frac{\hbar^2}{2m}\left(\frac{\Psi_{N-1} - 2\Psi_N}{d^2}\right) + \frac{V_{N-1}\Psi_{N-1} + 10V_N\Psi_N}{12} = E\left(\frac{\Psi_{N-1} + 10\Psi_N}{12}\right). \tag{4.12}$$

Equations (4.11) and (4.12) are indeed identical to Equation (4.9) setting $i = 1$ and $i = N$ respectively, when $\Psi_0 = 0$ and $\Psi_{N+1} = 0$.

Multiplying Equation (4.10) by B^{-1} yields:

$$\frac{-\hbar^2}{2m} B^{-1}A\Psi + V\Psi = E\psi. \tag{4.13}$$

The matrix Numerov's representation of the Hamiltonian is then:

$$H = \frac{-\hbar^2}{2m} B^{-1}A + V, \tag{4.14}$$

the first and second terms of Equation (4.14) are a representation of the kinetic and potential operators, respectively. The energy levels E and wavefunctions Ψ of the system are then simply obtained by computing the eigenvalues and eigenvectors of the matrix H [1].

4.2 Numerical domain

In this section, the approach used to determine the numerical domain is presented. Firstly, the boundaries x_1 and x_N of the numerical domain $[x_1, x_N]$ must be selected. Secondly, the step of the numerical method d, i.e. the distance between two successive points x_i and x_{i+1}, must be chosen.

However, before being able to choose the numerical domain, the maximum energy level the algorithm will look for, E_{max}, has to be selected. Calling the function solving the

[1] The linalg.eig function of the *python* package numpy is used at this end.

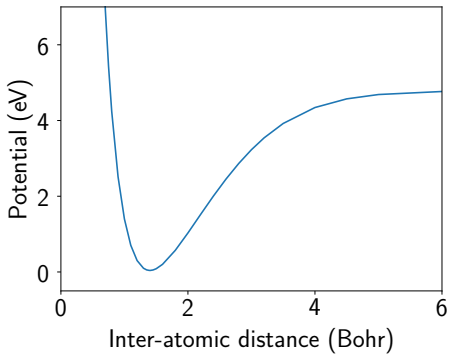

Figure 4.1: Example of bound potential.

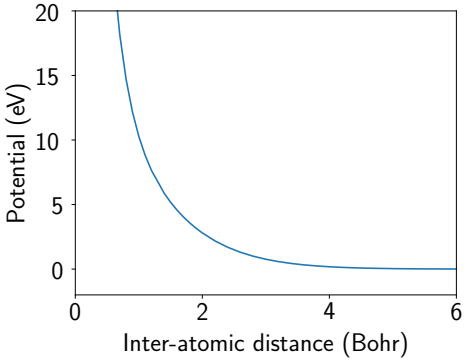

Figure 4.2: Example of unbound potential.

Schrödinger equation, the type of potential (bound or unbound) must be specified. The type "bound" must be chosen if the potential presents a well, the type "unbound" must be chosen otherwise [2] (see Figures 4.1 and 4.2). If the potential is unbound, E_{max} must be explicitly provided by the user. Otherwise, if the potential is bound, the algorithm is able to automatically compute a value for E_{max} as follows.

The potential V is provided in a text file, as a set of M points (x_j, V_j). The function $V(x)$ is obtained by interpolating in the domain $[x_1, x_M]$ and extrapolating linearly outside this domain [3].

The bound type potential is assumed to tends to infinity at $x = 0$ and to converge to a constant at $x = \infty$. In this case, if not provided by the user, E_{max} is automatically chosen as an energy slightly smaller than the value of the potential at infinity, i.e. $V(x = +\infty)$ (see Figure 4.3).

The value $V(x = +\infty)$ is approximated by the value V_j associated to the largest x provided in the potential text file [4]. Because a bound potential often quickly converges to a constant value, choosing as E_{max} an energy slightly smaller than $V(x = +\infty)$ allows to drastically decrease the size of the numerical domain and the computation time.

Moreover, it allows to avoid non-physical but numerically correct solutions corresponding to too high energies. Let E_{min} be the minimum of the potential $V(x)$, the value E_{max} is computed as follows:

$$E_{max} = V(x = +\infty) - s\frac{V(x = +\infty) - E_{min}}{100}, \tag{4.15}$$

where s is a scaling coefficient. Therefore, E_{max} equals $V(x = +\infty)$ minus s percents of

[2] For example if looking for continuum wavefunctions of a dissociative state.

[3] The function interpolate.interp1d(x_j, V_j, kind="linear" , fill_value="extrapolate") from the *Python* package *scipy* is used.

[4] Under this choice, lies the assumption that the user would provide additional points (x_j, V_j) if the physical potential would strongly fluctuate at large x.

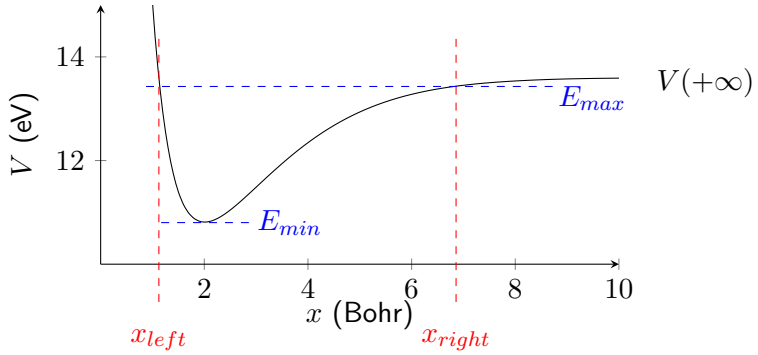

Figure 4.3: Solving the 1D Schrödinger equation for a bound potential, the algorithm chooses the value E_{max} slightly below the value of the potential at infinity $V(+\infty)$. The boundaries of the numerical domain are computed based on the x coordinates x_{left} and x_{right} of the intersections between the potential $V(x)$ and E_{max}.

the depth of the potential well. In practice, the value $s = 0.028646113\%$ allows to get the right number of energy levels for the D_2^+ molecular ion.

According to Mohandas et. al [24], the following procedure to select the step d leads to sufficient accuracy when looking for bound state solutions to attractive potentials. The step d is chosen depending on the de Broglie wavelength λ:

$$d = \frac{\lambda}{2\pi r} = \frac{1}{2\pi r} \frac{h}{\sqrt{2\mu(E_{max} - E_{min})}}, \tag{4.16}$$

where h is the Planck's constant, μ the reduced mass and r a parameter allowing the user to easily increase the accuracy of the computation if needed. Of course increasing r, therefore decreasing d, increases the accuracy of the solutions at the cost of additional computational resources. In practice setting $r = 2$ provided the desired accuracy.

As for the selection of the boundaries, the domain must be large enough to encompass the spatial region of interest and not to influence the physics of the problem. Indeed, if the boundaries of the numerical domain are too close to the boundaries of the physical potential, the solutions of the Schrödinger equation are invalid because they are forced to vanish at x_0 and x_{N+1} due to boundary conditions. On the other hand, choosing a too large domain implies wasting computation time and memory. It is particularly true using a matrix-based method, because the dimension of the matrix is $N \times N$, with the number of points in the numerical domain being N, the number of elements in the matrix (and therefore the memory consumption) scales as $\mathcal{O}(N^2)$. Moreover, computing eigenvalues and eigenvectors does not scale very well with the matrix dimensions since the corresponding computational complexity is $\mathcal{O}(N^3)$ [5].

Because E_{max} is known, it is possible to smartly choose the boundaries of the numerical

[5] More precisely $\mathcal{O}(N^\omega)$ with $2 < \omega < 2.376$.

domain when dealing with bound potentials. Let x_{left} and x_{right} be the leftmost and rightmost intersections of the function $V(x)$ with the constant function E_{max}, respectively [6] (see Figure 4.3). The values x_1 and x_N are then computed as follows:

$$x_1 = x_{left} - 2d, \tag{4.17}$$

$$x_N = x_{right} + 2d. \tag{4.18}$$

The $2d$ offset acts as a security margin assuring that the boundary conditions $\Psi_0 = 0$ and $\Psi_{N+1} = 0$ do not influence the solutions in the spatial region of interest.

When dealing with unbound potentials, the left boundary of the domain x_1 is computed from x_{left} as in the bound case. However, x_N must be explicitly specified to the program depending on the spatial region of interest. Note that, dealing with unbound potentials, the number of found solutions to the Schrödinger equation increases with the size of the numerical domain (see Figure 4.4). Indeed, the imposed boundary conditions are equivalent to putting the system in a box. The smaller the box, the higher the discretization of the quantum states and the smaller the number of possible states. The bigger the box, the closer the numerical representation of the system is to the free particle case and to the situation of a continuum of quantum states.

4.3 Normalization of bound state and continuum wavefunctions

The wavefunctions Ψ obtained after computing the eigenvalues and eigenvectors of the matrix H (Equation (4.14)) must still be normalized to be used in computations of observable quantities. Because the bound state solutions are square-integrable, their normalization is trivial:

$$\int |\Psi(x)|^2 dx = C \implies \Psi_{\text{normalized}} = \frac{\Psi}{\sqrt{C}}. \tag{4.19}$$

Let x_i be the points of the numerical domain, the computed wavefunctions are expressed in the spatial basis $\{\delta(x_i)\}$ and Equation (4.19) becomes:

$$\int \left(\sum_{i=1}^{N} \delta(x_i)\Psi^*(x)\right)\left(\sum_{j=1}^{N} \delta(x_j)\Psi(x)\right) dx = \sum_{i,j} \int \delta(x_i)\delta(x_j)|\Psi(x)|^2 dx = \sum_{i=1}^{N} |\Psi(x_i)|^2. \tag{4.20}$$

[6] If the user chooses to specify manually the value of E_{max}, he must ensure that the condition $E_{max} < V(x = +\infty)$ is fulfilled, otherwise two intersections may not be found.

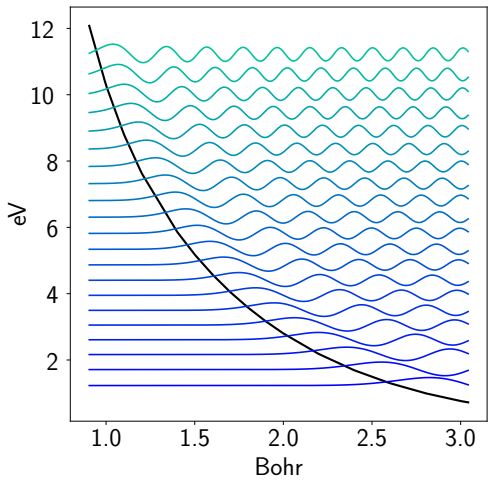

Setting $x_N = 3$ Bohr, 21 vibrational states are found.

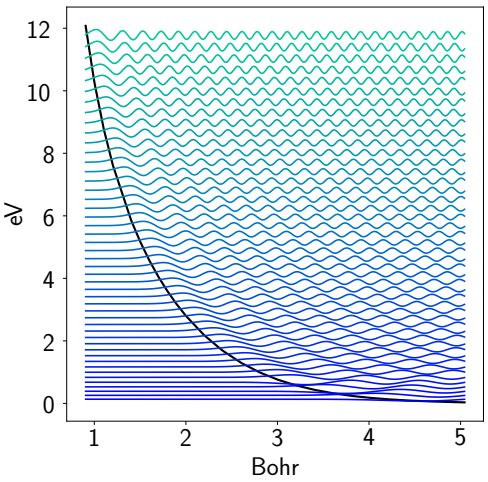

Setting $x_N = 5$ Bohr, 47 vibrational states are found.

Figure 4.4: Vibrational states of the $D_2(b^3\Sigma_u^+)$ unbound potential up to $E_{max} = 12$ eV. The black curve is the potential, the colored curves are some representations of the wavefunctions drawn around their corresponding energy levels.

The vector $\vec{\Psi} = (\Psi(x_1), ..., \Psi(x_i), ..., \Psi(x_N))$ is introduced and the normalization becomes:

$$\vec{\Psi}_{\text{normalized}} = \frac{\vec{\Psi}}{|\vec{\Psi}|}. \tag{4.21}$$

Because continuum wavefunctions are not square-integrable, their normalization is more tricky. At infinity ($x = +\infty$), the normalized continuum wavefunctions have the asymptotic form [25]:

$$\Psi(x) = \frac{1}{\sqrt{\pi\hbar}} \left(\frac{2\mu}{E}\right)^{1/4} \sin(kx + \phi), \tag{4.22}$$

where μ is the reduced mass, E the energy level of the continuum state, $k = \sqrt{2\mu E}/\hbar$ the wavenumber and ϕ an unknown phase. Numerically obtained wavefunctions have indeed a sinus-like form at large x. They are scaled such that the amplitude at large x matches the one of the analytical form presented in Equation (4.22). Let A be the amplitude at large x before normalization, the normalized continuum wavefunction $\vec{\Psi}_{\text{normalized}}$ is then obtained as follows:

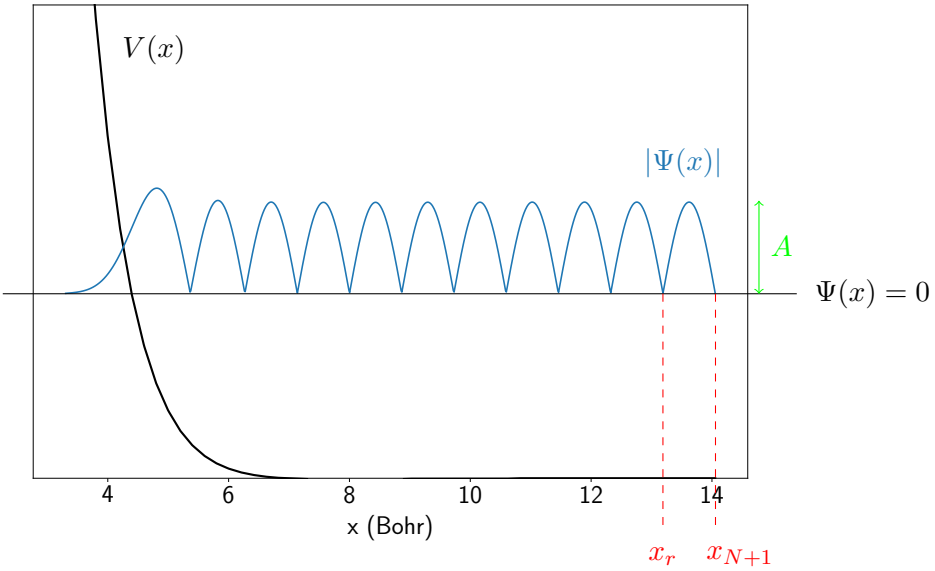

Figure 4.5: The amplitude of the non-normalized continuum wavefunction is found computing the maximum of the absolute value of the wavefunction, $|\Psi(x)|$, in the domain $[x_r, x_{N+1}]$, i.e. between the two last roots of the wavefunction $\Psi(x)$.

$$\vec{\Psi}_{\text{normalized}} = \frac{1}{\sqrt{\pi\hbar}} \left(\frac{2\mu}{E}\right)^{1/4} \frac{\vec{\Psi}}{A}. \tag{4.23}$$

To get the value of A, the algorithm looks for the two last roots of the function $\Psi(x)$ in the domain $[x_1, x_{N+1}]$ (see Figure 4.5). The last root is trivially x_{N+1}, since due to imposed boundary conditions, $\Psi_{N+1} = 0$. The penultimate, x_r, is found searching successively for a root in the domains $[x_{i-1}, x_i]$ for decreasing values of i and starting at $i = N$. The value of A is then the maximum of the function $f(x) = |\Psi(x)|$ in the domain $[x_r, x_{N+1}]$.

Chapter 5

Dissociation of D_2^+ due to charge exchange with the residual gas of the vacuum chamber

This Chapter discusses the interaction between the molecular ion D_2^+ with the residual gas of the vacuum chamber. The experiment allowing to study such interaction is performed switching off the negative beam of the confluent beams machine and setting up a D_2^+ source to feed the positive beam. This interaction is studied because it is a major source of background in the kinetic energy released (KER) measurements of the reaction $D_2^+ + D^- \rightarrow D_2^* + D$ studied in Chapter 6.

The current chapter focuses on the dissociation of the $(D_2^+ + e)$ system into two Deuterium atoms D, the corresponding final state being the dissociative state $D_2(b^3\Sigma_u^+)$:

$$D_2^+ + X \rightarrow D_2(b^3\Sigma_u^+) + X^+ = D + D + X^+, \tag{5.1}$$

where X represents the possible unknown components of the residual gas in the vacuum chamber [1]. Note that the reagents can react differently, for example by collision induced dissociative processes [15]:

$$D_2^+ + X \rightarrow D^+ + D + X, \tag{5.2}$$

$$D_2^+ + X \rightarrow D^+ + D^+ + e + X, \tag{5.3}$$

or by non-dissociative charge exchange:

$$D_2^+ + X \rightarrow D_2 + X^+. \tag{5.4}$$

[1] Example of possible components are Dihydrogen H_2 and Dinitrogen N_2.

Because due to not perfect vacuum, there is always residual gas in the chamber, these processes are potential sources of background in the study of any reactions involving the molecular ion D_2^+. However among these, the reaction (5.1) is the only one producing background in the measurements performed in the context of this work, which motivates the focus on reaction (5.1).

The two neutral Deuterium atoms are indeed able to hit the two detectors in the detection time frame. Moreover, since they inherit of more or less half the energy of D_2^+ in the laboratory frame while having each half its mass, the velocity of each Deuterium atom is similar to the velocities of the products of the process $D_2^+ + D^- \rightarrow D_2^* + D$. Therefore, because only the velocities of the detected particles are measured and not their mass, the pair (D, D) produced by reaction (5.1) may fool the momentum and energy conservation checks associated to the process $D_2^+ + D^- \rightarrow D_2^* + D$.

Reaction (5.2) does not produce background in the two-body KER measurements. Indeed, because ions are forced to avoid detectors by the electric field applied to steer the D2+ beam into a Faraday cup, the pair (D^+, D) is unable to hit the detectors and to be detected as a valid event. Moreover, because the element X is not part of one of the confluent beams, its velocity before collision is thermal and randomly distributed. Therefore, the pair (D, X) is unlikely to hit the two detectors during the detection time frame. One could argue that momentum of D_2^+ could be transferred to X during the collision, pushing X in the direction of the detectors. However in this case, the pair (D, X) would not comply to the momentum conservation constraint associated to the process $D_2^+ + D^- \rightarrow D_2^* + D$.

Likewise, products of reactions (5.3) and (5.4) are only composed of one neutral. The ions being unable to hit detectors due to electrostatic deflection, no pair of neutrals being likely to be detected exists and no background results from these reactions.

One may wonder why the interaction between the negatively charged beam D^- and the residual gas has not been studied in the same way as the interaction between the positively charged beam D_2^+ and the residual gas. The reason is that this reaction does not produce coincident events as reaction (5.1) would, for the same reason invoked above that collision partners X are essentially at rest.

This Chapter is organized as follows. The first section briefly presents the evolution of the number of detected events with the D_2^+ current. The second section shows how to compute the experimental kinetic energy released (KER) from the measurements performed by the two detectors. The third section explains the theoretical computation of the kinetic energy released by the reaction (5.1). Finally, the last section compares the experimental KER with theoretically computed KERs.

5.1 Evolution the number of events detected per second with the increase of the D_2^+ current

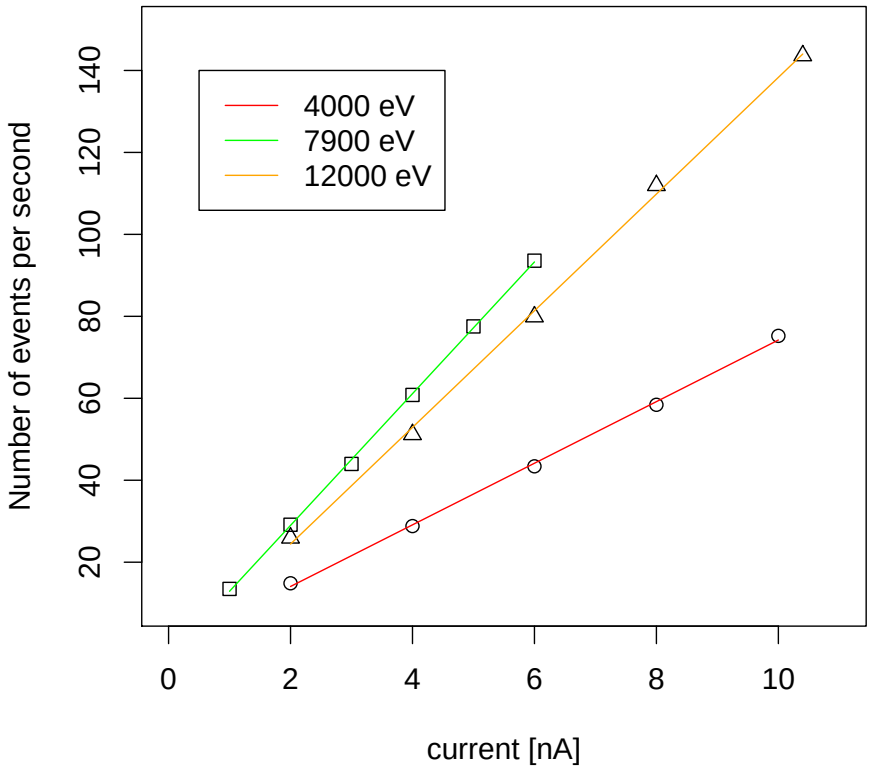

Figure 5.1: Evolution of the number of events detected per second with the increase of the D_2^+ cations beam current. Detected events are due to reaction (5.1). The different colored lines correspond to different energies for the particles of the beam in the laboratory frame.

This section presents the evolution of the number of events detected per second with the increase of the D_2^+ current. An event is detected if two Deuterium atoms reach the detectors in some carefully selected time frame. Measurements have been performed for three different beam energies: 4000 eV, 7900 eV and 12000 eV (see Figure 5.1).

The results show a linear increase of the number of events with respect to the current of the positive beam. This observation confirms the ability of the detection system to properly detect a small number of coincident events amongst an intense background generated by other dissociative processes generating single atoms.

The maximum number of detected events is reached for the intermediate beam energy 7900 eV. It means that at 4000 eV, some fragments miss the detectors due to a too low speed v_z in the beam direction $\hat{z}$. Indeed, due to the kinetic energy released by the dissociation, the components v_x and v_y of the velocity of the fragments are non zero (in

most cases). If v_z is too small, the time of flight for the fragments to reach the coordinate z of the detection planes is high. During this time, the fragments may run through a high distance along x and y therefore missing the area of the detectors. At the opposite, if the beam energy is too high, v_z may be too high for the fragments to reach the area of the detectors, the edge of which leaves a 20mm gap around the beam axis. In this case the fragments may not have enough time to move away from the axis of the beam and they may pass between the two detectors.

This experiment shows that, when studying interaction between two confluent beams, some background derives from the interaction between the ions of the beams with the ambient gas in the vacuum chamber. In the context of the reaction $D_2^+ + D^- \rightarrow D_2^* + D$ studied in Chapter 6, a major source of background is the reaction (5.1). It is interesting to know that this background increases linearly with the positive beam current. A consequence is that, if one needs to increase the number of events produced by the reaction $D_2^+ + D^- \rightarrow D_2^* + D$, doing so by increasing the current of the negative beam D^- will be less problematic than increasing the positive beam current D_2^+.

5.2 Computing from experimental measurements the kinetic energy released by the dissociation of a two-body system

This section explains how the kinetic energy released (KER) is computed from measurements of the dissociation of a two-body system.

Let t_1 and t_2 be the flight times of the bodies detected on the first and second detector, respectively. As explained in Chapter 2, the following data are provided by the experiment about a detected event: the positions of the impacts of the two bodies on the detectors in a laboratory frame centered at the position of the dissociation $\{(x_1, y_1, z_1), (x_2, y_2, z_2)\}$ and the difference between the two detection times $dT_{12} = t_2 - t_1$.

The velocities $\vec{V_i}$ of the two bodies in the laboratory frame are then:

$$\vec{V_1} = \left(\frac{x_1}{t_1}, \frac{y_1}{t_1}, \frac{z_1}{t_1}\right), \qquad \vec{V_2} = \left(\frac{x_2}{t_1 + dT_{12}}, \frac{y_2}{t_1 + dT_{12}}, \frac{z_2}{t_1 + dT_{12}}\right). \tag{5.5}$$

Moreover, because the energy of the beam E_0 as well as the masses m_1, m_2 of the two bodies are known, the velocity of the center of mass in the laboratory frame V_{cm} can be computed:

$$E_0 = \frac{(m_1 + m_2)V_{cm}^2}{2} \implies V_{cm} = \sqrt{\frac{2E_0}{m_1 + m_2}}. \tag{5.6}$$

The direction of the velocity of the center of mass is the direction of the beam $\hat{z}$, therefore $\vec{V_{cm}} = (0, 0, V_{cm})$. Conservation of momentum implies $m_1\vec{V_1} + m_2\vec{V_2} = (m_1 + m_2)\vec{V_{cm}}$:

$$\begin{cases} m_1 V_{1x} + m_2 V_{2x} = 0, \\ m_1 V_{1y} + m_2 V_{2y} = 0, \\ m_1 V_{1z} + m_2 V_{2z} = (m_1 + m_2) V_{cm}. \end{cases} \iff \begin{cases} \frac{m_1 x_1}{t_1} + \frac{m_2 x_2}{t_1 + dT_{12}} = 0, \\ \frac{m_1 y_1}{t_1} + \frac{m_2 y_2}{t_1 + dT_{12}} = 0, \\ \frac{m_1 z_1}{t_1} + \frac{m_2 z_2}{t_1 + dT_{12}} = (m_1 + m_2) V_{cm}. \end{cases} \tag{5.7}$$

The first equation of Equation (5.7) can be used to compute the arrival time of a body on the first detector t_1:

$$t_1 = \frac{-m_1 x_1 dT_{12}}{m_1 x_1 + m_2 x_2}. \tag{5.8}$$

The two last equations (as well as a third one coming from energy conservation), could be used to remove background events from the measurements since the momentum and energy conservation constraints must be fulfilled by events resulting from the physical process of interest. More generally, the center of mass position (x, y) may differ from that of the beam axis in the detection plane, i.e. $(0, 0)$, due to imperfect collimation of the beams. All three equations are thus needed to retrieve t_1 and the velocities $\vec{V_1}$ and $\vec{V_2}$.

However, if the bodies A and B of the two-body system have different masses, Equation (5.7) cannot be used because the mapping between m_A, m_B and m_1, m_2 is unknown. A first way to overcome this difficulty is to select as the heavier body the one having the less deviated from the beam trajectory. Unfortunately, this strategy may fail in case of highly uneven energy distribution between the fragments of the dissociation. A second way is to compute t_1 for the two cases $(m_1 = m_A, m_2 = m_B)$ and $(m_1 = m_B, m_2 = m_A)$, keeping only the result respecting at most momentum and energy conservation.

Now that t_1 is known, the velocities in the laboratory frame $\vec{V_1}$ and $\vec{V_2}$ can be computed from Equation (5.5). The velocities in the center of mass frame $\vec{v_i}$ are then trivially obtained as follows:

$$\vec{v_i} = \vec{V_i} - \vec{V_{cm}}. \tag{5.9}$$

Finally, the experimental KER is obtained:

$$\boxed{KER = \frac{1}{2}\left(m_1 v_1^2 + m_2 v_2^2\right).} \tag{5.10}$$

5.3 Computing the theoretical kinetic energy released by the transition from the fundamental electronic state of the $D_2^+(v)$ molecular ion to the dissociated state $D_2(b^3\Sigma_u^+)$ due to charge exchange with the residual gas

In this section, the kinetic energy released by the dissociation of the D_2^+ molecular ion due to charge exchange with the residual gas in the vacuum chamber,

$$D_2^+ + X \rightarrow D_2(b^3\Sigma_u^+) + X^+, \tag{5.11}$$

is theoretically computed.

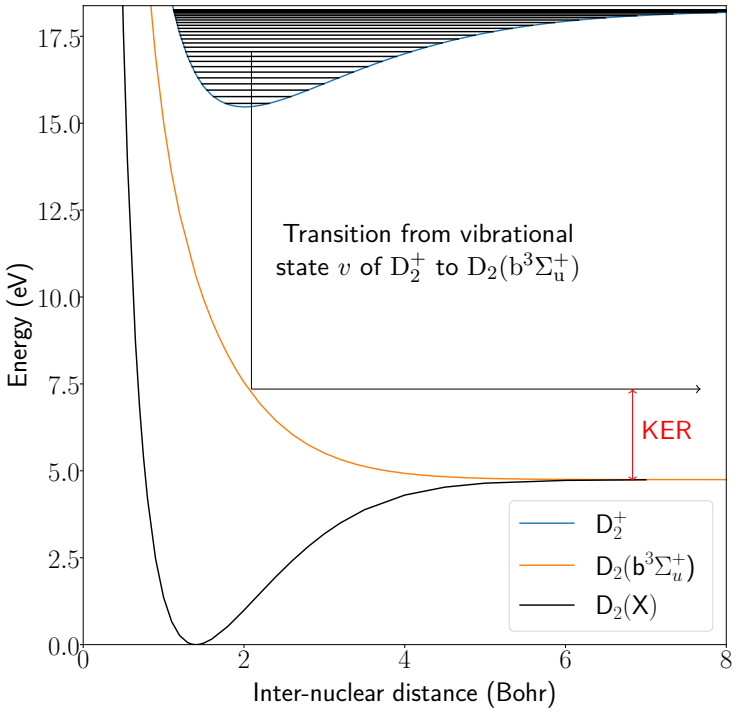

Figure 5.2: The kinetic energy released (KER) by the transition from the vibrational level v of the bound state D_2^+ to a continuum wavefunction of the dissociated state $D_2(b^3\Sigma_u^+)$ is the energy of the final continuum state, i.e. the eigenvalue of the corresponding continuum wavefunction, the zero of energy being defined as the bottom of the dissociated potential curve.

When there is a transition from a vibrational state of the ion D_2^+ to a continuum vibra-

tional wavefunction of the unbound $D_2(b^3\Sigma_u^+)$ state, the kinetic energy released by this process is the energy of the continuum wavefunction (see Figure 5.2) [2].

Let the wavefunction of the molecular ion D_2^+ in the vibrational level v_i be Ψ^i and ξ^j be a vibrational continuum wavefunction accessible in the unbound state $D_2(b^3\Sigma_u^+)$. Under the assumption of validity of the Franck-Condon principle, the probability P_{ij}^{tr} for the system to make the transition from Ψ^i to ξ^j is simply the squared modulus of the overlap integral:

$$P_{ij}^{tr} = |\langle \Psi^i | \xi^j \rangle|^2. \tag{5.12}$$

The matrix $FCM = [P_{ij}^{tr}]$ is referred as the Franck-Condon matrix. The Franck-Condon principle is valid if the inter-nuclear distance is constant during the transition from Ψ_i to ξ_j [26].

Since this study is limited to one-dimensional potentials and wavefunctions, Equation (5.12) becomes:

$$P_{ij}^{tr} = \left| \int_0^\infty \Psi^i(x)\xi^j(x)\ dx \right|^2, \tag{5.13}$$

where x is the inter-nuclear distance.

Because the bound state wavefunctions Ψ^i are non-null over a finite domain only, this integral is computed numerically using the grid $\{x_1, ...x_N\}$ associated to the bound-state wavefunction Ψ^i. The values of the wavefunction ξ^j over the grid associated to Ψ^i are obtained by interpolating ξ^j over its own grid, then evaluating the interpolation at all points of the grid of Ψ^i. The integral is finally computed using the trapezoidal rule [3]:

$$\int_{-\infty}^{\infty} \Psi^i(x)\xi^j(x)\ dx \approx \vec{\Psi}^i \cdot \vec{\xi}^j\ \Delta x - \frac{\Delta x}{2}\left(\Psi_1^i\xi_1^j + \Psi_N^i\xi_N^j\right), \tag{5.14}$$

where $\vec{\Psi}^i = (\Psi_1^i, ..., \Psi_k^i, ..., \Psi_N^i)$ and $\vec{\xi}^j = (\xi_1^j, ..., \xi_k^j, ..., \xi_N^j)$ with $\Psi_k^i = \Psi^i(x_k)$ and $\xi_k^j = \xi^j(x_k)$. Moreover, Δx is the step of the numerical domain. If the system resides in an initial state Ψ^i, the probability $p^{ker}(E_j)$ for the KER to be E_j is the probability $P_{ij}^{tr} = FCM_{ij}$ to make the transition from Ψ^i to a state ξ^j such that the energy associated to the state ξ^j is E_j:

$$p^{ker}(E_j) = FCM_{ij}. \tag{5.15}$$

In order to compute $p^{ker}(E_j)$, the continuum wavefunction ξ^j associated to the energy level E_j must be found from the only knowledge of E_j. In principle, since there is an infinite number of continuum wavefunctions, such ξ^j always exists for positive values of E_j.

[2] The zero of energy being defined as the bottom of the unbound potential $D_2(b^3\Sigma_u^+)$.

[3] This strategy is thousand times faster than interpolating both Ψ^i and ξ^j before integrating the product of these interpolations with the function integrate.quad from the python package scipy.

However, only a discrete set of continuum wavefunctions $\{\xi^1, ..., \xi^k, ..., \xi^M\}$ associated to a discrete set of energy levels $\{E_1, ..., E_k, ..., E_M\}$ are obtained through numerical computations (see the end of Section 4.2). The wavefunction ξ^k used to compute $p^{ker}(E_j)$ is selected such that the quantity

$$\Delta E = |E_k - E_j| \tag{5.16}$$

is minimized.

Now, the whole population of possible vibrational states Ψ^i is considered. Assuming that reaction (5.1) is the only possible one, the probability $P^{ker}_{\text{only } D_2(b^3\Sigma_u^+)}(E_j)$ for the KER to be E_j is then the sum of the probability for each Ψ^i to make the transition to ξ^j weighted by the probability $P^{vib}(i)$ for the molecular ion D_2^+ to be in the vibrational state Ψ^i:

$$P^{ker}_{\text{only } D_2(b^3\Sigma_u^+)}(E_j) = \sum_i FCM_{ij}\ P^{vib}(i). \tag{5.17}$$

However, as explained in the beginning of this chapter, other reactions are possible. The probability for the system to undergo the dissociative channel (5.1) instead of other channels such as reactions (5.2), (5.3) or (5.4) depends on the energies E_i of the initial state Ψ^i and E_j of the final state ξ^j. In other words, the cross section q of the reaction (5.1) depends on Ψ^i and ξ^j. Therefore, the KER distribution (Equation (5.17)) must be modified such that kinetic energies released by transitions $\Psi^i \rightarrow \xi^j$ with higher cross sections are considered as more probable. The valid expression for the KER distribution is then obtained by multiplying Equation (5.17) by the cross section $q(\Delta I(E_i, E_j))$ of the dissociative reaction (5.1):

$$P^{ker}(E_j) = \sum_i FCM_{ij}\ P^{vib}(i)\ q(\Delta I). \tag{5.18}$$

The argument ΔI of the function q is the energy defect. When considering the interaction of $D_2^+(v)$ with the residual gas $H_2(v = 0)$, the energy defect is the total energy of the reagents $D_2^+(v) + H_2(v = 0)$ minus the total energy of the products $D_2(b^3\Sigma_u^+) + H_2^+(v)$. Under the hypothesis that the ionization of the H_2 molecule is performed to the fundamental vibrational level, $H_2^+(v = 0)$, the difference of energy between H_2 and $H_2^+(v = 0)$ is simply minus the ionization potential of the H_2 molecule $IP_{H_2} \approx 15.4$eV and therefore:

$$\Delta I = E_i - E_j - IP_{H_2}. \tag{5.19}$$

Two different cross sections $q(\Delta I)$ have been tested: the first one is derived from the Demkov's model and the second one is proposed by De Bruijn [27].

5.3.1 Theoretical cross section: Demkov's model

The Demkov's model allows to compute the cross section of quasi-resonant dissociative charge exchange reactions [25]. In this section, charge exchange between a molecular ion referred as I (D_2^+) and a neutral molecule referred as M (H_2) is considered. The main steps of the demonstration of the cross section of reaction (5.1) are summarized.

The charge exchange is said to be quasi-resonant if the difference between the binding energies of the active electron in the two interacting entities is small [27]. Because D_2^+ and H_2^+ are very similar systems from the electronic point of view, the binding energy of the electron is identical when attached to one or the other. This motivates the use of a quasi-resonant charge exchange model.

Let R be the distance between the centers of mass of I and M. The probability for the electron to exchange is maximal when R is around a critical distance R_c. This is called the critical region. This critical region is crossed two times by the system, a first time when the two entities get closer until they reach an inter-distance $R < R_c$ and a second time when the entities move away from each other (see Figure 5.3).

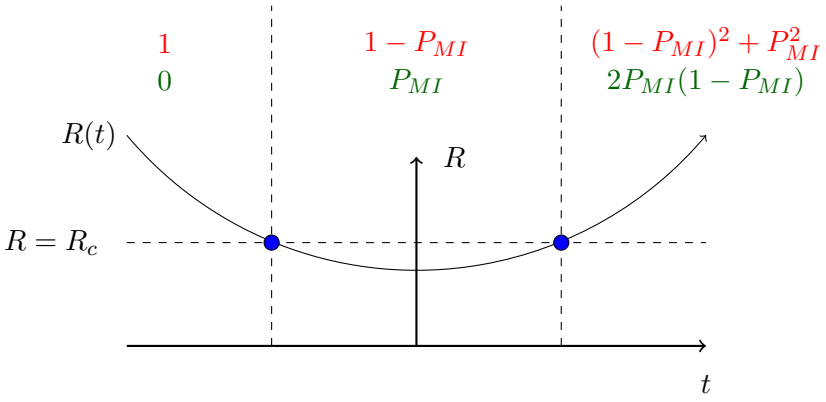

Figure 5.3: t is the time, R is the distance between the centers of mass of the molecule M and the molecular ion I, R_c is the critical region where the probability to exchange the electron is maximal and P_{MI} is the probability for the electron to move from M to I or vice versa when crossing the critical region. Expressions in red and green are the probabilities for the electron to be attached to M and I in the intervals delimited by vertical dashed lines, respectively. The electron is initially attached to the neutral molecule M. The molecule M and the molecular ion I get closer eventually crossing the critical region R_c a first time (left blue dot). Then, they keep getting closer until reaching a minimum inter-distance. Finally, the inter-distance R increases and the system crosses the critical region a second time (right blue dot).

Let $\phi_M(r_M)$ be the orbital of the neutral molecule and $\phi_I(r_I)$ be the orbital of the molecular ion. If the collision only implies two states, the Hamiltonian of the whole system writes:

$$H = \begin{pmatrix} E_M & h_{MI}(R) \\ h^*_{MI}(R) & E_I \end{pmatrix}, \tag{5.20}$$

where the coupling $h_{MI}(R)$ depends on the distance R between M and I. The normalized basis $\{\Psi_1, \Psi_2\}$ of this Hamiltonian is composed of linear combinations of ϕ_M and ϕ_I:

$$\begin{cases} \Psi_1 = c_1(R)\phi_M + c_2(R)\phi_I, \\ \Psi_2 = c_3(R)\phi_M + c_4(R)\phi_I. \end{cases} \tag{5.21}$$

Orthonormality of the basis $\{\Psi_1, \Psi_2\}$ implies:

$$\begin{cases} \Psi_1 = \cos(\theta(R))\ \phi_M + \sin(\theta(R))\ \phi_I, \\ \Psi_2 = -\sin(\theta(R))\ \phi_M + \cos(\theta(R))\ \phi_I, \end{cases} \tag{5.22}$$

with [4]

$$\frac{\sin(2\theta)}{\cos(2\theta)} = \tan(2\theta) = \frac{2|h_{MI}|}{E_M - E_I} \equiv \frac{2|h_{MI}|}{\Delta E}. \tag{5.23}$$

The Demkov's model assumes that ΔE does not depend on R and is therefore a constant. When the electron is very far from M or I the asymptotic forms of the orbitals depend on the position of the active electron as:

$$\phi_M(r_M) \propto \exp(-\alpha_M r_M), \tag{5.24}$$

$$\phi_I(r_I) \propto \exp(-\alpha_I r_I), \tag{5.25}$$

where α_i is a function of the binding energy. The exponential decrease of the orbitals with the distance of the electron from the corresponding entity implies the exponential decrease of the coupling between the two states with the distance R between M and I:

$$h_{MI}(R) = \frac{\Delta E}{2} \exp\left(-\frac{\alpha_M + \alpha_I}{2}(R - R_c)\right). \tag{5.26}$$

For distances R such that $R < R_c$, the exponential term in Equation (5.26) is greater than one and the coupling h_{MI} takes over the energy gap ΔE. In this case, from Equation (5.23):

$$\tan(2\theta) = \frac{2|h_{MI}|}{\Delta E} \to \infty \implies 2\theta \to \pm\frac{\pi}{2} \implies \theta \to \pm\frac{\pi}{4}. \tag{5.27}$$

[4] More details in the quantum mechanics book written by Cohen-Tannoudji et al. [28] page 419.

Equation (5.22) shows that the mixing of the orbitals is maximized for $\theta = \pm\pi/4$, each orbital having the same weight $\sqrt{2}/2$ in the expressions of the wavefunctions of the whole system. Choosing $\theta = \pi/4$:

$$\begin{cases} |\Psi_1\rangle = \frac{\sqrt{2}}{2}(|\phi_M\rangle + |\phi_I\rangle), \\ |\Psi_2\rangle = \frac{\sqrt{2}}{2}(-|\phi_M\rangle + |\phi_I\rangle). \end{cases} \tag{5.28}$$

When the orbitals are far from each other, i.e. $R >> R_c$:

$$|h_{MI}| \to 0 \implies \tan(2\theta) \to 0 \implies \theta = 0, \tag{5.29}$$

and there is no interaction between the two orbitals and no possible charge exchange:

$$\begin{cases} |\Psi_1\rangle = |\phi_M\rangle\,, \\ |\Psi_2\rangle = |\phi_I\rangle\,. \end{cases} \tag{5.30}$$

The temporal dependence of the wavefunction of the whole system $\Psi(x,t)$ is given by the time-dependent Schrodïnger's equation:

$$i\hbar\frac{\partial\Psi(x,t)}{\partial t} = H(t)\Psi(x,t). \tag{5.31}$$

One must be careful solving Equation 5.31 because some components of the Hamiltonian are not time independent. Indeed, the Demkov's model assumes $R - R_c = v_c t$, where v_c is a constant speed. Therefore, the coupling h_{MI} has the following time dependence:

$$h_{MI}(t) = \frac{\Delta E}{2}\exp\left(-\frac{\alpha_M + \alpha_I}{2}\ v_c t\right). \tag{5.32}$$

The solution of Equation (5.31) is then:

$$\Psi(x,t) = \exp\left(\frac{\int^t H(t)dt}{i\hbar}\right)\left(c_M(t)\,|\phi_M\rangle + c_I(t)\,|\phi_I\rangle\right), \tag{5.33}$$

the wavefunction $\Psi(x,t)$ being expended on the basis composed by the orbitals $\{\phi_M, \phi_I\}$. The quantity $|c_M(t)|^2$ is the probability for the electron to be still attached to the neutral molecule M at time t. The quantity $|c_I(t)|^2$ is the probability for the electron to be attached to the molecular ion I at time t.

Using the series expansion of the exponential:

$$\exp(x) = \sum_{k=0}^{\infty}\frac{x^k}{k!}, \tag{5.34}$$

$$\exp\left(\frac{\int^t H(t)dt}{i\hbar}\right)|\phi_i\rangle = \sum_{k=0}^{\infty}\frac{\left(\int^t H(t)dt\right)^k}{(i\hbar)^k k!}|\phi_i\rangle = \sum_{k=0}^{\infty}\frac{\left(\int^t H(t)dt\right)^{k-1}}{(i\hbar)^k k!}\int^t H(t)|\phi_i\rangle\,dt$$
$$= \sum_{k=0}^{\infty}\frac{\left(\int^t H(t)dt\right)^{k-1}}{(i\hbar)^k k!}\int^t E(t)|\phi_i\rangle\,dt = \sum_{k=0}^{\infty}\frac{\left(\int^t H(t)dt\right)^{k-2}}{(i\hbar)^k k!}\int^t E(t)dt\int^t H(t)|\phi_i\rangle\,dt$$
$$= \sum_{k=0}^{\infty}\frac{\left(\int^t H(t)dt\right)^{k-3}}{(i\hbar)^k k!}\left(\int^t E(t)dt\right)^2\int^t H(t)|\phi_i\rangle\,dt = ... = \exp\left(\frac{\int^t E(t)dt}{i\hbar}\right)|\phi_i\rangle\,. \tag{5.35}$$

And the expression of Ψ becomes:

$$\Psi(x,t) = c_M(t)\exp\left(-\frac{i}{\hbar}\int^t E_M(t)dt\right)|\phi_M\rangle + c_I(t)\exp\left(-\frac{i}{\hbar}\int^t E_I(t)dt\right)|\phi_I\rangle\,. \tag{5.36}$$

Multiplying $\Psi(x,t)$ by the phase $\exp(\frac{i}{\hbar}\int^t \frac{E_M+E_I}{2}dt)$ yields:

$$\Psi(x,t) = c_M(t)\exp\left(-\frac{i}{\hbar}\int^t \frac{\Delta E}{2}dt\right)|\phi_M\rangle + c_I(t)\exp\left(\frac{i}{\hbar}\int^t \frac{\Delta E}{2}dt\right)|\phi_I\rangle\,. \tag{5.37}$$

Then, using the time-dependent Schrodïnger's equation:

$$i\hbar\frac{\partial|\Psi(x,t)\rangle}{\partial t} = H|\Psi(x,t)\rangle\,, \tag{5.38}$$

$$\begin{cases} i\hbar\langle\phi_M|\frac{\partial|\Psi(x,t)\rangle}{\partial t} & = \langle\phi_M|H|\Psi(x,t)\rangle\,, \\ i\hbar\langle\phi_I|\frac{\partial|\Psi(x,t)\rangle}{\partial t} & = \langle\phi_I|H|\Psi(x,t)\rangle\,. \end{cases} \tag{5.39}$$

Inserting $\Psi(x,t)$ in the first and second relations of Equation (5.39) yields:

$$i\hbar\frac{dc_M(t)}{dt}\exp\left(-\frac{i}{\hbar}\int^t\frac{\Delta E}{2}dt\right) + i\hbar c_M(t)\exp\left(-\frac{i}{\hbar}\int^t\frac{\Delta E}{2}dt\right)\left(-\frac{i}{\hbar}\frac{\Delta E}{2}\right) =$$
$$\frac{\Delta E}{2}c_M(t)\exp\left(-\frac{i}{\hbar}\int^t\frac{\Delta E}{2}dt\right) + c_I(t)\exp\left(\frac{i}{\hbar}\int^t\frac{\Delta E}{2}dt\right)h_{MI}, \tag{5.40}$$

$$i\hbar\frac{dc_I(t)}{dt}\exp\left(\frac{i}{\hbar}\int^t\frac{\Delta E}{2}dt\right) + i\hbar c_I(t)\exp\left(\frac{i}{\hbar}\int^t\frac{\Delta E}{2}dt\right)\frac{i}{\hbar}\frac{\Delta E}{2}$$
$$= c_M(t)\exp\left(-\frac{i}{\hbar}\int^t\frac{\Delta E}{2}dt\right)h^*_{MI} + c_I(t)\exp\left(\frac{i}{\hbar}\int^t\frac{\Delta E}{2}dt\right)\left(\frac{-\Delta E}{2}\right). \tag{5.41}$$

Simplifying these expressions yields a coupled system of two equations with two unknowns (c_M and c_I):

$$\begin{cases} i\hbar\frac{dc_M(t)}{dt} = h_{MI}c_I(t)\exp\left(\frac{i}{\hbar}\int^t \Delta E dt\right), \\ i\hbar\frac{dc_I(t)}{dt} = h^*_{MI}c_M(t)\exp\left(-\frac{i}{\hbar}\int^t \Delta E dt\right). \end{cases} \tag{5.42}$$

Using mathematical tricks V. M. Andrianarijaona [25] uncouples and solves these equations [5]. Expressions for the two unknowns c_M and c_I are found and the ratio between the two populations computed:

$$\rho = \frac{|c_I|^2}{|c_M|^2} = \exp(-\gamma\pi). \tag{5.43}$$

The variable γ has the following expression:

$$\gamma = \frac{e\Delta E}{\hbar\lambda\ 9788.97\ v_c}, \tag{5.44}$$

where e is the electron charge in Coulomb, v_c the collision velocity in $\sqrt{\text{eV}}$ and λ a factor related to the binding energies of M and I. The units are m^{-1} for λ, eV for ΔE and J·s for $\hbar$. The constant 9788.97 converts v_c in m/s.

The probabilities P_{MM} and P_{II} for the electron to remain in the state $|\phi_M\rangle$ and $|\phi_I\rangle$ respectively, and P_{MI} for the electron to pass from the state $|\phi_M\rangle$ to $|\phi_I\rangle$ are:

$$\begin{cases} P_{MM} \approx \frac{1}{1+\exp(-\gamma\pi)}, \\ P_{II} = P_{MM}, \\ P_{MI} \approx \frac{\exp(-\gamma\pi)}{1+\exp(-\gamma\pi)}. \end{cases} \tag{5.45}$$

When considering the two crossings of the critical region R_c by the system, the probability for an effective charge exchange to happen is the probability for the electron to pass from the state $|\phi_M\rangle$ to the state $|\phi_I\rangle$ when first crossing the critical region multiplied by the probability for the electron to stay in the state $|\phi_I\rangle$ after the last crossing of the critical region, plus the probability for the electron to stay in the state $|\phi_M\rangle$ when first crossing the critical region multiplied by the probability to pass from the state $|\phi_M\rangle$ to the state $|\phi_I\rangle$ after the last crossing of the critical region (see Figure 5.3) :

$$q(\gamma) = P_{MI}P_{II} + P_{MM}P_{MI} = 2P_{MI}P_{MM} = \frac{2\exp(-\gamma\pi)}{(1+\exp(-\gamma\pi))^2}. \tag{5.46}$$

Using the following expression of the hyperbolic secant:

[5] See pages 78-80 in [25] for details.

$$\text{sech}x = \frac{2e^{-x}}{1+e^{-2x}} = \frac{1}{\cosh x}, \tag{5.47}$$

the probability becomes:

$$q(\gamma) = \frac{1}{2}\,\text{sech}^2\left(\frac{\gamma\pi}{2}\right) = \frac{1}{2\,\cosh^2(\frac{\gamma\pi}{2})}. \tag{5.48}$$

By definition, the energy difference between the orbitals of the molecule and of the molecular ion is the energy defect: $\Delta E = \Delta I$. The relative collision velocity v_c is assumed to be equal to the velocity of the molecular ions D_2^+ in the laboratory frame. The kinetic energy in the laboratory frame is the beam energy E_0 and is set to 8 keV. Therefore, because the mass of D_2 is $m = 4$:

$$v_c = \sqrt{\frac{2E_0}{m}} = \sqrt{4000} = 63.25\ \sqrt{\text{ev}}. \tag{5.49}$$

Because the neutral molecule is H_2 and the molecular ion is D_2^+, the parameter $\lambda = 0.53\ \text{bohr}^{-1}$. Therefore:

$$\frac{\gamma\pi}{2} = 0.191\Delta I. \tag{5.50}$$

This motivates the form of the cross section q with regard to the energy defect ΔI:

$$q(\Delta I) = \frac{1}{\cosh^2(0.191\Delta I)}. \tag{5.51}$$

5.3.2 Experimentally measured cross section

The second tested cross section $q(\Delta I)$ for reaction (5.1) has been measured experimentally by De Bruijn [27]. This function presents a plateau up to -9 eV then increases linearly with ΔI (see Figure 5.4). This cross section has been obtained studying the dissociation by charge exchange of H_2^+ due to interaction with Ar, Mg and Cs. However, because H_2^+ behaves identically to D_2^+ from the electronic point of view and because the Argon has the same ionization potential than the Dihydrogen H_2, which mostly composes the residual gas, this cross section is still relevant for reaction (5.1).

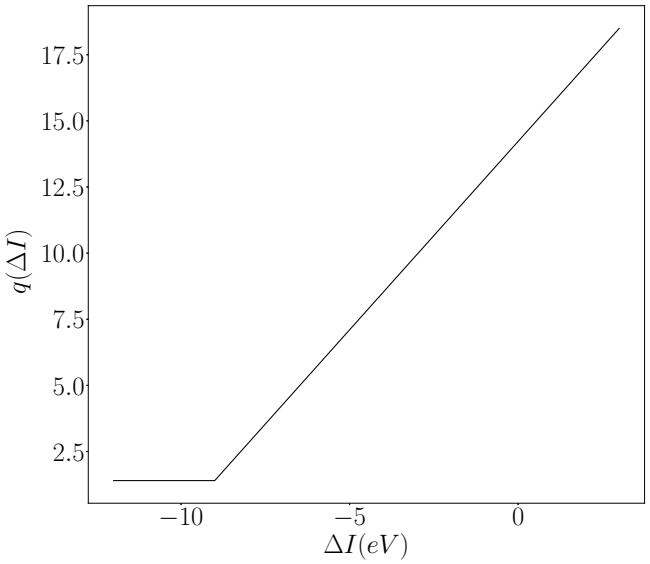

Figure 5.4: Cross section $q(\Delta I)$ as a function of the resonance energy defect for dissociative charge exchange of H_2+ through the $D_2(b^3\Sigma_u^+)$ state for Ar, Mg and Cs targets [27].

5.4 Comparison between the theoretically computed and experimentally measured kinetic energy releases

This sections makes the comparison between the experimental KER computed from measurements using Equation (5.10) and KERs computed from theories presented in Section 5.3.

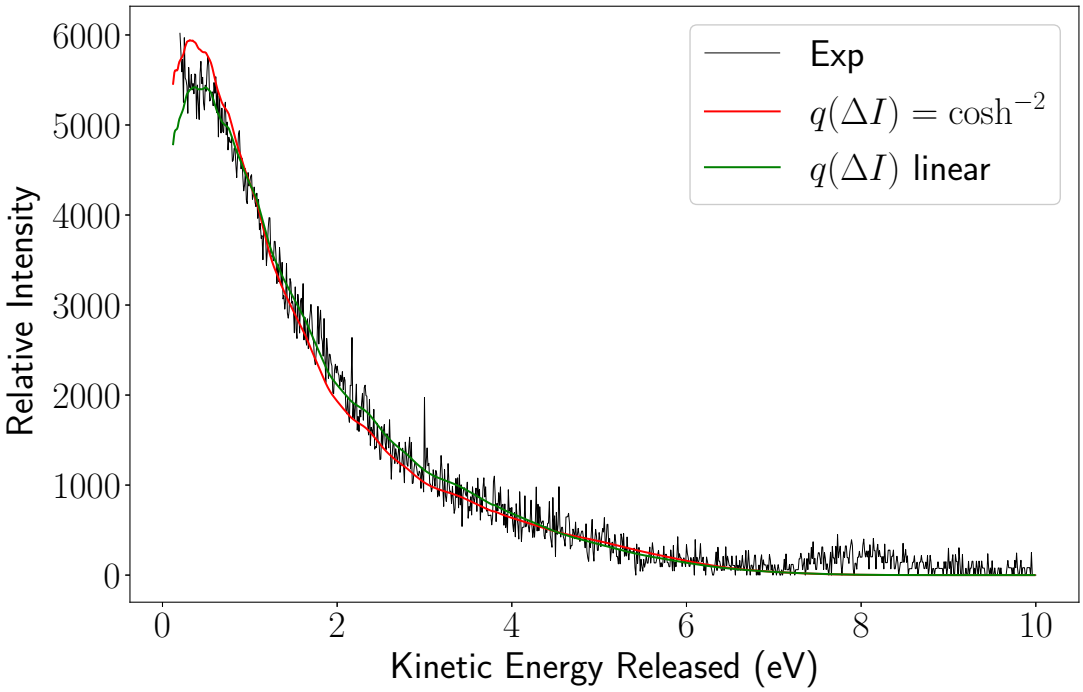

Figure 5.5: Comparison between the experimental KER and the theoretically computed KERs. The theoretical curves are obtained fitting the experimental curve with the function $f(E) = \alpha P^{ker}(E)$, α being the fitting parameter.

The amplitude of the theoretical KER distribution has no meaning as such. Therefore, this theoretical KER distribution is compared to the experimental KER distribution after fitting the experimental curve with the function $f(E) = \alpha P^{ker}(E)$, α being the fitting parameter. The result is presented in the Figure 5.5.

The theoretical KER computed with the linear function q proposed by De Bruijn [27] matches better the experimental results. The theoretical curve fits almost perfectly the experimental KER in this case. It confirms that the measured events are indeed the fragments of the dissociation of the molecular ion D_2^+ in two Deuterium atoms in the state $D_2(b^3\Sigma_u^+)$.

Several reasons may be advanced to explain the difference between the experimental curve and the theoretical curve computed with the Demkov's model. Firstly, this model does not consider the regions outside R_c. A more advanced model considering these regions like the Olson's model may output better results. Secondly, the Demkov's model is not supposed to be used on non-resonant charge exchange between two molecules [27]. Indeed, in this later case the exchange interaction is reported by De Brujn et al. to not only depend on the inter-molecular distance, but also on the orientation and other

internal parameters of the molecules.

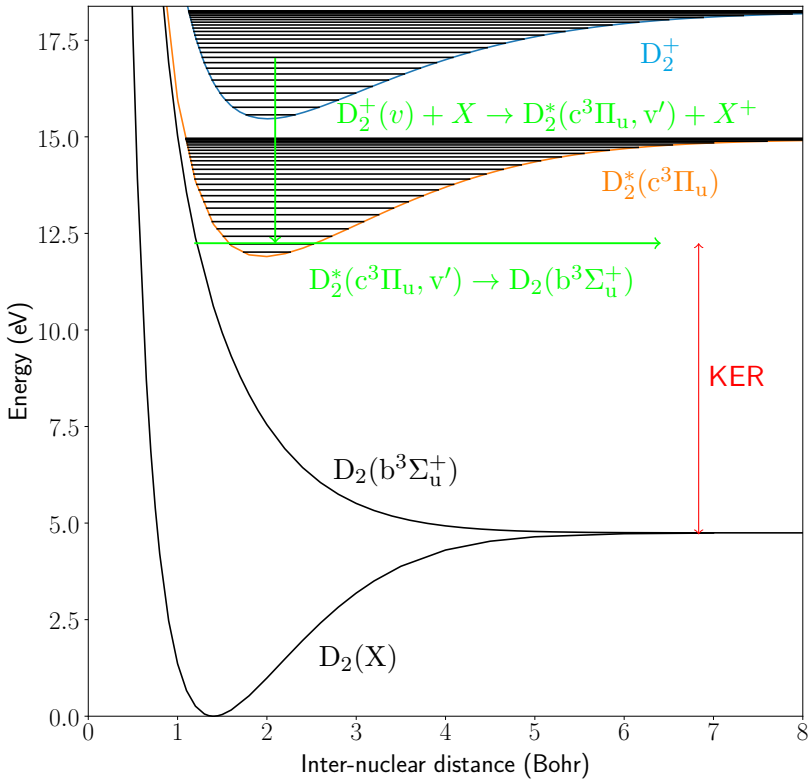

Figure 5.6: The metastable state $D_2^*(c^3\Pi_u)$ is first populated from D_2^+ due to charge exchange with the residual gas. Then, predissociation to two ground state Deuterium atoms occurs yielding discrete KER spectra around 8 eV [27]. This process explains the small bump observed in Figure 5.5.

The small bump at the edge of the experimental curve results from the predissociation of the metastable state $c^3\Pi_u$ of D_2^* populated after charge exchange of D_2^+ with the residual gas at $\approx$ 10 keV energy (see Figure 5.6). Indeed, De Bruijn [27] reports that this predissociative process is responsible for discrete KER spectra between 7.2 and 10.2 eV, the highest peak being observed around 8 eV [6].

[6]For an extensive study of the predissociation of the $c^3\Pi_u$ state, refer to the chapter VI of De Bruijn's thesis [27].

5.5 Conclusion

In this Chapter, the dissociation of D_2^+ due to charge exchange with the residual gas of the vacuum chamber, mostly composed of H_2, has been studied. The study of this reaction in particular has been motivated by the background it yields in measurements of events produced by the mutual neutralization reaction $D_2^+ + D^-$.

The experiment has allowed to observe a linear increase of the number of detected events with the D_2^+ current. Moreover, kinetic energy released by the reaction $D_2^+ + H_2 \rightarrow D + D + H_2^+$ has been computed using the Franck-Condon principle with an additional KER-dependent cross section. Two such cross sections have been compared.

The first one is obtained from the Demkov's model. The matching between the theoretical KER obtained with the Demkov's cross section and the experimental KER is satisfactory, though not perfect. Differences are expected to come from limitations of the Demkov's model.

The second tested cross section has been experimentally measured by De Bruijn [27]. Theoretical KER obtained with this second cross section are in perfect agreement with experimental measurements, the small bumps at the end of the experimental spectra being explained by predissociation of the metastable state $c^3\Pi_u$ of D_2^*.

In conclusion, this study proves that events observed by the two-body detector when the beam D_2^+ is the only active one (i.e. there is no beam D^-) are produced by the dissociation of D_2^+ due to charge exchange with H_2. The measured KER spectra produced by this background has been subtracted from the KER spectra produced by the reaction $D_2^+ + D^-$ studied in Chapter 6.

Chapter 6

Study of the mutual neutralization $D_2^+ + D^-$ based on the kinetic energy release

This Chapter focuses on the mutual neutralization reaction $D_2^+ + D^- \rightarrow D_2 + D$. Because the molecular ion D_2^+ has the same symmetry as the molecule D_2, vibrational wavefunctions of D_2^+ and D_2 are coupled [15]. This non-adiabatic coupling allows the capture of the extra electron attached to D^- by the D_2^+ molecular ion during a collision. Janev et al. [15] discuss the many possible output channels.

When the two ions are separated by an infinite distance, the energy of the state $D_2^+(v = 0) + D^-$ is 1.08 eV above the energy of the state $D_2(v = 0) + D^+$ and 0.754 eV below than the energy of the state $D_2^+(v = 0) + D(1s)$ [1] (see Figure 6.1). Therefore, at smaller inter-distances between the ions D_2^+ and D^-, the potential energy curve of the state $D_2^+(v = 0) + D^-$ intersects both the potential energy curves of the states $D_2(X^1\Sigma_g^+; v') + D^*(n \geq 2)$ and $D_2^*(N^{1,3}\Lambda_{\sigma'}; v') + D(1s)$ with $N \leq 4$ [15].

Due to these intersections, there is a competition between the output channel which yields an electronically excited D_2^* molecule up to $N = 4$ and an atom D in its fundamental electronic state:

$$D_2^+(v) + D^- \rightarrow D_2^*(v') + D, \tag{6.1}$$

and the output channel which yields a D_2 molecule in its fundamental electronic state and an atom D^* in an electronically excited state $n \geq 2$:

$$D_2^+(v) + D^- \rightarrow D_2(v') + D^*. \tag{6.2}$$

[1] The electronic affinity of the Hydrogen atom being 0.754 eV.

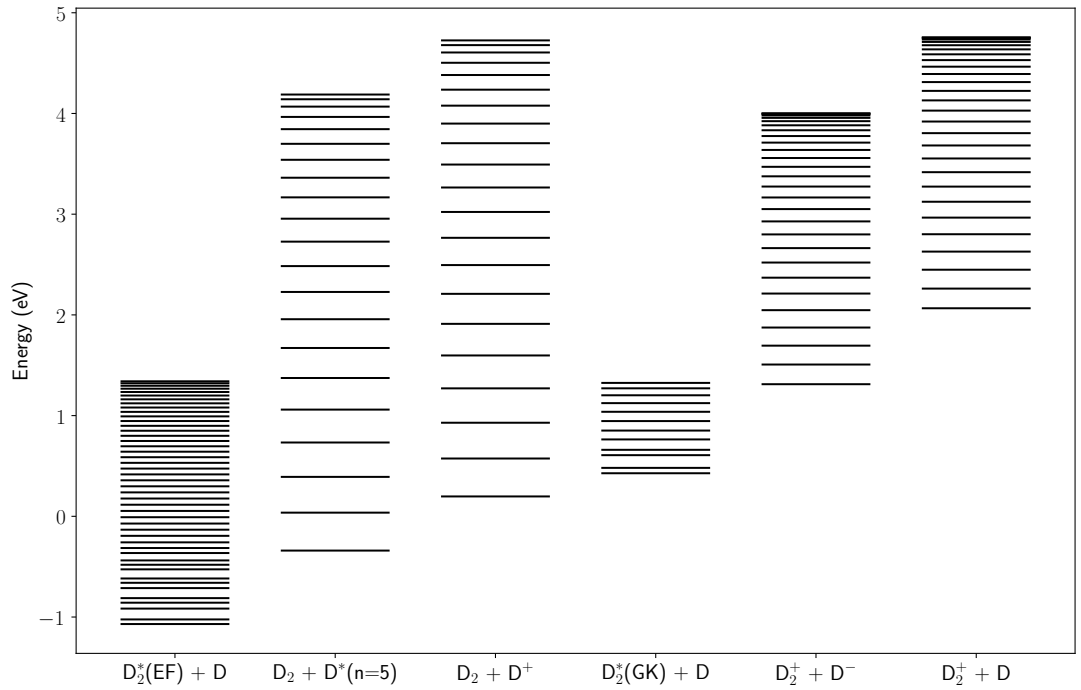

Figure 6.1: Energy level diagram for the system $D_2 + D$ with some of its ionic and excited forms. The energy of the state $D_2^+(v = 0) + D^-$ is between the energies of the states $D_2(v = 0) + D^+$ and $D_2^+(v = 0) + D(1s)$. Energies are expressed with respect to the minimum of the potential curve of the state $D_2 + D^+$.

The goal of this Chapter is to find out which of these two reactions is dominant at low collision energies. The experimental kinetic energy released (KER) by the reaction has been computed from measurements performed by the two-body detector presented in Section 2.1 using equations presented in Section 5.2. The experimental KER is compared to theoretical computation of the kinetic energy released by reactions (6.1) and (6.2).

The first section is about reaction (6.2). The related work about its cross section is first discussed then computed kinetic energies released by this reaction are presented and compared to the experimental KER. The second section is about reaction (6.2). This second section first discusses the possible electronic states for D_2^*. Then, the various followed strategies and made assumptions in order to compute the KER of this reaction are presented in increasing order of complexity.

6.1 The mutual neutralization reaction $D_2^+ + D^- \rightarrow D_2 + D^*$

This section is organized as follows. The first part presents the cross section of reaction (6.2) computed by Eerden et al. [29]. The second part details the theoretical computation of the KER distribution for reaction (6.2). The last part compares the experimental and theoretical KER distributions and discusses the results based on the related work of Eerden et al. [29] introduced in the first part.

6.1.1 Cross section as a function of the electronic level of the produced excited atom

Eerden et al. [29] presents a theoretical cross section for the mutual neutralization reaction:

$$H_2^+(v, J) + H^- \rightarrow H_2(v', J') + H_n^*,\ n \geq 2, \tag{6.3}$$

computed in the framework of the multiple-crossing Landau-Zener approximation.

Their cross section is a function of the quantum number n of the produced Hydrogen atom. For each value of n, the authors have averaged the contributions of the different angular momentum quantum numbers l. Moreover, the rotational and vibrational quantum numbers v' and J' have been selected to maximize the computed cross section. Therefore, the dependence of the cross section with regard to the energy difference between the vibrational levels of $H_2^+(v, J)$ and $H_2(v', J')$ is not known. It implies that Eerden et al. [29] do not provide enough information to compute the cross section as a function of the kinetic energy release.

The cross section presented by Eerden et al. [29] is a non-monotonic function of n (see Figure 6.2 and Table 6.1). The quantum number $n = 5$ corresponds to the maximum cross section: 4.4 10^{-16} m^2 at low collision energy E = 0.02 eV. The cross section then decreases for smaller and larger values of n, reaching $\approx$ 2 10^{-18} m^2 for $n = 2$ and $\approx 1.8\ 10^{-17}$ m^2 for $n = 8$ (still at 0.02 eV).

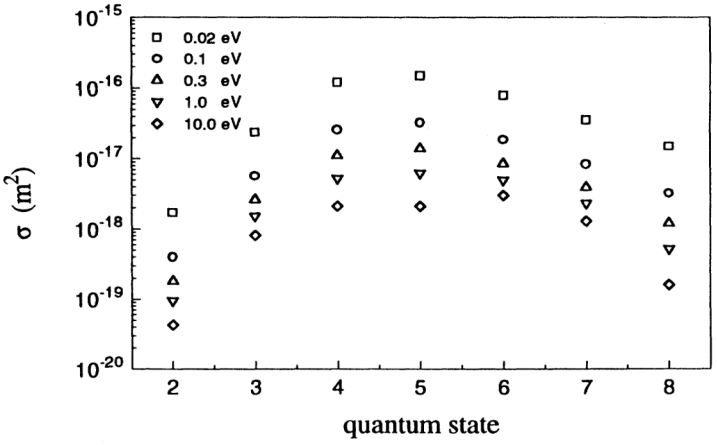

Figure 6.2: Cross section for reaction (6.2) as a function of the quantum number n for different collision energies. Figure source [29].

level	2	3	4	5	6	7	8
cross section (m^2)	$2\ 10^{-18}$	$2.2\ 10^{-17}$	$1.1\ 10^{-16}$	$4.4\ 10^{-16}$	$8\ 10^{-17}$	$3\ 10^{-17}$	$1.8\ 10^{-17}$

Table 6.1: Cross section for reaction (6.2) with a 0.02 eV collision energy as a function of the quantum number n. Source: reading Figure 6.2.

6.1.2 Computing the theoretical kinetic energy released by the mutual neutralization reaction $D_2^+ + D^- \rightarrow D_2 + D^*$

This section explains the computation of the kinetic energy released by the process:

$$D_2^+(v_i) + D^- \rightarrow D_2(v_j) + D_n^*, \tag{6.4}$$

where v_i and v_j are vibrational quantum numbers and n an electronic quantum number. The kinetic energy released by this reaction is the difference between the energy of the reagents and the energy of the products:

$$\begin{aligned} \Delta E(v_i, v_j, n) &= E(D_2^+(v_i) + D^-) - E(D_2(v_j) + D_n^*) && (6.5)\\ &= E(D_2^+(v_i) - D_2(v_j)) + E(D^- - D_n^*) && (6.6)\\ &= E(D_2^+(v_i) - D_2(v_j)) + E(D - D_n^*) - EA(D), && (6.7) \end{aligned}$$

where $E(x)$ returns the energy of the system x and EA(D) is the electronic affinity of the Deuterium atom. The first term $E(D_2^+(v_i) - D_2(v_j))$ is simply the energy difference

between the vibrational levels v_i of D_2^+ and v_j of D_2 [2] (see Figure 6.3). These energies will be referred as E_i and E_j, respectively. The vibrational states and energy levels of D_2^+ and D_2 are computed following the methodology presented in Chapter 4 (the results are presented in Appendix A).

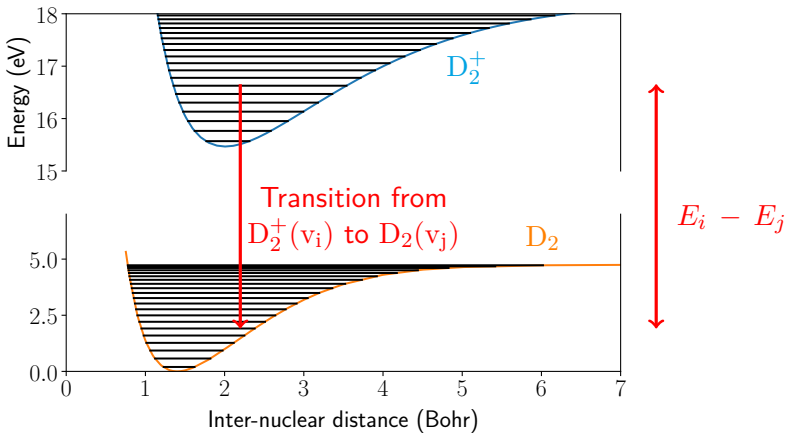

Figure 6.3: The energy difference between the reagent D_2^+ in the vibrational state v_i and the product D_2 in the vibrational state v_j is the energy difference between the vibrational levels v_i and v_j.

The second term is the energy difference between the fundamental (first) and excited (n-th) electronic levels of the Deuterium atom:

$$E(\mathrm{D} - \mathrm{D}_\mathrm{n}^*) = -13.6 \left(1 - \frac{1}{n^2}\right) \mathrm{eV}. \tag{6.8}$$

Finally, the electronic affinity of the Deuterium is the same as the one of the Hydrogen atom, EA(D) = 0.754 eV. The KER becomes:

$$\Delta E(v_i, v_j, n) = E_i - E_j - 13.6 \text{ eV} \left(1 - \frac{1}{n^2}\right) - 0.754 \text{ eV}. \tag{6.9}$$

As already explained in Section 5.3, the probability for the system to move from the vibtational state Ψ^i of D_2^+ to the vibtational state ξ^j of D_2 is given by the element FCM_{ij} of the Franck-Condon matrix. Considering the whole population of possible vibrational states, the probability $P^{transition}(i,j)$ to observe a transition from Ψ^i to ξ^j is the probability to be initially in the state Ψ^i multiplied by the probability to perform the transition:

[2] If the energies of the two systems are defined with regard to the same zero energy.

$$P^{transition}(i,j) = P^{vib}(i)\ FCM_{ij}, \tag{6.10}$$

where $P^{vib}(i)$ is the vibrational distribution of D_2^+. The probability [3] $P^{ker}(E)$ for a kinetic energy E to be released is then the sum of the contributions of transitions releasing a kinetic energy E:

$$P^{ker}(E) = \sum_i \sum_j P^{vib}(i)\ FCM_{ij}\ \exp\left(-\frac{(E - \Delta E(v_i, v_j, n))^2}{2\sigma^2}\right). \tag{6.11}$$

The gaussian factor annihilates the contribution of the transitions releasing a kinetic energy significantly different from E. Using a gaussian instead of a delta distribution at this end allows to smooth the output of the function avoiding step-like discretization effects. The width at half-height of the gaussian σ is related to the experimental uncertainty on the kinetic energy released measurement.

Let E_{cm} be the kinetic energy of the center of mass, i.e. the sum of the kinetic energies E_1 and E_2 of the two beams in the laboratory frame:

$$E_{cm} = \frac{(m_1 + m_2)V_{cm}^2}{2} = \frac{m_1 V_{cm}^2}{2} + \frac{m_2 V_{cm}^2}{2} = E_1 + E_2, \tag{6.12}$$

where m_i is the mass of the particles composing the i-th beam and $V_{cm} = V_1 = V_2$ the norm of the velocity of the center of mass. Approximating the detection system by a set of detectors residing in the same detection plane, the KER is obtained from measurements as follows:

$$KER = \frac{E_{cm}}{4z^2}\left((x_1 - x_2)^2 + V_{cm}^2\ dT_{12}^2\right), \tag{6.13}$$

where $z \approx 316$ cm is the coordinate of the detection plane on an axis collinear to the direction $\hat{z}$ of the beams, x_1 and x_2 are coordinates on an axis perpendicular to $\hat{z}$ of the impacts on the detectors and $dT_{12} = t_2 - t_1$ is the temporal difference between the two impacts (see Figure 6.4).

[3] Note that this probability distribution is not normalized. Normalizing KER distributions is useless in the context of this work.

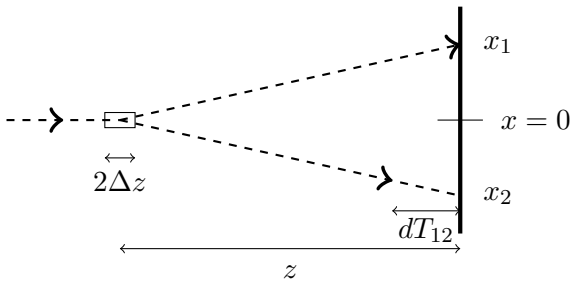

Figure 6.4: The confluent beams travel in the direction $\hat{z}$ at a velocity V_{cm}. Collisions happen in the observation cell which has a length of $2\Delta z$. The two particles then travel to the detection plane. The first particle hits a detector at the position x_1 and time t_1. The second particle hits a detector at position x_2 and time $t_2 = t_1 + dT_{12}$.

The absolute uncertainty on the KER measurement depends on the uncertainties on E_{cm}, $x_1 - x_2$, V_{cm}, dT_{12} and z. The absolute uncertainties $\Delta E_{cm} = 20$ eV, $\Delta(x_1 - x_2) = 100\mu$m, $\Delta V_{cm} = \Delta E_{cm}/\sqrt{2\mu E_{cm}}$ and $\Delta dT_{12} = 250$ ps follow from the limited accuracy of the measuring devices. The main contribution to the uncertainty on the KER is the uncertainty on z. Indeed, the collision may happen anywhere in the observation cell. The length of this cell is 7.5 cm which yields an uncertainty $\Delta z = 7.5/2$ cm. Neglecting the other minor uncertainties, the relative uncertainty on the KER measurement becomes:

$$\frac{\Delta KER}{KER} = \Delta\left(\frac{1}{z^2}\right) z^2 = \frac{2\Delta z}{z} = \frac{7.5}{316} \approx 2.5\%. \tag{6.14}$$

Because mot of the events in the experimental KER lie around 2 eV, $\Delta KER \approx 0.05$ eV. The value of σ is then defined such that the width at half-height of the gaussian is 0.05 eV:

$$\sigma = \frac{0.05}{\sqrt{2\ln 2}}. \tag{6.15}$$

6.1.3 Comparison between the experimental and theoretical KER distributions

In this section, the maxima of the theoretical and experimental KER distributions are compared. Reaction (6.2) may explain the experimental KER if these maximums are located at the same positions in the energy spectrum. The amplitudes of the theoretical curves have indeed been chosen arbitrary. There is no point in comparing them with the amplitude of the experimental curve. Moreover, the amplitude differences between the different parts of a same theoretical curve may change when taking into account the cross section as a function of the kinetic energy release. This dependence is unfortunately not provided by Eerden et al. [29].

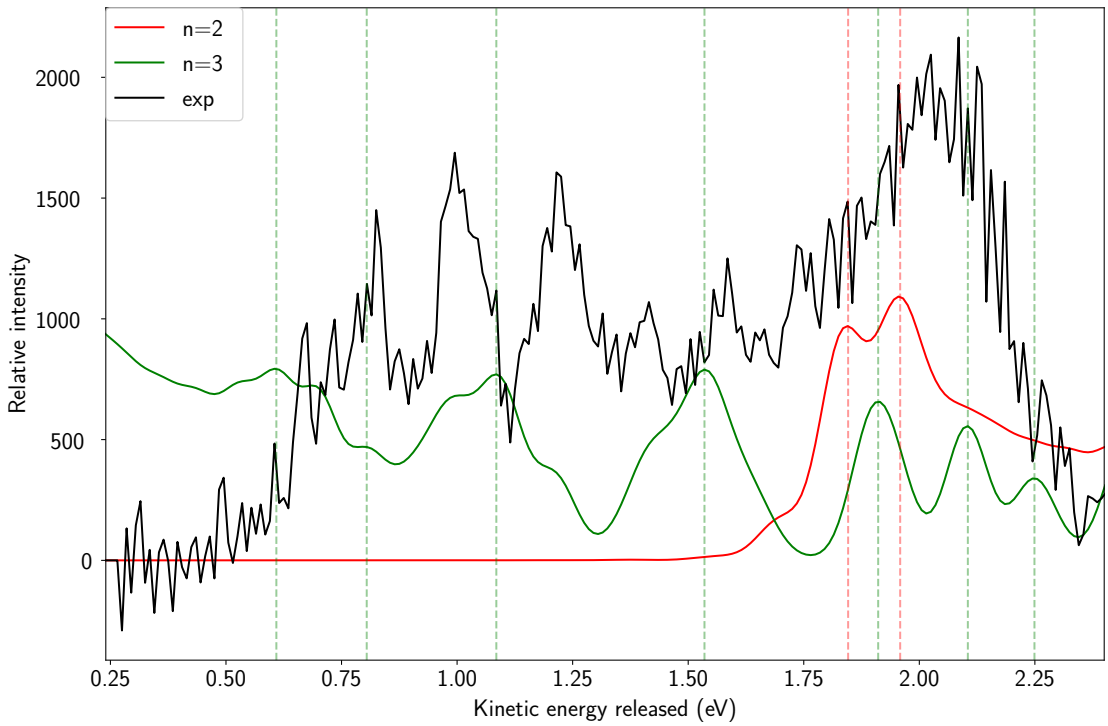

Figure 6.5: Comparison between the theoretical KER distributions computed from Equation (6.11) for $n = 2, 3$ and the experimental KER. The amplitudes of the theoretical curves are purely arbitrary. Vertical dashed lines are drawn at the locations of theoretical peaks in the energy spectrum.

Figure 6.5 compares the theoretical KER distributions for $n = 2$ and $n = 3$ with the experimental KER distribution. Five maxima out of seven of the $n = 3$ KER distribution match more or less convincingly peaks in the experimental distribution. For $n = 2$ the two only maxima match experimental peaks. However, assuming that the computations performed by Eerden et al. [29] are correct, the cross sections for the these values of n are at least one order of magnitude smaller than the cross section for $n = 5$ (see Table 6.1). Therefore these levels are not expected to play a major role in the explanation of the measured KER distribution.

Figure 6.6 compares the experimental KER distribution with the theoretical KER distributions computed from Equation (6.11) for the quantum numbers n associated to the highest cross sections. Eerden et al. [29] report that these quantum numbers are $n = 4, 5, 6$ (see Section 6.1.1). If reaction (6.2) is a dominant process with regard to the competing reaction (6.1) these three theoretical curves must explain most of the experimental curve. Counting optimistically, the ratio of matching peaks between theoretical and experimental curves are: 4/8 for $n = 4$, 6/8 for $n = 5$ and 7/10 for $n = 6$.

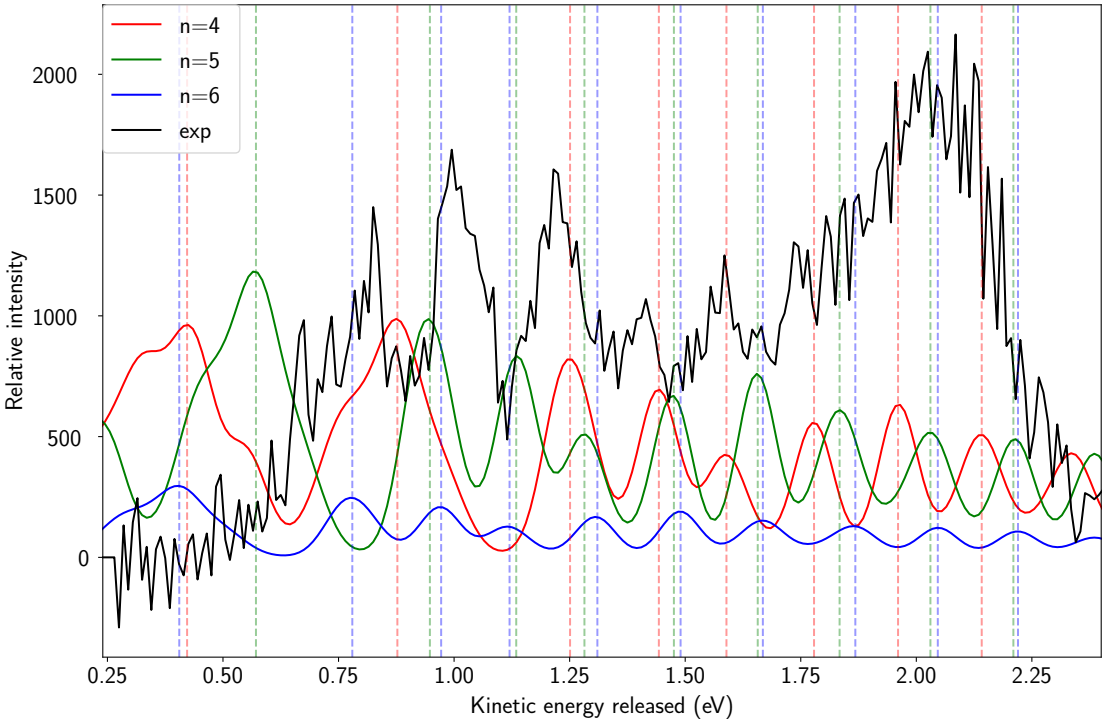

Figure 6.6: Comparison between the theoretical KER distributions computed from Equation (6.11) for $n = 4, 5, 6$ and the experimental KER. The amplitudes of the theoretical curves are purely arbitrary. Vertical dashed lines are drawn at the locations of theoretical peaks in the energy spectrum.

Figure 6.7 compares the theoretical KER distributions for $n = 7$ and $n = 8$ with the experimental KER distribution. Counting optimistically, the ratio of matching peaks between theoretical and experimental curves are: $5/11$ for $n = 7$ and $4/10$ for $n = 8$.

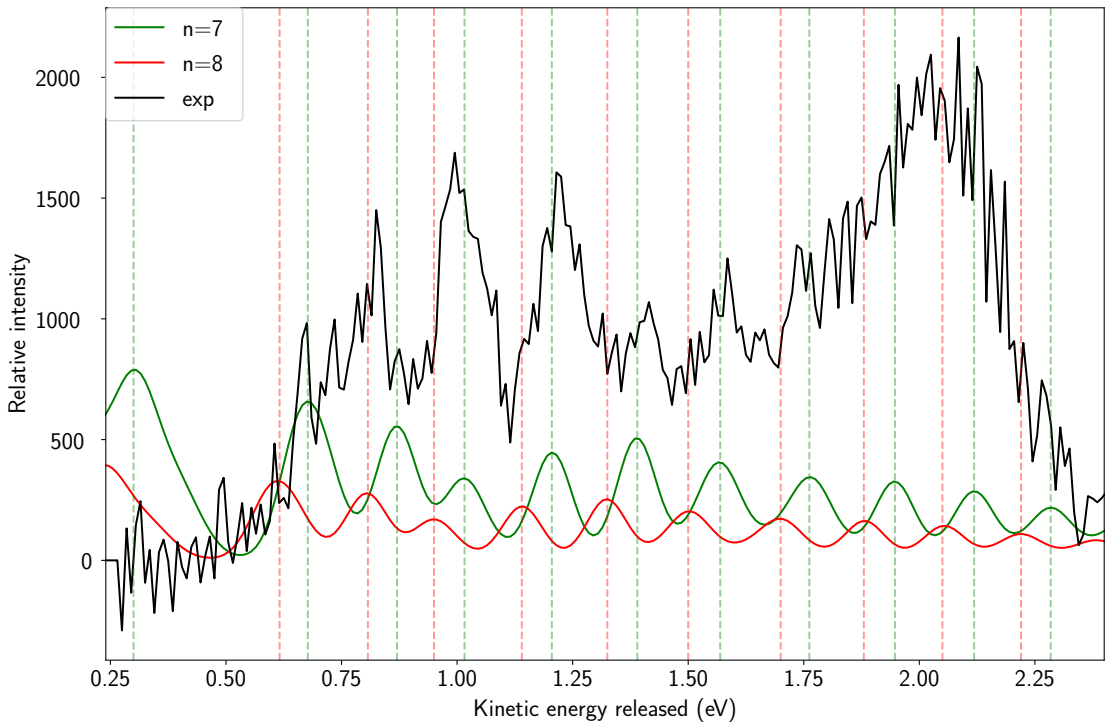

Figure 6.7: Comparison between the theoretical KER distributions computed from Equation (6.11) for $n = 7, 8$ and the experimental KER. The amplitudes of the theoretical curves are purely arbitrary. Vertical dashed lines are drawn at the locations of theoretical peaks in the energy spectrum.

It is hard to exclude completely the possibility of the contribution of some products of reaction (6.2) in the experimental KER. Indeed, the dependence of the cross section with regard to the kinetic energy release is unknown and the corresponding correction to the theoretical KER distributions has not been applied. Moreover, the global theoretical curve is a linear combination of the theoretical curves for each possible value of n.

Positions of all theoretical peaks in the energy spectrum are drawn on top of the experimental curve in Figure 6.8. The conclusion of this section is that reaction (6.2) is not the dominant process. It indeed fails to explain the overall shape of the experimental KER distribution as well as the presence of most peaks. Moreover, theoretical computations predict peaks where there aren't any. Furthermore, the number of matching peaks is at least as high for low cross section quantum numbers n as those for high cross section numbers n, which does not make a lot of sense. Finally, Eerden et al. [29] applied the asymptotic Landau-Herring formula to evaluate the coupling matrix elements. Its applicability to the present case is however questionable, since reaction (6.2) involves electron transfer to the D_2 ground state and excitation of the remaining D electron.

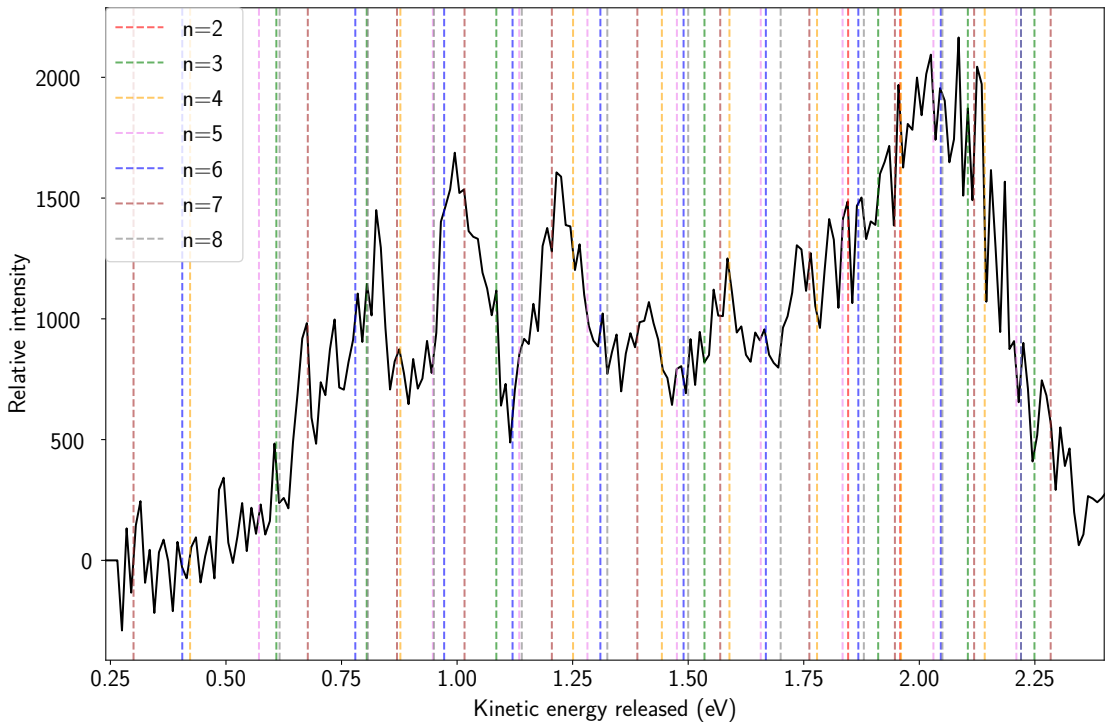

Figure 6.8: In black the experimental KER distribution. Vertical dashed lines are drawn at the positions of maximums in the KER distributions computed from Equation (6.11) for $n = 2, ..., 8$.

6.2 The mutual neutralization reaction $D_2^+(v) + D^- \rightarrow D_2^*(v') + D$

This section is organized as follows. In the first part, the formula used to compute the KER only considering the Franck-Condon principle, i.e. without introducing a partial cross section associated to each electronic excited state of D_2^*, is explained. In the second part, the results obtained with this formula are compared to the experimental KER. The third part presents the obtained results when modifying the Franck-Condon coefficients to take into account an eventual increase of the collision probability with the inter-nuclear distance of D_2^+. The fourth part explains the multi-channel Landau-Zener model which is applied by Liu et al. [30] to the reaction

$$H_2^+(\Sigma_g^+; v_i = 0) + H^-(1s^2) \rightarrow H_2^*(^{1,3}\Lambda_g; v_j = 0) + H(1s). \tag{6.16}$$

This model is supposed to give the partial cross sections associated to each output channel, i.e. to each output electronic and vibrational level of D_2^*. This four part also helps to assert the correctness of the software developed in the context of this

work because results obtained by Liu et al. [30] have been reproduced. The fifth part presents KER distributions obtained with the multi-channel Landau-Zener model in the simpler case in which only ground vibrational states are considered. The sixth part shows obtained KER distributions when introducing in the multi-channel Landau-Zener model all possible output vibrational levels (i.e. all vibrational levels of D_2^*). Finally, the seventh part presents KER distributions obtained when all vibrational levels of both D_2^+ and D_2^* are introduced in the model.

The objective of this section is to find out if reaction (6.1) is able to explain the observed experimental KER distribution. There are many excited states D_2^* and each one of them may contribute to the total KER distribution. The potential curves of the excited states D_2^* considered in the computation of the KER distribution are presented in Figures A.3 and A.14.

Group theory teaches us that the produced excited states D_2^* depend on the way the two bodies D_2^+ and D^- approach each other, i.e. on their relative velocity vector close to the time they interact (see Figure 6.9):

$$\vec{v}_r = \vec{v}_{D_2^+} - \vec{v}_{D^-}, \tag{6.17}$$

where $\vec{v}_{D_2^+}$ is the velocity of the center of mass of D_2^+. If the vector $\vec{v}_r$ is collinear with the axis of symmetry of D_2^+, the only possible symmetry for the output channel is Σ_g^+ [19]. Otherwise, if $\vec{v}_r$ is perpendicular to this axis, the possible symmetries are Σ_g^+, Π_u and Δ_g. In all other cases, all symmetries are allowed such as $\Sigma_g^+, \Sigma_u^+, \Pi_g, \Pi_u, \Delta_g, \Delta_u, ...$ Both singlet and triplet states are allowed. The collinear and perpendicular cases are naturally much less probable than an approach with a relative velocity neither collinear nor perpendicular to the axis of symmetry of D_2^+.

6.2.1 Computing the theoretical kinetic energy release

This section details the computation of the theoretical distribution of the kinetic energy released by reaction (6.1):

$$D_2^+(v_i) + D^- \rightarrow D_2^*(\Lambda_j, v_k) + D. \tag{6.18}$$

The kinetic energy release is the energy of the reagents minus the energy of the products:

$$\Delta E(v_i, \Lambda_j, v_k) = E(D_2^+(v_i) + D^-) - E(D_2^*(\Lambda_j, v_k) + D) \tag{6.19}$$

$$= E(D_2^+(v_i) - D_2^*(\Lambda_j, v_k)) + E(D^- - D) = E_i - E_{k,j} - EA(D), \tag{6.20}$$

where $E(x)$ is the energy of the state x, E_i is the energy of the i-th vibrational state of the molecular ion D_2^+, $E_{k,j}$ the energy of the j-th vibrational level of the k-th electronic

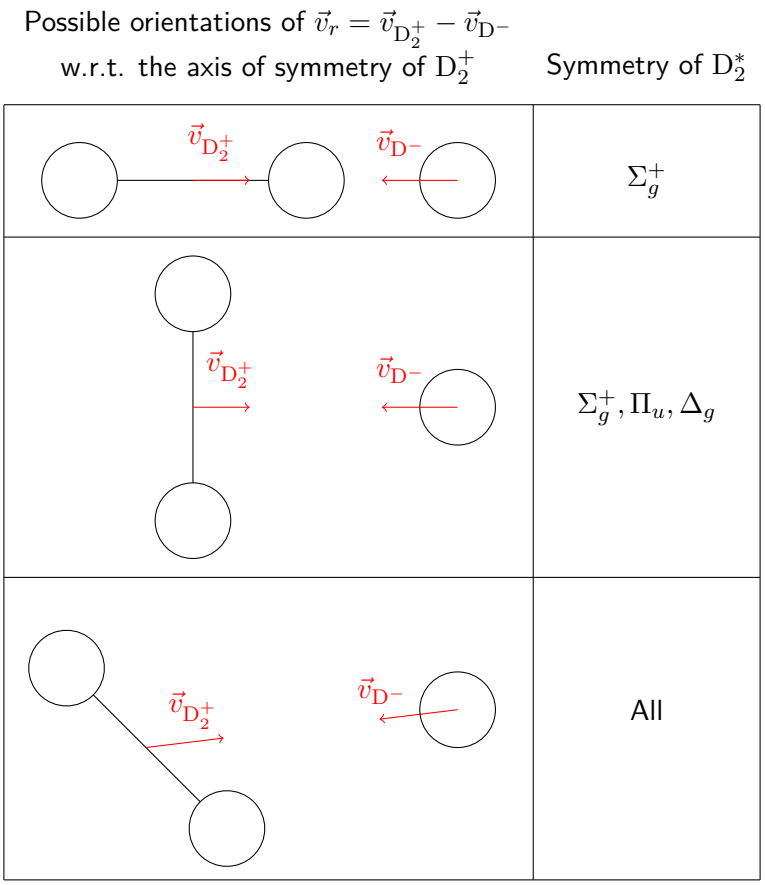

Figure 6.9: Symmetries of the molecule D_2* produced by reaction (6.1) allowed by group theory. In the first line of the table, the relative velocity vector is collinear with the axis of symmetry of D_2^+. In the second line, the relative velocity vector is perpendicular to this axis. The last line is an example of one of the many possible other cases for which all symmetries are allowed by group theory.

state of the excited molecule D_2^* and $EA(D)$ is the electronic affinity of the Deuterium atom. The vibrational energy levels of D_2^+ and of many excited states of the molecule D_2 are computed following the methodology presented in Chapter 4 (the results are presented in Appendix A). The KER distribution $P_j^{ker}(E)$ is then obtained proceeding in the same way as in Section 6.1.2:

$$P_j^{ker}(E) = \sum_i \sum_k P^{vib}(i)\ FCM_{ik}\ \exp\left(-\frac{(E - \Delta E(v_i, \Lambda_j, v_k))^2}{2\sigma^2}\right), \tag{6.21}$$

with $\sigma = \frac{0.05}{\sqrt{2\ln 2}}$.

6.2.2 Comparing the experimental KER distribution with theoretical KER distributions based on the Franck-Condon principle

This section presents KER distributions computed using Equation (6.21). These distributions are obtained only using the Franck-Condon matrix: the contribution from each electronic state D_2^* depends only on the energy differences between the vibrational states of D_2^+ and D_2^* and the overlapping integral between the possible initial and final wavefunctions.

The differences in cross section between the different electronic states D_2^* are not considered. Therefore, this method does not provide information about the relative contribution of each electronic state D_2^* to the total KER spectrum. The amplitude differences between the theoretical distributions obtained for the different excited electronic states are then purely arbitrary and have no physical meaning.

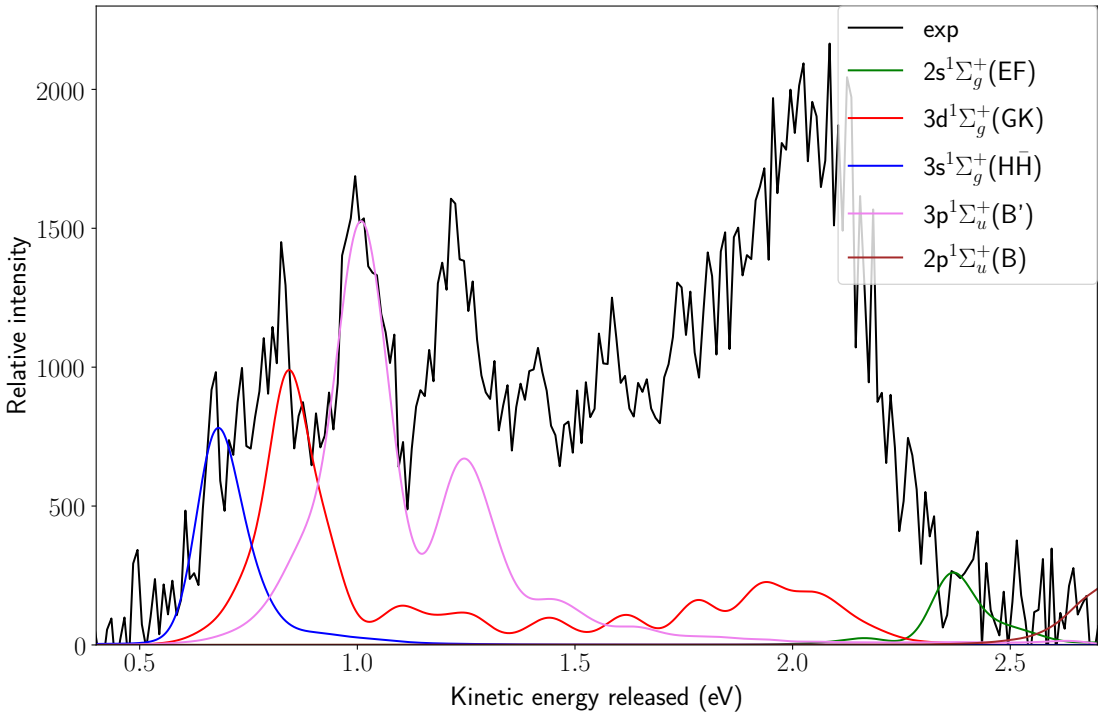

Figure 6.10: KER distributions for some singlet Σ_g^+ and Σ_u^+ states of D_2^* produced by Equation (6.21). These distributions have been computed with the Franck-Condon matrix. The amplitudes of the theoretical curves are purely arbitrary.

These results show that many states may be responsible for the experimental peaks and for the global shape of the curve up to 1.25 eV (see Figures 6.10 and 6.11). Moreover, only the state $3d^1\Sigma_g^+$(GK) may explain the massive number of events lying between 1.7

and 2.3 eV. However, using only the Franck-Condon principle is not sufficient. Indeed, according to this simple theory, if the state $3d^1\Sigma_g^+$(GK) would be responsible for as many events between 1.7 and 2.3 eV there should be a very high peak around 0.8 eV. The theory highly underestimates the contribution of high KERs transitions.

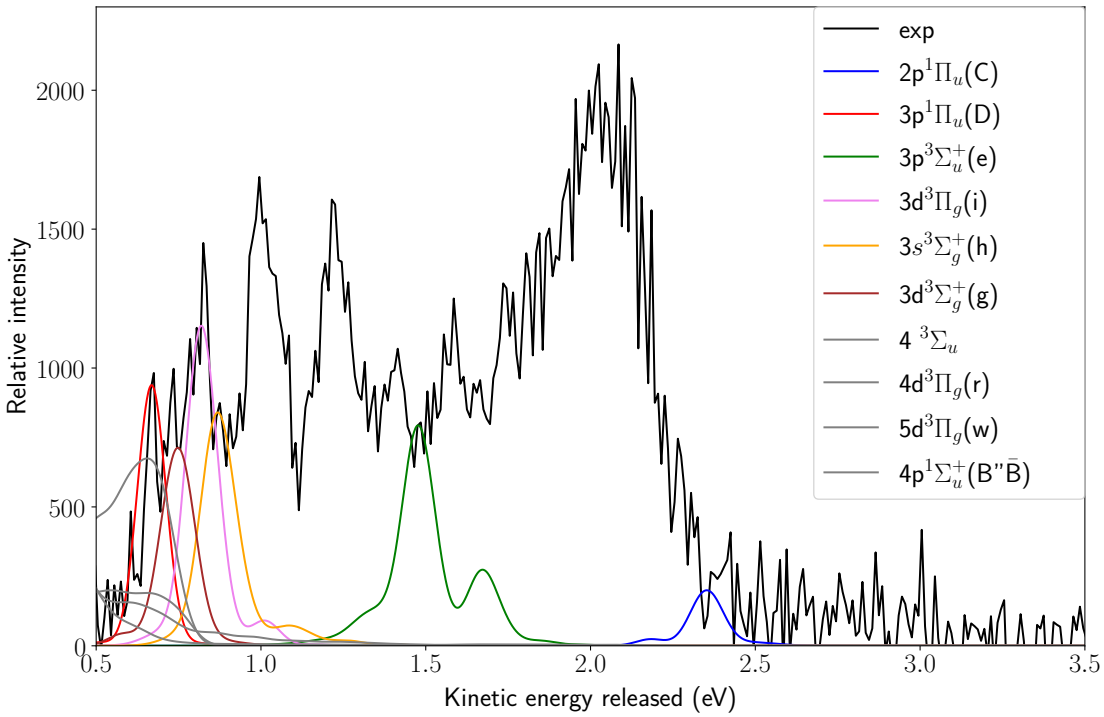

Figure 6.11: KER distributions for some states of D_2^* produced by Equation (6.21). These distributions have been computed with the Franck-Condon matrix. The amplitudes of the theoretical curves are purely arbitrary.

Given the particular importance of the state $3d^1\Sigma_g^+$(GK), the Franck-Condon matrix corresponding to the transition from D_2^+ to this state is presented in Figure 6.12b.

6.2.3 A cross section increasing with the inter-nuclear distance

This section presents the obtained KER distributions when introducing in the computations a cross section increasing with the inter-nuclear distance of the D_2^+ molecular ion. This cross section has been proposed by Dunn et al. [31] in the context of the photodissociation of D_2^+ and later used by Abdellahi El Ghazaly et al. [32] in the context of the electron impact dissociation of D_2^+.

This cross section is implemented by replacing the Franck-Condon coefficient FCM_{ij} in

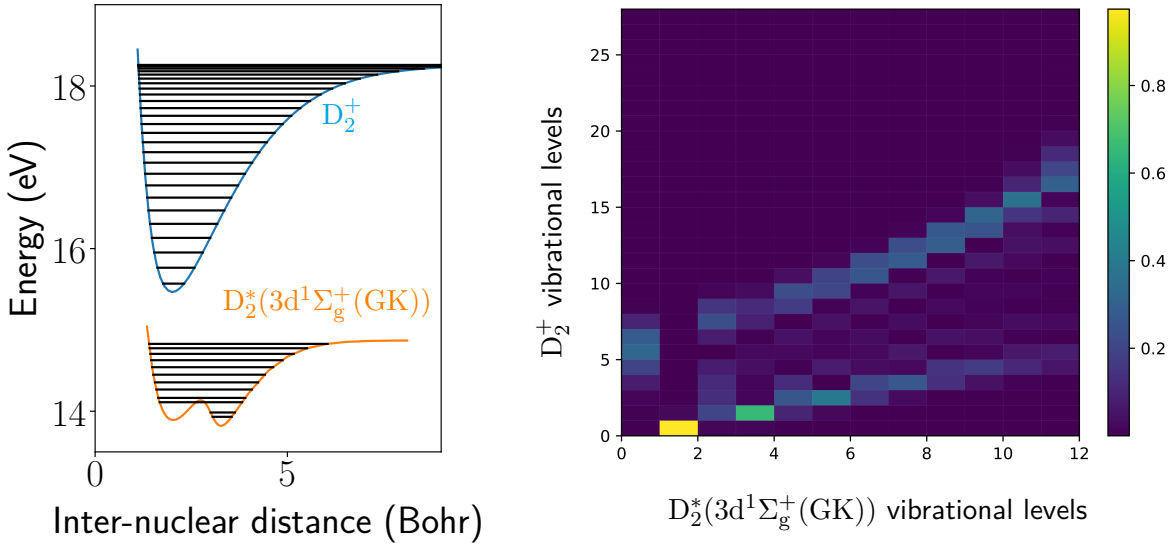

(a) Potential curves of D_2^+ and $D_2^*(3d^1\Sigma_g^+(GK))$ with their vibrational energy levels.

(b) Representation of the Franck-Condon matrix associated to the transition from $D_2^+(v_i)$ to $D_2^*(3d^1\Sigma_g^+(GK); v_j)$. The transitions from $v_i = 0$ to $v_j = 1$ and $v_i = 1$ to $v_j = 3$ have the highest Franck-Condon coefficients.

Figure 6.12: Additional information about D_2^+ and $D_2^*(3d^1\Sigma_g^+(GK))$.

Equation (6.21) by:

$$Q_{ij} = \left| \int_0^\infty \Psi^i(R) q(R) \xi^j(R) dR \right|^2, \tag{6.22}$$

where R is the inter-nuclear distance, and Ψ^i, ξ^j are vibrational wavefunctions of D_2^+ and D_2^*, respectively. The function q increases linearly with R (see Figure 6.13). Therefore, this cross section gives more weight in the KER distribution to the transitions $\Psi^i \to \xi^j$ such that both Ψ^i and ξ^j do not vanish at high inter-nuclear distances R.

The expression of the KER distribution then becomes:

$$P^{ker}(E) = \sum_i \sum_j P^{vib}(i) Q_{ij} \ \exp\left(-\frac{(E - \Delta E(v_i, v_j))^2}{2\sigma^2} \right). \tag{6.23}$$

The origin of this cross section may be explained intuitively as follows. Molecules in vibrational states associated to wavefunctions not vanishing at high R have a higher

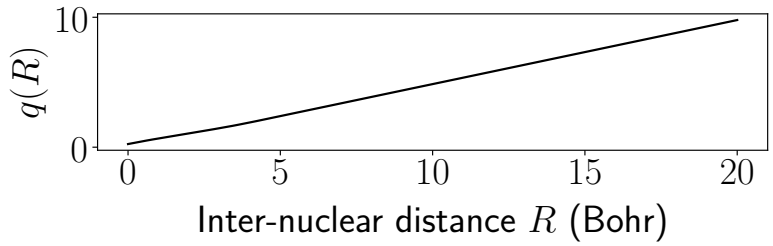

Figure 6.13: Cross section q as a function of the inter-nuclear distance R.

average inter-nuclear distance $\langle R \rangle$. Molecules with high $\langle R \rangle$ expand over larger volume and therefore have more probability to collide with other atoms (or molecules).

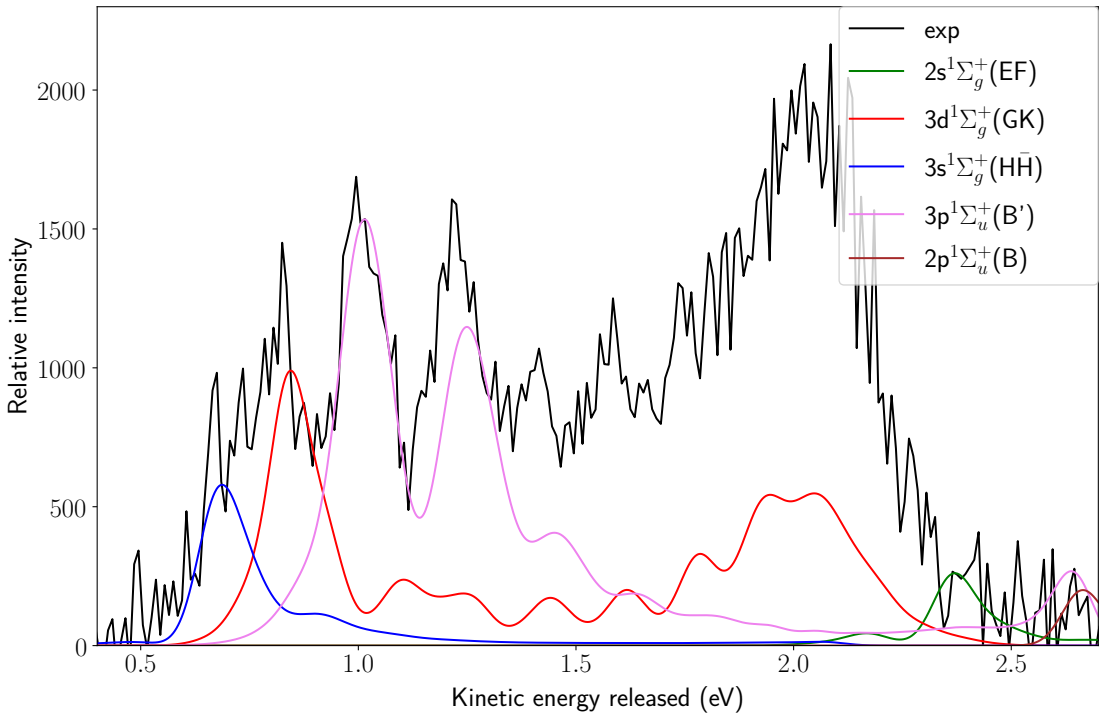

Figure 6.14: KER distributions for some singlet Σ_g^+ and Σ_u^+ states of D_2^* produced by Equation (6.23). These distributions have been computed with a cross section increasing linearly with the inter-nuclear distance. The amplitude of the theoretical curves are purely arbitrary.

The results are presented in Figures 6.14 and 6.15. The effect of the cross section is an

increase of the contribution of high KER transitions. It makes sense because, in D_2^+, the vibrational states with high inter-nuclear distances are those associated to the highest energy levels (see Figure A.1).

The obtained results are better than when using the Franck-Condon matrix. The state $3d^1\Sigma_g^+$(GK) matches better the first high peak around 0.8 eV as well as the high bump between 1.75 and 2.3 eV. The second and third high peaks, around 1 and 1.2 eV are quite well explained by the state $3p^1\Sigma_u^+$(B'). Finally, there are many states which could explain the peaks below 0.8 eV such as $3d^3\Pi_g$(i), $3d^3\Sigma_g^+$(g), $3p^1\Pi_u$(D),...

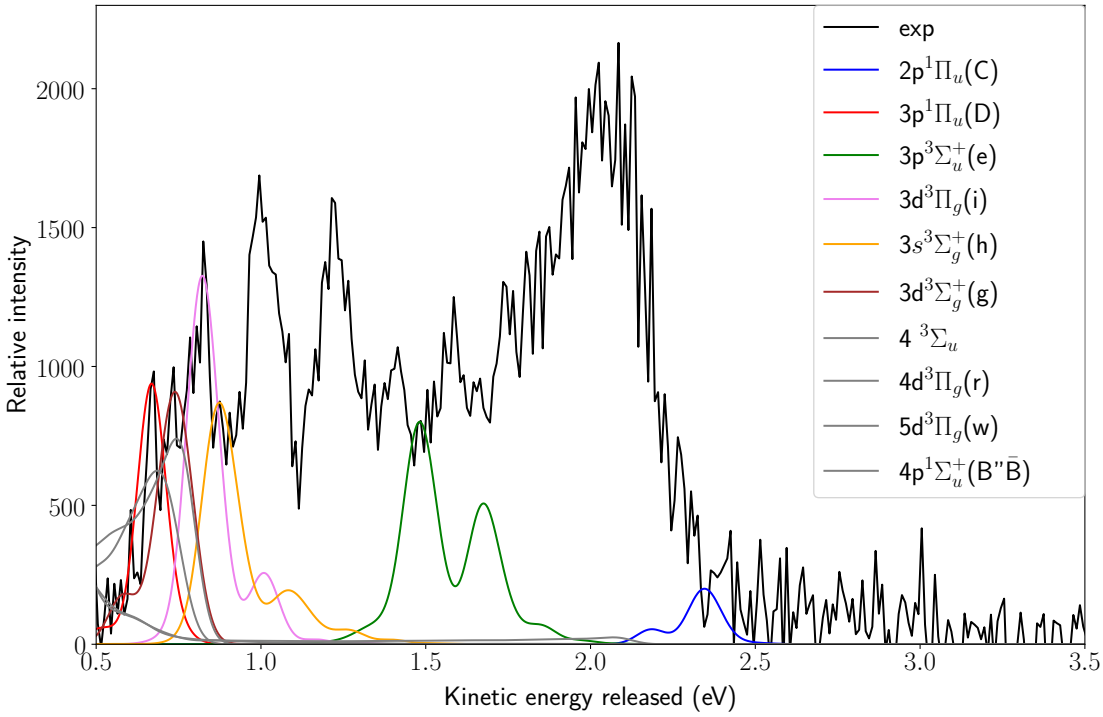

Figure 6.15: Theoretically computed KER distributions for some states of D_2^* produced by Equation (6.23). These distributions have been computed with a cross section increasing linearly with the inter-nuclear distance. The amplitude of the theoretical curves are purely arbitrary.

Unfortunately, the number of events between 1.75 and 2.3 eV is still highly underestimated. Moreover, this approach does not inform on the relative contribution of one electronic state of D_2^* with regard to the others. It is why the amplitudes of the theoretical KER distributions are arbitrary in Figures 6.14 and 6.15.

6.2.4 Cross section computed within the multi-channel Landau-Zener model

Using the multi-channel Landau-Zener model, Liu et al. [30] have computed the cross section of the mutual neutralization reaction:

$$\mathrm{H}_2^+(\Sigma_\mathrm{g}^+;\mathrm{v_i}=0)+\mathrm{H}^-(1\mathrm{s}^2)\rightarrow \mathrm{H}_2^*(^{1,3}\Lambda_\mathrm{g};\mathrm{v_j}=0)+\mathrm{H}(1\mathrm{s}), \tag{6.24}$$

which is similar to reaction (6.1). This section explains the multi-channel Landau-Zener model based on the contribution of Liu et al [30]. Their developments are further detailed and adapted to reaction (6.1).

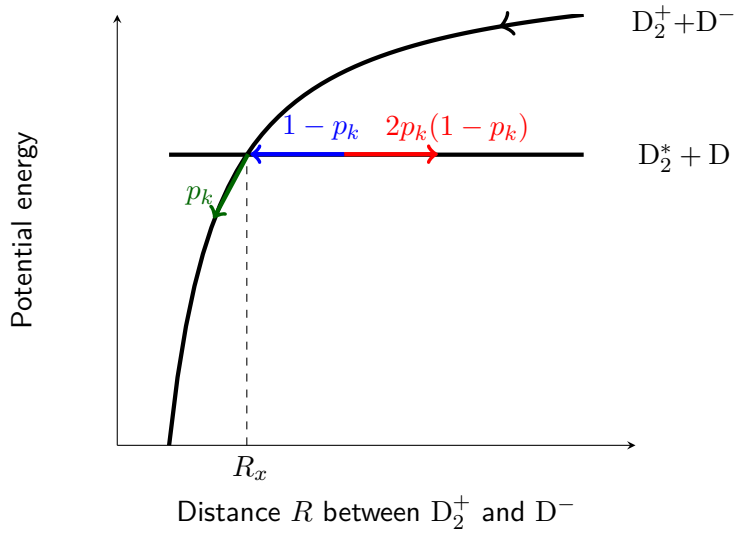

Figure 6.16: In the Landau-Zener model, the cross section depends on the crossing point R_x between the potential energy curves of the input channel ($\mathrm{D}_2^+ + \mathrm{D}^-$) and the output channel ($\mathrm{D}_2^* + \mathrm{D}$). The transition to the output channel can take place at both passages of the crossing point with a probability $1-p_k$. Once in the output channel, the system has a probability $1-p_k$ to come back to the input channel, and a probability p_k to remain in the output channel. Therefore, the mutual neutralization of the system $\{\mathrm{D}_2^+ + \mathrm{D}^-\}$ to one given state $\{\mathrm{D}_2^* + \mathrm{D}\}$ has a probability $p_k(1-p_k)$ to occur when the centers of mass of D_2^+ and D^- are separated by a distance $R = R_x$; because it happens once when D_2^+ and D^- are getting closer and once when they move away, the total mutual neutralization probability is $P = 2p_k(1-p_k)$. The probability for the system to stay in the input channel is $1-P$. Only one possible output channel D_2^* is represented. The curvature of the input channel potential curve is a consequence of the Coulomb interaction between D_2^+ and D^-.

In the Landau-Zener model, the interaction between the input channel $\{\mathrm{D}_2^+ + \mathrm{D}^-\}$ and

output channel $\{D_2^* + D\}$ is maximum when the distance between their centers of mass is such their potential energy curves intersect (see Figure 6.16).

Because D_2^* and D are neutral particles, the potential energy of the state $\{D_2^* + D\}$ is the sum of the potential energies of the particles D_2^* and D. This sum is a constant $E_{D_2^*+D}$. The potential energy of the state $\{D_2^+ + D^-\}$ is the total potential energy due to the electric force acting between the cation and the anion:

$$E_{D_2^+ + D^-} = \frac{q_1 q_2}{4\pi\epsilon_0 R} = -\frac{e^2}{4\pi\epsilon_0 R}, \tag{6.25}$$

where ϵ_0 is the vacuum permittivity, R is the distance between D_2^+ and D^-, and $q_1 = e, q_2 = -e$ are the electric charges of the cation D_2^+ and anion D^-, respectively. In atomic units, $e = 1$ and $k_e = 1/(4\pi\epsilon_0) = 1$ which yields:

$$E_{D_2^+ + D^-}(R) = -\frac{1}{R} \text{ hartree.} \tag{6.26}$$

At the position R_x of the crossing between the two potentials curves, the potential energies of the two systems are equal:

$$E_{D_2^+ + D^-} = -\frac{1}{R_x} = E_{D_2^* + D}. \tag{6.27}$$

The zero of energy is defined at $R = +\infty$ where D_2^+ and D^- are infinitely distant from each other:

$$E_{D_2^+ + D^-}(R = +\infty) = E_{D_2^+} + E_{D^-} = 0. \tag{6.28}$$

Therefore, $E_{D_2^*+D}$ is by definition the energy difference between the state $\{D_2^* + D\}$ and the zero of energy:

$$E_{D_2^*+D} - 0 = E_{D_2^*+D} - E_{D_2^+} - E_{D^-} = E_{D_2^*} - E_{D_2^+} + E_D - E_{D^-}. \tag{6.29}$$

If the vibrational states of D_2^* and D_2^+ are v_j and v_i respectively, the energy difference $E_{D_2^*} - E_{D_2^+}$ is the difference between the energies E_j of the j-th and E_i of the i-th vibrational levels of D_2^* and D_2^+, respectively. Moreover, $E_D - E_{D^-} = 0.754$ eV is the electron binding energy in D^-. Therefore, the energy of the state $\{D_2^* + D\}$ is simply the opposite of the kinetic energy ΔE released by the reaction (see Equation (6.20)):

$$E_{D_2^*+D} = E_j - E_i + 0.754 \text{ eV} = -\Delta E, \tag{6.30}$$

and the position R_x of the crossing between the two potentials curves is the inverse of the kinetic energy release:

$$R_x = \frac{1}{\Delta E} \text{ bohr}, \tag{6.31}$$

ΔE being expressed in hartree. Note that, in the particular case approached by Liu et al. [30] where only the transition from $v_i = 0$ to $v_j = 0$ is considered, the difference between the vibrational energy levels of H_2^+ and H_2^* is equal to the electron binding energy in H_2^*, referred as E_A. Indeed, most electronic states of H_2 have a Rydberg character, meaning their potential energy curves are parallel to that of H_2^+.

The expression of the coupling interaction H_{ic} between the ionic state $\{D_2^+ + D^-\}$ and the covalent state $\{D_2^* + D\}$ is given by the Landau-Herring's method [30]. This method is valid if the crossing points $R_{x,k}$ are far enough for the considered sates. This condition is fulfilled for all electronically excited states D_2^* but not for the fundamental electronic level $D_2(X)$. The Landau-Herring's method yields [30]:

$$H_{ic}(R) = 0.5 A_i A_c D R^{1/\gamma - 1} \exp(-\gamma R) S_{v_i, v_j}. \tag{6.32}$$

The variable γ is related to the orbital of the bound electron in D_2^*. This orbital depends on R, i.e. on the distance between the electron and the center of mass of the molecule, as $\exp(-\gamma R)$. Its value is related to the electron binding energy E_A which is computed from the difference between the potential energy curves of D_2^+ ($V_{D_2^+}$) and D_2^* ($V_{D_2^*}$):

$$E_A(r) = V_{D_2^+}(r) - V_{D_2^*}(r), \tag{6.33}$$

where r is the inter-nuclear distance and $V_{D_2^+}, V_{D_2^*}$ are expressed in hartree. This definition of E_A is an improvement over the definition proposed by Liu et al. [30] which consider E_A as independent of r and equal to the difference between the potential energy curves $V_{D_2^+}$ and $V_{D_2^*}$ evaluated at their minimum. In the definition adopted in this work, the binding of the electron to the molecule D_2^* depends on the molecular vibrational motion.

The value of γ is:

$$\gamma(r) = \sqrt{2E_A(r)}. \tag{6.34}$$

The factor D is related to the angular momentum λ of the electron in its final state and to the total spin S of D_2^*:

$$D = \sqrt{(2\lambda + 1)(2S + 1)}. \tag{6.35}$$

The value of S must be zero and one for singlet and triplet states of D_2^*, respectively. The value of λ is the quantum number associated with the orbital angular momentum at the united atom limit. For example, for $3s^1\Sigma_g^+(H\bar{H})$ $\lambda = 0$, for $3p^1\Sigma_u^+(B')$ $\lambda = 1$ and for $3d^1\Sigma_g^+(GK)$ $\lambda = 2$.

The coefficients $A_i = 1.12$ and A_c are normalization constants of the asymptotic radial wavefunctions of the active electron in D^- and D_2^*, respectively. Let Γ be the gamma function, the value of A_c is computed as follows:

$$A_c = \frac{\gamma(2\gamma)^{1/\gamma}}{\sqrt{\Gamma(1/\gamma + \lambda + 1)\Gamma(1/\gamma - \lambda)}}. \tag{6.36}$$

Finally, the factor S_{v_i,v_j} is the overlap integral between the wavefunction Ψ^i of the i-th vibrational state of D_2^+ and wavefunction ξ^j of the j-th vibrational state of the considered electronic excited state D_2^*:

$$S_{v_i,v_j} = \int_0^\infty \Psi^i(r)\xi^j(r)dr. \tag{6.37}$$

Liu et al. [30] report that setting $S_{v_i,v_j} = 1$ when considering only the ground vibrational states $v_i = 0$ and $v_j = 0$ is a good approximation. Because γ also depends on r it makes more sense to insert all r-dependent terms from Equation (6.32) in the integral which yields:

$$H_{ic}(R) = 0.5A_i D \int_0^\infty \Psi^i(r)\ A_c(\gamma(r))\ R^{1/\gamma(r)-1}\ \exp(-\gamma(r)R)\ \xi^j(r)\ dr. \tag{6.38}$$

In the diabatic picture (crossing of potential energy curves coupled by some interaction H_{ic}), p_k is the probability that the system remains on the incoming channel at the curve crossing $R_{x,k}$ and is computed as follows [30]:

$$p_k(b) = \exp\left(-\frac{\pi\Delta E_{ic}^2(R)}{2v_r(R,b)\Delta F(R)}\right)_{R=R_{x,k}}, \tag{6.39}$$

where $\Delta E_{ic}(R) \equiv 2H_{ic}(R)$ and $\Delta F(R)$ is the slope of the potential energy curve of the ionic state $\{D_2^+ + D^-\}$ minus the slope of the potential energy curve of the covalent state $\{D_2^* + D\}$:

$$\Delta F(R) = \frac{d}{dR}\left(-\frac{1}{R}\right) - \frac{d}{dR}E_{D_2^*+D} = \frac{1}{R^2}. \tag{6.40}$$

The function v_r is the radial relative collision velocity of D_2^+ and D^-:

$$v_r(R,b) = v\ \sqrt{1 + \frac{1}{RE} - \left(\frac{b}{R}\right)^2}, \tag{6.41}$$

where b (bohr) is the impact parameter, v the collision velocity, $E = \frac{1}{2}\mu v^2$ (hartree) and μ the reduced mass of the system $\{D_2^+ + D^-\}$ (expressed as a multiple of the electron

mass, the electron mass being set to unity). For pathological values of b and R such that v_r is complex or $v_r = 0$, $p_k(b)$ is set to zero.

Let's first consider the single output channel case (see Figure 6.16). The system passes two times by the same crossing point: once when D_2^+ and D^- are getting closer and once when they move away. Branching to the output channel may occur at both passages with a probability $1 - p_k$.

Once in the output channel, the system has a probability $1-p_k$ to come back in the input channel and a probability p_k to remain in the output channel. Mutual neutralization occurs either by branching to the output channel a the first pass then staying in the output channel at the second pass, either by avoiding the output channel at the first pass then branching to the output channel at the second pass. Therefore, the probability for the mutual neutralization to occur is [4]:

$$P_{\text{transition}}(b) = 2p_k(1 - p_k), \tag{6.42}$$

and the probability for the system to stay in the input channel is the probability p_k^2 to avoid going through the output channel at both passes, plus the probability to branch to the output channel at the first pass then branching back to the input channel at the second pass $(1 - p_k)^2$.

$$P_{\text{no transition}}(b) = p_k^2+(1-p_k)^2 = 1-2p_k+2p_k^2 = 1-2p_k(1-p_k) = 1-P_{\text{transition}}(b). \tag{6.43}$$

The situation in which there are $N > 1$ covalent output channels to different electronically excited state of D_2^* is now considered (see Figure 6.17). The potential energy curve of each output channel crosses the ionic potential energy curve of the input channel. The ionic potential energy curve crosses first the output channel k with the larger $R_{x,k}$. The variables $R_{x,k}$ are then sorted in descending orders such that:

$$R_{x,1} > R_{x,2} > ... > R_{x,N}. \tag{6.44}$$

Because there are multiple crossings, the total probability P_n to branch to the n-th output channel at the crossing point $R_{x,n}$ depends on the other crossings points. Liu et al. [30] report that, in the semi-classical approximation, the expression of P_n is:

$$P_n(b) = (1 - p_n)\left(\prod_{i=1}^{n} p_i\right)\left\{1 + \prod_{i=n+1}^{N} p_i^2 + (1 - p_{n+1})^2 + \sum_{i=n+1}^{N-1}(1 - p_{i+1})^2 \prod_{j=n+1}^{i} p_j^2\right\}, \tag{6.45}$$

if $n < N - 1$. Else if $n = N - 1$:

[4] The explicit dependence of p_k towards b is omitted for better readability.

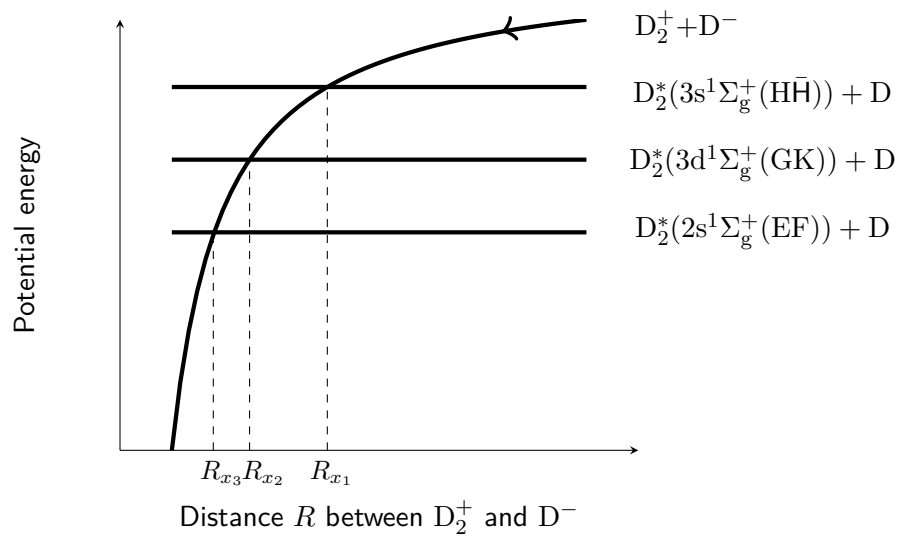

Figure 6.17: Example of a three channels Landau-Zener model. The potential energy curve of each state $D_2^*(\Lambda)$ crosses the ionic potential energy curve at a different crossing point. The input channel first meets the output channel i with the largest $R_{x,i}$. The probability P_n for the transition to occur to the n-th output channel depends on the other crossings.

$$P_{N-1}(b) = (1 - p_{N-1}) \left(1 + p_N^2 + (1 - p_N)^2\right) \prod_{i=1}^{N-1} p_i. \tag{6.46}$$

Finally, if $n = N$:

$$P_N(b) = 2(1 - p_N) \prod_{i=1}^{N} p_i. \tag{6.47}$$

The partial cross section for the output channel n is then computed as follows:

$$\sigma_n = 2\pi \int_0^{b_{x,n}} P_n(b) b \, db, \text{ with } b_{x,n} = R_{x,n} \sqrt{1 + \frac{1}{R_{x,n} E}}. \tag{6.48}$$

Liu et al. [30] claim that the transitions to the singlet and triplet states are mutually uncoupled. Therefore, they compute separately the partial cross sections for singlet and triplet states. In other words, only the crossings towards singlet (triplet) states are introduced in the multi-channel Landau-Zener computation of the partial cross sections of the singlet (triplet) H_2^* states.

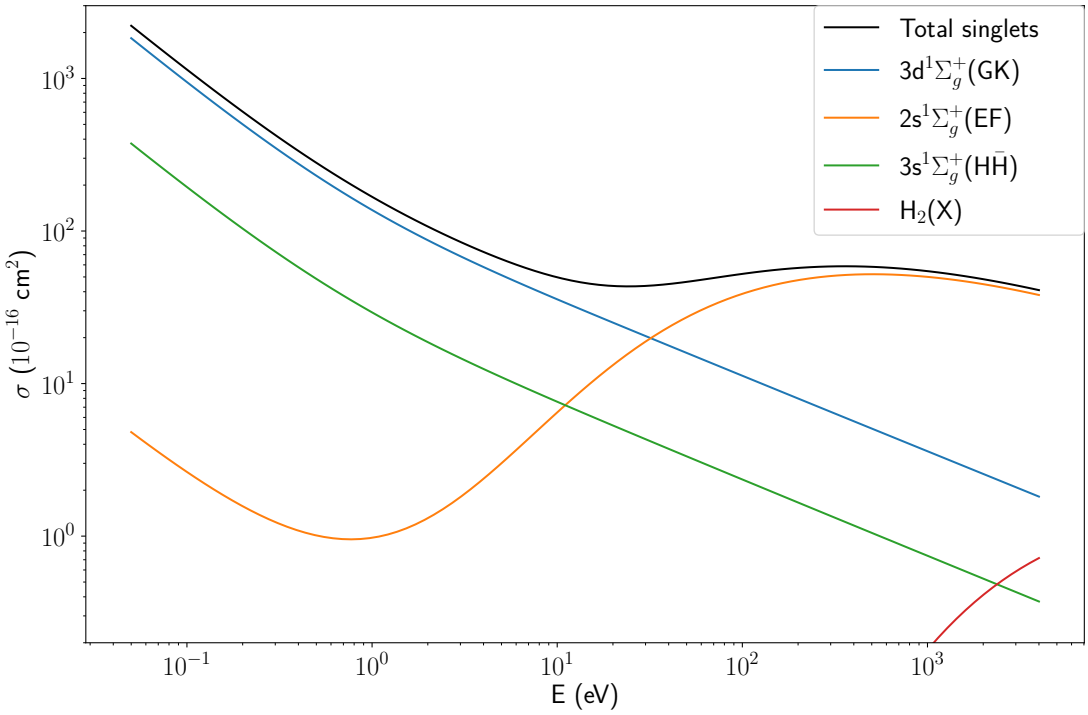

Figure 6.18: Partial cross sections of reaction (6.24) as a function of the collision energy $E = \mu v^2/2$ for the population of some H_2 and H_2^* singlet states computed in the framework of the multi-channel Landau-Zener model. Only the ground vibrational state $v_i = 0$ of H_2^+ is considered. Only four crossings have been considered: three with the ground vibrational state of three electronically excited states H_2^* and one with the ground electronic and vibrational state $H_2(X)$.

In order to assert the validity of the multi-channel Landau-Zener program developed for this work, the results presented by Liu et al. [30] have been reproduced. Figure 6.18 shows the partial cross sections σ_n for some singlet states as a function of the collision energy $E = \mu v^2/2$. Four crossings have been considered: the three crossings presented in Figure 6.17 (the only difference being the replacement of Deuterium atoms by Hydrogen atoms) and the crossing with the ground electronic state H_2. The obtained cross sections match perfectly those of Liu et al. [30].

Liu et al. [30] have also computed the partial cross sections for the triplet states $3s^3\Sigma_g^+$(h), $3d^3\Sigma_g^+$(g) and $2s^3\Sigma_g^+$(a). Figure 6.19 shows these partial cross sections σ_n as a function of the collision energy $E = \mu v^2/2$, computed with the multi-channel Landau-Zener program developed in the context of this work.

According to Liu et al. [30], the multi-channel Landau-Zener model is valid only if the distance between two subsequent crossing points $\Delta R_{x,i,i+1}$ is much larger than the

extension of the transition zone $\delta R_{x,i} \approx 1/\gamma$ associated with the crossing point $R_{x,i}$. This condition is required to avoid the overlapping of the transition zones [30]. It is why Liu et al. [30] have merged the two states $3s^3\Sigma_g^+$(h) and $3d^3\Sigma_g^+$(g) in a single virtual (h, g) state. The coupling interaction $H_{ic}^{(h,g)}$ and curve crossing point $R_x^{(h,g)}$ of the virtual state are computed from the coupling interactions and crossing points of $3s^3\Sigma_g^+$(h) and $3d^3\Sigma_g^+$(g) as follows:

$$H_{ic}^{(h,g)} = \sqrt{(H_{ic}^h)^2 + (H_{ic}^g)^2}, \quad R_x^{(h,g)} = \frac{R_x^h + R_x^g}{2}. \tag{6.49}$$

The transition probability at the curve-crossing of this virtual state is then:

$$\begin{aligned} p^{(h,g)}(b) &= \exp\left(-\frac{4\pi(H_{ic}^{(h,g)})^2}{2v_r(R_x^{(h,g)}, b)\Delta F(R_x^{(h,g)})}\right) \\ &= \exp\left(-\frac{4\pi(H_{ic}^h)^2}{2v_r(R_x^{(h,g)}, b)\Delta F(R_x^{(h,g)})}\right)\exp\left(-\frac{4\pi(H_{ic}^g)^2}{2v_r(R_x^{(h,g)}, b)\Delta F(R_x^{(h,g)})}\right). \end{aligned} \tag{6.50}$$

Because the crossings are very close $R_x^{(h,g)} \approx R_x^h \approx R_x^g$ and $p^{(h,g)}$ is approximately the product of the transition probabilities of the two real states:

$$p^{(h,g)}(b) \approx p^h(b)p^g(b). \tag{6.51}$$

The two states $3s^3\Sigma_g^+$(h) and $3d^3\Sigma_g^+$(g) have not been merged when computing the results presented in Figure 6.19. Therefore, the results of Liu et al. [30] show a single partial cross section curve for the virtual state (h, g) instead of two separated curves for the states $3s^3\Sigma_g^+$(h) and $3d^3\Sigma_g^+$(g). It follows that their total triplets cross section is smaller.

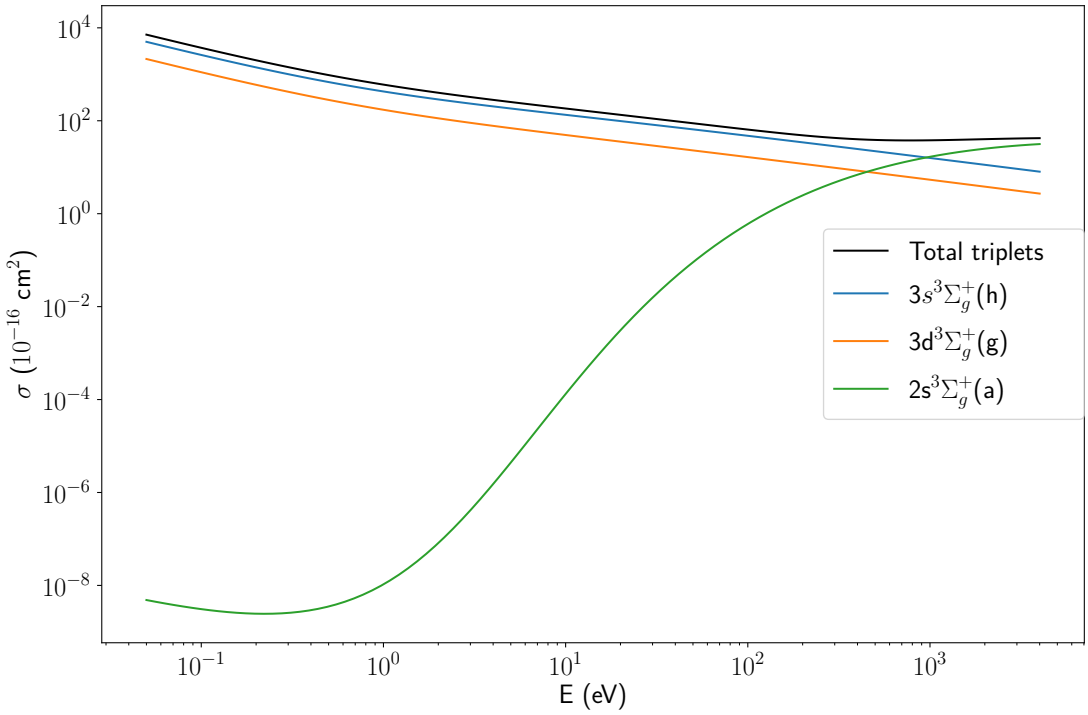

Figure 6.19: Partial cross sections of reaction (6.24) as a function of the collision energy $E = \mu v^2/2$ for the population of some H_2^* triplet states computed in the framework of the multi-channel Landau-Zener model. Only the ground vibrational state $v_i = 0$ of H_2^+ is considered. Only the crossings with the ground vibrational states of three electronically excited states H_2^* have been considered.

However, despite these differences, the obtained partial cross section for the state $2s^3\Sigma_g^+$(a) is identical to the one presented by Liu et al. [30]. Moreover, the partial cross section curve for their virtual state (h, g) lies between the two obtained curves for $3s^3\Sigma_g^+$(h) and $3d^3\Sigma_g^+$(g). These results are consistent and help to assert the correctness of the developed multi-channel Landau-Zener software. Results identical to Liu et al. [30] would have very likely been obtained if a single virtual state (h, g) would have been considered instead of two separated states.

Figure 6.20 shows the obtained partial cross sections when considering both the crossings with the singlet and triplet output channels in the same multi-channel Landau-Zener computation. In comparison with the separated singlets/triplets computation, the partial cross sections are slightly different but the global ordering between them remains identical.

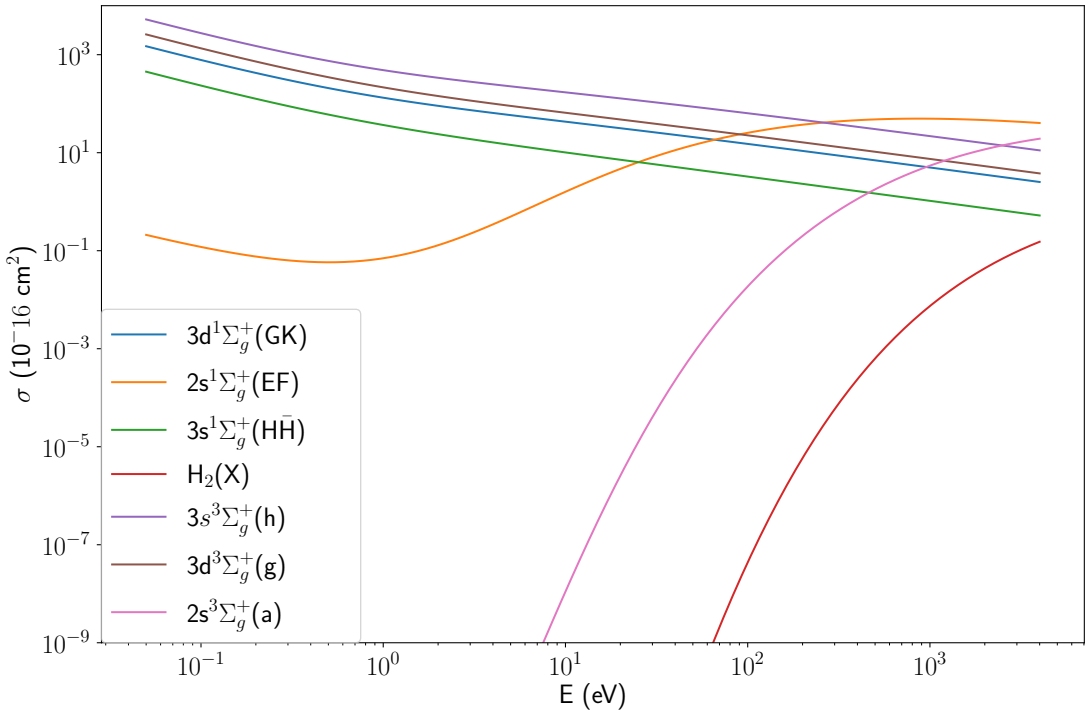

Figure 6.20: Partial cross sections of reaction (6.24) as a function of the collision energy $E = \mu v^2/2$ for the population of some H_2^* singlet and triplet states computed in the framework of the multi-channel Landau-Zener model. Only the ground vibrational state $v_i = 0$ of H_2^+ is considered. The crossings with the ground vibrational state of six electronically excited states H_2^* (three singlets and three triplets) have been considered, in addition to the crossing with the ground state $H_2(X)$.

6.2.5 Computation in the framework of the multi-channel Landau-Zener model of the theoretical kinetic energy released by transitions from the ground vibrational state of D_2^+ to the ground vibrational state of electronically excited states D_2^*

Considering for now only the transition from $D_2^+(v_i = 0)$ to $D_2^*(v_j = 0)$, i.e. all possible vibrational levels are not yet introduced in the multi-channel Landau-Zener model, the kinetic energy released by the transition to one electronically excited state D_2^* referred as the n-th, is computed as follows:

$$P^{ker}(E) = \sigma_n \ \exp\left(-\frac{(E - \Delta E(v_i = 0, v_j = 0))^2}{2\sigma^2}\right). \tag{6.52}$$

The value of σ has been reduced when computing the curves drawn in the following

figures such that the width at half-height of the gaussian is 0.005 eV to allow better visibility of the positions of the peaks.

Figure 6.21 presents a comparison between the KER distributions obtained when computing the partial cross sections of singlets and triplets separately or together. Results show that the resulting KER distributions are different. Therefore, the approximation made by Liu et al. [30] to consider the transitions to the singlet and triplet states as mutually uncoupled is incorrect.

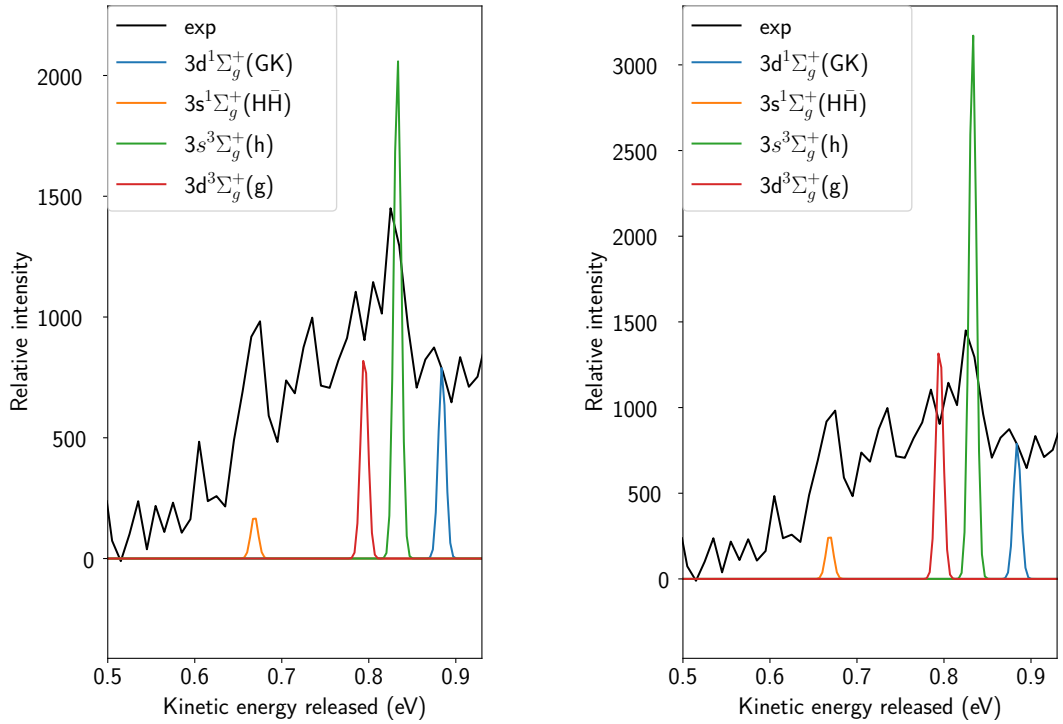

(a) Obtained KER distributions when computing the partial cross sections of singlets and triplets separately.

(b) Obtained KER distributions when computing the partial cross sections of singlets and triplets in the same multi-channel Landau-Zener computation.

Figure 6.21: Theoretically computed KER distributions for transitions from $D_2^+(v_i = 0)$ to three singlet states ($3d^1\Sigma_g^+$(GK), $2s^1\Sigma_g^+$(EF) and $3s^1\Sigma_g^+$(HH̄)) and three triplet states ($3s^3\Sigma_g^+$(h), $3d^3\Sigma_g^+$(g) and $2s^3\Sigma_g^+$(a)) of $D_2^*(v_j = 0)$. The relative amplitudes between the curves of the different states are given by the partial cross sections σ_n. The amplitudes of the different curves are multiplied by the same factor selected such that the amplitude of the peak associated to the state $3d^1\Sigma_g^+$(GK) matches the amplitude of the experimental curve. Because the partial cross sections of the states $2s^1\Sigma_g^+$(EF), $2s^3\Sigma_g^+$(a)) and D_2(X) are too weak at low energies, their KER distributions are not visible on the figures.

Figure 6.22 presents the KERs obtained when considering all crossings with all electronically excited states D_2^* presented in Figures A.3 and A.14. Vibration is still not considered for now.

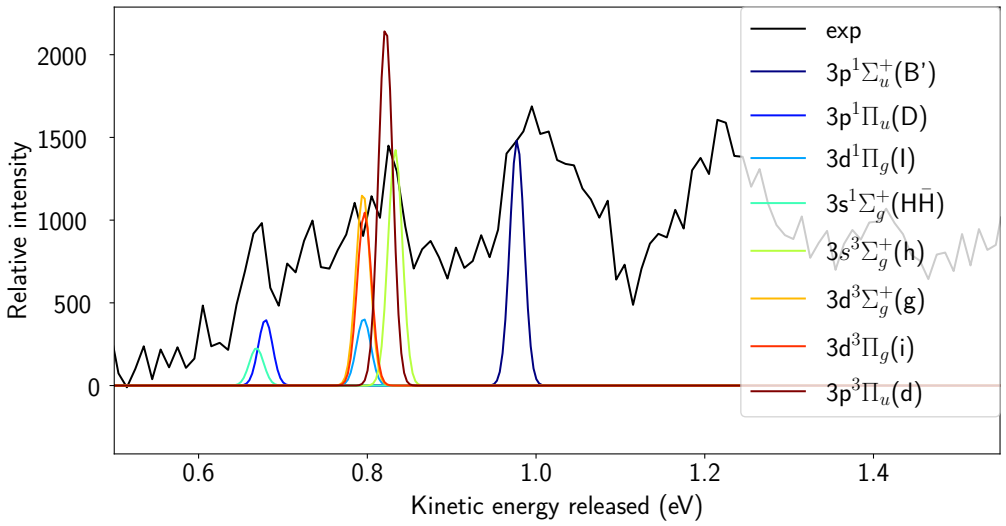

Figure 6.22: KERs for the reaction $D_2^+(v_i = 0) + D^- \rightarrow D_2^*(\Lambda_j, v_k = 0) + D$ obtained using the partial cross sections computed with the multi-channel Landau-Zener model and Equation (6.52). Only ground vibrational states have been considered. Crossings with all excited electronic states $D_2^*(\Lambda_j)$ presented in Figures A.3 and A.14 have been considered. States with negligible partial cross sections have been removed from the legend for better readability.

Results show that, without vibration, the state $3d^1\Sigma_g^+$(GK) which was a major state using only the Franck-Condon principle has a negligible cross section with respect to the other states presented in Figure 6.22. Moreover, there is no KER predicted by the theory above 1.1 eV despite the presence of many events in the experimental KER between 1.1 and 2.3 eV.

The first peak may be explained by the states $3s^1\Sigma_g^+(H\bar{H})$ and $3p^1\Pi_u$(D). The second one by a mix of several states among which the $3p^3\Pi_u$(d) has the highest partial cross section. The third peak is explained by the state $3p^1\Sigma_u^+$(B') which was already essential to explain this peak when using only the Franck-Condon principle. Unfortunately, the cross sections of the different states do not match the amplitudes of the experimental peaks. The reason is that, because their crossings are really close (see Figures A.3 and A.14), the states $3p^3\Pi_u$(d) , $3s^3\Sigma_g^+$(h), $3d^3\Sigma_g^+$(g), $3d^3\Pi_g$(i) and $3d^1\Pi_g$(I) cannot be considered as separate states in the multi-channel Landau-Zener model.

Comparing the results of this work to the ones of Liu et al. [30], it was noticed that the partial cross section of a virtual state σ_{tot} is roughly the average of the partial cross

sections of the real states that compose this virtual state. Therefore, the partial cross sections σ_n of these five real states have been reduced such that:

$$\sigma_{tot} = \frac{1}{5}\sum_n \sigma_n \quad \Longrightarrow \quad \sigma'_n = \frac{\sigma_n}{5}. \tag{6.53}$$

Figure 6.23 shows the impact of this modification [5].

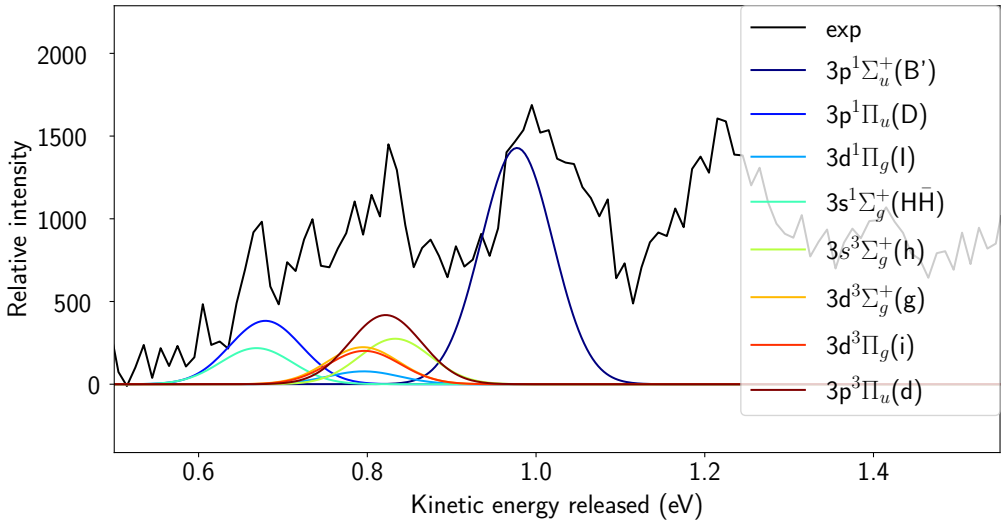

Figure 6.23: KERs for the reaction $D_2^+(v_i = 0) + D^- \rightarrow D_2^*(\Lambda_j, v_k = 0) + D$ obtained using the partial cross sections computed with the multi-channel Landau-Zener model and Equation (6.52). Only ground vibrational states have been considered. Crossings with all excited electronic states $D_2^*(\Lambda_j)$ presented in Figures A.3 and A.14 have been considered. States with negligible partial cross sections have been removed from the legend for better readability. Because the crossings of the states $3p^3\Pi_u(d)$, $3s^3\Sigma_g^+(h)$, $3d^3\Sigma_g^+(g)$, $3d^3\Pi_g(i)$ and $3d^1\Pi_g(I)$ are very close, their partial cross sections have been divided by their number (i.e. by five).

Figure 6.24 presents the final result obtained when summing KER distributions associated to all electronically excited states D_2^*. Results match quite well the experimental curve up to 1.1 eV considering that vibration has not yet been introduced in the multi-channel Landau-Zener model. Results then show that transitions between ground state vibrational levels are sufficient to explain the three most left peaks of the experimental KER.

[5] The distributions are larger than in Figure 6.22 because the parameter σ has been reset to 0.05 eV.

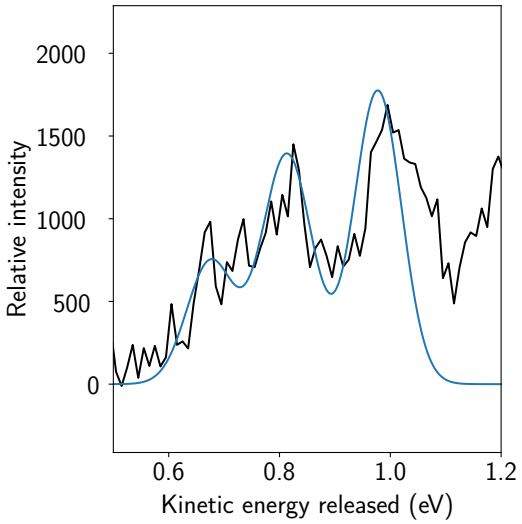

Figure 6.24: Sum of the KER distributions presented in Figure 6.23.

6.2.6 Computation in the framework of the multi-channel Landau-Zener model of the theoretical kinetic energy released by transitions from the ground vibrational state of D_2^+ to the excited vibrational states of electronically excited states D_2^*

This section introduces the vibrational levels of D_2^* in the multi-channel Landau-Zener computations. Only the ground vibrational state of D_2^+ is considered for now.

The results highlight the following differences with the computation considering only the ground vibrational state of D_2^* (see Figures 6.25 and 6.21b). The amplitude difference between the states $3s^3\Sigma_g^+(h)$ and $3d^3\Sigma_g^+(g)$ has slightly decreased. Moreover, the KER distribution produced by the state $3d^1\Sigma_g^+(GK)$ has moved to lower energies.

The explanation is that Equation (6.32) was used and the factor S_{v_i,v_j} was set to unity when ignoring the vibrational levels (see Equation (6.37)). The values E_A and γ were set to the relevant constant values. Now that vibrational levels of D_2^* are considered, H_{ic} is obtained by computing the integral over the inter-nuclear distance (i.e. using Equation (6.38)). This integral encompasses overlapping of the initial and final states vibrational wavefunctions like S_{v_i,v_j}.

As shown in the Franck-Condon matrix associated to the transition from $D_2^+(v_i)$ to $D_2^*(3d^1\Sigma_g^+(GK), v_j)$ (see Figure 6.12b) , the value of $S_{v_i=0,v_j=0}$ is much smaller than the value of $S_{v_i=0,v_j=1}$ (the Franck-Condon coefficient $FCM_{ij} = |S_{v_i,v_j}|^2$). Therefore, the transition from the ground vibrational state of $D_2^+(v_i = 0)$ to the first excited vibrational state $D_2^*(3d^1\Sigma_g^+(GK), v_j = 1)$ is much more favored by the system than the transition to the ground vibrational state $D_2^*(3d^1\Sigma_g^+(GK), v_j = 0)$ (see Figure 6.26).

The last difference is a new contribution from the state $2s^1\Sigma_g^+$(EF) due to the high partial cross section associated to the final vibrational state $v_j = 3$ (see Figure 6.26).

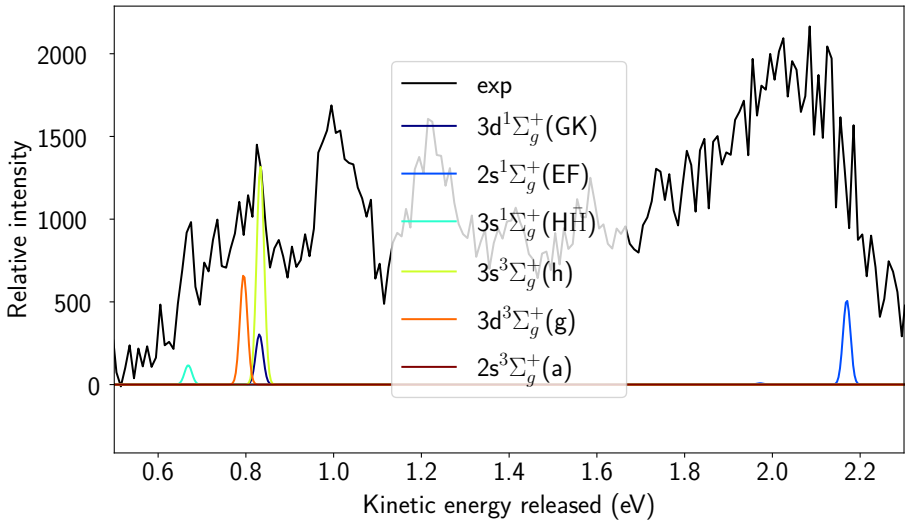

Figure 6.25: Theoretically computed KER distributions for transitions from $D_2^+(v_i = 0)$ to three singlet states ($3d^1\Sigma_g^+$(GK), $2s^1\Sigma_g^+$(EF) and $3s^1\Sigma_g^+$(H$\bar{\text{H}}$)) and three triplet states ($3s^3\Sigma_g^+$(h), $3d^3\Sigma_g^+$(g) and $2s^3\Sigma_g^+$(a)) of $D_2^*(v_j)$. Only the ground vibrational state has been considered for D_2^+ but all vibrational states have been considered for the electronically excited states D_2^*. The amplitudes of the different curves are multiplied by the same factor selected such that the amplitude of the peak associated to the state $3s^3\Sigma_g^+$(h) matches the amplitude of the experimental curve. Because the partial cross section of the state $2s^3\Sigma_g^+$(a)) is too small, its KER distribution is not visible on the figure.

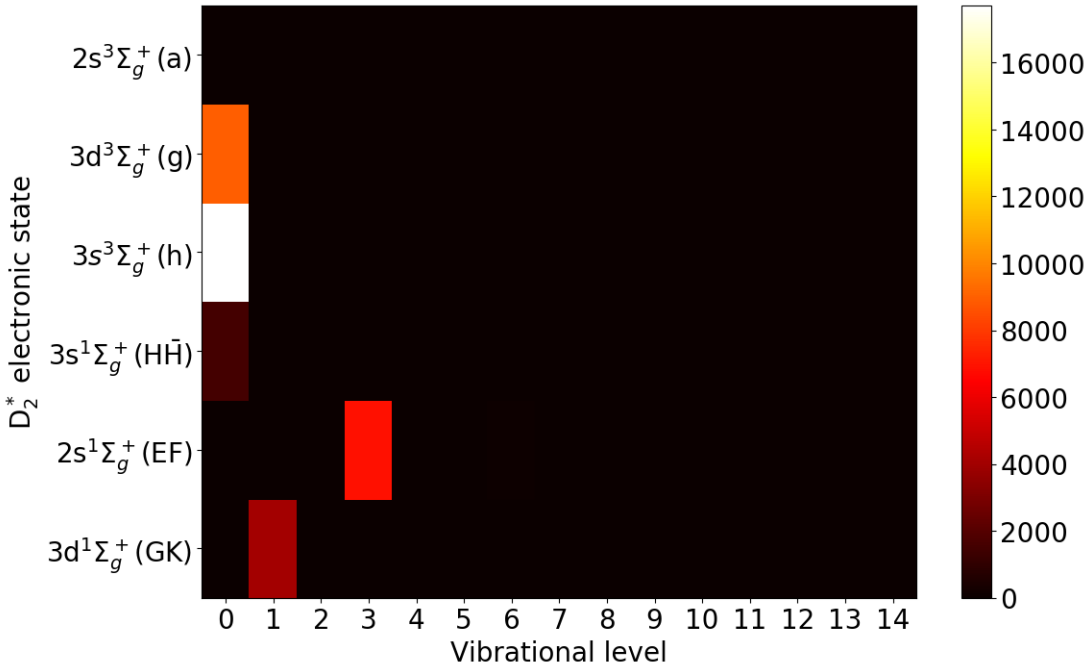

Figure 6.26: Colors represent the partial cross sections of vibrational states of some electronically excited states D_2^*.

Figures 6.27 presents the results obtained considering all electronically excited states presented in Figures A.3 and A.14 with all their vibrational states. The introduction of all possible vibrational levels of D_2^* has slightly modified the theoretical KER spectra (see Figure 6.22). Firstly, the state $3d^1\Sigma_g^+$(GK) contributes now slightly to the peak around 0.82 eV due to the high value of the partial cross section of the first excited vibrational level (see Figure 6.28). Secondly, a new contribution from the state $3p^3\Sigma_u^+$(e) has appeared around 1.25 eV due to the high partial cross section of its first excited vibrational state. Finally, due to small but non negligible cross section of the first excited vibrational level of $3p^1\Sigma_u^+$(B'), this state produces a small KER distribution centered at 0.8 eV (at the left of the bump explained by the state $3d^1\Sigma_g^+$(GK)).

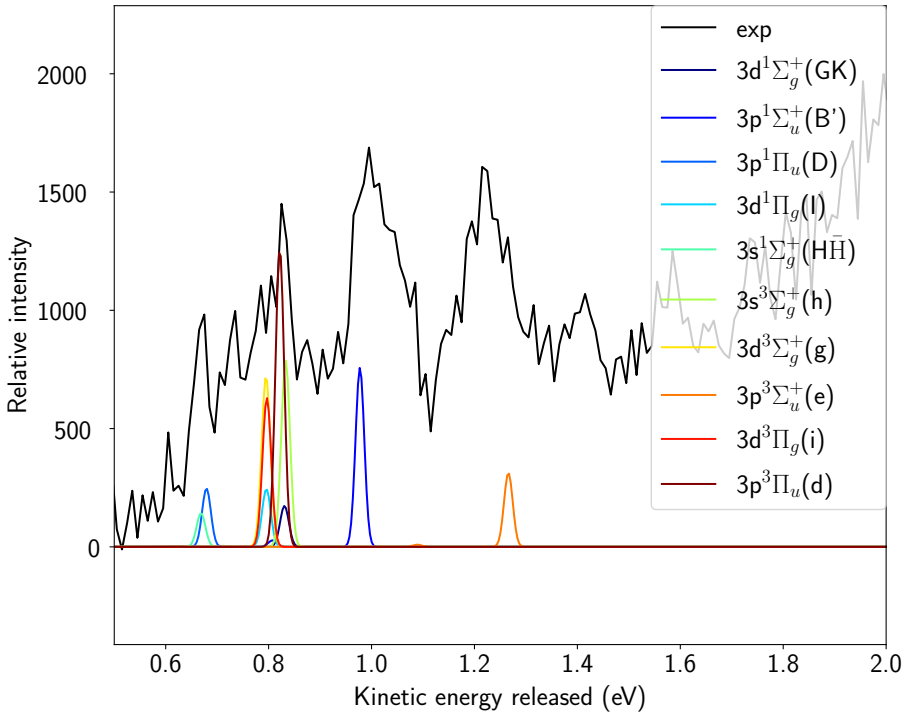

Figure 6.27: KER distributions obtained for all electronically excited states of $D_2^*(v_j)$ presented in Figures A.3 and A.14 with all their vibrational states (D_2^* states not displayed in the legend have negligible cross sections). The curves have been multiplied by the same factor such that the maximum of the curve $3p^3\Pi_u$(d) matches the experimental curve.

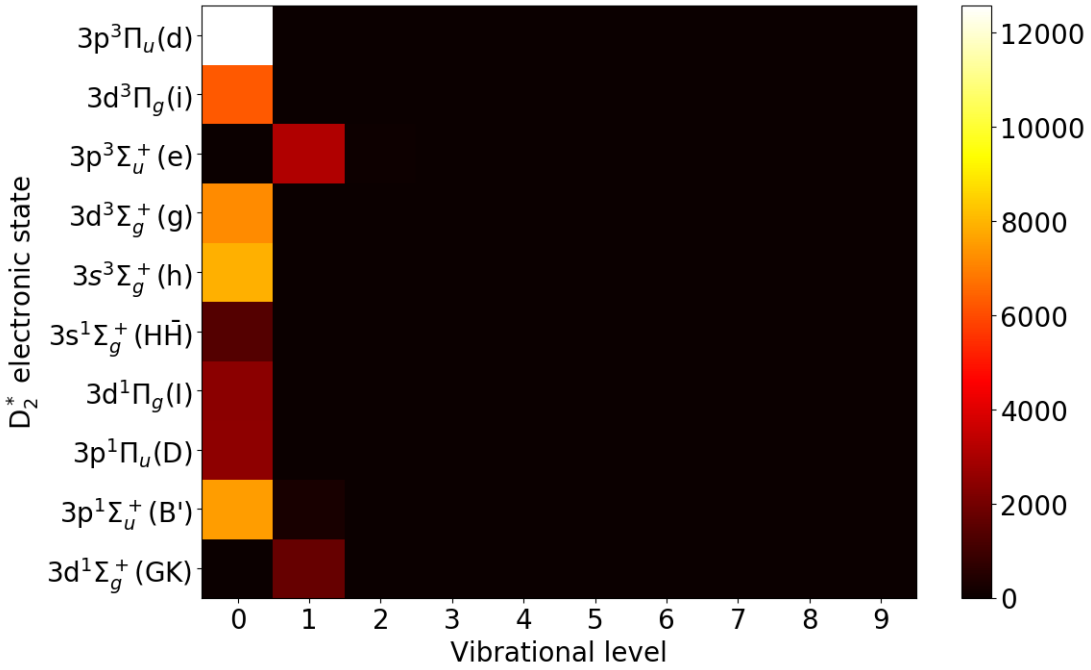

Figure 6.28: Colors represent the partial cross sections of vibrational states of some electronically excited states D_2^*. These partial cross sections have been obtained using the multi-channel Landau-Zener model considering the crossings with all electronically excited states of $D_2^*(v_j)$ presented in Figures A.3 and A.14 with all their vibrational states. $D_2^*(v_j)$ states not presented in the figure have negligible cross sections for all vibrational levels. Moreover, partial cross sections for vibrational levels higher than the ninth are negligible.

6.2.7 Computation in the framework of the multi-channel Landau-Zener model of the theoretical kinetic energy released by transitions from excited vibrational states of D_2^+ to the excited vibrational states of electronically excited states D_2^*

This section presents partial cross sections and KER distributions obtained when considering one initial excited vibrational state of D_2^+ and many vibrational states of D_2^*. Figures 6.29 and 6.30 show the results for $D_2^+(v_i = 1)$.

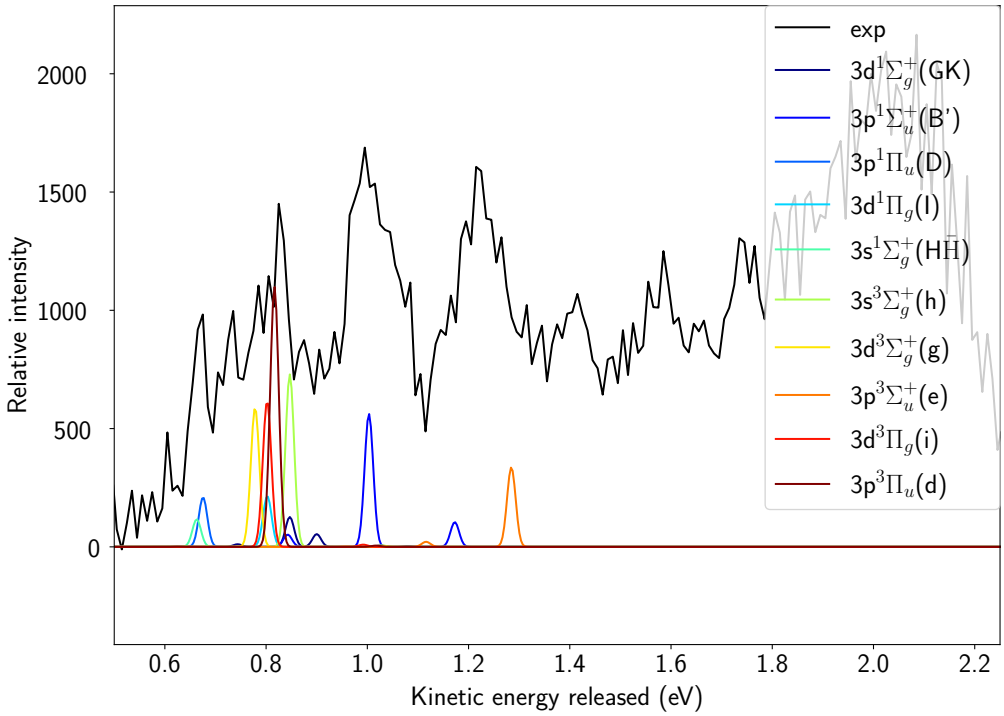

Figure 6.29: KER distributions obtained for all electronically excited states of $D_2^*(v_j)$ presented in Figures A.3 and A.14 with all their vibrational states (D_2^* states not displayed in the legend have negligible cross sections). Only the vibrational state $v_i = 1$ of D_2^+ has been considered. The curves have been multiplied by the same factor such that the maximum of the curve $3p^3\Pi_u$(d) matches the experimental curve.

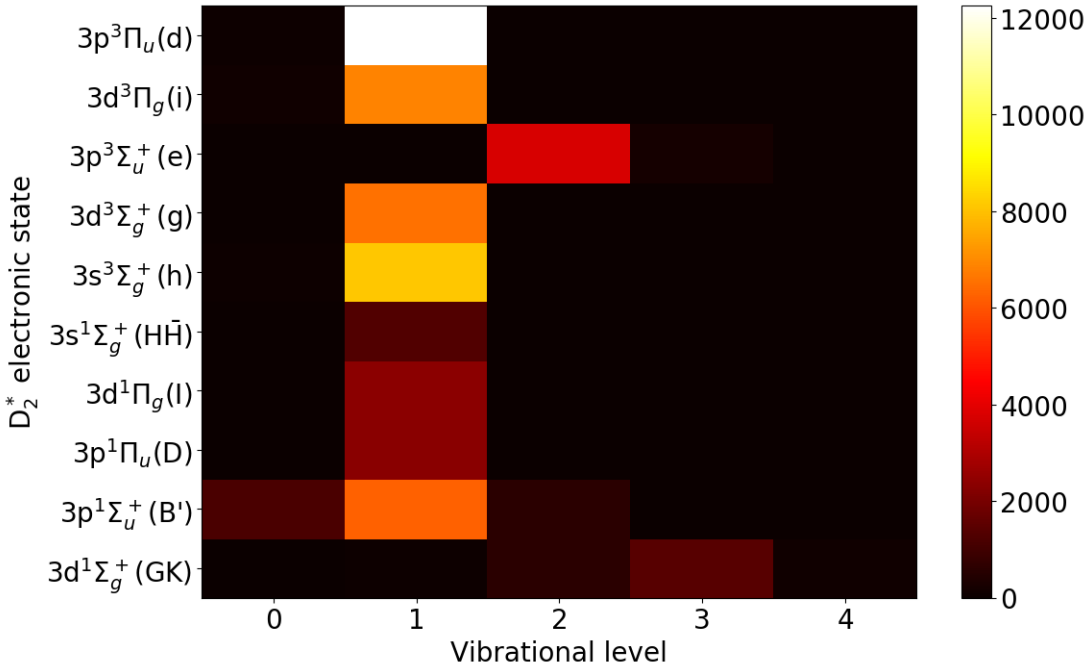

Figure 6.30: Colors represent the partial cross sections of vibrational states of some electronically excited states D_2^* considering only the vibrational state $v_i = 1$ of D_2^+. These partial cross sections have been obtained using the multi-channel Landau-Zener model considering the crossings with all electronically excited states of $D_2^*(v_j)$ presented in Figures A.3 and A.14 with all their vibrational states. $D_2^*(v_j)$ states not presented in the figure have negligible cross sections for all vibrational levels. Moreover, partial cross sections for vibrational levels higher than the sixth are negligible.

The vibrational states $v_i = 2$ and $v_i = 3$ are particularly important because most of the population of D_2^+ reside in these two states. Figure 6.31 presents the KER distributions obtained for $v_i = 2$ and Figure 6.32 the corresponding partial cross sections. The results are similar to the ones obtained for $v_i = 0$ (see Figure 6.27): the partial cross sections of the states contributing to KER distributions close to 0.8 eV seem highly overestimated with respect to the experimental curve. Moreover, there is still no contribution explaining the high number of events observed around 2 eV. The same conclusions apply to the results obtained for $v_i = 3$ (see Figures 6.33 and 6.34).

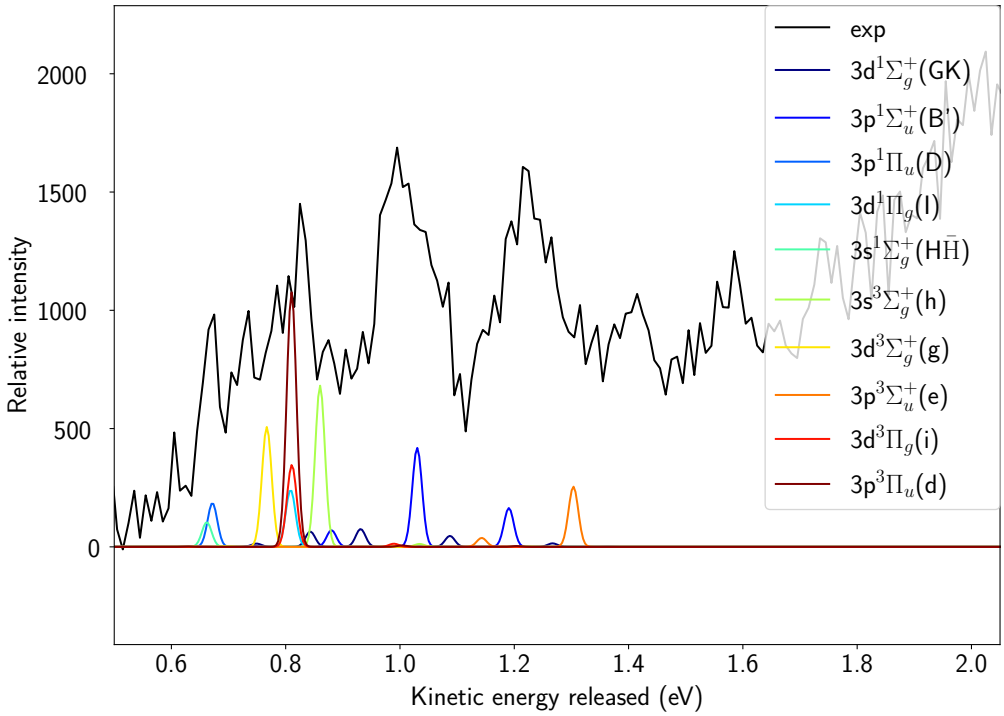

Figure 6.31: KER distributions obtained for all electronically excited states of $D_2^*(v_j)$ presented in Figures A.3 and A.14 with all their vibrational states (D_2^* states not displayed in the legend have negligible cross sections). Only the vibrational state $v_i = 2$ of D_2^+ has been considered. The curves have been multiplied by the same factor such that the maximum of the curve $3p^3\Pi_u$(d) matches the experimental curve.

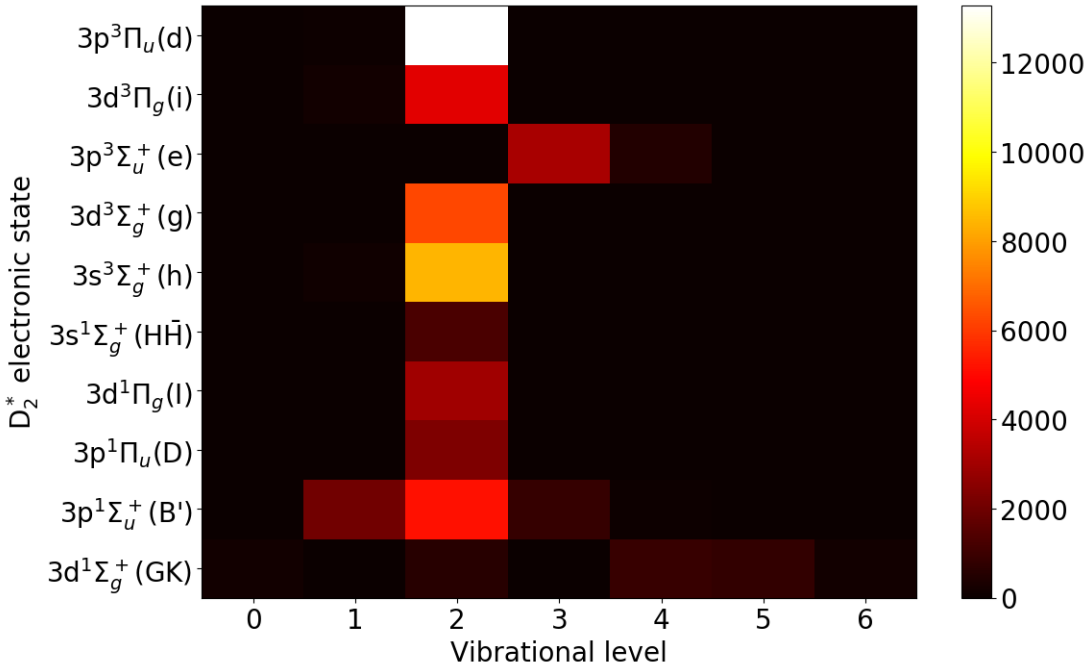

Figure 6.32: Colors represent the partial cross sections of vibrational states of some electronically excited states D_2^* considering only the vibrational state $v_i = 2$ of D_2^+. These partial cross sections have been obtained using the multi-channel Landau-Zener model considering the crossings with all electronically excited states of $D_2^*(v_j)$ presented in Figures A.3 and A.14 with all their vibrational states. $D_2^*(v_j)$ states not presented in the figure have negligible cross sections for all vibrational levels. Moreover, partial cross sections for vibrational levels higher than the sixth are negligible.

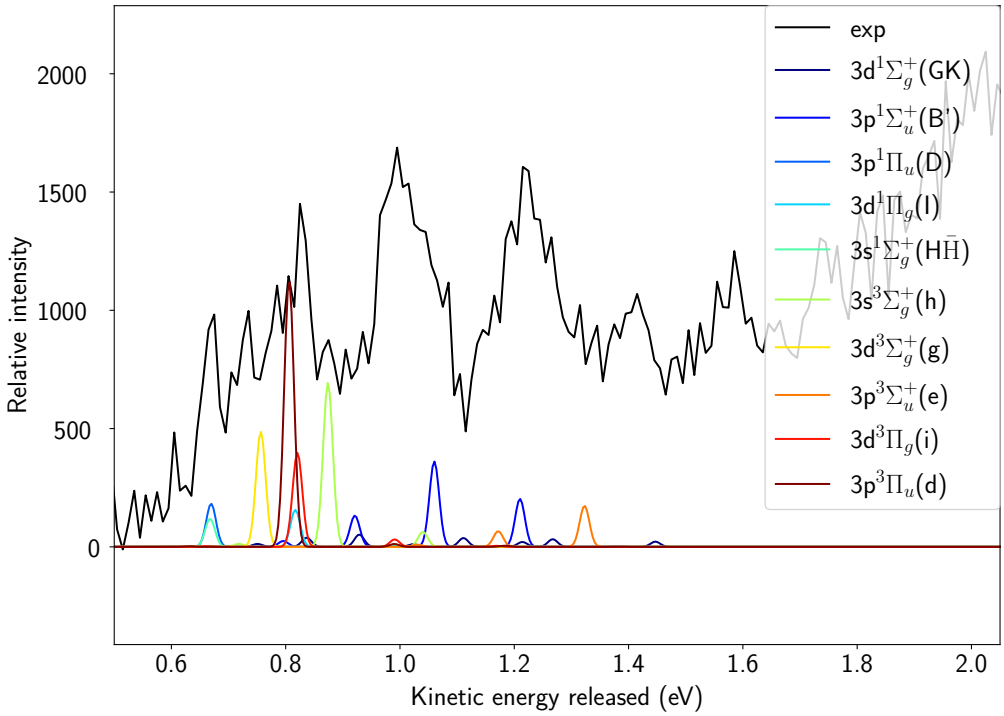

Figure 6.33: KER distributions obtained for all electronically excited states of $D_2^*(v_j)$ presented in Figures A.3 and A.14 with all their vibrational states ($D_2^*(v_j)$ states not displayed in the legend have negligible cross sections). Only the vibrational state $v_i = 3$ of D_2^+ has been considered. The curves have been multiplied by the same factor such that the maximum of the curve $3p^3\Pi_u$(d) matches the experimental curve.

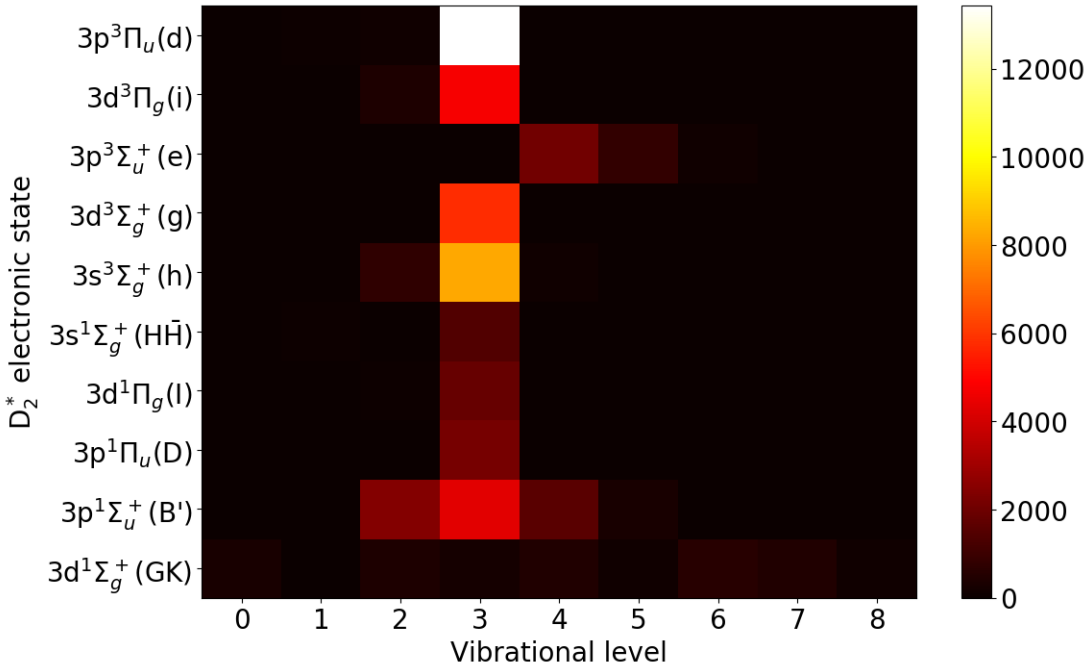

Figure 6.34: Colors represent the partial cross sections of vibrational states of some electronically excited states D_2^* considering only the vibrational state $v_i = 3$ of D_2^+. These partial cross sections have been obtained using the multi-channel Landau-Zener model considering the crossings with all electronically excited states of $D_2^*(v_j)$ presented in Figures A.3 and A.14 with all their vibrational states. $D_2^*(v_j)$ states not presented in the figure have negligible cross sections for all vibrational levels. Moreover, partial cross sections for vibrational levels higher than the sixth are negligible.

All the results for $v_i = 0$ to $v_i = 3$ show that the partial cross sections of states contributing to the KER distributions around 0.8 eV is overestimated with respect to the experimental curve. Figure 6.35 shows the KER distributions obtained when summing the contributions of all vibrational states v_i of D_2^+. Figure 6.36 shows the corresponding cross sections obtained summing the partial cross sections associated to all vibrational states of D_2^+. The contributions of triplet states around 0.8 eV seem overestimated with respect to the other contributions. The state $3p^1\Sigma_u^+$(B') remains essential to explain the two major experimental peaks around 1 and 1.25 eV.

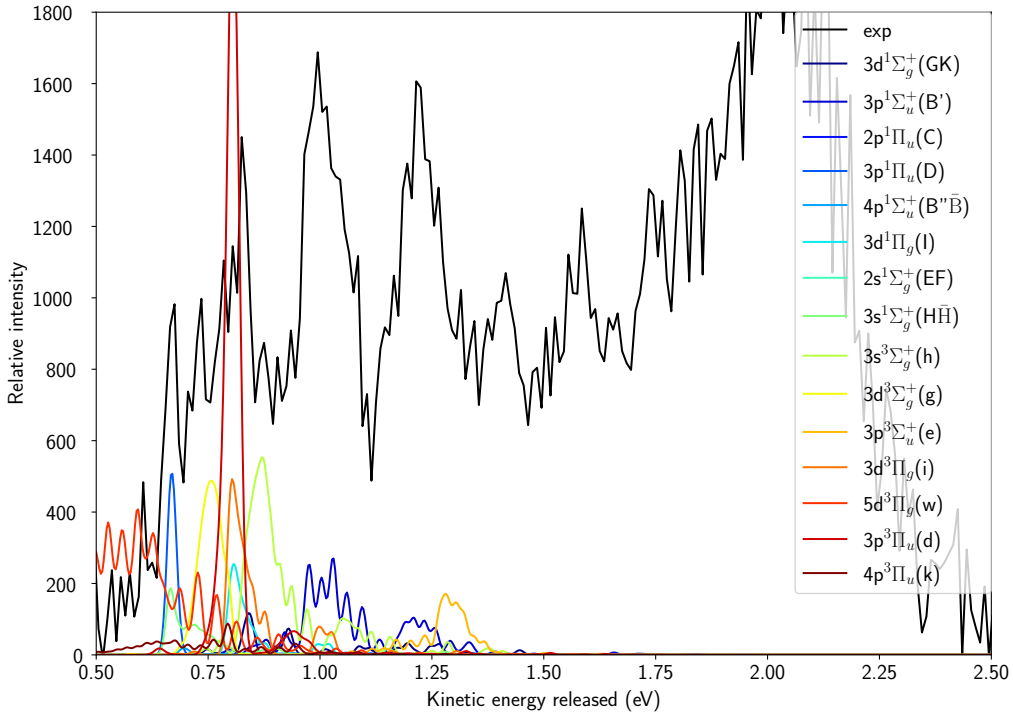

Figure 6.35: KER distributions obtained for all electronically excited states of $D_2^*(v_j)$ presented in Figures A.3 and A.14 with all their vibrational states (D_2^* states not displayed in the legend have negligible cross sections). The contributions of all vibrational states v_i of $D_2^+(v_i)$ have been considered. The curves have been multiplied by the same arbitrary factor.

The most plausible explanation for the too high cross sections of triplet states around 0.8 eV observed in Figure 6.35 is their possibly too short lifetime: they may predissociate before hitting the detector. In this case, their theoretical KER distributions would not be visible in the experimental KER. De Bruijn et al. [27] indeed report that many highly excited states of H_2 are predissociative such as $3p^3\Pi_u(d)$, $3p^1\Pi_u(D)$, $4p^1\Sigma_u^+(B''\bar{B})$, $4p^3\Pi_u(k)$, $3d^3\Sigma_g^+(g)$, $3d^1\Pi_g(I)$, $3d^3\Pi_g(i)$ and $3s^3\Sigma_g^+(h)$. In particular the state $3p^3\Pi_u(d)$ predissociates to the state $3p^3\Sigma_u^+(e)$. These states must nevertheless still be considered as possible output channels in the multi-channel Landau-Zener model. A second possible explanation is that the crossings associated to these states are too close and therefore these states cannot be considered as independent.

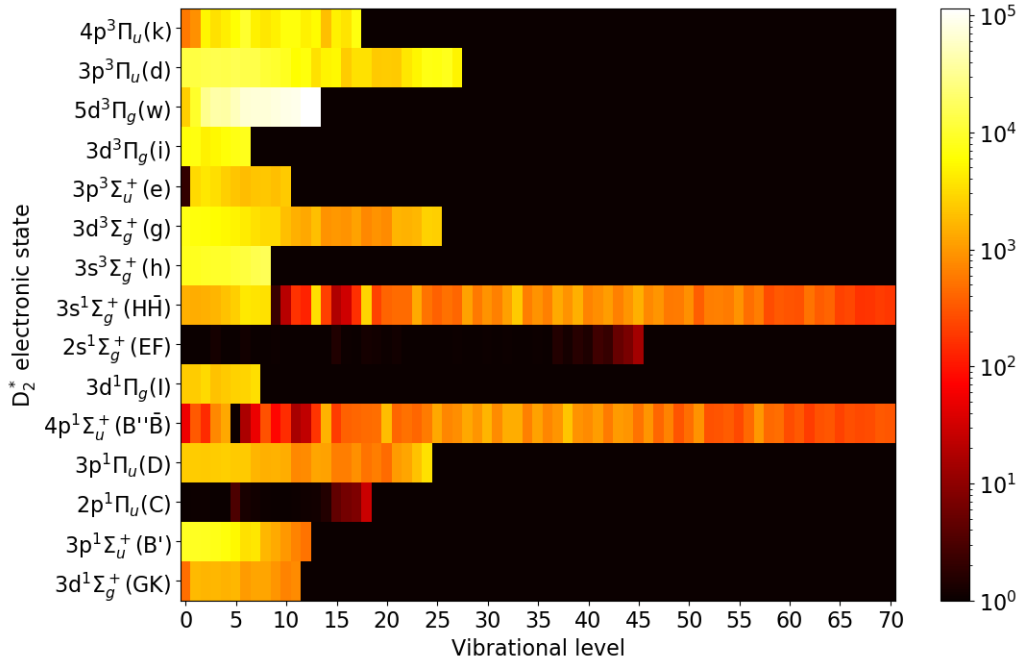

Figure 6.36: Colors represent the partial cross sections of vibrational states of some electronically excited states D_2^* considering all the vibrational state v_i of $D_2^+(v_i)$ (contributions from all v_i of D_2^+ to one vibrational state v_j of D_2^* have been summed). These partial cross sections have been obtained using the multi-channel Landau-Zener model considering the crossings with all electronically excited states of $D_2^*(v_j)$ presented in Figures A.3 and A.14 with all their vibrational states. $D_2^*(v_j)$ states not presented in the figure have negligible cross sections for all vibrational levels. Moreover, partial cross sections for vibrational levels higher than the seventieth are negligible.

Figure 6.37 shows the KER distributions of only singlet states. The two first major peaks around 0.7 and 0.8 eV are overestimated by computational results.

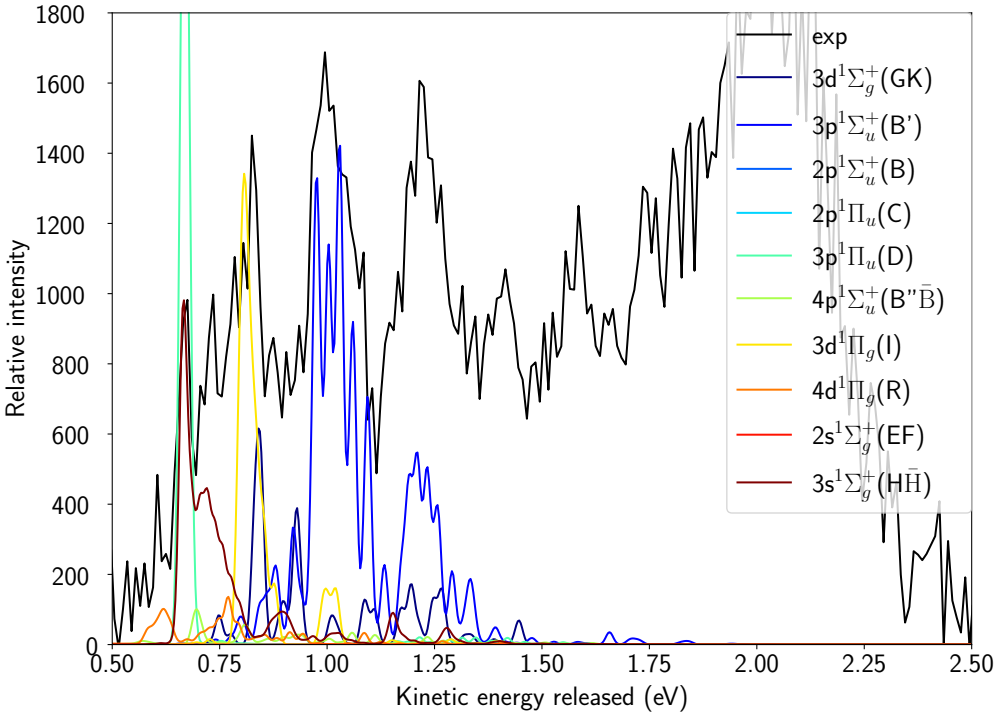

Figure 6.37: KER distributions for singlet states obtained including all electronically excited states of $D_2^*(v_j)$ presented in Figures A.3 and A.14 with all their vibrational states in the multi-channel Landau-Zener model ($D_2^*(v_j)$ singlet states not displayed in the legend have negligible cross sections). The contributions of all vibrational states v_i of $D_2^+(v_i)$ have been considered. The curves have been multiplied by the same arbitrary factor.

Figure 6.38 shows the KER distributions of only the non-predissociative singlet and triplet states. Figure 6.39 shows the total KER distribution obtained after summing the contributions of all these electronic excited states D_2^*.

The results explain the first peak around 0.7 eV, the third around 1 eV and the fourth around 1.2 eV. Several more or less rigorous strategies would allow to better match the second peak around 0.8 eV. A first one is to assume that some predissociative states only predissociate partially, i.e. their lifetimes would be high enough for a fraction of their initial population to make it to the detector and contribute to the KER distribution around 0.8 eV. A second one is to assume that, due to the approximate nature of the multi-channel Landau-Zener model when many crossings are close, the partial cross sections of some transitions to the states $3d^1\Sigma_g^+(GK)$ and $3s^1\Sigma_g^+(H\bar{H})$ are higher than the computed ones. These higher partial cross sections may increase the contributions of $3s^1\Sigma_g^+(H\bar{H})$ around 0.74 eV and $3d^1\Sigma_g^+(GK)$ around 0.8 eV.

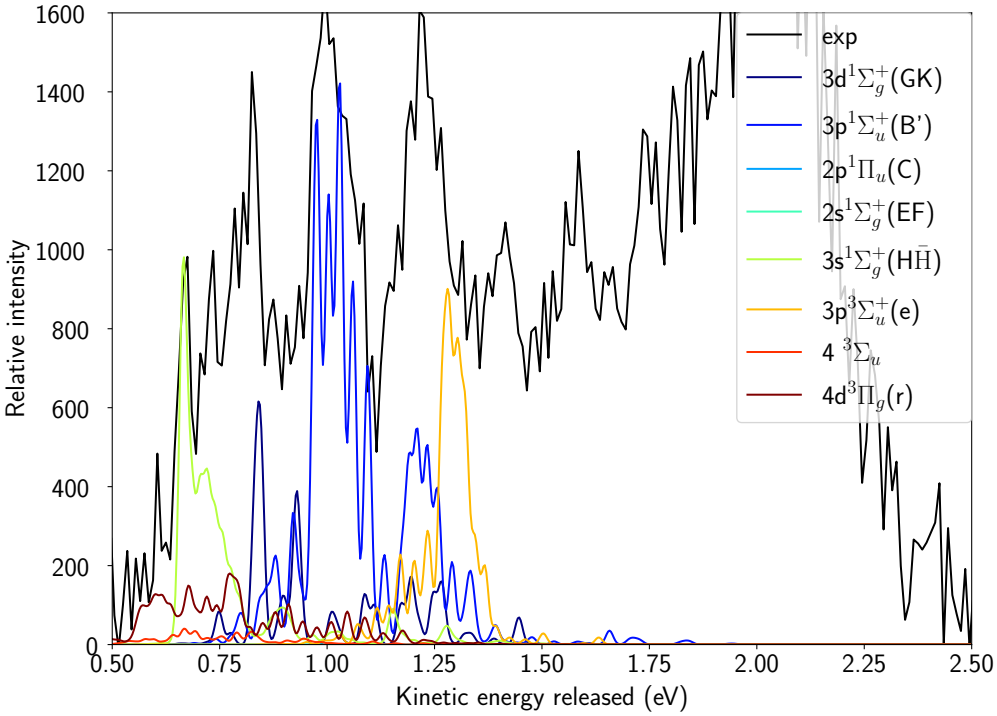

Figure 6.38: KER distributions of non-predissociative singlet and triplet states obtained including all electronically excited states of $D_2^*(v_j)$ presented in Figures A.3 and A.14 with all their vibrational states in the multi-channel Landau-Zener model ($D_2^*(v_j)$ non-predissociative singlet and triplet states not displayed in the legend have negligible cross sections). The contributions of all vibrational states v_i of $D_2^+(v_i)$ have been considered. The curves have been multiplied by the same arbitrary factor.

There are still no contributions at KER higher than 1.4 eV (see Figure 6.39).

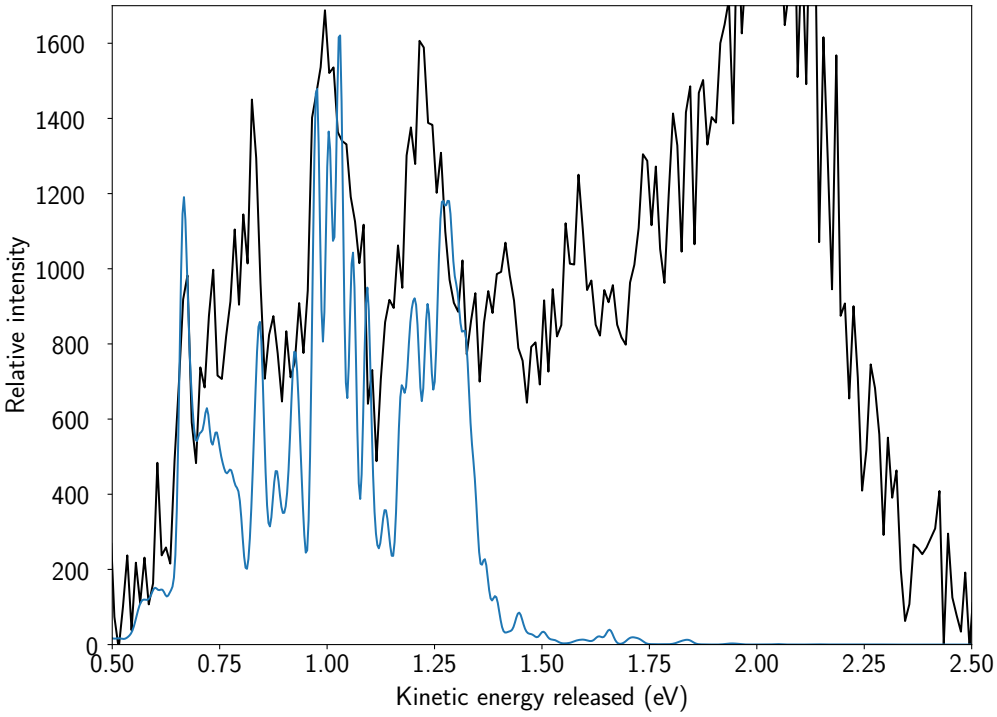

Figure 6.39: Total KER distribution of non-predissociative singlet and triplet states presented in Figure 6.38. The parameter $\sigma = 0.01/\sqrt{2\ln 2}$.

The last try with the multi-channel Landau-Zener model was to include output channels to both mutual neutralization reactions $D_2^+ + D^- \rightarrow D_2 + D^*$ and $D_2^+ + D^- \rightarrow D_2^* + D$. No contribution from reaction $D_2^+ + D^- \rightarrow D_2 + D^*$ has been observed in the computed KER distributions.

6.3 Conclusion

This section presents a reflection on the results obtained in this Chapter.

The pure Franck-Condon approach has firstly allowed to identify the excited electronic states D_2^* most populated by the reaction $D_2^+ + D^- \rightarrow D_2^* + D$. These are the singlet states $3s^1\Sigma_g^+(H\bar{H})$, $3d^1\Sigma_g^+(GK)$ and $3p^1\Sigma_u^+(B')$. Other singlet states are excluded because they are predissociative or because their theoretical contribution to the KER really does not match the experimental curve (see Figure 6.10 and 6.11).

The multichannel Landau-Zener approach yields conclusions compatible with the pure Franck-Condon approach. Results show that theoretical computations do not match at all the experimental curve when all KER contributions from triplet states are considered

(see Figure 6.35). Moreover, the singlet state $3d^1\Pi_g(I)$, reported by De Bruijn [27] as being predissociative, must indeed be removed for the amplitude of the peak around 0.8 eV not to be far too great (see Figure 6.37).

This approach has the advantage, with respect to the pure Franck-Condon one, to output partial cross sections associated to each transition. Results then show that the singlet states $3s^1\Sigma_g^+(H\bar{H})$, $3d^1\Sigma_g^+(GK)$ and $3p^1\Sigma_u^+(B')$ indeed explain quite well the experimental curve up to 1.3 eV. However, there are missing contributions between 0.7 and 0.8 eV as well as around 1.25 eV. Including the contribution of the triplet state $3p^3\Sigma_u^+(e)$ allows to much better fit the experimental peak around 1.25 eV (see Figure 6.38). This triplet state is not mentioned by De Bruijn [27] as predissociative, although other sources claim that every triplet states of D_2^* are predissociative.

The experimental KER above 1.3 eV is probably not explained for the following reason. The multi-channel Landau-Zener model does not take into account the increased cross section with vibrational excitation of D_2^+. This increase is due to the larger amplitude of the vibrational motion in excited vibrational states which allows electron capture at larger distance.

This hypothesis is strengthened by the results obtained in Section 6.2.3. Results obtained with a cross section increasing with inter-nuclear distance of D_2^+ show much more predicted events between 1.3 and 2.3 eV. Furthermore, the shape of the theoretical KER computed for the $3d^1\Sigma_g^+(GK)$ electronically excited states D_2^* is very similar to the shape of the experimental curve above 1.3 eV (see Figure 6.40). The number of high KER events is still underestimated with this cross section, maybe because the used cross section has not been computed for the same physical process. Another possibility is that, due to the high number of competing output channels for the reaction $D_2^+ + D^-$, this cross section must be inserted somehow in an improved multichannel Landau-Zener model.

According to results from the multichannel Landau-Zener model, contributions between 1.3 and 2.3 eV come only from transitions to $3p^1\Sigma_u^+(B')$ (see Figure 6.38). The contributions from the state $3d^1\Sigma_g^+(GK)$ in this energy range observed when using only the Franck-Condon principle (see Figure 6.10) are not favored by the Landau-Zener model: all these contributions have disappeared in Figure 6.38.

The theoretical peak from the state $3d^1\Sigma_g^+(GK)$ around 0.8 eV being too small by a factor two, the real partial cross section of the state $3d^1\Sigma_g^+(GK)$ seems underestimated by the model. This is most probably due to the non-validity of the multichannel Landau-Zener model when the different crossings are too close.

To wrap up, the experimental KER curve is most probably explained as follows. The first peak around 0.7 eV results from the contribution of the state $3s^1\Sigma_g^+(H\bar{H})$. Up to 0.8 eV, the KER may be explained by a combination of the contributions from $3s^1\Sigma_g^+(H\bar{H})$, $3d^1\Sigma_g^+(GK)$ and $3p^1\Sigma_u^+(B')$. In particular, the high peak around 0.8 eV is mostly explained by $3d^1\Sigma_g^+(GK)$. The two massive peaks around 1 and 1.25 eV are explained by the state $3p^1\Sigma_u^+(B')$. Contribution from $3p^1\Sigma_u^+(B')$ to this second peak is expected

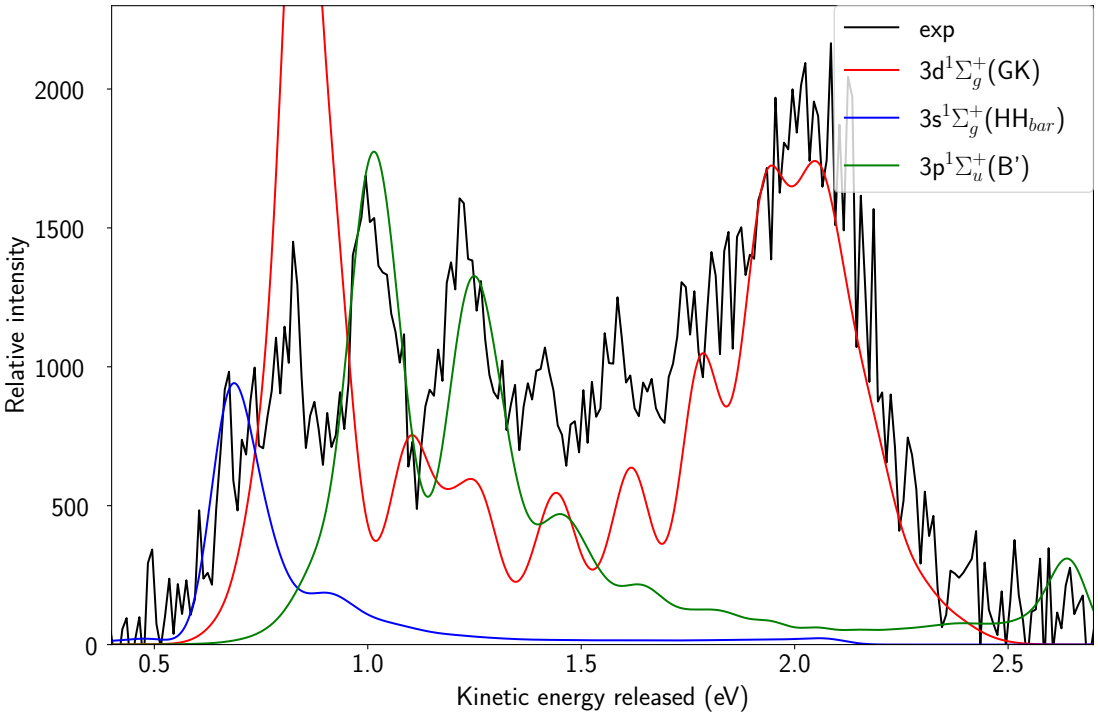

Figure 6.40: KER distributions computed with the method presented in Section 6.2.3. The different curves are multiplied by an arbitrary factor. The shape of the state $3d^1\Sigma_g^+(GK)$ looks like the one of the experimental curve above 1.3 eV.

to grow if the dependence of the cross section with the rovibrational level of D_2^+ is considered.

Finally, the rest of the experimental KER curve in the range 1.3 to 2.3 eV is expected to be mostly explained by $3d^1\Sigma_g^+(GK)$ with potential contributions from $3p^1\Sigma_u^+(B')$. This last statement is purely speculative and based only on results from the Franck-Condon principle (see Figure 6.10).

Improvements at the theoretical level are needed to be able to explain with certainty the experimental KER. The multi-channel Landau-Zener model needs to be extended to properly consider rovibrational excitation and to yield the partial cross sections for transitions from any vibrational level of D_2^+ to any vibrational level of any electronic level D_2^*. Moreover, this model needs a proper way to handle proximity of many crossings. Indeed, Liu et al. [30] only approaches the case when two crossings are close.

Chapter 7

Study of the dissociative mutual neutralization $D_2^+ + D^-$ based on the kinetic energy release

This Chapter focuses on the production of three neutral Deuterium atoms due to charge exchange between the molecular ion D_2^+ and the anion D^-:

$$D_2^+(v) + D^- \rightarrow D + D + D. \tag{7.1}$$

This mutual neutralization is indeed predicted to produce many dissociations to three neutral atoms [15]. Janev et al. [15] report that the state $H_2^+(v = 0) + H^-$ is coupled to all states of the molecule H_3 apart from the dissociative ground state. As a result of vibronic coupling with the dissociative ground state, the excited states of H_3 are unstable and they predissociate:

$$D_2^+(v) + D^- \rightarrow D_3^* \rightarrow D + D + D. \tag{7.2}$$

On the other hand, according to Janev et al. [15], the first excited state of H_3 can be highly populated due to $H_2^+(v = 0) + H^-$ collisions. This state may dissociates to $H_2(b^3\Sigma_u^+) + H$, where $H_2(b^3\Sigma_u^+)$ is the unbound state already discussed in Chapter 5. This process produces three Hydrogen atoms in their fundamental electronic state and is one channel explaining reaction (7.1):

$$D_2^+(v = 0) + D^- \rightarrow D_3^*(^2B_2) \rightarrow D_2(b^3\Sigma_u^+) + D \rightarrow D + D + D. \tag{7.3}$$

Another possible channel is the mutual neutralization of $D_2^+(v)$ and D^- to a predissociative excited D_2^* state:

$$D_2^+(v_i) + D^- \rightarrow D_2^*(v_j) + D \rightarrow D + D + D. \tag{7.4}$$

De Bruijn [27] and Janev et al. [15] indeed report that many excited states of H_2 are predissociative such as $D^1\Pi_u(v)$ and $d^3\Pi_u(v)$ for $v \geq 3$.

Finally, gerade $N = 2, 3$ triplet states are radiatively coupled with the unbound dissociative $D_2(b^3\Sigma_u^+)$ state:

$$D_2^+(v_i) + D^- \rightarrow D_2^*(N = 2, 3\ \Lambda_g; v_j) + D \rightarrow D_2(b^3\Sigma_u^+) + D \rightarrow D + D + D. \tag{7.5}$$

The goal of this Chapter is to confirm that a dissociative mutual neutralization process is observed at low collision energies and to identify the followed channel. This Chapter is organized as follows. The first section explains how the kinetic energy released by an event is computed from time and space measurements performed by the three detectors. The second section presents the used techniques to remove as much background as possible from the measurements data set. The third section is about the computation of the acceptance of the detection system. Finally, the last section discusses the Dalitz plot and the KER distributions computed from experimental data.

7.1 Computing from experimental measurements the kinetic energy released by the dissociation of an homogeneous three-body system

This section explains how the kinetic energy release (KER) is computed from measurements of the dissociation of a three-body system. The three bodies are assumed to have the same mass such that $m_1 = m_2 = m_3$.

Let t_1, t_2 and t_3 be the flight times of the bodies detected on the first, second and third detector, respectively. As explained in Chapter 2, the following data are provided by the experiment about a detected event: the positions of the impacts of the two bodies hitting the position-sensitive detectors in a laboratory frame centered at the position of the dissociation $\{(x_1, y_1, z_1), (x_2, y_2, z_2)\}$, the difference between the two detection times related to the position-sensitive detectors $dT_{12} = t_2 - t_1$ and the difference between the two detection times related to the first position-sensitive detector and to the position-insensitive detector $dT_{13} = t_3 - t_1$. Moreover, because the positions of the detection planes are known, z_3 is known too.

The velocities $\vec{V_i}$ of the three bodies in the laboratory frame are then:

$$\begin{cases} \vec{V_1} = \left(\frac{x_1}{t_1}, \frac{y_1}{t_1}, \frac{z_1}{t_1}\right), \\ \vec{V_2} = \left(\frac{x_2}{t_1+dT_{12}}, \frac{y_2}{t_1+dT_{12}}, \frac{z_2}{t_1+dT_{12}}\right), \\ \vec{V_3} = \left(\frac{x_3}{t_1+dT_{13}}, \frac{y_3}{t_1+dT_{13}}, \frac{z_3}{t_1+dT_{13}}\right). \end{cases} \tag{7.6}$$

Moreover, because the energy of the beam E_0 as well as the masses m_1, m_2, m_3 of the three bodies are known, the velocity of the center of mass in the laboratory frame V_{cm} can be computed:

$$E_0 = \frac{(m_1+m_2+m_3)V_{cm}^2}{2} \implies V_{cm} = \sqrt{\frac{2E_0}{m_1+m_2+m_3}}. \tag{7.7}$$

The direction of the velocity of the center of mass is the direction of the beam $\hat{z}$, therefore $\vec{V}_{cm} = (0, 0, V_{cm})$. Conservation of momentum implies $m_1\vec{V}_1 + m_2\vec{V}_2 + m_3\vec{V}_3 = (m_1+m_2+m_3)\vec{V}_{cm}$, and because the three bodies are identical $m_1 = m_2 = m_3$ and $\vec{V}_1 + \vec{V}_2 + \vec{V}_3 = 3\vec{V}_{cm}$:

$$\begin{cases} V_{1x} + V_{2x} + V_{3x} = 0, \\ V_{1y} + V_{2y} + V_{3y} = 0, \\ V_{1z} + V_{2z} + V_{3z} = 3V_{cm}. \end{cases} \iff \begin{cases} \frac{x_1}{t_1} + \frac{x_2}{t_1+dT_{12}} + \frac{x_3}{t_1+dT_{13}} = 0, \\ \frac{y_1}{t_1} + \frac{y_2}{t_1+dT_{12}} + \frac{y_3}{t_1+dT_{13}} = 0, \\ \frac{z_1}{t_1} + \frac{z_2}{t_1+dT_{12}} + \frac{z_3}{t_1+dT_{13}} = 3V_{cm}. \end{cases} \tag{7.8}$$

Equation (7.8) is composed of three equations with three unknowns x_3, y_3 and t_1. The unknowns x_3 and y_3 can be computed when knowing t_1:

$$\begin{cases} x_3 = -(t_1 + dT_{13})\left(\frac{x_1}{t_1} + \frac{x_2}{t_1+dT_{12}}\right), \\ y_3 = -(t_1 + dT_{13})\left(\frac{y_1}{t_1} + \frac{y_2}{t_1+dT_{12}}\right). \end{cases} \tag{7.9}$$

The unknown t_1 is found solving the last equation:

$$\begin{aligned} (t_1+dT_{12})(t_1+dT_{13})z_1 + t_1(t_1+dT_{13})z_2 + t_1(t_1+dT_{12})z_3 &= 3V_{cm}t_1(t_1+dT_{12})(t_1+dT_{13}), \\ t_1^2z_1 + z_1t_1(dT_{12}+dT_{13}) + dT_{12}dT_{13}z_1 + t_1^2z_2 + t_1dT_{13}z_2 + t_1^2z_3 + t_1dT_{12}z_3 & \\ = 3V_{cm}t_1(t_1^2 + t_1(dT_{12}+dT_{13}) + dT_{12}dT_{13}). & \end{aligned} \tag{7.10}$$

The variables $\alpha = dT_{12}dT_{13}$ and $\beta = dT_{12} + dT_{13}$ are introduced. The equation is a third degree polynomial:

$$-3t_1^3V_{cm} + t_1^2(z_1+z_2+z_3-3V_{cm}\beta) + t_1(z_1\beta + z_2dT_{13} + z_3dT_{12} - 3V_{cm}\alpha) + \alpha z_1 = 0. \tag{7.11}$$

Let's define $a = -3V_{cm}, b = z_1+z_2+z_3-3V_{cm}\beta, c = z_1\beta + z_2dT_{13} + z_3dT_{12} - 3V_{cm}\alpha$ and $d = \alpha z_1$. The polynomial becomes:

$$at_1^3 + bt_1^2 + ct_1 + d = 0. \tag{7.12}$$

The three possible solutions for this equation are:

$$t_1^I = \frac{\left(\sqrt{(-27a^2d+9abc-2b^3)^2+4(3ac-b^2)^3}-27a^2d+9abc-2b^3\right)^{1/3}}{3\ 2^{1/3}a} - \frac{2^{1/3}(3ac-b^2)}{3a\left(\sqrt{(-27a^2d+9abc-2b^3)^2+4(3ac-b^2)^3}-27a^2d+9abc-2b^3\right)^{1/3}} - \frac{b}{3a}, \quad (7.13)$$

$$t_1^{II} = -\frac{(1-i\sqrt{3})}{6\ 2^{1/3}a}\left(\sqrt{(-27a^2d+9abc-2b^3)^2+4(3ac-b^2)^3}-27a^2d+9abc-2b^3\right)^{1/3} + \frac{(1+i\sqrt{3})(3ac-b^2)}{3\ 2^{2/3}a\left(\sqrt{(-27a^2d+9abc-2b^3)^2+4(3ac-b^2)^3}-27a^2d+9abc-2b^3\right)^{1/3}} - \frac{b}{3a}, \quad (7.14)$$

$$t_1^{III} = -\frac{(1+i\sqrt{3})}{6\ 2^{1/3}a}\left(\sqrt{(-27a^2d+9abc-2b^3)^2+4(3ac-b^2)^3}-27a^2d+9abc-2b^3\right)^{1/3} + \frac{(1-i\sqrt{3})(3ac-b^2)}{3\ 2^{2/3}a\left(\sqrt{(-27a^2d+9abc-2b^3)^2+4(3ac-b^2)^3}-27a^2d+9abc-2b^3\right)^{1/3}} - \frac{b}{3a}. \quad (7.15)$$

For each solution, values for x_3 and y_3 are computed from Equation (7.9). Therefore, there are three possible sets of values for the unknowns t_1, x_3, y_3: $(t_1^I, x_3^I, y_3^I), (t_1^{II}, x_3^{II}, y_3^{II})$ and $(t_1^{III}, x_3^{III}, y_3^{III})$. These sets are used to compute from Equation (7.6) the possible velocities $(\vec{V}_1^I, \vec{V}_2^I, \vec{V}_3^I), (\vec{V}_1^{II}, \vec{V}_2^{II}, \vec{V}_3^{II})$ and $(\vec{V}_1^{III}, \vec{V}_2^{III}, \vec{V}_3^{III})$.

Among these mathematically valid solutions, the physical solution must comply to energy conservation. Because the binding energies are very small compared to the kinetic energies in play in the laboratory frame (the energy of a beam being around 10 keV), it is sufficient to check for kinetic energy conservation. Therefore, the set such that the kinetic energy is the best conserved, i.e. such that the quantity:

$$\Delta E_{cin} = \left| \sum_{i=1}^{3} \frac{m_i V_i^2}{2} - \left(\sum_{i=1}^{3} m_i \right) \frac{V_{cm}^2}{2} \right| \quad (7.16)$$

is minimized, is selected among the three possible ones.

In order to remove background from measurements, events such that the computed points (x_3, y_3) are outside the surface of the position-insensitive detector are removed

from the data set. For the remaining events, the velocities in the center of mass are computed as follows:

$$\vec{v}_i = \vec{V}_i - \vec{V}_{cm}. \tag{7.17}$$

Finally, the experimental KER is obtained:

$$\boxed{KER = \frac{1}{2}\left(m_1 v_1^2 + m_2 v_2^2 + m_3 v_3^2\right) = \frac{m_1}{2}\left(v_1^2 + v_2^2 + v_3^2\right).} \tag{7.18}$$

7.2 Background filtering

This section explains the followed method to remove as much background as possible from the data. Figure 7.1 is a plot of the whole initial data set of events in the dT_{12}/dT_{13} space. In this space, the area containing the signal is easily identified among areas with only background events. The total number of events is 52840.

Nearly almost all the events outside the red rectangle drawn in Figure 7.1 are pure background. A first filtering it then to discard all these events from the data set. There remain 23927 events after this first filtering. Then, a second filtering process applies depending on the computed positions for the position-insensitive detector. The coordinates (x_3, y_3) of the impact of a particle on the position-insensitive detector are computed from equations related to momentum conservation. When, for an event, the computed coordinates are not included in the position-insensitive detector area, the event is discarded.

A KER distribution, which gives the number of events detected with a particular KER, is computed from the remaining 11377 events. Since these events are composed of signal plus background, the contribution of the remaining background events to the KER distribution must still be removed.

The contribution of the remaining background events is evaluated as follows. A set of background events is selected from a different area of the dT_{12}/dT_{13} space (for example from the area in the green rectangle drawn in Figure 7.1). These events live in the same dT_{12} domain (roughly $dT_{12} \in [60, 210]$ ns) than the kept events, but in a different dT_{13} domain.

They are moved in the same dT_{13} domain performing a rotation by an angle θ in the dT_{12}/dT_{13} space (see Figure 7.1), then a translation in the direction $\widehat{dT}_{13}$. In other words, the values for dT_{12} and dT_{13} of the background events are modified to match the values of the kept events, while the values for (x_1, x_2, y_1, y_2) of the background events are not changed. Finally, a KER distribution is computed from these modified background events and subtracted from the KER distribution computed from the signal plus background events (events in the red rectangle in Figure 7.1), yielding the KER distribution $N_{exp}(\text{ker})$.

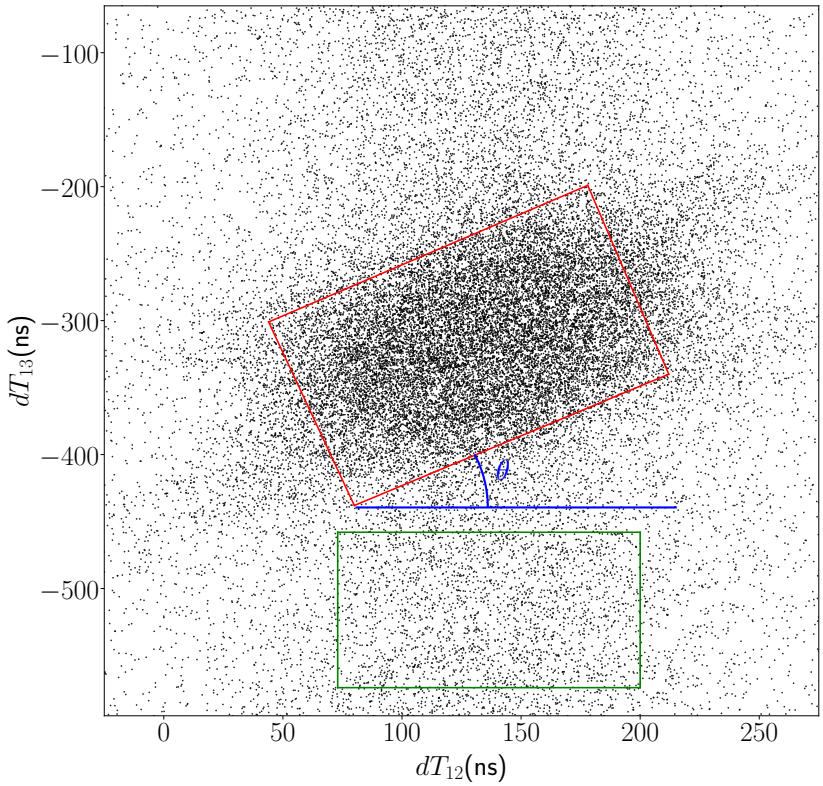

Figure 7.1: Plot of the initial data set of events in the dT_{12}/dT_{13} space. The area inside the red rectangle is composed of signal plus background. The area in the green rectangle is only composed of background events.

7.3 Acceptance of the three-body detection system

Because the detection system only covers a fraction of the surface which encompasses the area where dissociations occur, some events are not detected (see Figure 7.2). Indeed, the corresponding fragments miss the detection system. The acceptance of the detection system is the number of events detected over the total number of events. Experimentally computed KER must be corrected depending on this acceptance to take into account missed events due to the limited solid angle covered by the detection system. This section explains how this acceptance, which is a function of the KER, is computed for the three-body detection system.

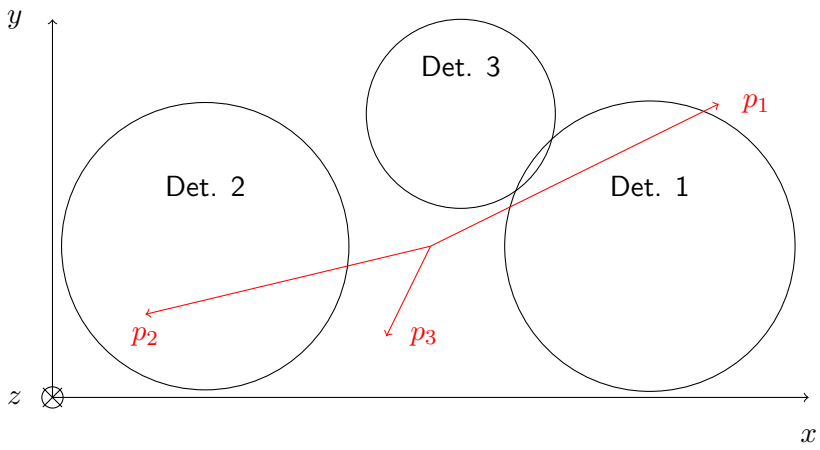

Figure 7.2: Because the detection system only covers a small solid angle, some valid events are not detected. In this Figure, the three black circles are the three detectors. The particle p_2 hits the detector Det. 2, but the particles p_1 and p_3 miss the detectors Det. 1 and Det 3. Therefore, this valid event is not detected. The KER of the generated event is 5.9 eV.

The acceptance is computed by simulation. The idea is, for the whole range of KER of interest, to generate a high number of events with a random distribution of velocities. The generated events must of course satisfy momentum and energy conservation. Then, knowing the geometries of the detection system as well as the beam energy and the velocities of the generated events, the software checks if the generated events would be detected by the detection system. In other words, the software checks if the trajectories followed by the fragments intersect the three detection planes in such a way that this event is considered as valid (see Figure 7.3). Finally, summing the number of detected events for each value of KER then dividing by the total number of events generated for each value of KER, a function giving the acceptance depending on the KER is obtained.

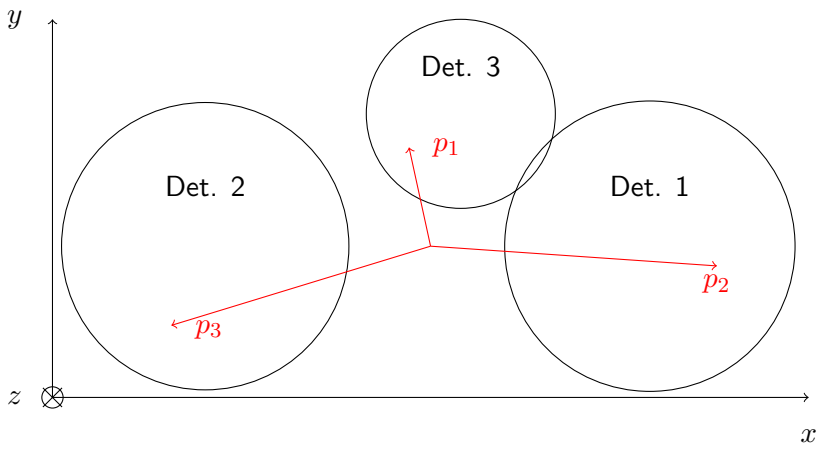

Figure 7.3: Example of detected event, each particle hit a different detector. The KER of the generated event is 3 eV.

The events are generated as follows. The components of the velocities in the center of mass frame $\vec{v}_1$ and $\vec{v}_2$ of the two first particles 1 and 2 are generated using an uniform distribution for each component (see Figure 7.4). The uniform distribution returns randomly a value in the range $[-1, 1]$.

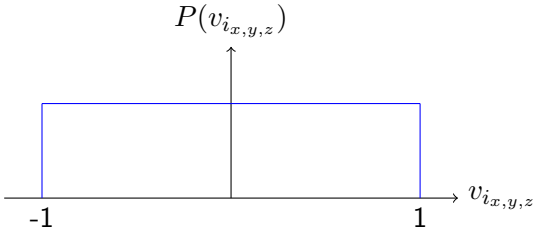

Figure 7.4: Uniform distribution over the domain $[-1, 1]$.

Because, by definition of the center of mass frame:

$$\sum_{i=1}^{3} m_i \vec{v}_i = 0, \tag{7.19}$$

the velocity of the third particle must be:

$$\vec{v}_3 = -\vec{v}_1 - \vec{v}_2. \tag{7.20}$$

Unfortunately, by computing the third velocity with this method, the distribution for $\vec{v}_3$ is not uniform. Indeed, $\vec{v}_3$ is obtained summing two uniform variables and the sum of two uniform distributions is not an uniform distribution (see Figure 7.5). The resulting

distribution covers the domain $[-2, 2]$ and has a triangular shape. Therefore, the distribution of generated events would not represent the physical reality, and the computation of the acceptance would be biased.

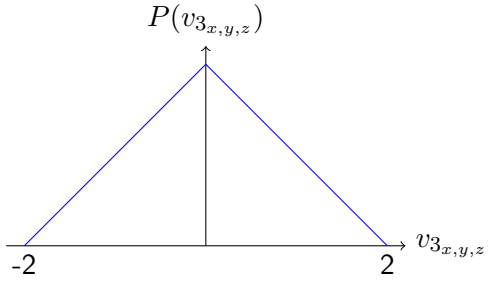

Figure 7.5: Sum of two uniform distributions over the domain $[-1, 1]$. This sum is not an uniform distribution.

A first solution is to generate the components of $\vec{v}_3$ in the same way than the components of $\vec{v}_1$ and $\vec{v}_2$, then only keeping the events such that $\vec{v}_3 = -\vec{v}_1 - \vec{v}_2 + \Delta$, where Δ is a sufficiently small violation of momentum conservation. Unfortunately, this method is very inefficient and only allows to generate a few events by minute.

A second solution is to keep the events such that:

$$\sum_{i=1}^{3} v_i^2 < c, \tag{7.21}$$

where c is a constant, and to discard the other generated events. The constant c has been selected by a try-error process until the resulting $\vec{v}_3$ distribution appears to be uniform. The used value is $c = 1$. This filter only keeps events such that the components of $\vec{v}_3$ are close to zero (see Figure 7.6). In other words, the distribution of $v_{3_{x,y,z}}$ is only used in the domain where the distribution is nearly uniform, i.e. where the triangular-shaped distribution may be well approximated by a rectangle. Indeed, from Equation (7.21) $\vec{v}_3$ must comply to:

$$v_3^2 < 1 - v_1^2 - v_2^2 \Leftrightarrow ||\vec{v}_3|| < \text{Real}\left(\sqrt{1 - v_1^2 - v_2^2}\right). \tag{7.22}$$

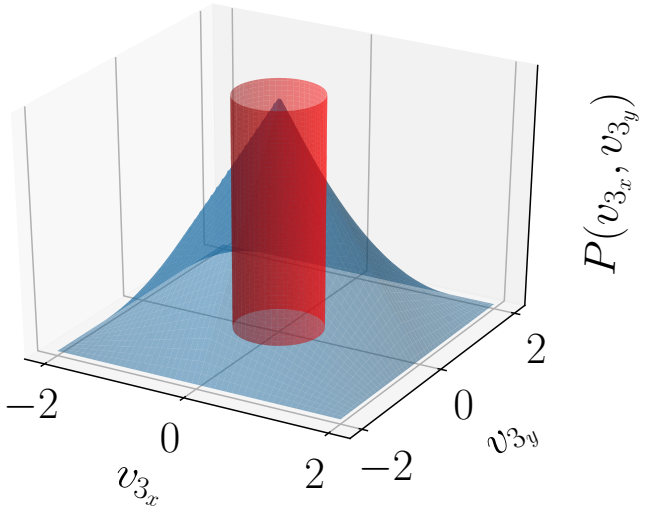

Figure 7.6: In blue is represented the probability to generate an event for which the x and y components of the velocity of the third particle are v_{3_x} and v_{3_y}. Events with v_{3_x} and v_{3_y} values falling inside the red cylinder are kept, the other events are discarded. The radius of the red cylinder has been set to $1/\sqrt{3}$ for illustration purposes, in general this radius depends on v_1, v_2 and v_{3_z}.

Therefore, the vector $\vec{v}_3$ is confined in a sphere whose radius r is $r = \text{Real}\left(\sqrt{1 - v_1^2 - v_2^2}\right)$ in the space $(\hat{x}, \hat{y}, \hat{z})$. The maximum possible value for v_3 occurs when $v_1 = v_2 = 0$. In this case:

$$v_3^2 < 1 \Leftrightarrow v_3 < 1. \tag{7.23}$$

Therefore, the components of $\vec{v}_3$ are confined in the domain $[-1, 1]$ like the components of $\vec{v}_1$ and $\vec{v}_2$.

If $v_{3_z} = 0$, the distribution $P(v_{3_x}, v_{3_y})$ can be drawn in a 3D plot. Figure 7.6 shows that in this case, the applied filter is equivalent to restrict the use of the distribution in a cylindrical area centered at $(v_{3_x} = 0, v_{3_y} = 0)$. If this area is sufficiently small, the distribution for $\vec{v}_3$ is uniform in good approximation.

The 2D histogram Dalitz plot presented in Figure 7.7 shows that the different possible distributions of the kinetic energy released among the three particles are covered with same probability.

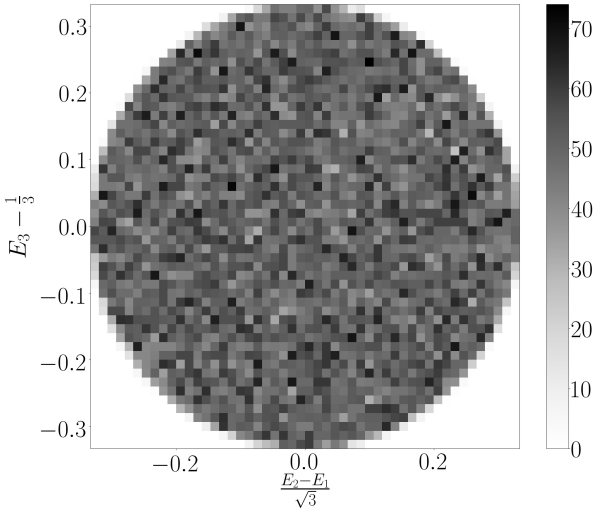

Figure 7.7: Two-dimensional histogram of the Dalitz plot of 10^5 generated events for which the kinetic energy released is 3 eV. This plot shows that the different possible distributions of the kinetic energy released among the three particles are covered with same probability: there seems to be no big area of the circle with more events than others. There are however local differences between adjacent tiles which are expected to disappear when the number of generated events tends to infinity.

Now that the components of the velocities are generated uniformly, velocities must be modified for the kinetic energy in the center of mass of the generated events to match the desired KER. Velocities must be scaled by a coefficient α such that (remember that the three particles have same mass m in the current experiment):

$$\alpha^2 \frac{m}{2}(v_1^2 + v_2^2 + v_3^2) = \text{ker} \implies \alpha = \sqrt{\frac{2 \text{ KER}}{m(v_1^2 + v_2^2 + v_3^2)}}. \tag{7.24}$$

The final velocities are $\vec{v}_{i_{\text{final}}} = \alpha \vec{v}_i$. The velocities in the laboratory frame of the generated events are:

$$\vec{V}_i = \vec{v}_{i_{\text{final}}} + \vec{V}_{cm}, \tag{7.25}$$

with $\vec{V}_{cm} = \sqrt{\frac{2E_0}{m_1+m_2+m_3}}\hat{z}$, E_0 being the beam energy. From the velocities in the laboratory frame, the trajectories of the three particles can be tracked from the location of the dissociation. If each trajectory intersects the plane of a different detector, the event is considered as detected. The acceptance a is then finally obtained (a plot of the acceptance is shown in Figure 7.8):

$$a(\text{ker}) = \frac{\text{number of detected events(ker)}}{\text{number of generated events(ker)}}. \tag{7.26}$$

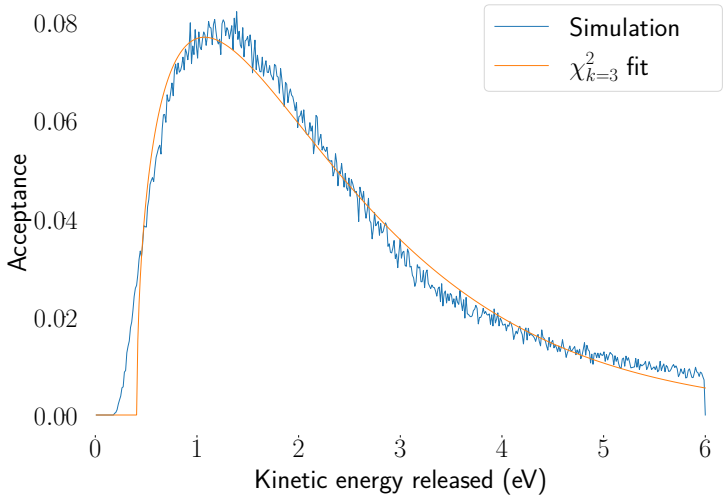

Figure 7.8: Acceptance as a function of the KER for the three-body detection system.

The experimentally obtained KER distribution $N_{exp}(\text{ker})$, which gives the number of events detected with a particular KER, is corrected with the acceptance as follows:

$$N(\text{ker}) = \frac{N_{exp}(\text{ker})}{a(\text{ker})}. \tag{7.27}$$

7.4 Results and discussion

This section presents and discusses the Dalitz plot composed of the events remaining after background removal (see Figure 7.9) as well as plots of KER distributions.

Galster et al [33] report that the Dalitz plots of the predissociation of H_3 and D_3 are composed of structured patterns. These patterns reveal preferred momentum distributions. On the contrary, the Dalitz plot in Figure 7.9 does not reveal such patterns. This excludes the predissociation (reactions (7.2) and (7.4)) as the main processes taking part in the production of these fragments. Another possible explanation is the disappearance of these structures observed for well defined D_3 rovibrational states due to the broad vibrational distribution of D_2^+.

The events density is higher in the area of the Dalitz plot corresponding to low normalized kinetic energies of the third particle $E_3 < 1/3$ (see Figure 7.9a). Indeed, 77% of the

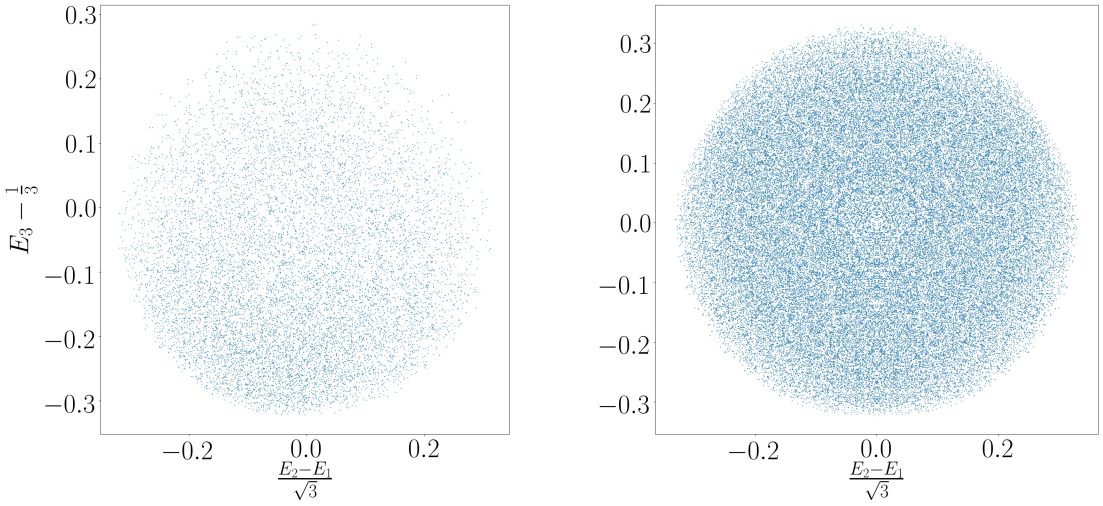

(a) For this Dalitz plot, E_1, E_2 and E_3 referred to the normalized kinetic energies of the particles detected on the first, second and third detector, respectively.

(b) This Dalitz plot is obtained summing the contributions of the six possible permutations between E_1, E_2 and E_3: $\{E_1 \leftrightarrow$ detector 1, $E_2 \leftrightarrow$ detector 2, $E_3 \leftrightarrow$ detector 3$\}$, $\{E_1 \leftrightarrow$ detector 2, $E_2 \leftrightarrow$ detector 1, $E_3 \leftrightarrow$ detector 3$\}$,...

Figure 7.9: Dalitz plots composed of events remaining after the noise removal.

events are located below the line $E_3 = 1/3$ in the Dalitz plot (see Figure 7.9). This may be explained by geometrical arguments. Firstly, the third detector is smaller than the first and second detectors. Therefore, the third detector misses more particles with high velocities in the directions parallel to the detector plane (i.e. v_{3_x} and v_{3_y}). Secondly, the first detector is slightly shadowed by the third detector. Due to this, events with low energies E_1 and high energies E_2 and E_3 may be missed out, slightly altering the observed distribution. Note that the differences in the measured KER distribution due to the geometrical properties of the detection system are corrected by the acceptance. However the Dalitz plot in Figure 7.9 has not received such corrections. This non-uniform behavior disappears when summing all possible permutations between E_1, E_2 and E_3 (see Figure 7.9b).

When an histogram of the Dalitz plot presented in Figure 7.9a is divided by the acceptance, an homogeneous distribution of events in the Dalitz plot is more or less retrieved (see Figure 7.10b). It's an argument in favor of the correctness of the acceptance computation.

Figure 7.11 shows that the acceptance correction increases the slope of the distribution without altering its overall shape. Figure 7.12 shows that, due to the low number of events detected experimentally, the quantity of background in measurements is signifi-

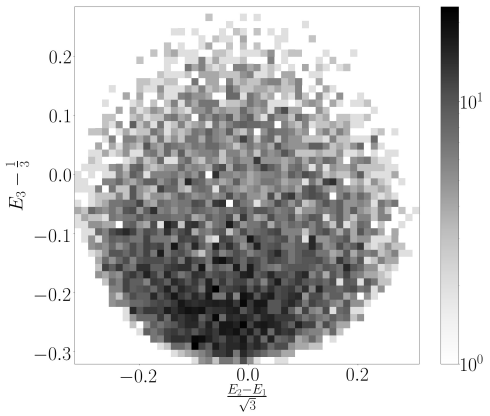

(a) Histogram of the Dalitz plot presented in Figure 7.9a.

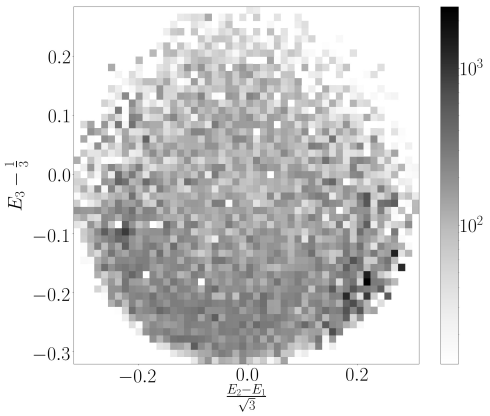

(b) Histogram of the Dalitz plot presented in Figure 7.9a weighted by the inverse of the acceptance.

cant. The influence of background is more problematic in low acceptance area.

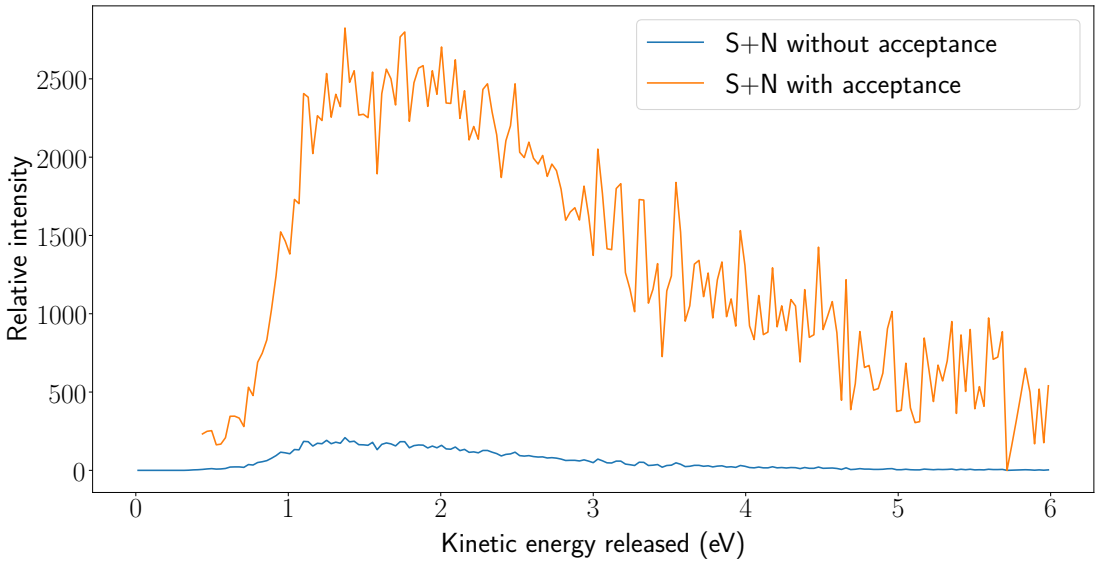

Figure 7.11: Distribution of kinetic energy released by events in the kept area of the dT_{12} /dT_{13} space (red rectangle in Figure 7.1). In blue and orange are plotted the distributions not corrected and corrected by the acceptance a, respectively.

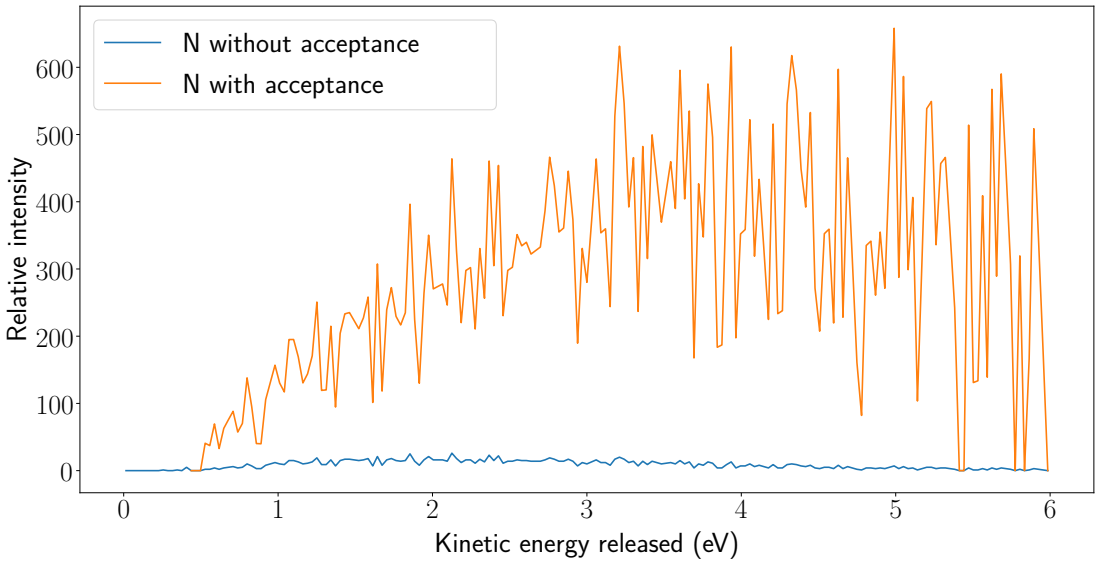

Figure 7.12: Distribution of kinetic energy released by background events (translated green rectangle in Figure 7.1). In blue and orange are plotted the distributions not corrected and corrected by the acceptance a, respectively.

Figure 7.13 presents the final KER distribution obtained after removing the estimated contribution of background events from the KER distribution. Since there is no sharp peak in the distribution, this is not a predissociation process. The observed process is a dissociation to the continuum. All kinetic energies between 0 and approximately 4 eV are possible, the most probable being around 1.5 eV.

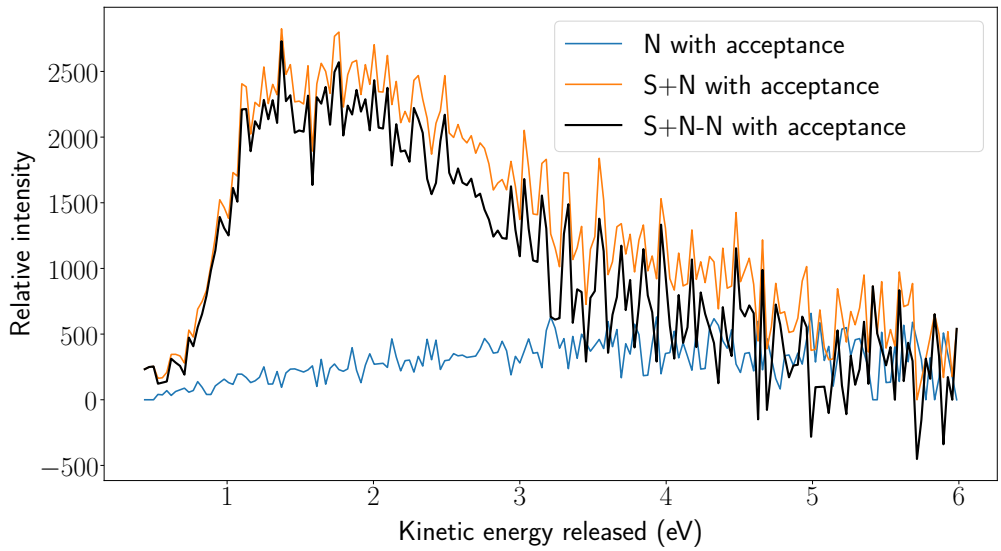

Figure 7.13: Plot of the KER distributions produced by background events (in blue) and by all events in the kept area of the dT_{12} /dT_{13} space (in orange). The black curve is the KER distribution of all events in the kept area of the dT_{12} /dT_{13} space minus the contribution of the background events. For all KER distributions, acceptance correction has been applied.

Figure 7.14 shows, for each detector, the kinetic energy distribution of the detected particles. The distributions related to the first and second detectors are very similar with maxima around 0.6 and 0.95 eV. Because the third detector is smaller than the two others, its distribution is less spread and much more concentrated near 0 eV, with maxima around 0.2 and 0.45 eV.

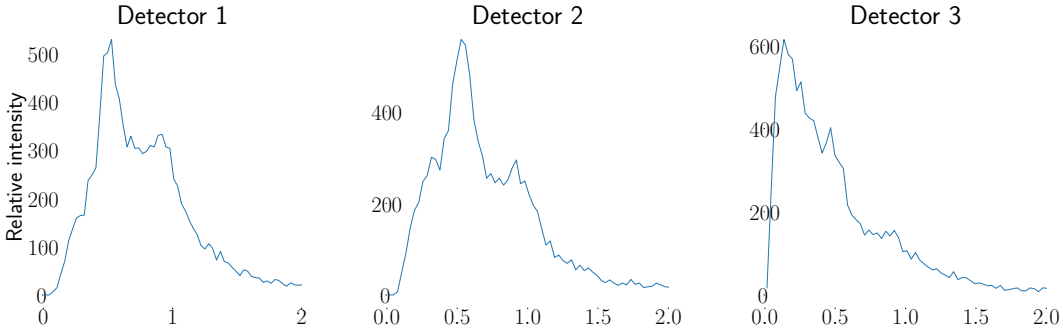

Figure 7.14: Distribution of the kinetic energy (eV) of the particles detected on each detector (only valid events have been counted).

The observed KER distributions may be explained by reactions (7.3) or (7.5). Both these channels transit by:

$$\mathrm{D}_2(\mathrm{b}^3\Sigma_\mathrm{u}^+) + \mathrm{D} \rightarrow \mathrm{D} + \mathrm{D} + \mathrm{D}. \tag{7.28}$$

However, in this experiment, the distance between the two ions D_2^+ and D^- is most often higher than the equilibrium distance of the equilateral H_3 system. Indeed, let b_{max} be the maximum impact parameter, the cross section is proportional to πb_{max}^2. Therefore, much less events would be observed if the smaller distances would responsible for most of the observed signal. It follows that reaction (7.5) is expected to be the main process explaining the three-body signal:

$$\mathrm{D}_2^+(\mathrm{v_i}) + \mathrm{D}^- \rightarrow \mathrm{D}_2^*(\mathrm{N} = 2, 3\ \Lambda_\mathrm{g}; \mathrm{v_j}) + \mathrm{D} \rightarrow \mathrm{D}_2(\mathrm{b}^3\Sigma_\mathrm{u}^+) + \mathrm{D} + \gamma \rightarrow \mathrm{D} + \mathrm{D} + \mathrm{D} + \gamma. \tag{7.29}$$

Because the passage from the state D_2^* to the state $\mathrm{D}_2(\mathrm{b}^3\Sigma_\mathrm{u}^+)$ is a radiative transition, the energy and momentum conservation laws assumed in Section 7.1 are not valid. Fortunately, because the energy E_γ carried away by the photon is only around 4 eV, this energy is negligible with regard to the kinetic energies of the Deuterium atoms in the laboratory frame. Moreover, the momentum p_γ of the photon is also negligible with regard to the momentum p_a of the Deuterium atom in the center of mass frame. Indeed:

$$E_\gamma = h\nu = \frac{hc}{\lambda} = p_\gamma c \approx 4 \text{ eV} \implies p_\gamma \approx \frac{4 \text{ eV}}{c} \approx 2\ 10^{-27} \text{ kg m/s}, \tag{7.30}$$

$$E_D \approx 1 \text{ eV} = \frac{p_a^2}{2m_D} \implies p_a \approx \sqrt{2m_D E_D} = 3\ 10^{-23} \text{ kg m/s}, \tag{7.31}$$

where h is the Planck's constant, ν the frequency of the photon, c the speed of light, λ the wavelength of the photon, E_D a plausible kinetic energy of the Deuterium atom and m_D the mass of a Deuterium atom.

Figure 7.14 shows KER distributions composed of a contribution from a dissociation to the continuum as well as a few peaks. The two Deuterium atoms produced by the dissociation of the state $\mathrm{D}_2(\mathrm{b}^3\Sigma_\mathrm{u}^+)$ are responsible for the continuum part (see Figure 7.15). The observed peaks in Figure 7.14 are then explained by the released first Deuterium atom in Equation (7.28).

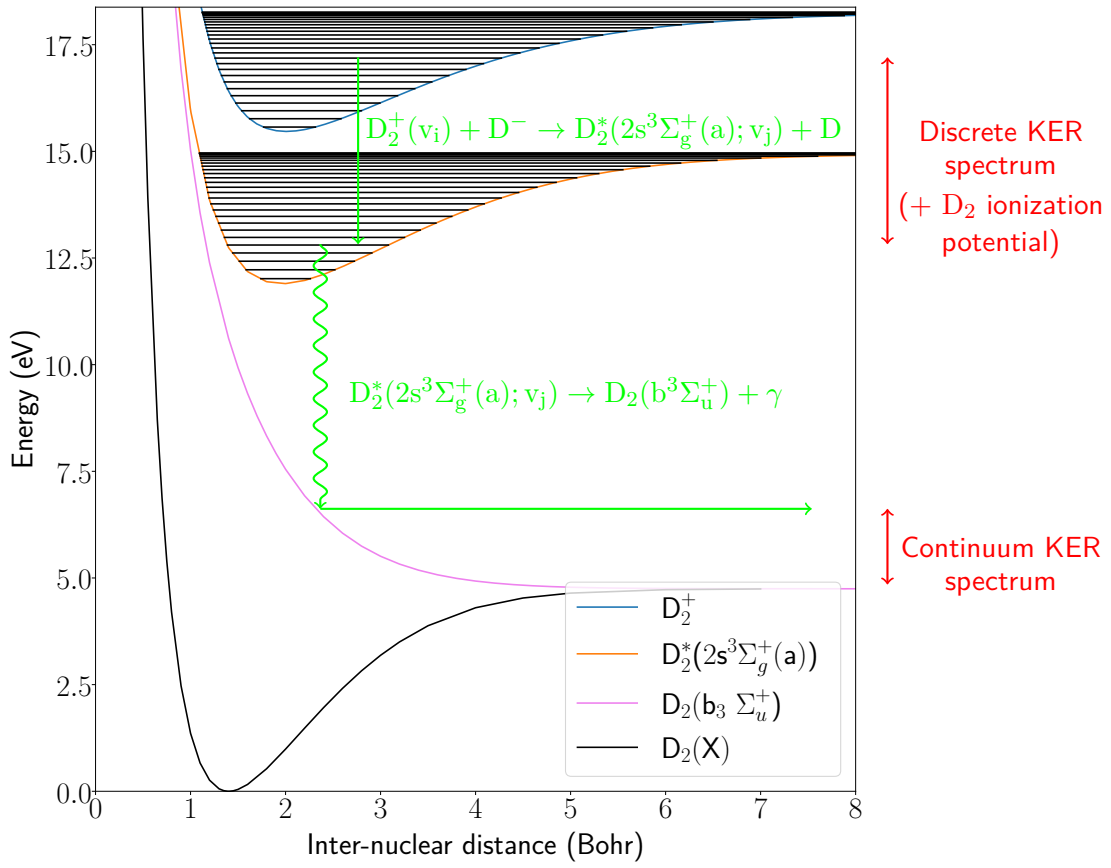

Figure 7.15: Vibrational levels of gerade $N = 2, 3$ triplet states like $D_2^*(2s^3\Sigma_g^+(a))$ are first populated due to the mutual neutralization of D_2^+ with D^-. This first transition explains the discrete peaks in the KER distributions presented in Figure 7.14. Then, the state $D_2^*(2s^3\Sigma_g^+(a))$ dissociates due to radiative coupling with the state $D_2(b^3\Sigma_u^+)$. This second transition explains the continuum part of the KER spectra presented in Figure 7.14.

Indeed, the energies of the reagents $D_2^+(v_i)$ and D^- as well as of the product D_2^* are obviously discrete energy levels. Therefore, by energy conservation, the energy of the released first D atom is:

$$E(D) = E(D_2^+(v_i) + D^-) - E(D_2^*). \tag{7.32}$$

Because being the difference of two discrete energy spectra, the possible values for $E(D)$ also produce a discrete energy spectrum.

7.5 Conclusion

In this Chapter, measurements of three-particles events produced by the mutual neutralization of D_2^+ with D^- have been analyzed and interpreted.

Firstly, it was shown that finding out the KER and the velocities of the three particles from spatial knowledge about only two of the three particles is possible using equations given by momentum and energy conservation.

Secondly, only background areas in the time-of-flight space (dT_{12}/dT_{13}) have been located and used to subtract contributions from background to the experimental KER spectrum. Thirdly, a software has been developed to compute the acceptance of the three-body detection system by numerical simulation.

Finally, the background and acceptance-corrected experimental KER spectrum has been analyzed. This three-body KER has the mark of a dissociation to the continuum process. However, peaks appear in the per-detector KER spectra.

It follows that the main process involved in the three-body events production is expected to be the mutual neutralization of D_2^+ and D^- to gerade $N = 2, 3$ triplet states of D_2^* radiatively coupled to the dissociative state $D_2(b^3\Sigma_u^+)$. It was explained that the mutual neutralization to gerade $N = 2, 3$ triplet states of D_2^* indeed justifies the peaks in the per-detector KER spectra while the radiative coupling to the dissociative state explains the continuum-like shape of the three-body KER spectrum.

Conclusion and Future work

This section presents additional thoughts about the obtained results and ideas to go beyond the work done. A summary of the whole contribution has already been presented at the end of the introduction.

In this work, the mutual neutralization of $D_2^+(v)$ with D^- has been studied. A first conclusion is the difficulty to interpret the results due to the huge number of input and output channels. The input channels are the 28 vibrational states of $D_2^+(v)$, all populated in different proportions.

The output channels are all possible combinations of $D_2(X, v')$ vibrational levels (21) and D_n^* excited electronic levels (7 considered) in the output channel $D_2(X, v') + D_n^*$, plus all possible pairs of electronic and vibrational levels of $D_2^*(\Lambda, v')$ in the output channel $D_2^*(\Lambda, v') + D$.

The number of different excited electronic states Λ considered in this work is 21, not all possible Λ have been considered, in particular Δ states have been ignored. The situation is still worse if the rotational populations of D_2^+, D_2, D_2^* are considered. Moreover, the possibility for the system to switch between input channels $D_2^+(v) + D^- \rightarrow D_2^+(v' \neq v) + D^-$ have not been considered either.

Available theoretical models are far from being able to compute the partial cross sections of the different transitions. Indeed, for the reaction $D_2^+(v) + D^- \rightarrow D_2(X, v') + D_n^*$, Eerden et al. [29] only present a maximum total cross section $\sigma(n)$ for each electronic level n of D_n^*, while a function yielding the cross section for each possible transition $\sigma(v, n, v')$ is needed to compare rigorously their theoretical computations with our experimental measurements.

For the reaction $D_2^+(v) + D^- \rightarrow D_2^*(\Lambda, v') + D$, Liu et al. [30] only consider six excited electronic states. Moreover, they separate the singlet and triplet states in their multichannel Landau-Zener model, which seems unjustified. They do not consider the excited rovibrational levels in the input and output channels.

Furthermore, the model requires that subsequent crossings between the input ionic curve and the output covalent curves are separated by a minimal distance. They only propose a way to deal with two close crossings. However, when considering more than twenty excited electronic states with all their vibrational levels, all crossings are close to other crossings and the proper way to deal with this difficulty is unclear.

On the other hand, the way some parameters of their model must be computed, like the electron binding energy in D_2 referred as E_A in their paper and the orbital angular momentum of the electron λ at the united atom limit, when vibrational states are considered, is not crystal-clear either.

Indeed, defining λ at the united atom limit may not always be representative of the electronic state at large internuclear distances. Tests revealed that changing the value of λ has a substantial impact on the computed partial cross sections. Progress must be achieved from the theoretical side, at least to refine the definition of these parameters to the vibrationally excited case.

Moreover, to our knowledge, there exists no theoretical attempt to compute partial cross sections considering output channels of the two reactions $D_2^+(v) + D^- \rightarrow D_2(X, v') + D_n^*$ and $D_2^+(v) + D^- \rightarrow D_2^*(\Lambda, v') + D$ in the same model. In this work, output channels of the reaction $D_2^+(v) + D^- \rightarrow D_2(X, v') + D_n^*$ have been added to the multi-channel Landau-Zener of Liu et al. [30]. Results show negligible cross sections for these output channels with respect to cross sections for reaction $D_2^+(v) + D^- \rightarrow D_2^*(\Lambda, v') + D$.

However, because the transferred electron is the 1s of D^- and not its weakly bound one, the Landau-Zener model may be inappropriate to describe the reaction $D_2^+(v) + D^- \rightarrow D_2(X, v') + D_n^*$. Eerden et al. [29] nonetheless use this model to compute the cross section of this reaction.

On the experimental side, producing molecular ions D_2^+ only in their ground vibrational state is too difficult. It is unfortunate, because performing this experiment with ground state D_2^+ would remove complexity from the experimental KER spectrum and simplify its analysis.

Despite this difficulties, some advancements have been made. Both computations from the Franck-Condon principle and the multi-channel Landau-Zener model show that the singlet states $3s^1\Sigma_g^+(H\bar{H}), 3d^1\Sigma_g^+(GK)$ and $3p^1\Sigma_u^+(B')$ are essential to explain the experimental KER.

Indeed, the only state other than $3s^1\Sigma_g^+(H\bar{H})$ contributing to the peak around 0.7 eV in the KER spectrum is $3p^1\Pi_u(D)$, a state explicitly reported by De Bruijn [27] as predissociative. There are no other non-predissociative states than $3d^1\Sigma_g^+(GK)$ and $3p^1\Sigma_u^+(B')$ able to explain the peaks around 0.8, 1 and 1.25 eV.

Moreover, the shape of the KER computational spectrum yielded by the reaction $D_2^+(v) + D^- \rightarrow D_2(X, v') + D_n^*$ really does not match the experimental KER. This, with the fact that the experimental KER spectrum up to 1.3 eV is well explained by the excited D_2 output channel, exclude the excited D_n^* output channel to be the dominant one. This would be consistent with the fact that the reaction $H^+ + H^- \rightarrow H^* + H$ is known to be favored over $H^+ + H^- \rightarrow H + H^*$, i.e. the atom receiving the electron becomes the excited one.

Still, the unexplained part of the experimental KER spectrum between 1.3 and 2.3 eV is a thorny problem. The high number of events in this KER range is hard to understand

because transitions yielding these high KER involve sparsely populated D_2^+ vibrational levels. Four main hypotheses are left to be studied in a future work.

As explained in more details in Section 6.3, a first possible explanation would be an increase of the cross section with the increase of the vibrational excitation of D_2^+. Such phenomenon is reported to have a huge impact on the cross sections of other reactions such as the photodissociation and electron impact dissociation of D_2^+. This effect is not taken into account in the multi-channel Landau-Zener model.

A second explanation, less plausible, would be that the experimental KER is explained by the two reactions. Up to 1.3 eV it would be explained mainly by the reaction $D_2^+(v) + D^- \rightarrow D_2^*(\Lambda, v') + D$ and above 1.3 eV mainly by the reaction $D_2^+(v) + D^- \rightarrow D_2(X, v') + D_n^*$. This last reaction is indeed able to populate the KER spectrum in this range, in particular the output channel to $n = 2$ (see Figures 6.5, 6.6 and 6.7). This would imply that the multi-channel Landau-Zener model is indeed unfit to compute partial cross sections of this last reaction, because it predicts negligible cross sections for this one. Its cross section $\sigma(v, n, v')$, unknown to date, would for one reason or the other, be negligible for KER up to 1.3 eV and high above.

A third possibility is the presence of channels increasing the vibrational population of D_2^+ before its mutual neutralization with D^- in the interaction region. For example:

$$D_2^+(v_i) + H_2(v_0) \rightarrow D_2^+(v_f > v_i) + H_2(v_0'), \tag{7.33}$$

$$D_2^+(v_i) + D^- \rightarrow D_2^+(v_f > v_i) + D^-, \tag{7.34}$$

$$D_2^+(v_i) + D^- \rightarrow D_3^* \rightarrow D_2^+(v_f > v_i) + D + e, \tag{7.35}$$

the study of the existence and plausibility of such channels or other possible channels is left for future work. The first channel is not expected to be the explanation because the D_2^+ vibrational population has been measured by Urbain et al. [22] in the same machine with likely the same background gas. The third one is not much probable because, as already explained, formation of D_3 requires shorter distances between D_2^+ and D^- than the ones expected in the experiment. Contrariwise, the second one may happen in this experiment, and not in the one performed to measure the D_2^+ vibrational population by Urbain et al. [22], because the negative ions beam in this last experiment was O^- instead of D^-. However, the low density of the beams ($< 10^5$ particles per cm^3) renders multiple collisions very unlikely.

Finally, a last hypothesis is the contamination of the two-body KER measurements by three-body events (see Figure 7.16). Indeed, the study of the dissociative mutual neutralization of D_2^+ with D^- revealed the presence of many atomic Deuterium pairs hitting in coincidence the two position-sensitive detectors.

Figure 7.16 shows background from three-body events in the two-body KER. A lot of background events above 1.3 eV are observed. Shapes of the red and green curves do not match the experimental curve, but some background filtering techniques applied on the experimental KER have not been applied on those curves.

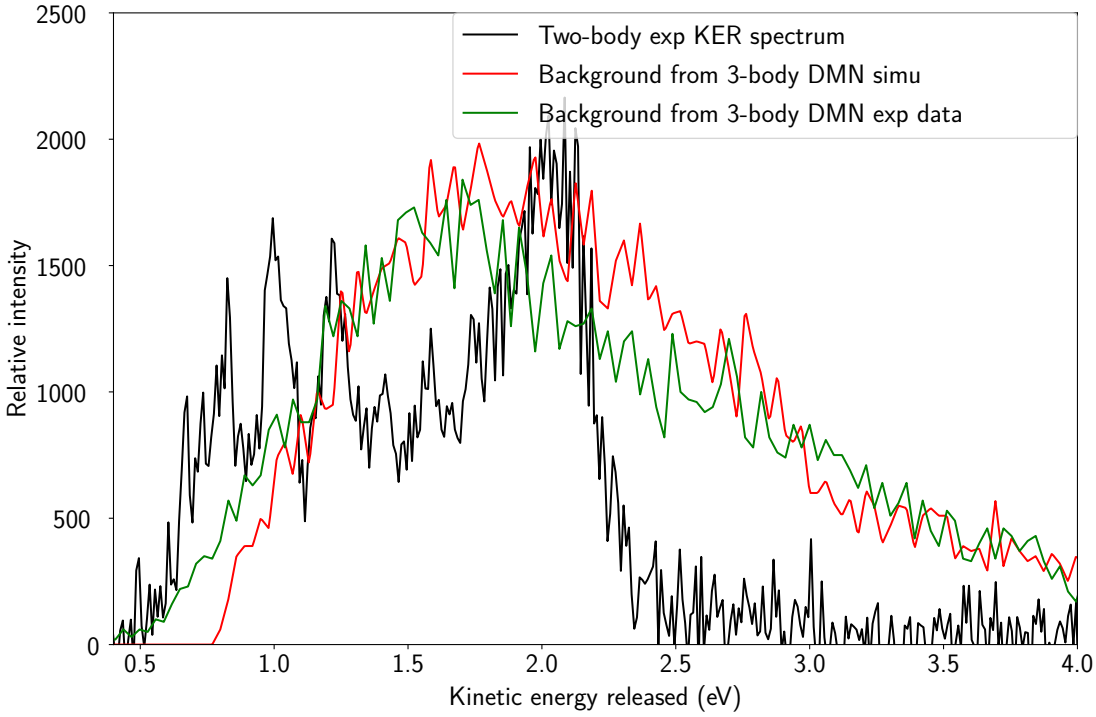

Figure 7.16: Background in the two-body KER spectrum due to two Deuterium atoms produced by the dissociative mutual neutralization of $D_2^+ + D^- \rightarrow D + D + D$. The background in red has been computed by software-assisted simulation: all generated three-body events valid the momentum conservation check associated to the process $D_2^+ + D^- \rightarrow D_2^* + D$. The background in green is obtained from all measured three-body events, most of them not satisfying this momentum conservation check. Measurements from the two position-sensitive detectors are treated like two-body $D_2^* + D$ events to produce the green and red curves. These curves have been multiplied by arbitrary factors.

The green curve is simply the two-body KER obtained when considering the measurements of three-body events on the two position-sensitive detectors as two-body events. The red curve has been obtained by simulation. Three-body events have been generated with a half-circle three-body KER distribution (see Figure 7.17). This distribution is an approximation by the half-circle analytical formula of the measured three-body KER distribution presented in Figure 7.13.

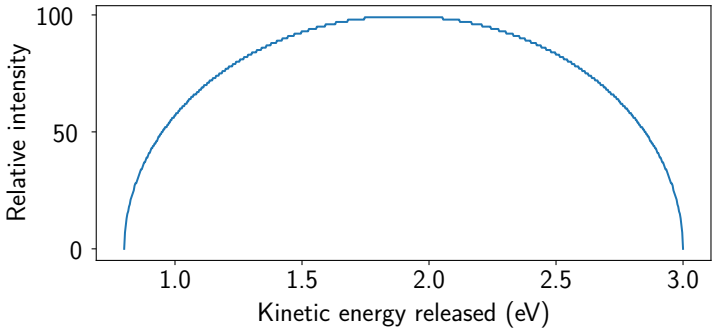

Figure 7.17: Half-circle shaped three-body KER distribution used to generate the three-body events yielding the two-body KER red curve in Figure 7.16.

Velocities $(\vec{v_1}, \vec{v_2}, \vec{v_3})$ in the center of mass frame of the three-body generated events satisfy by construction the momentum conservation check associated with the two-body events $D_2^* + D$, in addition to their own momentum conservation constraint. Velocity of the first particle $\vec{v_1}$ is generated randomly such that each component lies between -1 and 1. Then $\vec{v_2}, \vec{v_3}$ are obtained as follows:

$$\vec{v_2} = -\vec{v_1}/2 \quad \vec{v_3} = -\vec{v_1} - \vec{v_2}. \tag{7.36}$$

Velocities are then scaled by the same factor to produce the desired three-body KER. They satisfy both $D_2^+ + D^- \rightarrow D + D + D$ and $D_2^+ + D^- \rightarrow D_2^* + D$ momentum conservation equations:

$$\begin{cases} \vec{v_1} + \vec{v_2} + \vec{v_3} = \vec{v_1} - \vec{v_1}/2 - \vec{v_1} + \vec{v_1}/2 = 0, \\ \vec{v_1} + 2\vec{v_2} = \vec{v_1} - \vec{v_1} = 0, \end{cases} \tag{7.37}$$

where the velocity $\vec{v_2}$ is associated to the heavier particle (i.e. D_2^*). Red curve in Figure 7.16 is the two body KER spectrum produced by these events when treating the (D, D) pair as (D_2^*, D) when computing the KER.

This shows that some three-body events are able to bypass the momentum conservation check used to filter events produced by the reaction $D_2^+ + D^- \rightarrow D_2^* + D$ from background. However, other techniques are used to filter valid events, such as checking if the center of mass of detected particles matches the expected one. This last check may prevent three body events from polluting the two-body KER. A deeper reflection on this possibility is left for future work.

Appendix A

Vibrational states of the D_2^+ molecular ion and D_2 molecule

In this Appendix are gathered data about the computed vibrational states for the most relevant potentials [1].

[1] The amplitudes of the wavefunctions are adapted depending on the spacing between successive energy levels for better readability. The energies are given in electronvolts as measured from the bottom of the D2 ground state potential well.

A.1 Vibrational states of the D_2^+ molecular ion

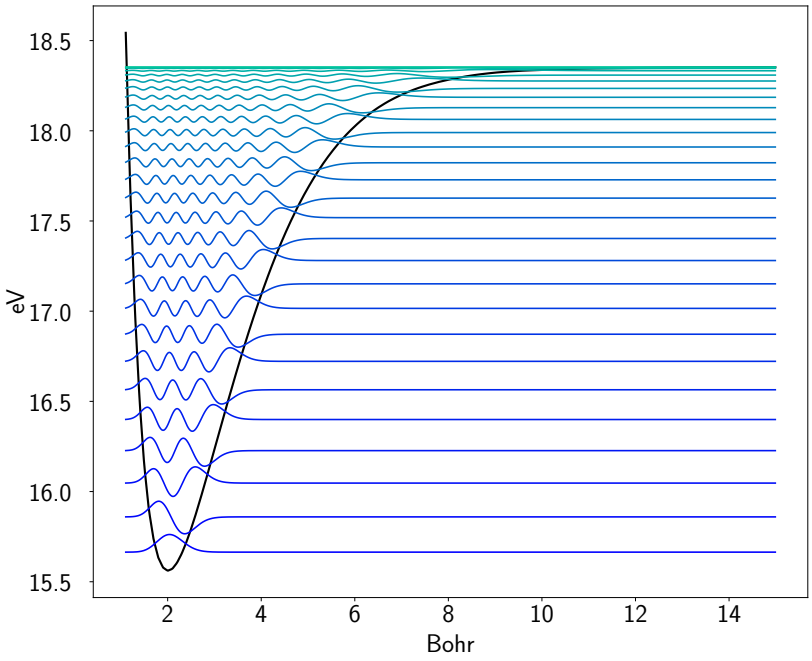

Figure A.1: Representation of the vibrational states (colored curves) computed with the potential of the D_2^+ molecular ion (black curve).

level	0	1	2	3	4	5	6
energy (eV)	15.664	15.860	16.047	16.227	16.399	16.564	16.722
level	7	8	9	10	11	12	13
energy (eV)	16.872	17.015	17.152	17.281	17.403	17.518	17.627
level	14	15	16	17	18	19	20
energy (eV)	17.728	17.823	17.910	17.990	18.063	18.128	18.186
level	21	22	23	24	25	26	27
energy (eV)	18.235	18.276	18.309	18.333	18.347	18.352	18.353

Table A.1: Energy levels of the vibrational states computed with the potential of the D_2^+ molecular ion.

A.2 Vibrational states of the fundamental electronic state of the $D_2(X)$ molecule

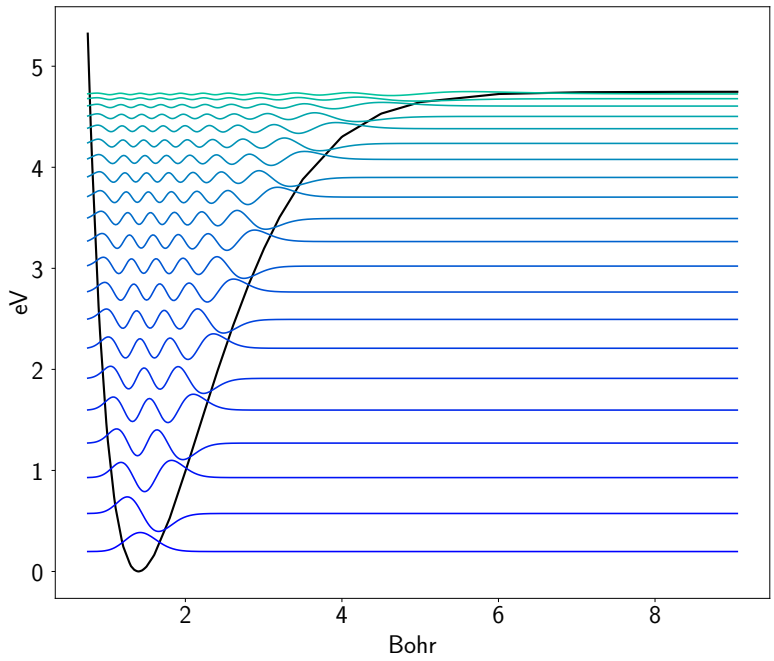

Figure A.2: Representation of the vibrational states (colored curves) computed with the potential of the fundamental electronic state of the $D_2(X)$ molecule (black curve).

level	0	1	2	3	4	5	6
energy (eV)	0.197	0.574	0.929	1.271	1.597	1.911	2.209
level	7	8	9	10	11	12	13
energy (eV)	2.495	2.765	3.022	3.265	3.493	3.705	3.900
level	14	15	16	17	18	19	20
energy (eV)	4.078	4.236	4.382	4.503	4.606	4.679	4.726

Table A.2: Energy levels of the vibrational states computed with the potential of the fundamental electronic state of the $D_2(X)$ molecule (black curve).

A.3 Vibrational states of electronically excited states of the D_2 molecule

A.3.1 Singlet system

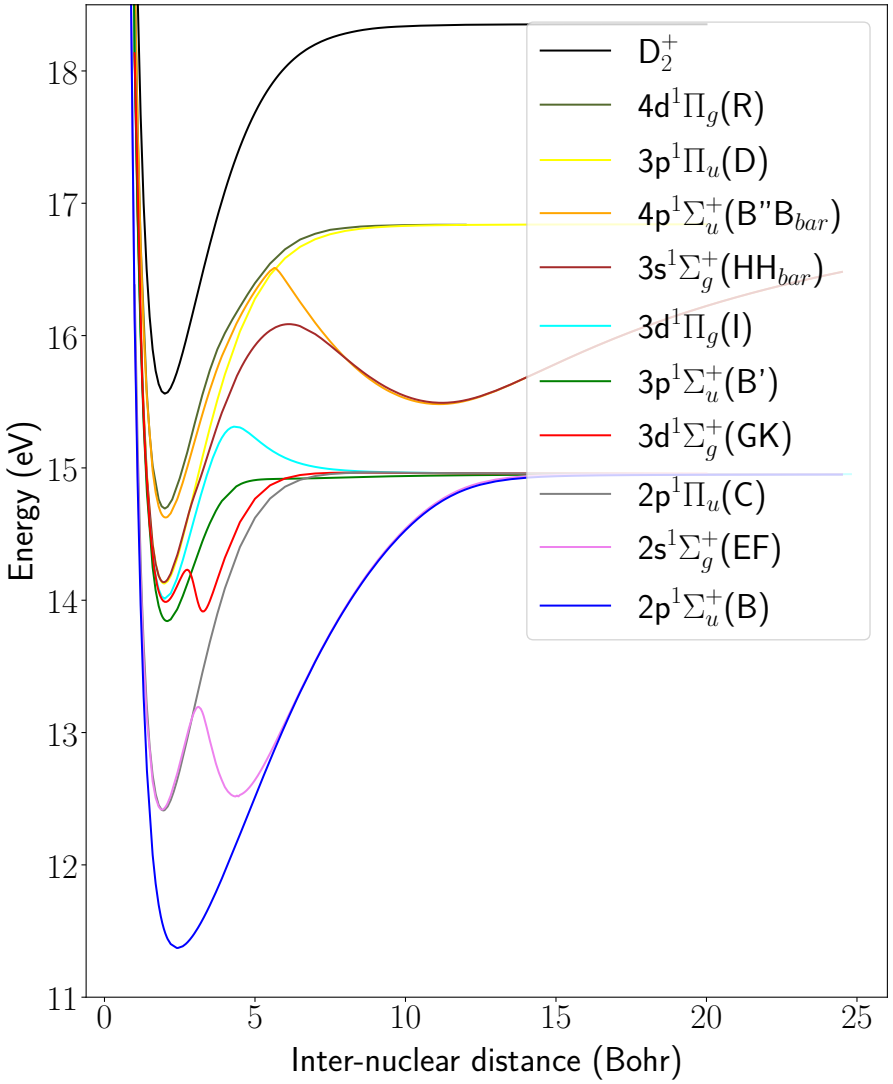

Figure A.3: Singlet states considered when studying the reaction $D_2^+ + D^- \rightarrow D_2^* + D$.

Orbital Σ

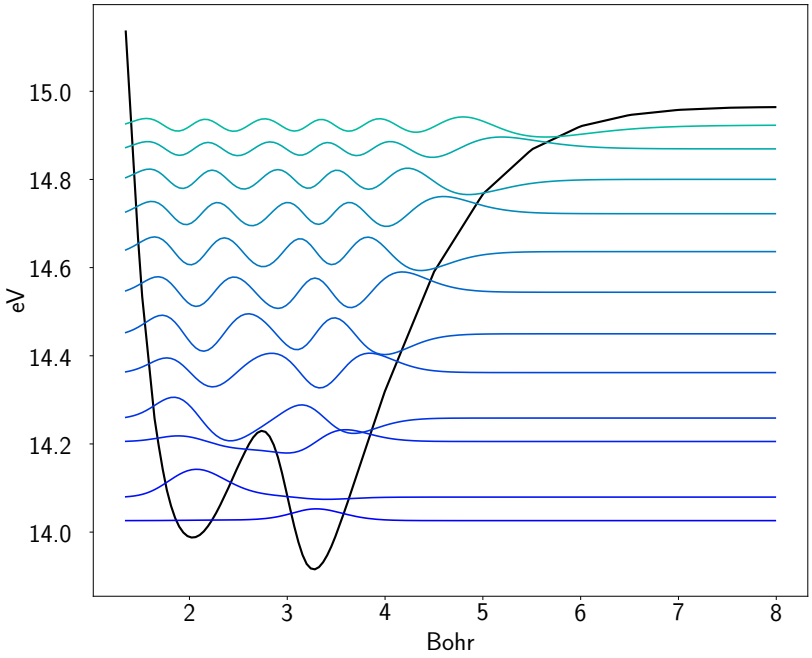

Figure A.4: Representation of the vibrational states (colored curves) computed with the potential of the $3d^1\Sigma_g^+$(GK) electronically excited state of the D_2 molecule (black curve).

level	0	1	2	3	4	5	6
energy (eV)	14.026	14.079	14.206	14.259	14.362	14.450	14.544
level	7	8	9	10	11	12	13
energy (eV)	14.636	14.722	14.800	14.869	14.923		

Table A.3: Energy levels of the vibrational states computed with the potential of the $3d^1\Sigma_g^+$(GK) electronically excited state of the D_2 molecule.

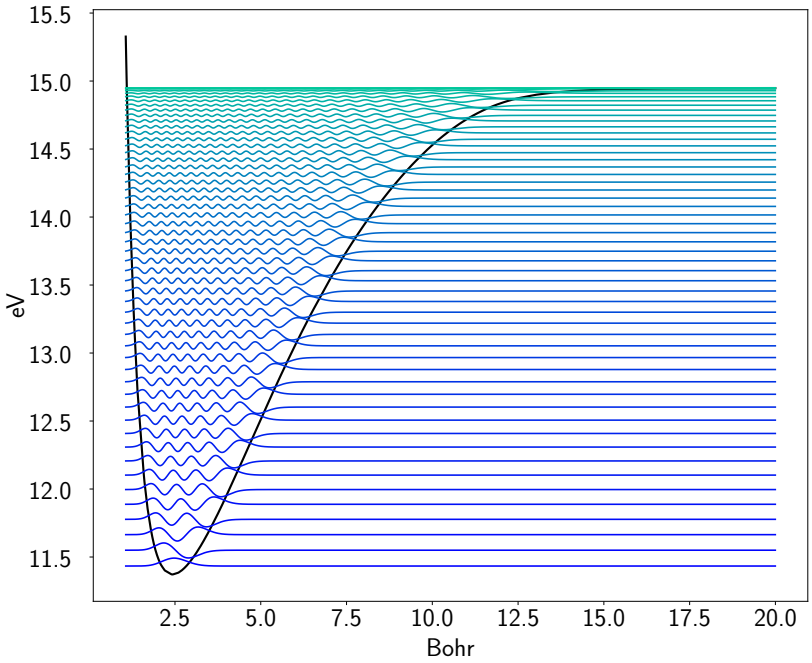

Figure A.5: Representation of the vibrational states (colored curves) computed with the potential of the $2p^1\Sigma_u^+(B)$ electronically excited state of the D_2 molecule (black curve).

level	0	1	2	3	4	5	6
energy (eV)	11.434	11.550	11.664	11.777	11.888	11.996	12.102
level	7	8	9	10	11	12	13
energy (eV)	12.206	12.308	12.409	12.506	12.603	12.697	12.789
level	14	15	16	17	18	19	20
energy (eV)	12.879	12.967	13.053	13.137	13.220	13.300	13.379
level	21	22	23	24	25	26	27
energy (eV)	13.456	13.532	13.606	13.678	13.749	13.818	13.885
level	28	29	30	31	32	33	34
energy (eV)	13.951	14.015	14.078	14.139	14.199	14.257	14.313
level	35	36	37	38	39	40	41
energy (eV)	14.368	14.421	14.473	14.523	14.572	14.619	14.664
level	42	43	44	45	46	47	48
energy (eV)	14.707	14.747	14.786	14.822	14.855	14.884	14.909
level	49	50	51	52	53	54	55
energy (eV)	14.929	14.942	14.947	14.950			

Table A.4: Energy levels of the vibrational states computed with the potential of the $2p^1\Sigma_u^+$(B) electronically excited state of the D_2 molecule.

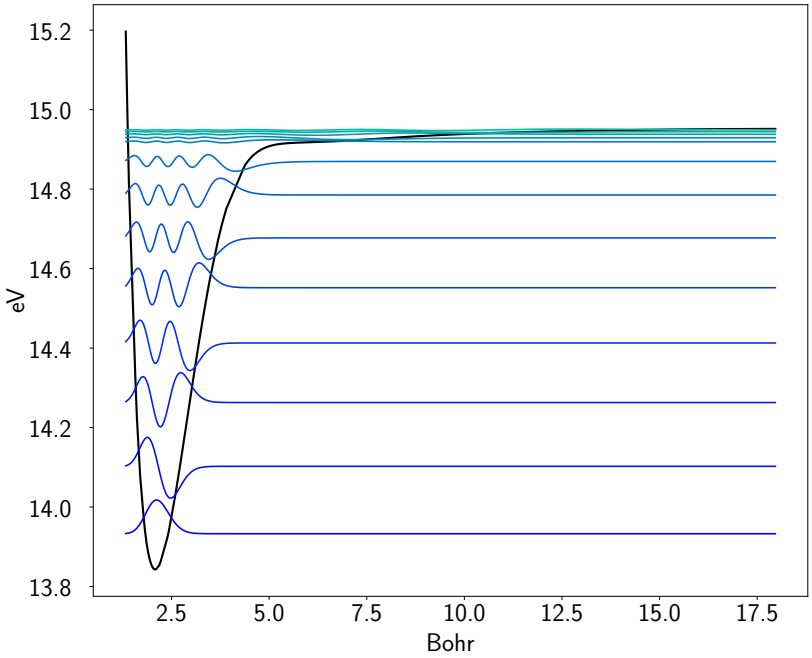

Figure A.6: Representation of the vibrational states (colored curves) computed with the potential of the $3p^1\Sigma_u^+(B')$ electronically excited state of the D_2 molecule (black curve).

level	0	1	2	3	4	5	6
energy (eV)	13.933	14.102	14.263	14.413	14.552	14.677	14.785
level	7	8	9	10	11	12	13
energy (eV)	14.870	14.919	14.929	14.938	14.944	14.949	

Table A.5: Energy levels of the vibrational states computed with the potential of the $3p^1\Sigma_u^+(B')$ electronically excited state of the D_2 molecule.

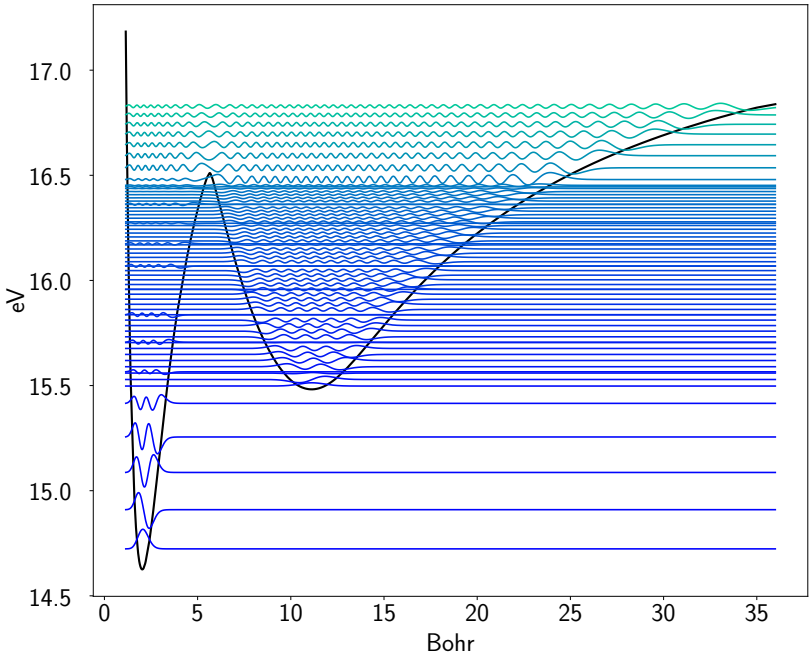

Figure A.7: Representation of the vibrational states (colored curves) computed with the potential of the $4p^1\Sigma_u^+(B''\bar{B})$ electronically excited state of the D_2 molecule (black curve). Above -15.5 eV only a fifth of the vibrational states are drawn for better readability.

level	0	1	2	3	4	5	6
energy (eV)	14.723	14.910	15.087	15.255	15.415	15.498	15.529
level	7	8	9	10	11	12	13
energy (eV)	15.559	15.565	15.590	15.619	15.648	15.677	15.704
level	14	15	16	17	18	19	20
energy (eV)	15.706	15.732	15.759	15.785	15.811	15.837	15.837
level	21	22	23	24	25	26	27
energy (eV)	15.862	15.887	15.911	15.934	15.957	15.958	15.981
level	28	29	30	31	32	33	34
energy (eV)	16.003	16.025	16.047	16.068	16.069	16.089	16.110
level	35	36	37	38	39	40	41
energy (eV)	16.130	16.150	16.169	16.174	16.188	16.207	16.225
level	42	43	44	45	46	47	48
energy (eV)	16.243	16.261	16.272	16.279	16.296	16.313	16.329
level	49	50	51	52	53	54	55
energy (eV)	16.346	16.362	16.362	16.377	16.393	16.408	16.423
level	56	57	58	59	60	61	62
energy (eV)	16.437	16.445	16.452	16.466	16.480	16.493	16.506
level	63	64	65	66	67	68	69
energy (eV)	16.516	16.525	16.536	16.548	16.559	16.571	16.582
level	70	71	72	73	74	75	76
energy (eV)	16.593	16.604	16.614	16.624	16.635	16.645	16.656
level	77	78	79	80	81	82	83
energy (eV)	16.666	16.676	16.686	16.696	16.705	16.715	16.724
level	84	85	86	87	88	89	90
energy (eV)	16.734	16.743	16.752	16.761	16.770	16.778	16.787
level	91	92	93	94	95	96	97
energy (eV)	16.796	16.804	16.812	16.820	16.828	16.836	

Table A.6: Energy levels of the vibrational states computed with the potential of the $4p^1\Sigma_u^+(B''\bar{B})$ electronically excited state of the D_2 molecule.

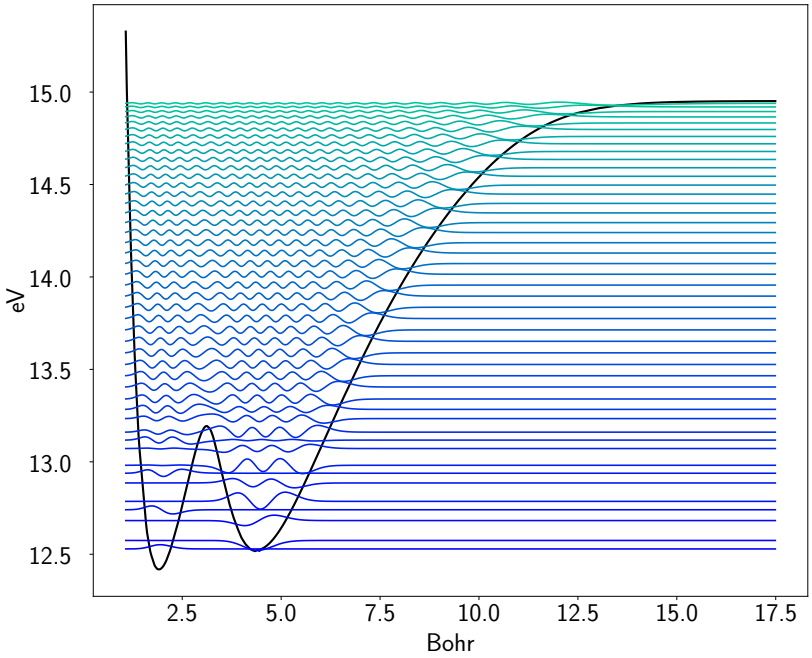

Figure A.8: Representation of the vibrational states (colored curves) computed with the potential of the $2s^1\Sigma_g^+$(EF) electronically excited state of the D_2 molecule (black curve).

level	0	1	2	3	4	5	6
energy (eV)	12.529	12.575	12.682	12.741	12.786	12.886	12.938
level	7	8	9	10	11	12	13
energy (eV)	12.981	13.072	13.118	13.160	13.234	13.284	13.340
level	14	15	16	17	18	19	20
energy (eV)	13.405	13.466	13.527	13.590	13.652	13.714	13.775
level	21	22	23	24	25	26	27
energy (eV)	13.836	13.896	13.956	14.015	14.072	14.129	14.185
level	28	29	30	31	32	33	34
energy (eV)	14.240	14.294	14.346	14.398	14.448	14.497	14.544
level	35	36	37	38	39	40	41
energy (eV)	14.591	14.635	14.679	14.720	14.760	14.798	14.833
level	42	43	44	45	46	47	48
energy (eV)	14.866	14.895	14.920	14.939			

Table A.7: Energy levels of the vibrational states computed with the potential of the $2s^1\Sigma_g^+$(EF) electronically excited state of the D_2 molecule.

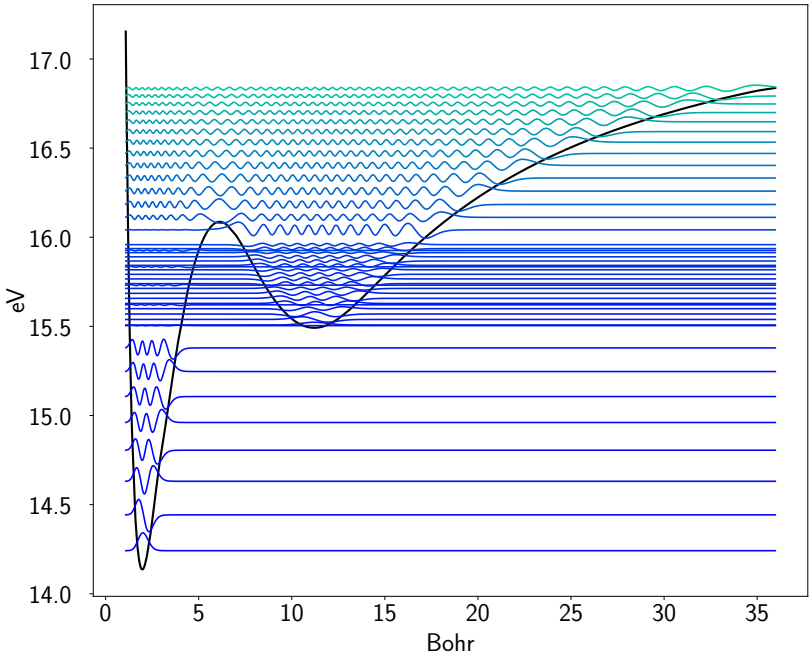

Figure A.9: Representation of the vibrational states (colored curves) computed with the potential of the $3s^1\Sigma_g^+(H\bar{H})$ electronically excited state of the D_2 molecule (black curve). Above -16 eV only a fifth of the vibrational states are drawn for better readability.

level	0	1	2	3	4	5	6
energy (eV)	14.242	14.443	14.631	14.805	14.961	15.106	15.247
level	7	8	9	10	11	12	13
energy (eV)	15.379	15.504	15.508	15.539	15.569	15.599	15.621
level	14	15	16	17	18	19	20
energy (eV)	15.629	15.657	15.685	15.713	15.731	15.740	15.766
level	21	22	23	24	25	26	27
energy (eV)	15.792	15.818	15.834	15.842	15.867	15.890	15.914
level	28	29	30	31	32	33	34
energy (eV)	15.926	15.936	15.959	15.980	16.001	16.007	16.022
level	35	36	37	38	39	40	41
energy (eV)	16.041	16.060	16.072	16.080	16.096	16.112	16.125
level	42	43	44	45	46	47	48
energy (eV)	16.139	16.154	16.169	16.184	16.199	16.214	16.229
level	49	50	51	52	53	54	55
energy (eV)	16.244	16.259	16.274	16.289	16.303	16.318	16.332
level	56	57	58	59	60	61	62
energy (eV)	16.347	16.361	16.375	16.389	16.403	16.417	16.430
level	63	64	65	66	67	68	69
energy (eV)	16.444	16.457	16.470	16.483	16.496	16.508	16.521
level	70	71	72	73	74	75	76
energy (eV)	16.533	16.545	16.557	16.569	16.581	16.593	16.604
level	77	78	79	80	81	82	83
energy (eV)	16.615	16.626	16.637	16.648	16.659	16.669	16.679
level	84	85	86	87	88	89	90
energy (eV)	16.690	16.700	16.710	16.719	16.729	16.738	16.748
level	91	92	93	94	95	96	97
energy (eV)	16.757	16.766	16.775	16.784	16.792	16.801	16.809
level	98	99	100	101	102	103	104
energy (eV)	16.818	16.826	16.834				

Table A.8: Energy levels of the vibrational states computed with the potential of the $3s^1\Sigma_g^+(H\bar{H})$ electronically excited state of the D_2 molecule.

Orbital Π

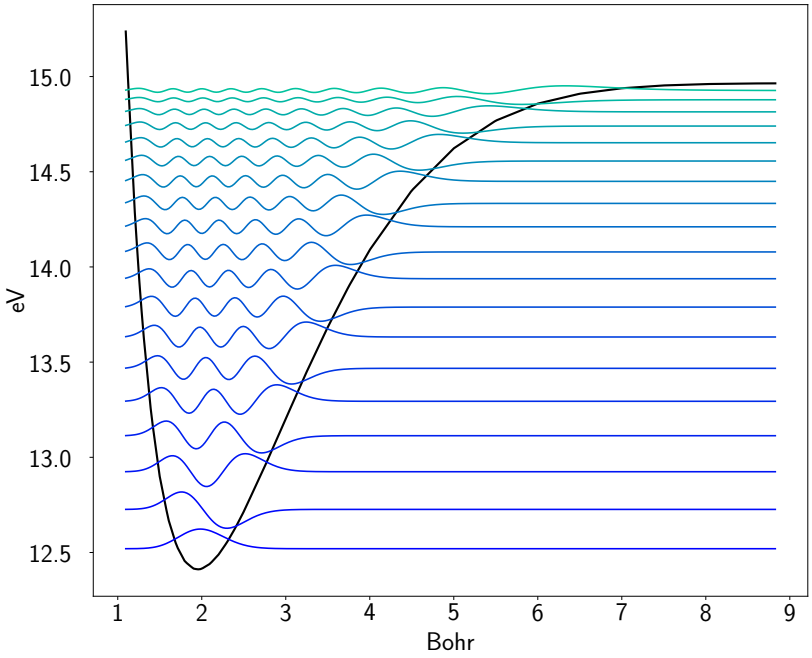

Figure A.10: Representation of the vibrational states (colored curves) computed with the potential of the $2p^1\Pi_u(C)$ electronically excited state of the D_2 molecule (black curve).

level	0	1	2	3	4	5	6
energy (eV)	12.520	12.726	12.924	13.113	13.294	13.467	13.632
level	7	8	9	10	11	12	13
energy (eV)	13.789	13.938	14.079	14.211	14.334	14.450	14.556
level	14	15	16	17	18	19	20
energy (eV)	14.652	14.740	14.815	14.878	14.927		

Table A.9: Energy levels of the vibrational states computed with the potential of the $2p^1\Pi_u(C)$ electronically excited state of the D_2 molecule.

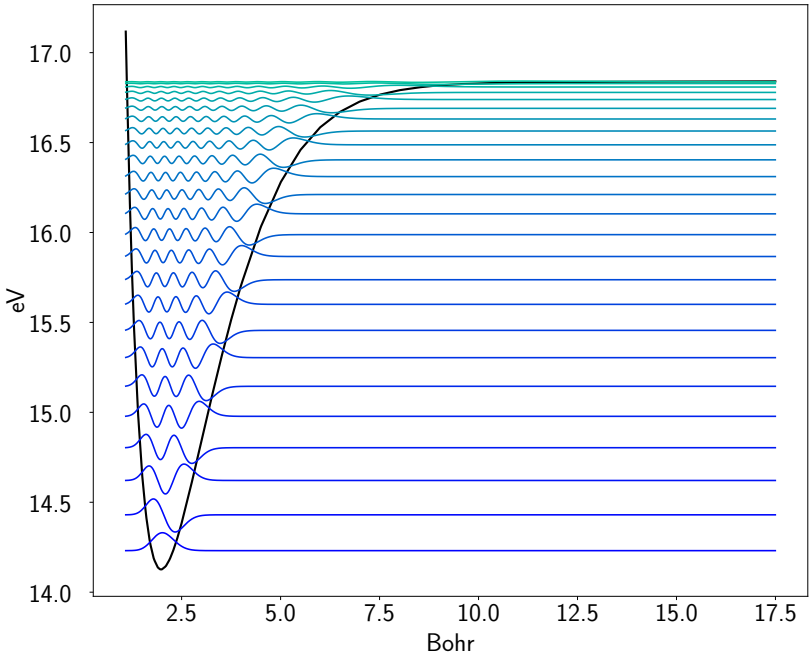

Figure A.11: Representation of the vibrational states (colored curves) computed with the potential of the $3p^1\Pi_u(D)$ electronically excited state of the D_2 molecule (black curve).

level	0	1	2	3	4	5	6
energy (eV)	14.231	14.430	14.621	14.803	14.978	15.145	15.304
level	7	8	9	10	11	12	13
energy (eV)	15.456	15.600	15.737	15.866	15.988	16.104	16.211
level	14	15	16	17	18	19	20
energy (eV)	16.311	16.404	16.488	16.564	16.631	16.690	16.739
level	21	22	23	24	25	26	27
energy (eV)	16.779	16.809	16.828	16.837			

Table A.10: Energy levels of the vibrational states computed with the potential of the $3p^1\Pi_u(D)$ electronically excited state of the D_2 molecule.

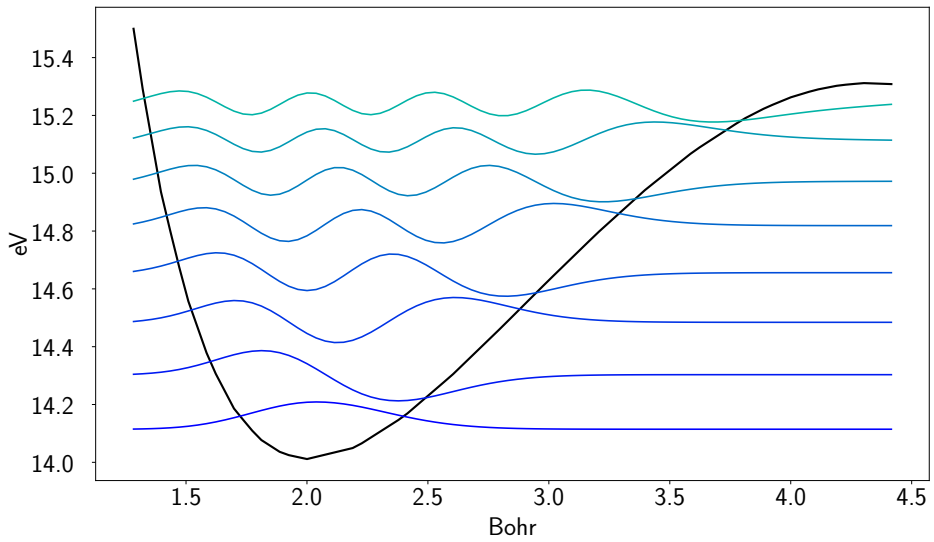

Figure A.12: Representation of the vibrational states (colored curves) computed with the potential of the $3d^1\Pi_g(I)$ electronically excited state of the D_2 molecule (black curve).

level	0	1	2	3	4	5	6
energy (eV)	14.115	14.303	14.484	14.656	14.819	14.972	15.114
level	7	8	9	10	11	12	13
energy (eV)	15.241						

Table A.11: Energy levels of the vibrational states computed with the potential of the $3d^1\Pi_g(I)$ electronically excited state of the D_2 molecule.

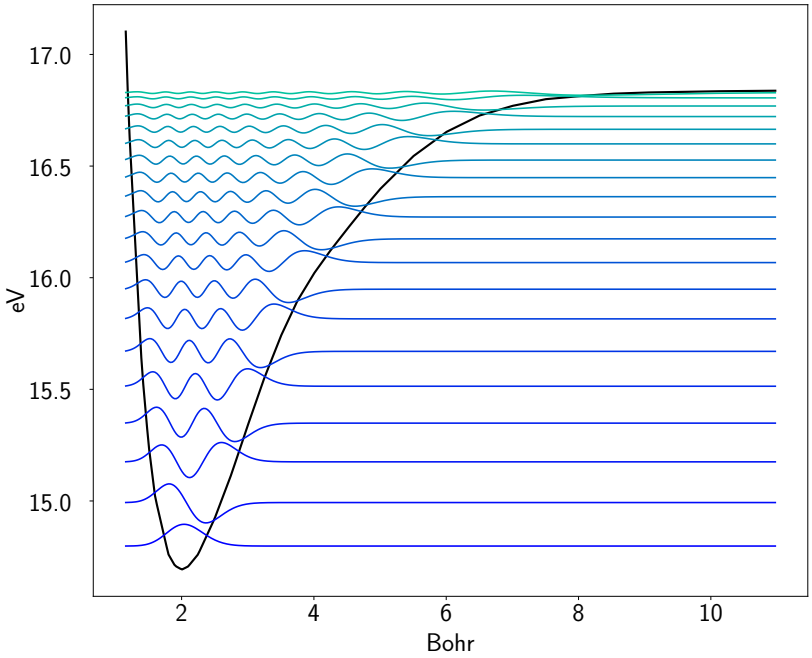

Figure A.13: Representation of the vibrational states (colored curves) computed with the potential of the $4d^1\Pi_g(R)$ electronically excited state of the D_2 molecule (black curve).

level	0	1	2	3	4	5	6
energy (eV)	14.798	14.993	15.175	15.349	15.514	15.670	15.816
level	7	8	9	10	11	12	13
energy (eV)	15.948	16.068	16.174	16.272	16.363	16.448	16.527
level	14	15	16	17	18	19	20
energy (eV)	16.599	16.665	16.722	16.769	16.805	16.829	

Table A.12: Energy levels of the vibrational states computed with the potential of the $4d^1\Pi_g(R)$ electronically excited state of the D_2 molecule.

A.3.2 Triplet system

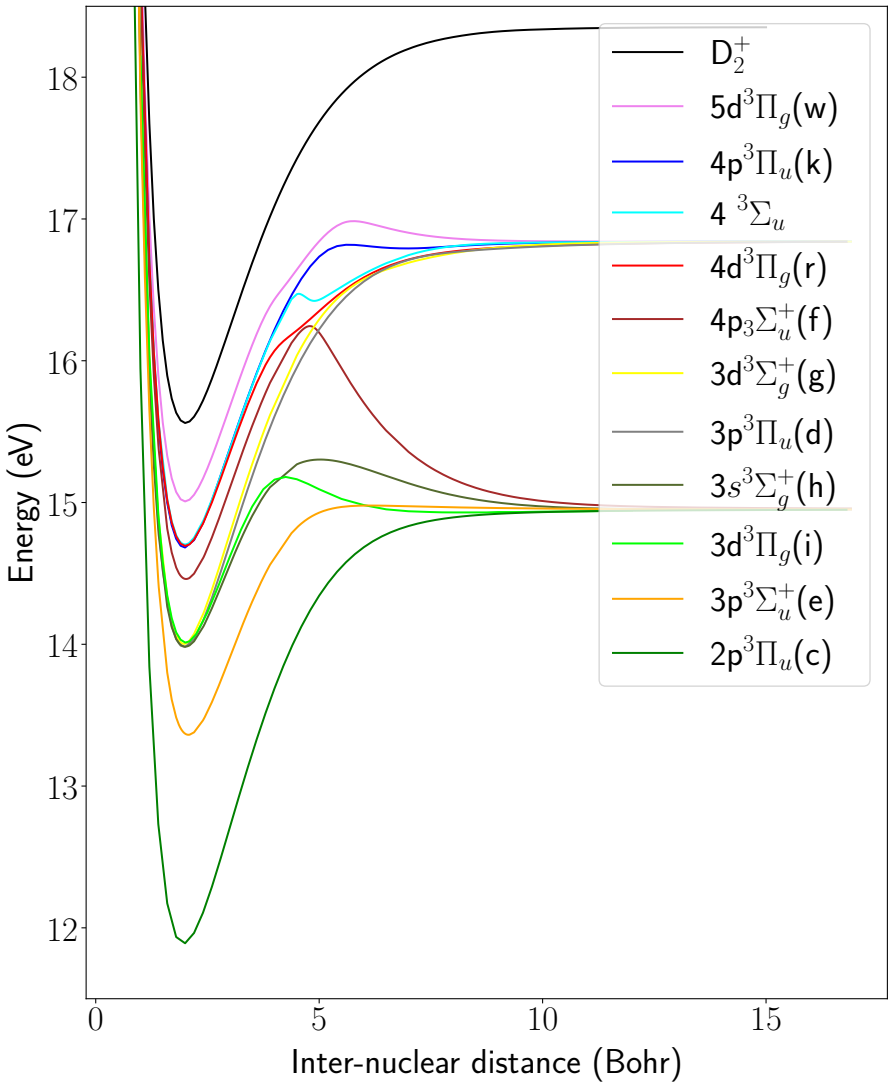

Figure A.14: Triplet states considered when studying the reaction $D_2^+ + D^- \rightarrow D_2^* + D$.

Orbital Σ

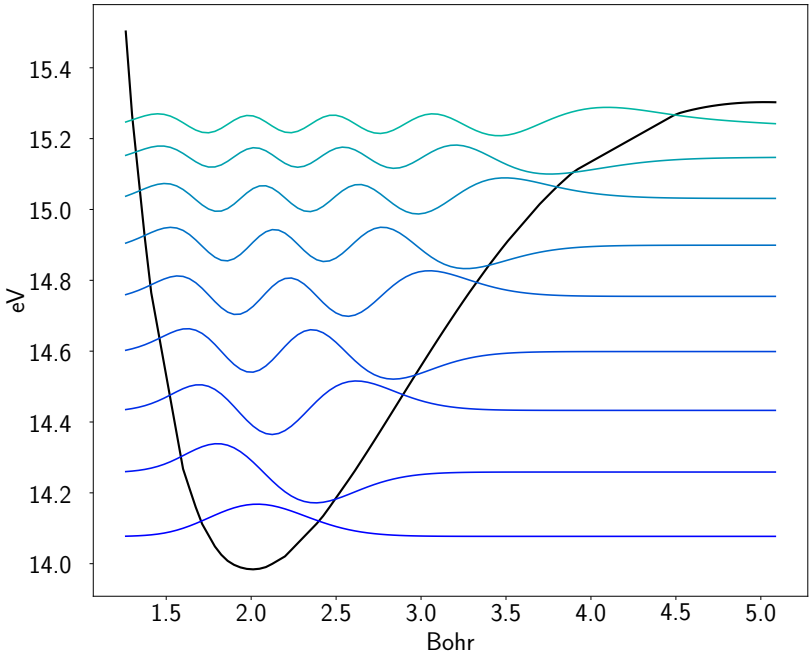

Figure A.15: Representation of the vibrational states (colored curves) computed with the potential of the $3s^3\Sigma_g^+(h)$ electronically excited state of the D_2 molecule (black curve).

level	0	1	2	3	4	5	6
energy (eV)	14.077	14.259	14.433	14.599	14.755	14.899	15.031
level	7	8	9	10	11	12	13
energy (eV)	15.147	15.241					

Table A.13: Energy levels of the vibrational states computed with the potential of the $3s^3\Sigma_g^+(h)$ electronically excited state of the D_2 molecule.

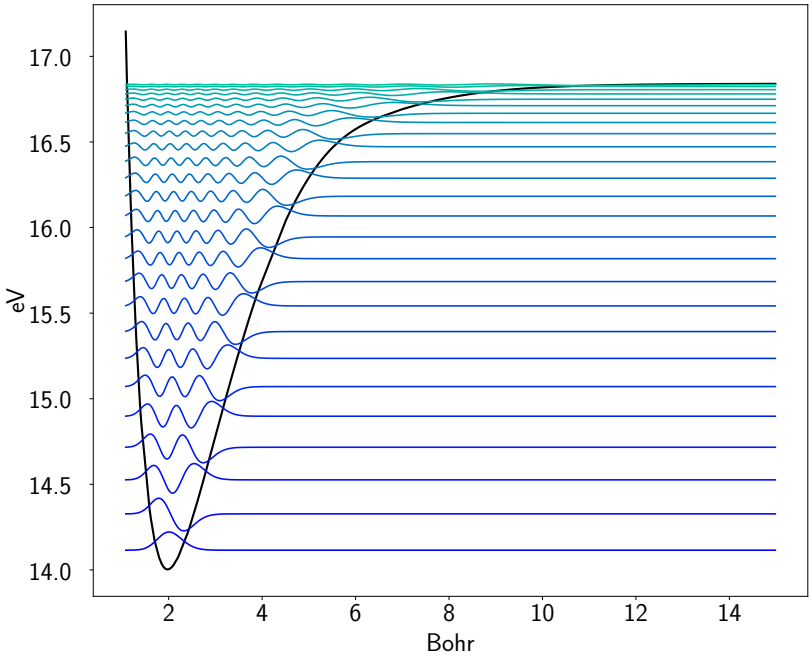

Figure A.16: Representation of the vibrational states (colored curves) computed with the potential of the $3d^3\Sigma_g^+(g)$ electronically excited state of the D_2 molecule (black curve).

level	0	1	2	3	4	5	6
energy (eV)	14.115	14.327	14.526	14.716	14.898	15.071	15.236
level	7	8	9	10	11	12	13
energy (eV)	15.392	15.542	15.684	15.818	15.945	16.068	16.183
level	14	15	16	17	18	19	20
energy (eV)	16.288	16.385	16.472	16.549	16.614	16.667	16.712
level	21	22	23	24	25	26	27
energy (eV)	16.750	16.781	16.806	16.824	16.835		

Table A.14: Energy levels of the vibrational states computed with the potential of the $3d^3\Sigma_g^+(g)$ electronically excited state of the D_2 molecule.

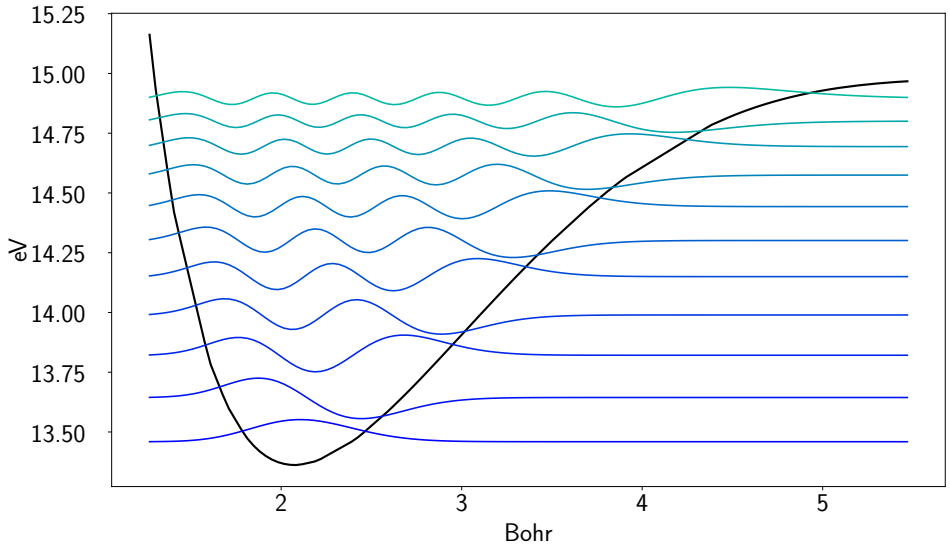

Figure A.17: Representation of the vibrational states (colored curves) computed with the potential of the $3p^3\Sigma_u^+(e)$ electronically excited state of the D_2 molecule (black curve).

level	0	1	2	3	4	5	6
energy (eV)	13.459	13.644	13.821	13.990	14.150	14.301	14.443
level	7	8	9	10	11	12	13
energy (eV)	14.575	14.694	14.801	14.895			

Table A.15: Energy levels of the vibrational states computed with the potential of the $3p^3\Sigma_u^+(e)$ electronically excited state of the D_2 molecule.

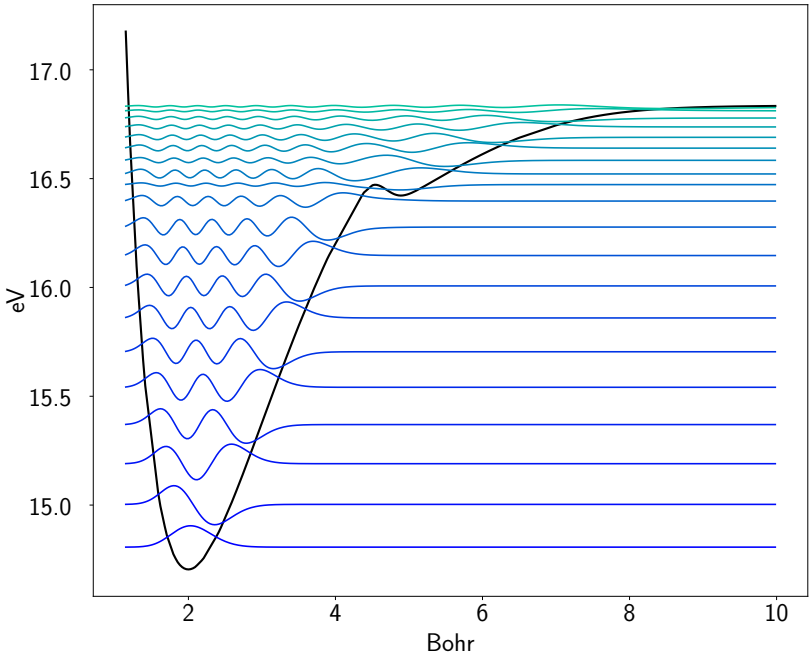

Figure A.18: Representation of the vibrational states (colored curves) computed with the potential of the fourth triplet sigma $4^3\Sigma_u$ electronically excited state of the D_2 molecule (black curve).

level	0	1	2	3	4	5	6
energy (eV)	14.807	15.003	15.190	15.370	15.541	15.704	15.860
level	7	8	9	10	11	12	13
energy (eV)	16.007	16.147	16.277	16.397	16.473	16.521	16.584
level	14	15	16	17	18	19	20
energy (eV)	16.640	16.690	16.738	16.779	16.811	16.832	

Table A.16: Energy levels of the vibrational states computed with the potential of the fourth triplet sigma $4^3\Sigma_u$ electronically excited state of the D_2 molecule.

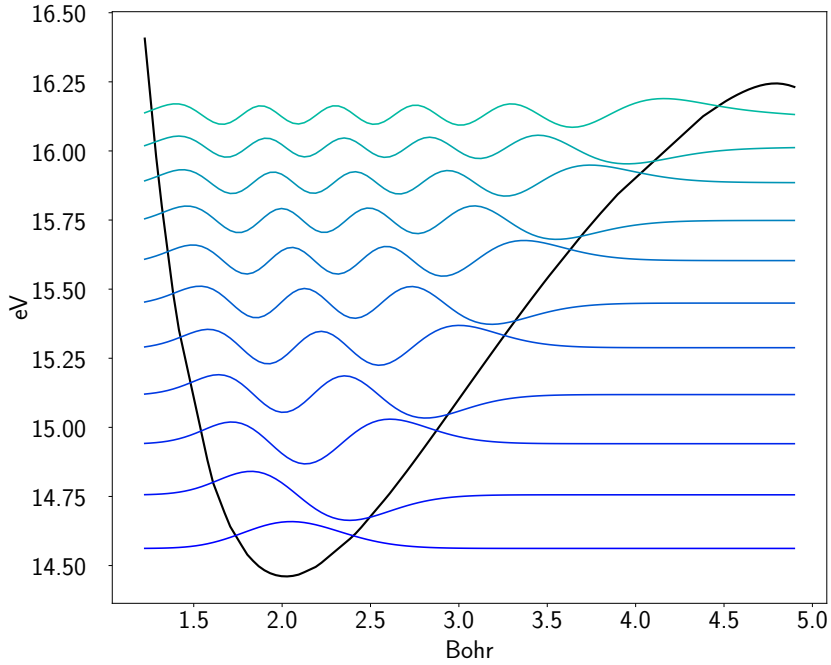

Figure A.19: Representation of the vibrational states (colored curves) computed with the potential of the $4p_3\Sigma_u^+(f)$ electronically excited state of the D_2 molecule (black curve).

level	0	1	2	3	4	5	6
energy (eV)	14.562	14.756	14.941	15.119	15.288	15.450	15.603
level	7	8	9	10	11	12	13
energy (eV)	15.749	15.885	16.012	16.130			

Table A.17: Energy levels of the vibrational states computed with the potential of the $4p_3\Sigma_u^+(f)$ electronically excited state of the D_2 molecule.

Orbital Π

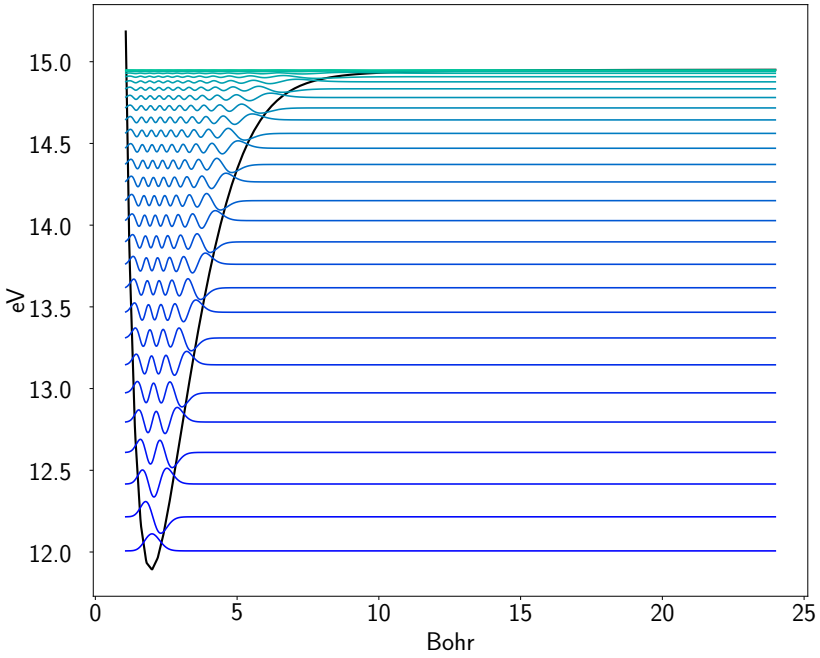

Figure A.20: Representation of the vibrational states (colored curves) computed with the potential of the $2p^3\Pi_u(c)$ electronically excited state of the D_2 molecule (black curve).

level	0	1	2	3	4	5	6
energy (eV)	12.007	12.215	12.416	12.609	12.795	12.974	13.145
level	7	8	9	10	11	12	13
energy (eV)	13.310	13.467	13.617	13.760	13.898	14.028	14.150
level	14	15	16	17	18	19	20
energy (eV)	14.264	14.371	14.470	14.561	14.644	14.717	14.781
level	21	22	23	24	25	26	27
energy (eV)	14.834	14.877	14.908	14.929	14.941	14.947	14.950

Table A.18: Energy levels of the vibrational states computed with the potential of the $2p^3\Pi_u(c)$ electronically excited state of the D_2 molecule.

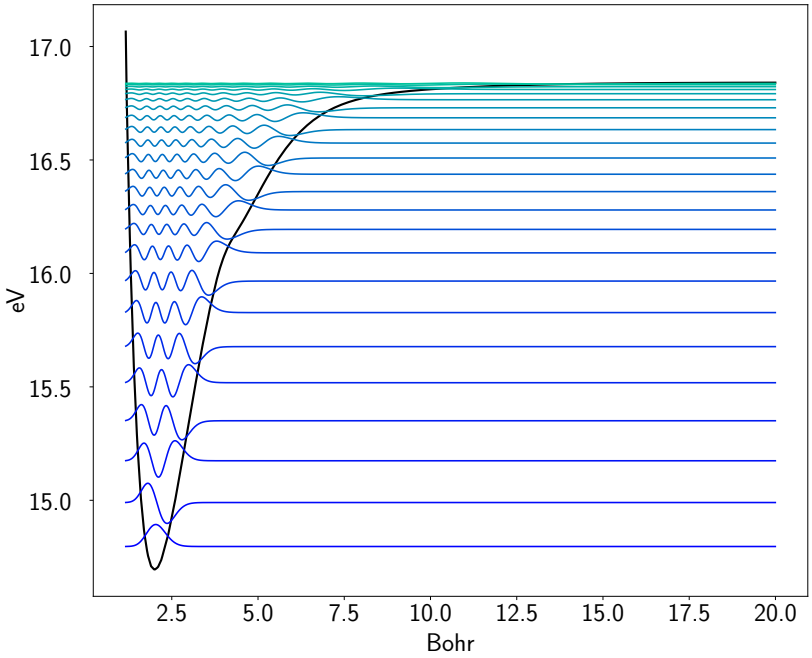

Figure A.21: Representation of the vibrational states (colored curves) computed with the potential of the $4d^3\Pi_g(r)$ electronically excited state of the D_2 molecule (black curve).

level	0	1	2	3	4	5	6
energy (eV)	14.796	14.990	15.174	15.351	15.518	15.677	15.827
level	7	8	9	10	11	12	13
energy (eV)	15.966	16.091	16.194	16.280	16.361	16.437	16.509
level	14	15	16	17	18	19	20
energy (eV)	16.574	16.634	16.686	16.730	16.765	16.792	16.811
level	21	22	23	24	25	26	27
energy (eV)	16.823	16.832	16.837				

Table A.19: Energy levels of the vibrational states computed with the potential of the $4d^3\Pi_g(r)$ electronically excited state of the D_2 molecule.

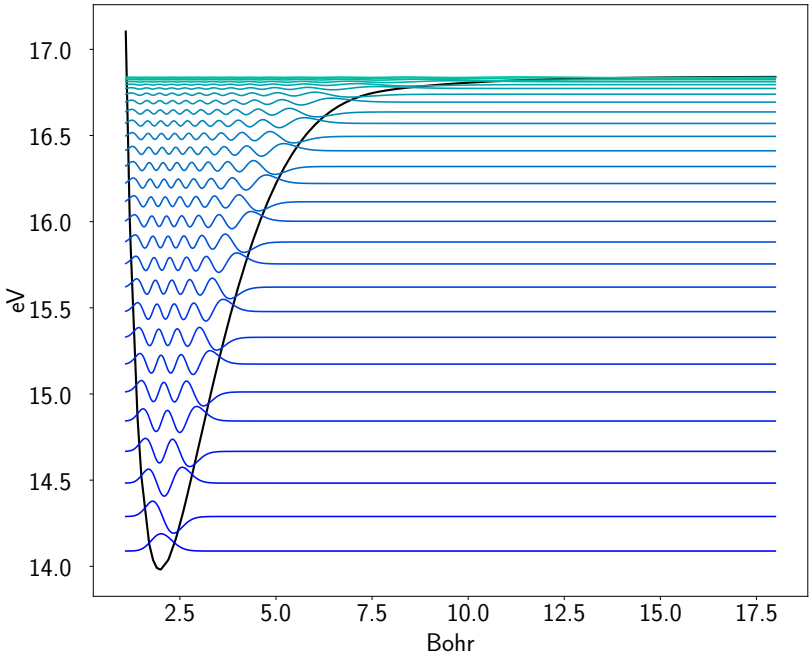

Figure A.22: Representation of the vibrational states (colored curves) computed with the potential of the $3p^3\Pi_u(d)$ electronically excited state of the D_2 molecule (black curve).

level	0	1	2	3	4	5	6
energy (eV)	14.089	14.289	14.483	14.667	14.843	15.012	15.173
level	7	8	9	10	11	12	13
energy (eV)	15.329	15.478	15.620	15.755	15.882	16.002	16.115
level	14	15	16	17	18	19	20
energy (eV)	16.221	16.320	16.411	16.495	16.570	16.637	16.693
level	21	22	23	24	25	26	27
energy (eV)	16.739	16.773	16.795	16.812	16.824	16.833	16.838

Table A.20: Energy levels of the vibrational states computed with the potential of the $3p^3\Pi_u(d)$ electronically excited state of the D_2 molecule.

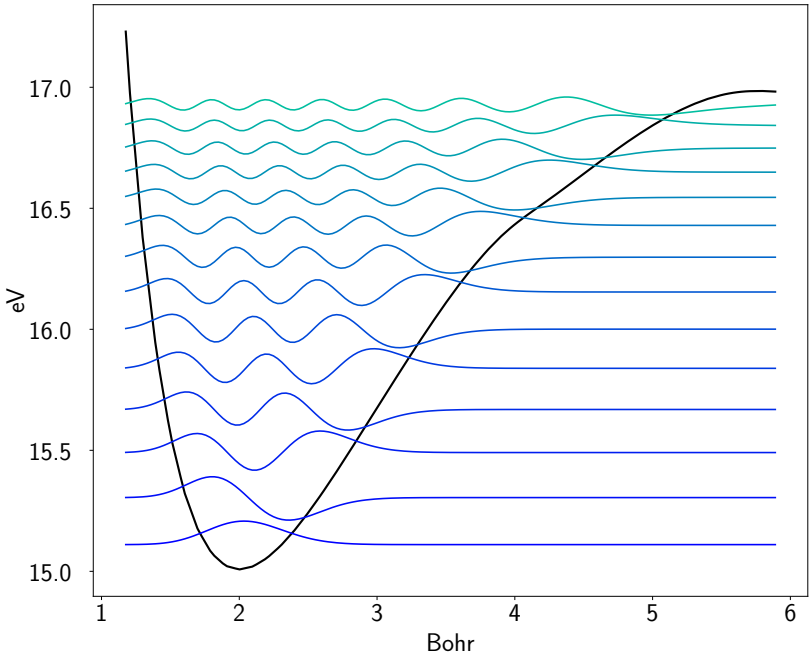

Figure A.23: Representation of the vibrational states (colored curves) computed with the potential of the $5d^3\Pi_g(w)$ electronically excited state of the D_2 molecule (black curve).

level	0	1	2	3	4	5	6
energy (eV)	15.110	15.305	15.491	15.669	15.839	16.001	16.154
level	7	8	9	10	11	12	13
energy (eV)	16.298	16.429	16.545	16.649	16.749	16.842	16.928

Table A.21: Energy levels of the vibrational states computed with the potential of the $5d^3\Pi_g(w)$ electronically excited state of the D_2 molecule.

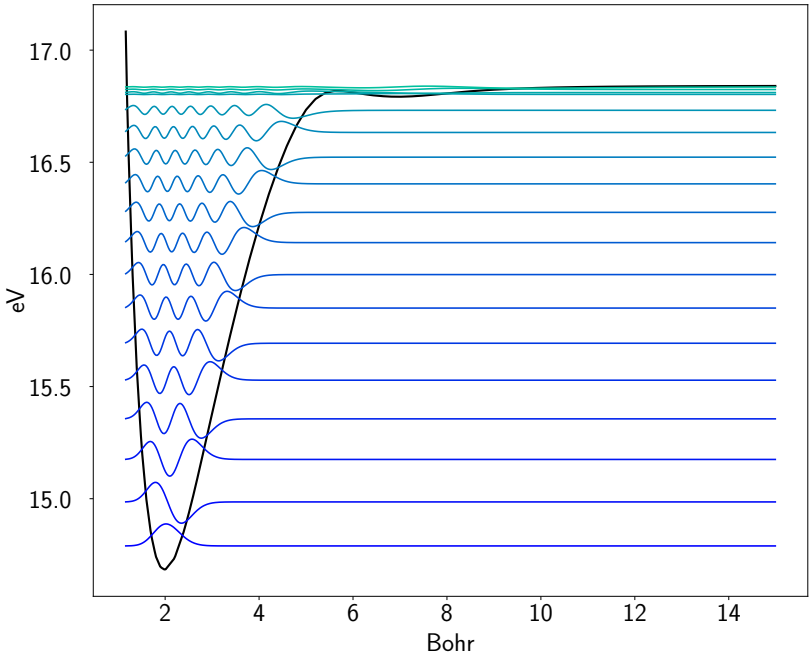

Figure A.24: Representation of the vibrational states (colored curves) computed with the potential of the $4p^3\Pi_u(k)$ electronically excited state of the D_2 molecule (black curve).

level	0	1	2	3	4	5	6
energy (eV)	14.789	14.986	15.175	15.356	15.528	15.693	15.850
level	7	8	9	10	11	12	13
energy (eV)	15.999	16.142	16.277	16.404	16.523	16.633	16.732
level	14	15	16	17	18	19	20
energy (eV)	16.803	16.811	16.824	16.836			

Table A.22: Energy levels of the vibrational states computed with the potential of the $4p^3\Pi_u(k)$ electronically excited state of the D_2 molecule.

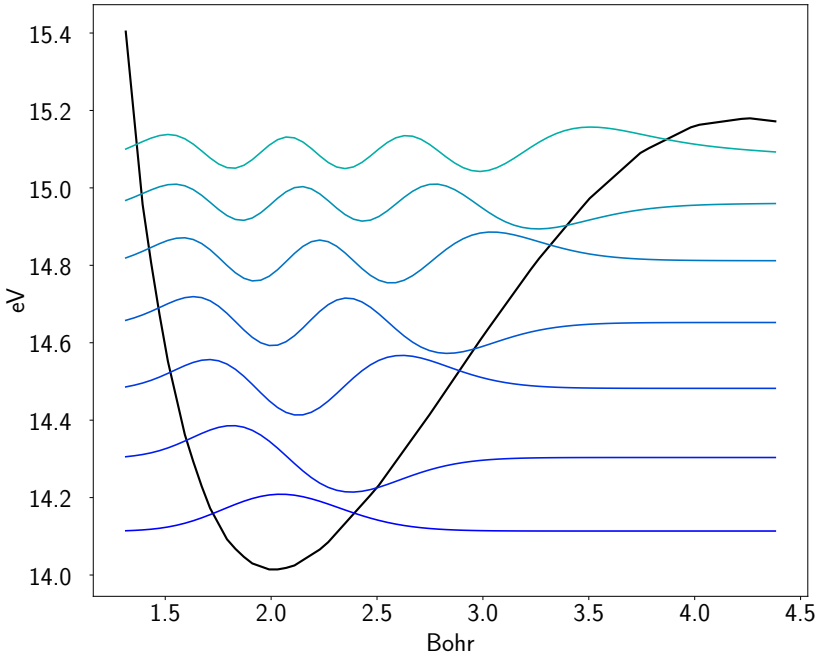

Figure A.25: Representation of the vibrational states (colored curves) computed with the potential of the $3d^3\Pi_g(i)$ electronically excited state of the D_2 molecule (black curve).

level	0	1	2	3	4	5	6
energy (eV)	14.114	14.304	14.482	14.652	14.812	14.960	15.091

Table A.23: Energy levels of the vibrational states computed with the potential of the $3d^3\Pi_g(i)$ electronically excited state of the D_2 molecule.

Bibliography

[1] Wikipedia contributors. Nuclear fusion — Wikipedia, the free encyclopedia. https://en.wikipedia.org/w/index.php?title=Nuclear_fusion&oldid=875833813, 2018. [Online; accessed 1-January-2019].

[2] Wikipedia contributors. Lawson criterion — Wikipedia, the free encyclopedia. https://en.wikipedia.org/w/index.php?title=Lawson_criterion&oldid=876116645, 2018. [Online; accessed 1-January-2019].

[3] Pierre-Paul de Breuck, Benjamin Liégeois, Nicolas Marchal, Joao Amaro, Lancelot de Halleux, Ludovic Bontemps. Thermonuclear fusion in iter: An application of superconducting magnets. 2018.

[4] John David Jackson. *Classical electrodynamics*. Wiley, New York, NY, 3rd ed. edition, 1999.

[5] Robert Tye. Improvement of diamagnetic measurement on the tcv (tokamaka configuration variable). 12 2018.

[6] EUROfusion. Tokamak principle. https://www.euro-fusion.org/de/news/n/detail/News/tokamak-principle/.

[7] U Fantz and D Wuenderlich. Franck–condon factors, transition probabilities, and radiative lifetimes for hydrogen molecules and their isotopomeres. *Atomic Data and Nuclear Data Tables - AT DATA NUCL DATA TABLES*, 92:853–973, 11 2006.

[8] Ursel Fantz and Jacques Lettry. Focus on sources of negatively charged ions. *New Journal of Physics*, 20:060201, 06 2018.

[9] Katsuyoshi Tsumori and Motoi Wada. Diagnostics tools and methods for negative ion source plasmas, a review. *New Journal of Physics*, 19, 03 2017.

[10] M. Bacal and M. Wada. Negative hydrogen ion production mechanisms. *Applied Physics Reviews*, 2(2):021305, 2015.

[11] G Serianni, P Agostinetti, M Agostini, V Antoni, D Aprile, C Baltador, M Barbisan, M Brombin, M Cavenago, G Chitarin, M Dalla Palma, R Delogu, F Fellin,

N Fonnesu, N Marconato, R Pasqualotto, A Pimazzoni, E Sartori, S Spagnolo, M Spolaore, P Veltri, B Zaniol, and M Zaupa. Neutralisation and transport of negative ion beams: physics and diagnostics. *New Journal of Physics*, 19(4):045003, 2017.

[12] F Taccogna and P Minelli. Pic modeling of negative ion sources for fusion. *New Journal of Physics*, 19(1):015012, 2017.

[13] B Heinemann, U Fantz, W Kraus, L Schiesko, C Wimmer, D Wünderlich, F Bonomo, M Fröschle, R Nocentini, and R Riedl. Towards large and powerful radio frequency driven negative ion sources for fusion. *New Journal of Physics*, 19(1):015001, 2017.

[14] F.F. Chen. Rf plasma sources for semiconductor processing. *Advanced Plasma Technology*, 2006.

[15] Ratko K Janev, Detlev Reiter, and Ulrich Samm. *Collision processes in low-temperature hydrogen plasmas*, volume 102. Forschungszentrum Jülich, Zentralbibliothek, 2003.

[16] Gilles Cartry, Dmitry Kogut, Kostiantyn Achkasov, Jean-Marc Layet, Thomas Farley, Alix Gicquel, Jocelyn Achard, Ovidiu Brinza, Thomas Bieber, Hocine Khemliche, Philippe Roncin, and Alain Simonin. Alternative solutions to caesium in negative-ion sources: a study of negative-ion surface production on diamond in h 2 /d 2 plasmas. *New Journal of Physics*, 19(2):025010, 2017.

[17] R. Gutser, C. Wimmer, and U. Fantz. Work function measurements during plasma exposition at conditions relevant in negative ion sources for the iter neutral beam injection. *Review of Scientific Instruments*, 82(2):023506, 2011.

[18] D. Wünderlich, S. Dietrich, and U. Fantz. Application of a collisional radiative model to atomic hydrogen for diagnostic purposes. *Journal of Quantitative Spectroscopy and Radiative Transfer*, 110(1):62 – 71, 2009.

[19] T. Launoy. *Étude de réactions astrochimiques impliquant des paires d'ions (Unpublished doctoral dissertation)*. PhD thesis, Université libre de Bruxelles, Faculté des Sciences – Chimie, Bruxelles, Augustus 2018.

[20] Baptiste Fabre. *Paquets d'onde vibrationnels créés par ionisation de* H_2 *en champ laser intense*. PhD thesis, Université Catholique de Louvain, Faculté des Sciences, Département de Physique, December 2005.

[21] Nzeyimana Théodore. *Étude expérimentale de l'association ionisante entre l'ion* O^- *et divers ions positifs (*D^+*,* C^+*,* N^+*,* O^+*,* H_2^+*,* CO^+ *et* N_2^+*)*. PhD thesis, Université Catholique de Louvain, Faculté des Sciences, Département de Physique, mai 2003.

[22] Staicu Casagrande, T Nzeyimana, EA Naji, Nathalie de Ruette, B Fabre, Arnaud Le Padellec, and Xavier Urbain. Abstraction and insertion mechanisms in reactive collisions of H_2^+ and D_2^+ with O^-. *The European Physical Journal D - Atomic, Molecular, Optical and Plasma Physics*, 31, 12 2004.

[23] F. Brouillard and J.W. McGowan. *Physics of Ion-Ion and Electron-Ion Collisions*. Nato ASI Subseries B:. Springer US, 2013.

[24] Mohandas Pillai, Joshua Goglio, and Thad G. Walker. Matrix numerov method for solving schrödinger's equation. *American Journal of Physics*, 80(11):1017–1019, 2012.

[25] Vola Masoandro Andrianarijaona. *Mesure de l'énergie interne d'ions moléculaires par imagerie à trois dimensions, Application aux réactions d'ionisation associative d'atomes métastables*. PhD thesis, Université Catholique de Louvain, Faculté des Sciences, Département de Physique, Unité de physique atomique et moléculaire, July 2002.

[26] Nathalie de Ruette. *Sélectivité rovibrationnelle de l'ionisation de H_2 en champ laser intense, Analyse détaillée de la dissociation induite par électron ou photon d'ions H_2^+ préparés par laser.* PhD thesis, Université Catholique de Louvain, Faculté des Sciences, Département de Physique, december 2007.

[27] Dik De Bruijn. *Dissociative charge exchange of H_2^+ investigated with a two-particle-detector*. PhD thesis, FOM-Institute for Atomic and Molecular Physics, The Netherlands, December 1983.

[28] C. Cohen-Tannoudji, B. Diu, and F. Laloë. *Mecanique quantique*. Number vol. 1 in Collection Enseignement des sciences, 16. Masson, 1973.

[29] M J. J. Eerden, M.C.M. Sanden, D K. Otorbaev, and Daan Schram. Cross section for the mutual neutralization reaction $H_2^+ + H$, calculated in a multiple-crossing landau-zener approximation. *Physical review. A*, 51:3362–3365, 05 1995.

[30] Chang-Lun Liu, J G Wang, and R.K. Janev. Mutual neutralization in slow H_2^+H collisions. *Journal of Physics B: Atomic, Molecular and Optical Physics*, 39:1223, 02 2006.

[31] Gordon H. Dunn. Photodissociation of H_2^+ and D_2^+: Theory. *Physical Review - PHYS REV X*, 172:1–7, 08 1968.

[32] M O Abdellahi El Ghazaly, J Jureta, X Urbain, and P Defrance. Total cross sections and kinetic energy release for the electron impact dissociation of H_2^+ and D_2^+. *Journal of Physics B: Atomic, Molecular and Optical Physics*, 37(12):2467, 2004.

[33] U. Galster, F. Baumgartner, U. Müller, H. Helm, and M. Jungen. Experimental and quantum-chemical studies on the three-particle fragmentation of neutral triatomic hydrogen. 72(6):062506, December 2005.

UNIVERSITÉ CATHOLIQUE DE LOUVAIN
École polytechnique de Louvain
Rue Archimède, 1 bte L6.11.01, 1348 Louvain-la-Neuve, Belgique | **www.uclouvain.be/epl**